

# Energy Optimization of a Solar-Thermal Driven Ejector Refrigeration System

Nkosinathi Shongwe

A dissertation submitted to the Faculty of Engineering and the Built Environment, University of the Witwatersrand, Johannesburg, in fulfilment of the requirements for the degree of Master of Science in Engineering.

Johannesburg, January 2021

# Declaration

I declare that this dissertation is my own, unaided work, except where otherwise acknowledged. It is being submitted for the degree of Master of Science in Engineering in the University of the Witwatersrand, Johannesburg. It has not been submitted before for any degree or examination at any other university.

Signed this 22nd day of January 2021

A handwritten signature in black ink, appearing to read 'Nkosinathi Shongwe', written in a cursive style.

Nkosinathi Shongwe

# Acknowledgements

I would like to thank the Almighty God for blessing me with endless support which saw me through various challenging times during the course of my studies. Without His protection and guidance, this work would have not been successful.

I would like to thank the following people who made this dissertation possible:

Dr Aggrey Mwesigye and Dr Hammed Roohani for their non ending patience, guidance, encouragement, and supervision which was very important in seeing this study through.

I would also like to thank my postgraduate colleagues for their support and motivational inspiration which was vital in completing this study.

Lastly, I would like to thank my family for their non ending support and encouragement throughout my studies.

# Abstract

The performance of a solar thermal powered Ejector Refrigeration System (ERS) is highly dynamic and is greatly affected by the solar and weather conditions under the considered location. From previously conducted studies, it has been shown that the performance of the system is also highly dependent on the type of working fluid considered. However, investigations on suitable working fluid selection have shown that there is a significant gap in finding working fluids that deliver high Coefficient of Performance (COP) values whilst being environmentally friendly and non hazardous. Moreover, the dynamic performance of the ERS under South African solar and weather conditions is not well documented compared to other locations across the globe.

With the goal of studying the dynamic performance of the ejector refrigeration system, a steady state, real gas model of the ejector was developed in Engineering Equation Solver (EES). The steady state model was validated against published data for R134a, R245fa, R290, and R1234ze(Z). R1234ze(Z) was considered as the adequate working fluid as it gave high COP values and is an environmentally benign refrigerant. The developed model was then coupled with a transient system simulation software (TRNSYS) for observation and optimization under variable solar radiation and ambient conditions experienced in Johannesburg, Durban, Upington, Bloemfontein and Cape Town.

Findings from the study showed how optimal performance was also affected by the slope of the solar collectors, the size of the collector surface area, and the capacity of the hot water storage tank. Optimization was conducted by varying the size of the solar collectors, slope of the solar collectors, and the storage capacity of the hot water tank to achieve optimal performance. During the optimization process, the key performance indices are the system's Coefficient of Performance, Generator Temperature, and Critical Condenser Temperature. Location based analysis of the solar ERS showed that the system is best suited for locations with low ambient temperatures. From the cities considered, Johannesburg and Cape Town provided the highest Overall Coefficient of Performance values over the 24 hour period with respective daytime averages of 0.334 and 0.345. The ERS in Bloemfontein closely follows the performance of systems in Johannesburg and Cape Town (especially between 8:00 and 10:00), with a daytime average overall coefficient of performance value of 0.279 which is due to low ambient temperatures. Thereafter, the overall system coefficient of performance values degrade to become similar to those experienced in Durban (with daytime average values of 0.237) due to high ambient temperature values which require system operation at high generator temperature values. The Upington ERS attains the lowest overall system coefficient of

performance values (with a daytime average of 0.187) as a result of the extremely high ambient temperature values which demand system operation at high generator temperature values.

The general conclusion of the study is that the optimal performance of the solar-powered ejectors is achieved in areas with low ambient temperatures (Johannesburg and Capetown) as they allow for system operation at low TG values. Low-performance figures are achieved in Upington as a result of high ambient temperatures which require the system to operate at high generator temperature. To achieve high generator temperatures, the system is required to have large solar collectors (44 sq meters) which have to be coupled to a large hot storage tank (6 cubic meters) to achieve prolonged operation hours.

## Published Work

N. Shongwe, A. Mwesigye, and H. Roohani., Performance Analysis and Optimization of a Solar Driven R134a Ejector Refrigeration System, *In Conference Proceedings of the 6th Southern African Solar Energy Conference SASEC 2019*, November 25-27, 2019, East London, South Africa, ISBN = 978-0-7972-1825-3, Paper ID. 26.

# Contents

<b>Declaration</b>	<b>i</b>
<b>Acknowledgements</b>	<b>ii</b>
<b>Abstract</b>	<b>iii</b>
<b>Published Work</b>	<b>v</b>
<b>Nomenclature</b>	<b>xi</b>
<b>List of Acronyms</b>	<b>xiii</b>
<b>1 Introduction</b>	<b>1</b>
1.1 Background Information . . . . .	1
1.2 Problem Statement . . . . .	4
1.3 Objectives . . . . .	5
1.3.1 Overall Objectives . . . . .	5
1.3.2 Specific Objectives . . . . .	5
1.4 Significance of the Research . . . . .	5
1.5 Research Methodology . . . . .	7
1.6 Outline of the Dissertation . . . . .	7
<b>2 Literature Review</b>	<b>9</b>
2.1 Introduction . . . . .	9
2.2 Conventional Vapour Compression Cooling System . . . . .	9
2.3 Solar Electric: Photovoltaic (PV) Powered Refrigeration Systems . . . . .	11
2.4 Heat-Driven Refrigeration Systems . . . . .	13
2.4.1 Absorption Refrigeration Systems . . . . .	13
2.4.2 Desiccant Systems . . . . .	14
2.4.2.1 Solid Desiccant Systems . . . . .	14
2.4.2.2 Liquid Desiccant Systems . . . . .	16
2.4.3 Adsorption Systems . . . . .	17
2.4.4 The Ejector Refrigeration System . . . . .	18
2.4.4.1 The Ejector Device . . . . .	20

2.4.4.2	Performance Studies of the Ejector Refrigerator . . . . .	21
2.4.4.3	The solar-driven Ejector Refrigerator . . . . .	23
2.4.4.4	The solar-powered Ejector Studies . . . . .	24
2.4.4.5	Solar Collector Consideration for solar-powered Ejector Re- frigerators . . . . .	24
2.4.4.6	Working Fluid Selection on Ejector Refrigeration Systems . .	27
2.4.4.7	Alternative Applications of the Ejector . . . . .	28
2.4.5	Modified Ejector Coupled Studies . . . . .	29
2.5	Solar Energy Within South Africa . . . . .	30
<b>3</b>	<b>Numerical Modelling and Validation of Ejector Refrigeration System</b>	<b>31</b>
3.1	Introduction . . . . .	31
3.2	The Ejector Model . . . . .	32
3.3	Model Validation . . . . .	38
3.3.1	Validation of the R1234ze(Z) Ejector Performance . . . . .	38
3.3.2	Validation of EES Ejector Model for R134a . . . . .	39
3.3.3	Validation of R245fa Ejector Model . . . . .	39
3.3.4	Validation of EES Ejector performance: R290 . . . . .	40
<b>4</b>	<b>Development and Validation of TRNSYS Model</b>	<b>42</b>
4.1	Introduction . . . . .	42
4.2	The solar-powered Ejector Refrigeration System Model . . . . .	42
4.3	TRNSYS Components Modelling . . . . .	45
4.3.1	Hot Water Storage Tank Model . . . . .	45
4.3.2	Evacuated Tube Collectors Model . . . . .	46
4.3.3	Weather Data Model . . . . .	47
4.3.4	Flow Circulation Pump Model . . . . .	47
4.3.5	TRNSYS Ejector Modelling . . . . .	47
4.3.6	Energy Balance Calculator . . . . .	48
4.4	TRNSYS Model Validation . . . . .	49
4.4.1	Validation of Solar Collector and Weather File Coupling . . . . .	49
4.4.2	Validation of the Solar Thermal System . . . . .	50
<b>5</b>	<b>Results and Discussion</b>	<b>53</b>
5.1	Steady-State Analysis of the Ejector Refrigeration System . . . . .	53
5.1.1	Analysis of R134a ERS in Critical Mode . . . . .	53
5.1.1.1	Effect of EAR, Generator Temperature and Evaporator Tem- perature on ERS Performance . . . . .	53
5.1.1.2	Analysis of R134a ERS in Sub-critical Mode . . . . .	58
5.1.2	Performance Analysis of the R1234ze(Z) Ejector . . . . .	60



5.2	Parametric Analysis of the R1234ze(Z) Solar Thermal Ejector . . . . .	62
5.3	Ejector performance results in Johannesburg . . . . .	62
5.4	Ejector performance results in Upington . . . . .	73
5.5	Ejector performance results in Durban . . . . .	84
5.5.1	Solar Fraction Analysis . . . . .	88
5.6	Ejector performance results in Cape Town . . . . .	91
5.6.1	Solar Collector Optimization . . . . .	97
5.7	Ejector performance results in Bloemfontein . . . . .	99
5.8	$COP_{overall}$ Analysis for Cape Town and Upington . . . . .	109
5.9	$COP_{overall}$ Analysis for Johannesburg, Durban, and Bloemfontein . . . . .	112
<b>6</b>	<b>Conclusions and Recommendations</b>	<b>119</b>
6.1	Conclusions . . . . .	119
6.2	Recommendations . . . . .	122
<b>7</b>	<b>References</b>	<b>129</b>

# List of Figures

1	Solar cooling technologies [19] . . . . .	3
2	A schematic of a vapour compression cycle with a T-S diagram [48] . . . . .	10
3	Schematics of various PV powered cooling systems [20] . . . . .	12
4	A schematic of a desiccant system[53] . . . . .	15
5	A schematic of a liquid desiccant system . . . . .	17
6	The ejector refrigeration System . . . . .	18
7	A schematic of the ejector [40] . . . . .	20
8	A schematic of a modified ejector compression cycle [68]. . . . .	29
9	A schematic of flow through an ejector[60] . . . . .	32
10	Solar cooling technologies [19] . . . . .	37
11	TRNSYS layout of a solar thermal ERS . . . . .	42
12	Details of the ejector performance data when stored in the Type 42a data file . . . . .	48
13	Collector Exit Temperature variation at different collector areas . . . . .	52
14	Tank Exit Temperatures at different Tank Storage Volumes . . . . .	52
15	Effect of Ejector Area Ratio (EAR) on performance at $T_g = 75^\circ\text{C}$ . . . . .	54
16	Effect of EAR on performance at $T_g = 85^\circ\text{C}$ . . . . .	55
17	Variation of $\mu$ at $T_g = 80^\circ\text{C}$ and variable EAR and $T_e$ . . . . .	55
18	Variation of $\mu$ at EAR of 3.32, variable $T_g$ and $T_e$ . . . . .	56
19	Effect of EAR on performance at $T_g = 75$ . . . . .	57
20	Effect of EAR on performance at $T_g = 85$ . . . . .	58
21	Variation of $\dot{Q}_{cool}$ and $T_c$ . . . . .	59
22	Variation of COP and $T_c$ . . . . .	59
23	Variation of $\dot{Q}_{cool}$ and $T_c$ . . . . .	60
24	Variation of COP and $T_c$ . . . . .	60
25	Effect of EAR on performance at $T_g = 85^\circ\text{C}$ . . . . .	61
26	Performance of an R1234ze(Z) ejector at various $T_g$ and ambient adjusted $T_c$ . . . . .	61
27	Variation of the ejector's COP at different $A_{Coll}$ . . . . .	63
28	Variation of $T_g$ with $A_{Coll}$ . . . . .	64
29	Variation of $T_c^*$ with $A_{Coll}$ . . . . .	65

30	COP variation at different $Vol_{Tank}$ with $A_{Coll} = 36$ . . . . .	66
31	$T_g$ at various $Vol_{Tank}$ capacities, $A_{Coll} = 36 m^2$ . . . . .	66
32	$\dot{Q}_{cool}$ at various $Vol_{Tank}$ capacities with $A_{Coll} = 36$ . . . . .	67
33	$T_c^*$ at different $Vol_{Tank}$ , $A_{Coll} = 36$ . . . . .	68
34	COP & $\eta_{coll}$ at different $Vol_{Tank}$ Capacities . . . . .	68
35	$COP_{overall}$ at different $Vol_{Tank}$ Capacities . . . . .	69
36	$T_c^*$ at different $A_{Coll}$ slope angles . . . . .	70
37	$T_g$ variation at different $A_{Coll}$ slope angles . . . . .	71
38	COP variation at different $A_{Coll}$ angles . . . . .	71
39	COP and $\eta_{coll}$ variation at $A_{Coll}$ slope angles . . . . .	72
40	$COP_{overall}$ variation at different $A_{Coll}$ Slopes . . . . .	72
41	COP at different tank boiling point limits . . . . .	73
42	$T_c^*$ variation at different tank boiling point limits . . . . .	74
43	$T_g$ variation at different tank boiling point limits . . . . .	75
44	$T_g$ variation at different $A_{Coll}$ sizes . . . . .	75
45	COP variation at different $A_{Coll}$ sizes . . . . .	76
46	$T_c^*$ behaviour at different $A_{Coll}$ sizes . . . . .	77
47	$T_g$ at different tank sizes, $A_{Coll}$ and $Vol_{Tank}$ . . . . .	78
48	COP at plot different $Vol_{Tank}$ and $A_{Coll}$ . . . . .	79
49	$T_c^*$ at different tank sizes, $A_{Coll}$ and $Vol_{Tank}$ . . . . .	80
50	$\eta_{coll}$ & COP variation at different $A_{Coll}$ & $Vol_{Tank}$ . . . . .	80
51	$COP_{overall}$ variation at different $A_{Coll}$ & $Vol_{Tank}$ . . . . .	80
52	$T_g$ variation at different $Vol_{Tank}$ , $A_{Coll}$ . . . . .	82
53	$T_c^*$ variation at different $Vol_{Tank}$ , $A_{Coll}$ . . . . .	82
54	$T_c^*$ variation at different collector slope angles . . . . .	83
55	$T_g$ variation at different collector slope angles . . . . .	83
56	COP variation at different Collector Slope Angles . . . . .	83
57	$\eta_{coll}$ & COP variation at different collector slope angles . . . . .	83
58	$COP_{overall}$ variation at different collector slope angles . . . . .	84
59	COP variation at different $A_{Coll}$ and $Vol_{Tank}$ . . . . .	85
60	$T_c^*$ variation at different $A_{Coll}$ and $Vol_{Tank}$ . . . . .	86
61	$T_g$ variation at different $A_{Coll}$ , $Vol_{Tank}$ . . . . .	86
62	COP variation at different $A_{Coll}$ and $Vol_{Tank}$ . . . . .	87
63	$T_c^*$ variation at different $A_{Coll}$ and $Vol_{Tank}$ . . . . .	87
64	$T_g$ variation at different $A_{Coll}$ and $Vol_{Tank}$ . . . . .	87
65	COP & $\eta_{coll}$ variation at different $A_{Coll}$ & $Vol_{Tank}$ . . . . .	89
66	$COP_{overall}$ variation at different $Vol_{Tank}$ . . . . .	89
67	COP variation at different collector slope angles . . . . .	89
68	$T_g$ variation at different collector slope angle . . . . .	90

69	$T_c^*$ variation at different collector slope angles . . . . .	90
70	COP variation at different collector slope angles . . . . .	91
71	$COP_{overall}$ variation at different collector slope angles . . . . .	91
72	COP variation at different $A_{Coll}$ and $Vol_{Tank}$ . . . . .	92
73	$T_g$ variation at different $A_{Coll}$ and $Vol_{Tank}$ . . . . .	93
74	$T_c^*$ variation at different $A_{Coll}$ and $Vol_{Tank}$ . . . . .	93
75	COP variation at different $A_{Coll}$ and $Vol_{Tank}$ . . . . .	94
76	$T_g$ variation at different $A_{Coll}$ and $Vol_{Tank}$ . . . . .	95
77	$T_c^*$ variation at different $A_{Coll}$ and $Vol_{Tank}$ . . . . .	96
78	COP & $\eta_{coll}$ variation at different $A_{Coll}$ and $Vol_{Tank}$ . . . . .	97
79	$COP_{overall}$ variation at different $A_{Coll}$ & $Vol_{Tank}$ . . . . .	97
80	COP variation at different collector slope angles . . . . .	97
81	$T_c^*$ variation at different collector slope angles . . . . .	98
82	$T_g$ variation at different collector slope angles . . . . .	98
83	COP & $\eta_{coll}$ variation at different Collector slope angles . . . . .	99
84	$COP_{overall}$ variation at different collector slope angles . . . . .	99
85	COP variation at different $A_{Coll}$ with $Vol_{Tank} = 4 m^3$ . . . . .	100
86	$T_c^*$ variation at different $A_{Coll}$ with $Vol_{Tank} = 4 m^3$ . . . . .	100
87	$T_g$ variation at different $A_{Coll}$ with $Vol_{Tank} = 4 m^3$ . . . . .	101
88	$T_g$ variation at different $A_{Coll}$ and $Vol_{Tank}$ . . . . .	102
89	COP variation at different $A_{Coll}$ and $Vol_{Tank}$ . . . . .	103
90	$T_c^*$ variation at different $A_{Coll}$ and $Vol_{Tank}$ . . . . .	103
91	COP & $\eta_{coll}$ variation at $A_{Coll} = 36 m^2$ with variable $Vol_{Tank}$ . . . . .	104
92	$COP_{overall}$ variation at $A_{Coll} = 36 m^2$ with variable $Vol_{Tank}$ . . . . .	105
93	COP variation at different collector slope angles . . . . .	106
94	$T_g$ variation at different collector slope angles . . . . .	107
95	$T_c^*$ variation at different collector slope angles . . . . .	107
96	COP & $\eta_{coll}$ variation at different collector slope angles . . . . .	107
97	$COP_{overall}$ variation at different collector slope angles . . . . .	108
98	Overall COP variation at different $A_{Coll}$ , $Vol_{Tank} = 3 m^3$ . . . . .	109
99	Optimized $COP_{overall}$ variation at Cape Town and Upington . . . . .	110
100	$T_g$ variation at Cape Town and Upington . . . . .	112
101	$T_c^*$ variation at Cape Town and Upington . . . . .	112
102	Optimized $COP_{overall}$ variation in Bloemfontein, Durban, and Johannesburg . . . . .	113
103	$T_g$ variation across Bloemfontein, Durban, and Johannesburg . . . . .	114
104	$T_c^*$ and $T_c$ variation in Johannesburg . . . . .	114
105	$T_c^*$ variation in Durban . . . . .	115
106	$T_c^*$ variation in Bloemfontein . . . . .	115
107	$T_c^*$ and $T_{am}$ variation in Bloemfontein, Durban, and Johannesburg . . . . .	116

108	Optimized $COP_{overall}$ variation across Cape Town, Bloemfontein, and Johannesburg . . . . .	117
109	$T_c^*$ and $T_{am}$ variation in Johannesburg and Cape Town . . . . .	118
110	$T_g$ variation in Johannesburg and Cape Town . . . . .	118
111	Upington optimal collector slope angle . . . . .	130
112	Durban optimal collector slope angle . . . . .	131
113	Cape Town optimal collector slope angle . . . . .	132
114	Bloemfontein optimal collector slope angle . . . . .	133
115	Johannesburg optimal collector slope angle . . . . .	134

# List of Tables

3	Theoretical studies on the ERS . . . . .	23
4	Review of solar-powered ERS studies . . . . .	26
5	ERS working fluid selection (Adopted From [22, 66]) . . . . .	27
6	Validation of the R1234ze(Z) ejector performance . . . . .	38
7	Validation of R134a ejector model . . . . .	39
8	Performance data for an R245fa ejector model . . . . .	40
9	Effect of $T_g$ on the critical $T_c$ at fixed $T_e$ (8 °C) . . . . .	40
10	Validation of the effect of $T_e$ on the COP at the $T_g$ of 90 °C . . . . .	41
11	System components and their specified values . . . . .	44
12	Collector operating parameters . . . . .	50
13	Annual useful energy gain at various collector slope angles . . . . .	50
14	Ejector geometry specification [60] . . . . .	53
15	Ejector geometry [28] . . . . .	60
16	Optimised system configuration . . . . .	109
17	Optimized system configuration . . . . .	113
18	Optimized system configuration . . . . .	117

# Nomenclature

$A_{Coll}$	Collector Surface Area, [m <sup>2</sup> ].
$A$	Collector Area, [m <sup>2</sup> ].
$COP_{overall}$	COP of the Solar Powered Ejector.
$CO_2$	Carbon Dioxide.
$Coll_{Fluid}$	Collector Working Fluid.
$F_R$	Overall collector heat removal efficiency factor.
$I_T$	global radiation incident on the solar collector.
$M_{node}$	Mass of fluid in tank node, [kg].
$P_{cc}$	Critical Condenser Pressure, [kPa].
$SO_2$	Sulphur Dioxide.
$T_c$	Condenser Temperature, [°C].
$T_e$	Evaporator Temperature, [°C].
$T_g$	Generator Temperature, [°C].
$T_{am}$	Ambient Temperature, [°C].
$T_c^*$	Critical Condenser Temperature, [°C].
$T_i$	Inlet temperature of fluid to collector, [°C].
$T_o$	Outlet temperature of fluid to collector, [°C].
$U_{L/T}$	Thermal Loss - Temperature Dependency Coefficient, [°C].
$U_L$	Overall thermal loss coefficient of the collector per unit Area, [m <sup>2</sup> ].
$Vol_{Tank}$	Storage Tank Volume.
$\Delta T_{nodal}$	Temperature difference across the node, [°C].
$\dot{Q}_{Cooling}$	Evaporator Cooling Capacity, [kW].
$\dot{Q}_{cool}$	Evaporator Cooling Capacity.
$\dot{Q}_u$	Useful Collector Heat Gain, [kW].
$\dot{m}_{max}$	Pump maximum flowrate, [kg/s].
$\dot{m}_{net}$	Net mass flowrate into tank node, [kg/s].
$\dot{m}_o$	Pump outlet flow rate.
$\dot{m}_p$	motive fluid mass flow-rate, [kg/s].
$\eta_{coll}$	Efficiency of Collector.
$\mu$	entrainment ratio.

$\tau\alpha_n$	Product of the cover transmittance and the absorber absorptance at normal incidence.
$a_0$	Intercept Efficiency.
$a_1$	Negative of first order efficiency coefficient.
$a_2$	Negative of second order efficiency coefficient.
$a_t$	primary nozzle throat velocity, [m/s].
$T_{out,pump}$	Pump Outlet Temperature, [°C].
$C_p$	Specific Heat Capacity at Constant Pressure, [kJ/kg·K].
M	Molecular Mass.
STR	System Thermal Ratio.
$U_{Gen}$	Generator Heat Transfer Coefficient.



# List of Acronyms

1-D	one-dimensional.
ALT	atmospheric lifetime.
CFCs	chlorofluorocarbons.
COP	Coefficient of Performance.
CPV	Concentrating Photovoltaic.
CSP	Concentrating Solar Power.
DHI	Diffuse Horizontal Irradiance.
DNI	Direct Normal Irradiation.
EAR	Ejector Area Ratio.
EES	Engineering Equation Solver.
ERS	Ejector Refrigeration System.
ETC	Evacuated Tube Collectors.
FPC	flat plate collectors.
GHI	Global Horizontal Irradiance.
GWP	global warming potential.
HCFCs	hydrochlorofluorocarbons.
HFCs	hydrofluorocarbons.
HFOs	Hydrofluoroolefins.
HVAC	Heating, Ventilation and Air Conditioning.
IAM	Incident Angle Modifier.
ODP	ozone depletion potential.
PV	Photovoltaic.
SF	Solar Fraction.

TMY2 Typical Meteorological Year 2.

# 1 Introduction

## 1.1 Background Information

Over the past years, the South African electricity utility company (ESKOM) has been struggling to provide cheap and reliable electricity [1]. Insufficient electricity supply has resulted in recurring power cuts over the past years [2, 3]. The cause of power interruptions has been attributed to delays in the completion of additional power stations and poor reliability of the old power stations [4]. One of the outcomes of inadequate and expensive electricity supply has been the decline in economic activity and growth within South Africa [5]. This is because the escalating cost of electricity has marginalised profits of small business entities whilst the inadequate supply has also affected operations in large scale industries such as the mining and manufacturing sector [6]. Inadequate electricity supply does not only affect the economic hubs but also affects the rural areas since these areas continue to have no access to electricity. The rural electrification rate is at 77% and the lack of funding for developing more transmission infrastructure and generating more electricity means that approximately three million people remain without access to electricity [4].

Considering that a significant percentage (about 90%) of the electricity available within South Africa is coal-generated, the country experiences high pollutant emissions ( $CO_2$ ,  $SO_2$ , particulate matter, and Nitrogen oxide) from the combustion of fossil fuel (coal and diesel) [4, 7]. Such emissions are known to have detrimental effects on human health which can even result in shortened life expectancy due to exposed people experiencing lung cancer, strokes, heart attacks, and even birth defects[8]. The high levels of pollution and subsequent health hazards experienced around coal-fired power stations has motivated environmental rights organisations to take legal action against the South African government for failing to enforce stringent laws against ESKOM's emissions [9].

High emissions of  $CO_2$ , which is a greenhouse gas, are a major contributor to global warming. In 2015, South Africa was responsible for close to half of Africa's greenhouse gas emissions which also meant that the country ranked 12th in the global list of large  $CO_2$  emitters [10]. As a developing continent, Africa is considered to be in one of the most vulnerable continents when it comes to experiencing the effects of climate change. This is because most of the farming activities are highly dependent on weather conditions which means that food scarcity is likely to be a major outcome of climate change. Subsequent occurrences will be malnutrition which will likely increase the occurrence and widespread of diseases. Extreme

weather conditions such as floods, droughts, and destructive storms are an anticipated outcome which is going to affect various infrastructure and crop production as well [11]. As a continent that is currently faced with development challenges ( such as low Global Warming Potential (GDP) per capita, low infrastructural development and widespread poverty), the implementation of some of the required mitigation strategies to counteract the anticipated impact of climate change are not likely to be implemented [11].

Taking into account the above challenges, it is apparent South Africa's electricity supply has to be increased to cater for the high demand [12]. Future supply provisions have to account for the continuously increasing population of the country as it equates to an increase in electricity demand [12]. It is also evident that electricity generation from fossil fuel combustion is not sustainable and harms both the environment and human health. Alternative, clean and renewable, forms of energy are the only plausible source of electricity as they do not pose any form of danger against the environment and human health. Currently, renewable energy accounts for 10% (4981 MW) of South Africa's electric energy mix with the leading source of energy being wind power [4].

An analysis of electricity usage within the commercial sector shows that Heating, Ventilation and Air Conditioning (HVAC) systems account for 26 % of total consumption whilst the industrial sector uses about 20 % [13]. These figures highlight the energy-intensive nature of HVAC equipment which inherently makes it the largest single end-use contributor to energy demand [13]. For developed countries (such as UAE, USA, and the UK), electricity usage for HVAC applications is above 50% of total energy consumption within the residential sector [14]. Globally, energy consumption within buildings amounts to 40% of the total global energy consumption [15, 16]. While the South African energy usage values on HVAC equipment seem to be low, when compared to the overall global values, one can anticipate an increase as urbanization and improved lifestyle requirements spread throughout various parts of the country.

Since thermal comfort is a requirement of a comfortable and productive environment, it is evident that alternative methods of delivering thermal comfort without consuming excessive electricity are worth exploring. Part of these solutions can be implemented through the design of passive cooling and heating buildings whereby thermal comfort is achieved without heavily relying on mechanical equipment [17]. This form of cooling technique requires careful selection of building materials and the provision of air pathways within the building which will respectively dissipate heat quickly and channel any undesired heat out of the building [18]. In cases where this technology can not guarantee effective cooling or heating of occupied building spaces, mechanical powered cooling systems are required [17]. Mechanical driven cooling systems are reliable and effective compared to passive systems and hence they

dominate the global air conditioning market[17]. However, the high energy intensity nature of mechanical driven systems highlights the motivation of finding alternative methods of space conditioning.

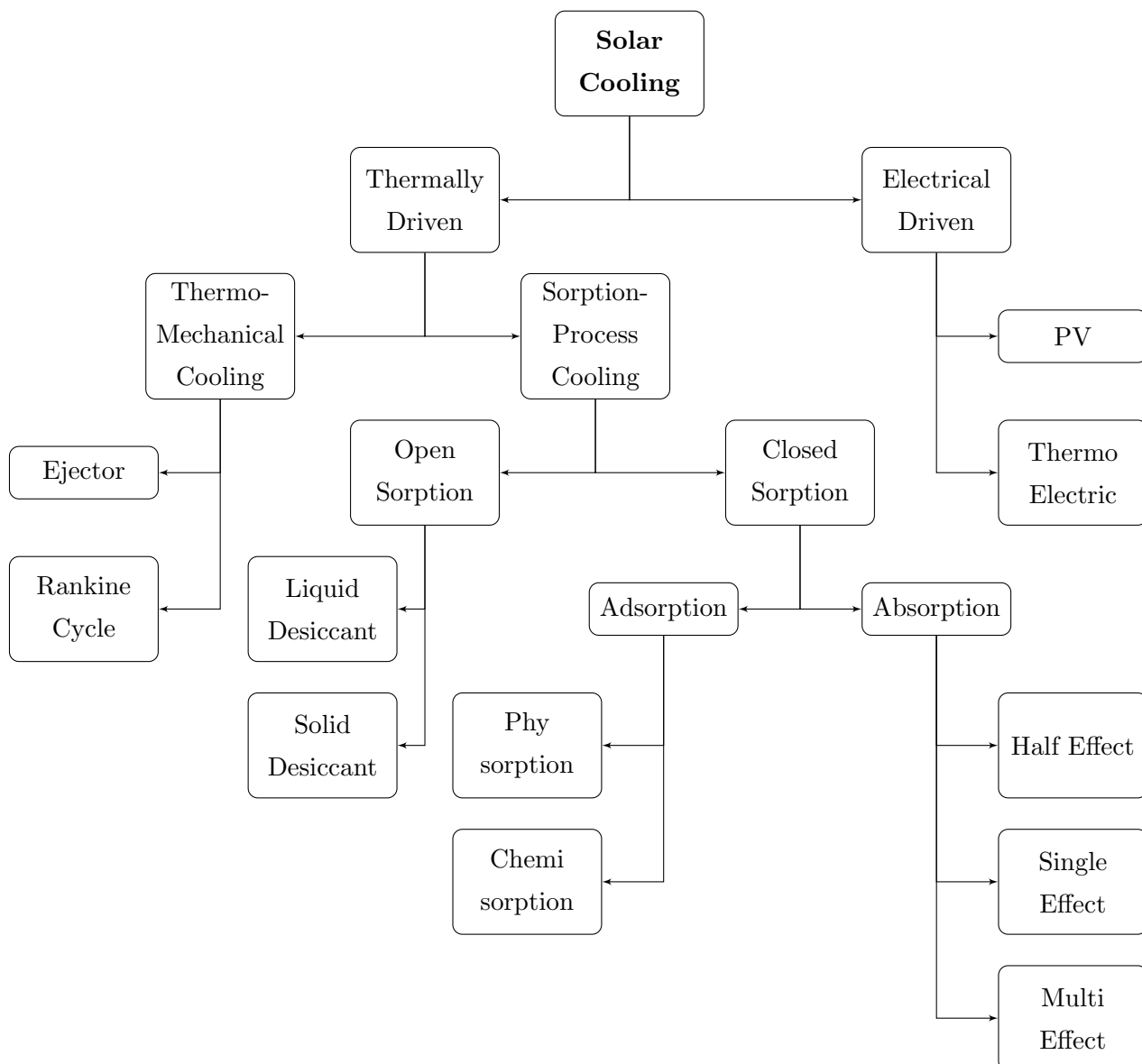


Figure 1: Solar cooling technologies [19]

Solar-powered cooling technologies form part of alternative space conditioning technologies [20, 21]. Figure 1 shows that solar cooling systems can be split into two categories, thermally driven and electrically driven with the former being divided to thermo-mechanical and sorption process cooling [19]. These systems offer the benefit of achieving space cooling without the heavy use of electricity [20, 12]. This then relates to a reduction in cooling costs and fossil fuel emissions in cases where electricity production is from coal. In some of these technologies, the advantage of using environmentally friendly working fluids is also realised. Such

working fluids are characterized by having low ozone depletion potential (ODP) and global warming potential (GWP) which helps in terms of minimizing any negative impact on the environment [22].

Fortunately for South Africa, the country has an abundant solar energy resource [7, 23]. Annually, most parts of the country receive Direct Normal Irradiation (DNI) radiation exceeding 2100 kW/m<sup>2</sup> with the hottest areas of the country (the Northern Cape) receiving over 3000 kW/m<sup>2</sup>, annually [23]. Such solar radiation has been evaluated and proven to be ideal for generating Concentrating Solar Power (CSP) powered electricity [23, 24]. An assessment of the generation of electricity through CSP technology in ideal locations within South Africa found that the electricity generation potential was at 547.6 GW [25]. This figure exceeds South Africa's 2025 anticipated electricity demand three to five folds [25]. The abundance of solar radiation within this region enhances the chances of achieving good performance in solar cooling systems as there would be abundant driving energy. Simultaneous exploitation of alternative (less electricity-intensive) space conditioning systems would also assist in reducing the high electricity demand within the country which would inherently result in less greenhouse gas emissions.

However, the efficient performance of solar cooling technologies is also reliant on the ambient conditions of the location being considered [19]. The ERS, the principal system considered in this study, is highly dependant on the evaporator temperature ( $T_e$ ), condenser temperature  $T_c$ , and generator temperature ( $T_g$ ) [26, 27]. These parameters vary according to ambient temperatures (affects  $T_c$ ) and the availability of thermal energy (affects  $T_g$ ) which are both directly dependent on the intensity of solar radiation. With more attention being focused towards the use of environmentally friendly working fluids, several studies have investigated the behaviour of the ERS under environmentally benign refrigerants [28, 29]. Due to the lack of published information on the performance of a solar-powered ERS under South African weather conditions, the feasibility of using this system is an unknown [30]. Compared to other solar cooling technologies, the ERS experiences low COP values which are further reduced when the system is powered by solar thermal energy [31, 32]. Optimization studies have shown the importance of using appropriate ejector geometries, solar collector type, solar collector sizes, and storage tank sizes to achieve high overall system COP values [33, 34, 35, 36].

## 1.2 Problem Statement

Solar-powered ejector refrigeration systems are widely known for low COP values which limits their application for heating and cooling purposes. However, several studies have shown the

potential of achieving improved system performance through parametric analysis and optimization of setup components [26, 36, 27]. Moreover, the system's dependence on location-based weather conditions (ambient temperature and solar radiation) affects the amount of harvested solar thermal energy, which determines the exact operating generator and condenser temperatures. To accurately model the thermal inertia effects of the system due to highly variable solar radiation and ambient temperatures, a transient solar thermal model of the system has to be coupled to the ejector refrigeration system. Considering the lack of published studies on the transient behaviour of solar-powered ejector systems under South African conditions, optimized performance of such a system remains unknown.

## 1.3 Objectives

### 1.3.1 Overall Objectives

The overall objective of the work is to study and optimize the performance of a solar thermal ejector refrigeration system operating under the solar irradiation and ambient temperatures that are experienced in the South African cities of Johannesburg, Durban, Upington, Bloemfontein and Cape Town.

### 1.3.2 Specific Objectives

The specific objectives of this project are:

- Develop and validate a thermodynamic model of a solar thermal ejector refrigeration system using an environmentally friendly working fluid.
- Investigate the transient performance of the solar thermal ejector refrigeration system operating within the considered cities.
- Optimize the performance of the solar thermal ejector refrigeration system to suit the high solar irradiation values and ambient conditions experienced within the considered locations.

## 1.4 Significance of the Research

The availability of cheap and reliable electricity supply has been a major issue within South Africa [1, 2, 3]. The country's electrification rate currently sits at 77% meaning there are about 3 million individuals who do not have access to utility-supplied electricity [4]. A breakdown of electricity usage within South Africa indicates that about 26% of produced electricity

is used for HVAC applications [13]. These figures highlight the great usage of electricity to provide thermal comfort through the operation of HVAC equipment in the commercial and residential sectors. Considering that thermal comfort is a prerequisite for ensuring productive space occupation, investigations on how to cheaply achieve it are worth exploring [16]. Achieving thermal comfort from renewable and sustainable forms of energy would help with eliminating an increase in electricity demand (and subsequent production) as a result of population growth [16, 14]. This would subsequently reduce greenhouse gas emissions from the combustion of fossil fuel.

Since the demand for air-conditioning is proportional to solar radiation, utilizing solar energy is a logical way to meet the increasing demand for cooling[37]. Upon reviewing most solar-powered thermal powered cooling technologies, the ERS proves to be the simplest which makes it easier and possibly cheaper to implement [38, 19, 39]. The ejector refrigeration cycle also has an advantage of operating better than the other cycles when utilizing low-grade thermal energy which makes it the best cycle to consider when looking at using solar thermal energy as a heat source [40]. Absorption systems have been previously used but their major issue is that they have high installation and maintenance costs which are primarily due to the limited availability of specialized professionals [20]. Desiccant systems also have a high cost of ownership and another issue of only being suitable for low humidity areas like deserts [20].

In most of the analyses that have been conducted on the ejector cycle, it has been found that increasing the evaporator temperature and also increasing the generator temperature generally results in considerably improved system performance [22, 29, 40]. Both of these factors can be easily achievable within most parts of the South African environment as there is an abundance of high intensity solar thermal energy and the ambient conditions are generally not that extreme [41, 42]. The advantage of the latter being that the evaporator temperature of the system would not have to be at low single-digit temperatures which then promises higher COP values within the South African environment [30].

In comparison to the other solar cooling systems, the ejector has a known disadvantage of low COP values [40], [43],[44] [37]. This issue then requires that the system is optimized by considering the climatic conditions in which it is going to operate on as this will determine the operating temperatures of the generator, ejector, and condenser. Some of the numerous investigations on the optimized performance of a solar ejector cycle have been conducted for the climatic conditions in the Mediterranean [45], Athens [46] and Loughborough [29] whereby the systems were optimized to suit the relevant climatic conditions and hence result in improved performance. This shows that the climatic conditions at the considered geographic location have a major influence on the performance of the cycle. Since the effect of



high-intensity solar irradiation and average ambient air temperature conditions experienced throughout South Africa have not yet been considered, an investigation on the optimized performance of a solar-driven ejector cycle operating under such conditions has to be conducted.

Studies on the selection of environmentally friendly working fluids have indicated that an agreement on which fluid gives the best system performance whilst being safe has not yet been reached [22, 37, 32]. These studies revealed that a compromise usually has to be made between high system performance and on the risk of causing negative environmental impact [22, 47]. This issue highlights the need for investigating the performance of more environmentally friendly working fluids which can possibly result in the high-performance of a solar thermal ejector cycle operating under the high-intensity solar radiation of South Africa.

## 1.5 Research Methodology

Through the existence of high-performance computers, dynamic analysis of both simple and abstract engineering-related problems has become cheaper and easier to perform. Such problems have been accurately analysed through the development of numerical models, simulating the performance of the system without having to perform complex and expensive experiments. This has ensured the generation of accurate results within a short period of time without having to experience the cost-related problems of experiments.

This approach was employed in the current study whereby the performance of a solar-powered refrigeration system was studied. The steady-state performance of the ejector was considered through the development of a mathematical model of the ejector in EES. The model was validated with published data whereby different ejector geometries and operating parameters were considered. The parameters of interest during this process were the critical condenser temperature ( $T_c^*$ ), the coefficient of performance (COP), the entrainment ratio ( $\mu$ ), and the critical condenser pressure ( $P_{cc}$ ). The dynamic analysis of the system was carried out in another numerical analysis software, TRNSYS, whereby the variable effect of both solar radiation and ambient conditions were taken into account. The TRNSYS model was also validated from published data found in literature. Upon validation, the performance of the system was conducted over various locations in South Africa.

## 1.6 Outline of the Dissertation

The dissertation consists of six chapters which are arranged in the following order:

- **Chapter 1** serves as the introduction of the dissertation which entails background information on the ejector, defines the problem statement and objectives. The significance of this topic is also highlighted together with the methodology to be followed.
- **Chapter 2** goes through the literature on various cooling systems with more emphasis on solar-powered systems. Literature on studies conducted on simple ejector refrigerators and solar-driven ejectors is also outlined in this chapter.
- **Chapter 3** covers the steady-state mathematical model of the ejector and its validation across various working fluids. Model validation is based on results found in published papers.
- **Chapter 4** details the development and validation of the TRNSYS model. The mathematical model of the considered system components (collectors, hot water storage tank, and pumps) is briefly described in this section and the operation of the TRNSYS model is described.
- **Chapter 5** shows the results obtained from steady-state and transient analysis of the ejector. The results are analyzed and discussed in this chapter.
- **Chapter 6** has the conclusions that are drawn from the obtained results. Recommendations on the possible improvement of the study are also found on this chapter.

## 2 Literature Review

### 2.1 Introduction

In this chapter, a review of various solar cooling systems is undertaken. A brief description of the different types of solar collectors is also considered. Detailed literature on the analysis of the main system of interest, ERS, will also be given in this section.

### 2.2 Conventional Vapour Compression Cooling System

This type of cooling system is the most popular system used for HVAC and refrigeration purposes. The conventional cooling system is based on the vapour compression cycle (shown in [Figure 2](#)) which makes use of mechanical energy (such as rotary action from an electric motor) to drive a compressor. The function of the compressor is to increase the pressure and temperature of the refrigerant after it has exited the evaporator in vapour form. The temperature increase that is experienced during the compression process enables the occurrence of the heat rejection process within the condenser. During the heat rejection process, the refrigerant undergoes a phase change from superheated vapour (at the condenser inlet) to saturated liquid (at the condenser exit). The saturated liquid then goes through an expansion valve where its temperature and pressure is lowered back to the two-phase region. This two-phase mixture is transferred back to the evaporator where the refrigerant gets to extract heat from the conditioned space. The heat that is added into the refrigerant causes the refrigerant to evaporate again until it has all turned into a saturated vapour mixture where the process restarts itself again.

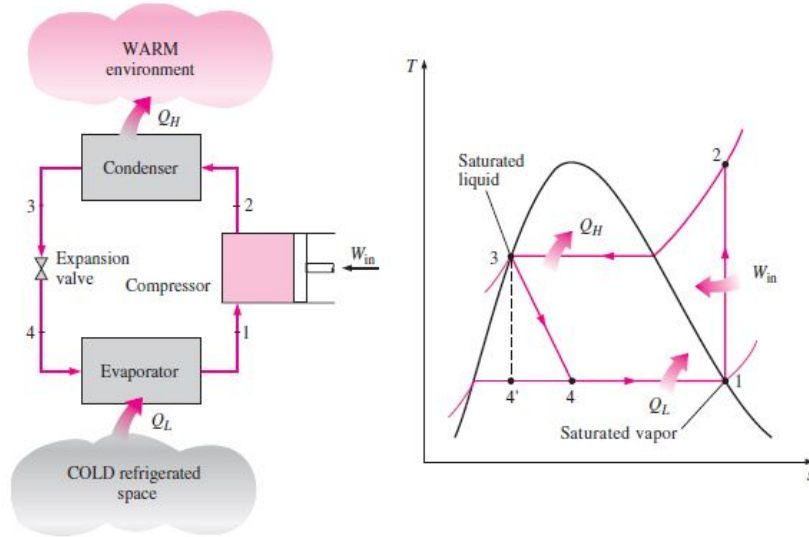


Figure 2: A schematic of a vapour compression cycle with a T-S diagram [48]

This type of cycle is capable of achieving conditioned space temperatures of  $-30\text{ }^{\circ}\text{C}$  depending on the type of refrigerant used [20]. This type of cycle can also operate in reverse mode which means that instead of extracting heat, it can supply heat to a certain environment. The coefficient of performance for such a system is evaluated by taking the ratio of the supplied heat to that of the amount of work supplied and this ratio must always be above one [48]. To achieve improved performance specifications, the cycle can be modified to have an economizer in the form of a flash chamber or a direct contact heat exchanger. The addition of this component results in a system that requires less compression work per unit mass of flow and hence provides improved efficiencies when compared to single-stage compression systems[48]. The flash chamber performs the task of separating liquid part of the refrigerant from the vapour part. The saturated vapour stream is sent to the heat exchanger to mix with another vapour stream exiting the first stage of vapour compression. A single mixed stream exits this heat exchanger at an intermediate temperature to undergo the second stage of compression which leads to the heat rejection process.

Another way of achieving improved performance for the standard vapour compression cycle is to modify it to incorporate an intermediate heat exchanger which connects two vapour compression cycles. This type of arrangement is often referred to as a cascade vapour compression refrigeration cycle. Whilst the refrigerant in the first cycle operates at low temperatures, it rejects heat to the second cycle which operates at higher temperatures. These two cycles usually operate on different refrigerants as they would have to experience different working temperatures and pressure [48].

In South Africa, the use HVAC systems is the largest single end-use electricity consuming

activity within the commercial sector which amount to 26% of the total electricity produced [13]. For the industrial sector, HVAC equipment consumes about 20% of the total electricity. These high electricity consumption rates have been attributed to the intensive nature of HVAC systems in demanding large energy supply which is worsened by misuse and failure of performing adequate maintenance. Some of these factors, especially the maintenance factor, can be a result of the complex nature of the systems as they make use of several individual components such as huge compressors, fans, dampers and intricate control systems. In other countries such as America and Australia, where the use of HVAC systems is more popular as it extends to residential buildings as well, the share of energy consumed by these systems can reach to levels of 50% [13][49].

## 2.3 Solar Electric: PV Powered Refrigeration Systems

Due to the high electricity consumption associated with HVAC systems, alternative cooling systems have been developed as possible alternatives. A special type of these systems are those that utilize the free energy of the sun to directly generate electricity or harvest the heat to increase the pressure and temperature of a certain working fluid. Solar Electric systems make use of photovoltaic cells to convert sunlight to electricity. The electricity is then used to power an electrically driven air conditioner unit. Within this system, there are two main categories which depend on whether the system is connected or not connected to the main power grid. With the grid-connected PV cooling systems, the electricity that is generated by the PV panels is transferred to the main power grid [20]. The independent systems have batteries which store the electricity generated by the panels and the system uses this stored electricity when there is no sunshine for the panels to generate electricity [20]. Within the grid-connected systems, PV cooling is only possible when there is sunshine and in times when there is none, the air conditioning unit operates from the main grid line. Based on the connections of electricity monitoring meters, it is also possible to have two system configurations which are the net metering and FiT (Feed-in Tariff) configurations [20]. In the former configuration, the building in which the panels are installed is fitted with a meter that accounts for the difference between the electricity consumed by the building (from the main grid) and that which is supplied by the PV panels to the building. A schematic of this form of arrangement is shown in [Figure 3a](#). In the Fit configuration (shown in [Figure 3b](#)), two meters are used where one is connected to the PV panels and accounts for the electricity generated by the panels and supplied to the grid, the other meter is connected to the electric equipment and hence accounts for the total electricity consumed by the appliances. In this situation, all the electricity that is generated by the panels is sent to the main grid and the owners of the panels are paid for the electricity they have supplied to the grid.

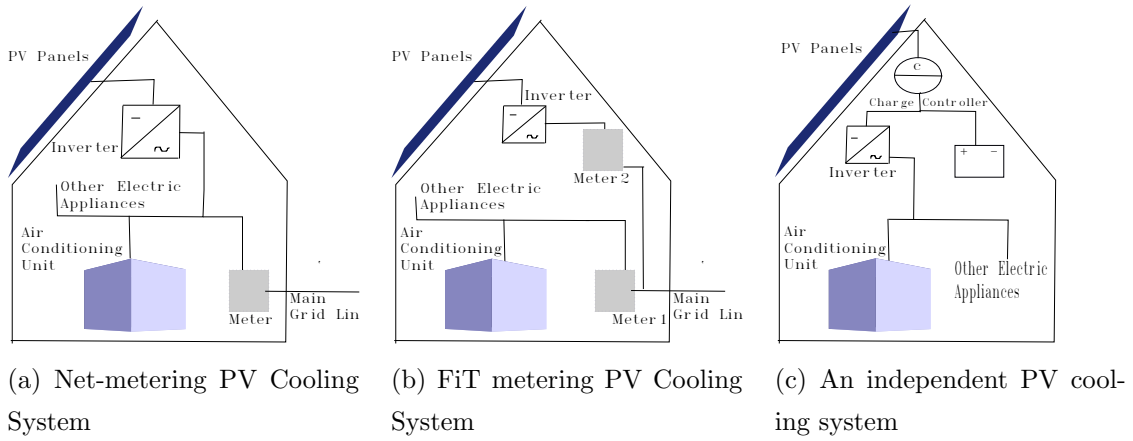


Figure 3: Schematics of various PV powered cooling systems [20]

The success of these systems is dependent on the type of electricity pricing system being used. The usual three systems are peak tariff which occurs during mid-day and has the highest electricity cost, shoulder tariff occurs during early morning and late evening and the last one is off-peak tariff which is for electricity usage at night (and the cheapest of all three) [20]. When these pricing systems are considered, the need to use PV cooling becomes apparent as it would help to reduce electricity consumption during peak hours and hence result in electricity cost-cutting. With the grid-independent systems, the air conditioning system runs purely on electricity that is generated by the PV panels. For operation during periods when there is no sunshine, the system's performance is dependent on the capacity of the electricity storage batteries. The connection between the involved components is shown in Figure 3c. Due to the high cost of battery storage and the short lifespan of the batteries in comparison to the rest of the components, this system is rarely used [20]. Another limitation is that the system best operates in countries that have very hot temperatures during the day which allows for the storage of excess energy. These type of areas are only limited within the Tropical zone (between tropics of Cancer and Capricorn) [20].

The advantage of such a system is that it can be assembled from commercially available components. This then makes the whole system to be cheaper than thermal driven ones [20]. The other advantage of this kind of system is that the produced electricity can be used for powering other electric appliances when the air conditioning system is not being used (as shown in Figure 3c). For small scale applications (below 30kW<sub>r</sub>), PV cooling systems have also been found to be more economically feasible when compared to thermal driven systems [20].

## 2.4 Heat-Driven Refrigeration Systems

These are split into two categories which are active and passive systems. Passive methods are those which involve intelligent building design to minimize heating and cooling loads and the movement of the involved working fluid is due to thermo-syphonic action [50]. Active systems use equipment to collect, store and distribute solar heat in a controlled manner [51]. They are also split into two categories which are liquid and air-based systems. Even though the two systems use different types of working fluids, their operation is quite similar in that they both use solar collectors as fluid heaters, the fluid is propelled by a pump or fan to transport the energy from the collector to storage and then to the conditioned space [51]. The different types of solar assisted heating and cooling systems are ejector systems, desiccant systems, adsorption and absorption systems. For these type of systems, the required thermal energy from the heat source must be in the temperature range of 55-95 °C which can be sufficiently provided by solar collectors [52].

Liquid-based heat-driven systems use a heat source to vaporize the working fluid. They differ from the conventional vapour compression cycle in that the working fluid is not pressurized whilst it is simultaneously being vaporized. The source of heat used in these type of systems could be in the form of waste heat which is produced by any industrial process. Part of the heat sources that can be considered for such cycles is solar energy which forms the category of systems that are referred to as solar heating and cooling systems. Depending on the source of heat used, it then becomes possible to have heating and cooling systems which use less electricity and hence lower the demand from the main grid [40]. Reduced electricity demand also means that there can be a possible reduction in carbon dioxide emissions from electricity productions involving the combustion of fossil fuels.

### 2.4.1 Absorption Refrigeration Systems

This type of refrigeration system is used when there is the availability of an inexpensive thermal energy source that can supply heat within the temperature range of 100 to 200 °C [48]. In most cases, the source of heat could be geothermal, solar energy or even waste heat from plant equipment such as boilers or heat exchangers. Instead of having a compressor (for adding pressure and thermal energy into the fluid as in vapour compression systems), the system makes use of several components (a generator, regenerator, pump, heat energy collector, rectifier and absorber) to provide this same effect. The advantage of using this type of system over the conventional vapour compression refrigeration cycle is that the work input that is required is quite small since the working fluid is compressed whilst it is in liquid form compared to compressing a vapour which has a high specific volume [48]. The disadvantages of such a system come from the large number of involved components which result in a high

cost of installation and often cause the need for more installation space. The low levels of efficiency also mean that larger cooling towers will be needed for the heat rejection phase [48]. When the above factors are considered, it then becomes apparent why these type of systems are only used in large industrial and commercial applications.

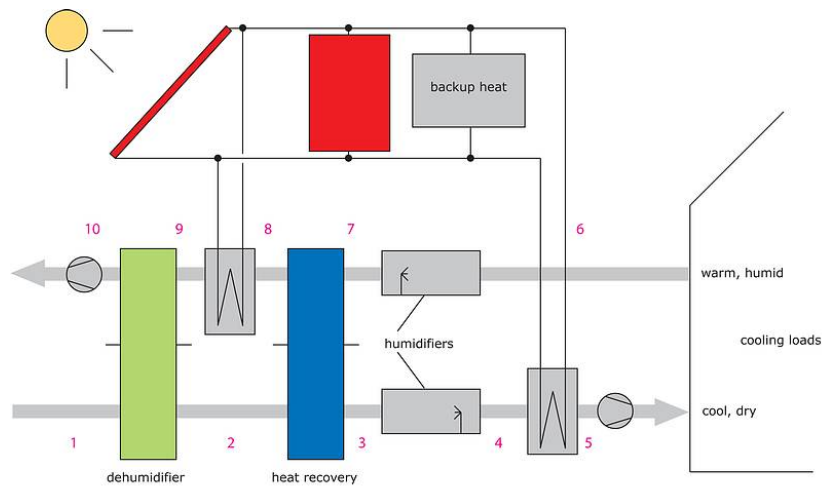
## **2.4.2 Desiccant Systems**

Desiccant systems are split into two categories, solid and liquid systems which is dependent on whether the desiccant material is solid or liquid.

### **2.4.2.1 Solid Desiccant Systems**

This type of system is mostly applicable in conditions where the humidity is low and the heating demand is also low [38]. This type of system is considered to be an open system because the working fluid (which is air) is discharged into ambient conditions after it has been used to provide the cooling effect. A new air supply is then taken into the system to replace the discarded air. The bases of operation of this cycle is due to the combination of evaporative cooling and dehumidification of the ambient air through the use of desiccant materials [38]. A desiccant material is a hygroscopic (moisture absorbing) material which can either be solid or liquid. A schematic of a solid desiccant type of system is shown in [Figure 4](#).





- Conditioned Air Supply

1. warm ambient air
2. warm dehumidified air
3. pre-cooled air
4. cooled and humidified air
5. solar heated air (for cooled weather )

- Exhaust Air Process

1. warm and humid air
2. saturated and humidified air
3. preheated air
4. solar thermal heated air
5. discharged hot air

Figure 4: A schematic of a desiccant system[53]

The cycle begins with the entry of warm air into the slowly rotating desiccant wheel (across the point 1 and 2) whereby the air is dehumidified through the absorption of water. The air then enters a heat recovery wheel (stage 2 to 3) whereby the heat that was gained by the air in the dehumidifier is removed which results in pre-cooling of the air. This is then followed by a controlled humidification process (stage 3-4) which causes the desired drop in the temperature of the air. In cases whereby the air has to be warm, across stages 4-5, heat collected from solar collectors is transferred onto the air stream which is then delivered into the conditioned room.

The second part of the process involves the extraction of warm and humid air from the room. After leaving the room, the air passes through a humidifier (across stage 6 and 7) which adds enough moisture to the air such that it is close to reaching its saturation point. The purpose of this is to allow for the full exploitation of the fluid's cooling potential which then results in the achievement of effective heat recovery across the process 7 to 8. The low temperature of the humidified air at point 7 helps with the extraction of heat from the

air leaving the dehumidifier at stage 2. Before being passed through the dehumidifier, the air is heated with heat within the range of 50 to 75 °C from the solar collectors. This is done to ensure that the sorption wheel is regenerated [53]. With referral to Figure 4, it can be seen that a heat storage device (backup heat) has been included as part of the involved components for optimum performance of the system. The heat collector that is used in this case is the flat plate solar thermal collector.

As the above system is only suitable for cases where the humidity levels are low, in cases where the ambient humidity is high, the system has to be modified to allow for evaporative cooling [53]. The modifications that can be made involve the selection of an air-to-air heat exchanger that can support both dehumidification and simultaneous cooling of the supply air. Dehumidifying the air can be done through sorptive coatings of the heat exchanger wall and cooling can be done by the exhaust air after it has gone through the humidification process [53]. The inclusion of such a heat exchanger is believed to improve the efficiency of the system [53].

#### 2.4.2.2 Liquid Desiccant Systems

This type of system is similar to the solid desiccant type except that the sorption medium is a hygroscopic solution [20]. The most common types of sorption materials include lithium chloride, triethylene glycol, lithium bromide and liquid calcium chloride which can either be directly sprayed to the air stream (which is going to provide the cooling effect) or be used within a carrier matrix in the form of a rotating wheel (like in the solid system)[20]. A schematic of how this system works is shown in Figure 5 whereby it can be seen that the process begins with the intake of ambient air which gets passed through a filter to remove dust and other unwanted particles from the air. The air is passed through the absorber which performs the task of removing moisture from the air. In this process, the absorber is soaked with the concentrated salt solution which then absorbs the moisture from the air and hence results in the dilution of the solution [20]. As the moisture removal process increases the temperature of the air, it becomes necessary to cool the air before supplying it to the conditioned space.

This cooling process is done through a heat exchanger which employs an evaporative cooler to cool return air which then cools the supply air. Inside the heat exchanger, the supply and return air streams remain separated [20]. The last part of this process involves the regeneration of the concentrated salt solution through the use of a solar thermal collector (or any other heat source) to remove the previously absorbed water from the solution. With this type of system, it is possible to achieve a minimum air supply temperature of 16 °C with heat source temperatures of 45- 70 °C which happens to be lower than that of closed system absorption and adsorption chillers [20].

The advantage of this system is that most of the components used are commercially available and hence make it less difficult to assembly such a system. The low regeneration temperature of some of the solutions (such as calcium chloride which regenerates at  $41^{\circ}C$ ) makes it possible to employ cheap solar thermal collectors which operate at low efficiencies [20]. The fact that most of the solutions have a higher storage density makes it possible for them to be pumped and stored for regeneration later [20].

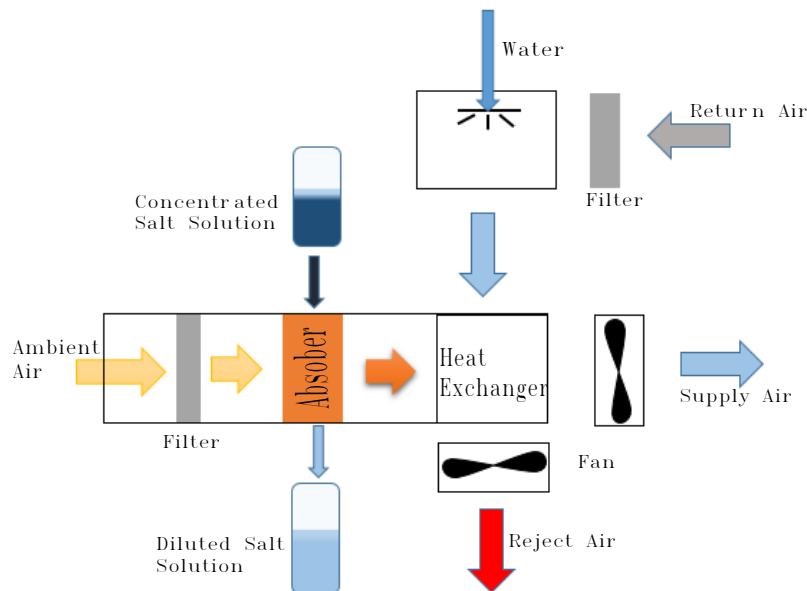


Figure 5: A schematic of a liquid desiccant system

### 2.4.3 Adsorption Systems

The operation of this type of system is based on the unique ability of certain materials to adsorb large quantities of vapour [38]. This ability is attributed to the involvement of Van der Waals forces which allow the fluid molecules to fix themselves onto the walls of the solid materials [54]. The advantage of this system over the conventional vapour system is that the working fluid used is a mixture of water and ammonia which do not pose a threat to the ozone layer.

During the heat supply process, the absorber bed is initially at a low temperature which enables it to adsorb the refrigerant. Once the bed has adsorbed enough of the refrigerant to reach saturation it is then heated which then causes the refrigerant to be released from it to flow into the condenser. In the condenser, the working fluid undergoes a phase change where by its latent heat is removed and it becomes liquefied. It is this heat that gets supplied to the space that requires heating. The isolation valve that is between the evaporator and

the condenser is then opened which then allows for the free flow of the refrigerant from the condenser into the evaporator.

When all the refrigerant has entered the evaporator and has had its temperature lowered, it is then transferred to the absorber bed where it gets to be re-absorbed. For the cooling cycle, the refrigerant starts in its liquid state (at a low temperature) and gets to absorb some of the heat that is within the conditioned space which then results in its evaporation. The temperature of the absorbent bed is also lowered to allow for the adsorption of the refrigerant. The time taken to cool the absorbent results in a discontinuity in the operation of the cycle which is its main disadvantage. To solve this issue, the system is designed to have two or more adsorbent beds which are connected by a series of valves to both the evaporator and condenser. In this type of set-up, one bed would be heated to allow for heat to be supplied through the condenser whilst the other bed would be connected to the evaporator to allow for adsorption [54]. The two beds would have to be heated and cooled alternatively to make the cycle continuous. The efficiency of this system is improved by the addition of more beds which allows for the reuse of the heat being rejected by the beds themselves [54].

#### 2.4.4 The Ejector Refrigeration System

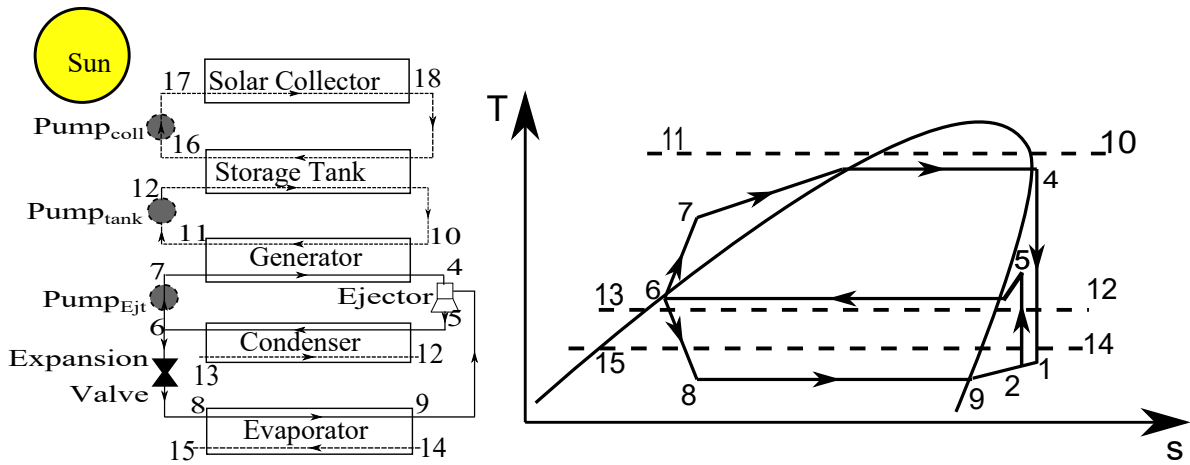


Figure 6: The ejector refrigeration System

The Ejector Refrigeration System ERS differs from the conventional vapour compression as it does not have a compressor but it uses a pump, a boiler (or generator) and an ejector as shown in Figure 6a. In the case of solar-driven systems, the heat source is solar thermal energy which is harnessed by a solar collector to generate high temperature and pressure vapour within the boiler. The vapour flows into the primary inlet of the ejector whilst the secondary inlet draws low-pressure refrigerant from the evaporator. The low pressure at the secondary

inlet allows for the evaporation of the refrigerant in the evaporator at a low pressure which then helps with generating the desired refrigerating effect [40]. As shown in Figure 6, the exhausts of the ejector are transferred to the condenser where heat is rejected from the working fluid. The heat rejection process turns the refrigerant from a vapour state to a liquid state. Upon exiting the condenser, a fraction of the refrigerant goes through the throttling process which takes it back to the evaporator whilst the remainder of the fluid is pumped to the boiler.

The temperature and pressure at which the system components get to operate in are dependent on the amount of heat that is supplied to the refrigerant in the boiler and the amount of refrigerating effect that is desired (which is to be distributed through the evaporator) [40]. The local climate also has an effect as it will determine the temperature of the fluid within the condenser to allow for successful heat rejection [40]. Usually, the work input of the pump is less than 1% of the heat supplied to the boiler and hence not considered when evaluating the C.O.P which is then calculated as shown in Equation 1 [40, 55].

$$C.O.P = \frac{\text{refrigeration effect at the evaporator}}{\text{heat input at the boiler}} \quad (1)$$

The overall performance of a solar ejector refrigeration system is given in Equation 2 [40]. From Equation 2 it can be seen that the overall performance of the system is dependent on both the performance of the ejector refrigeration cycle and that of the solar system [40].

$$COP_{overall} = \eta_{solar} \times COP_{ejector\ cycle} \quad (2)$$

Compared to other heat-driven cycles and the conventional vapour compression cycle, the ERS has the advantage of being mechanically simple since it has fewer moving parts. This means that the system can be expected to have low maintenance costs and a long lifespan [22]. Simplicity also means that the cost of construction and operating is relatively low [29]. From an environmental impact perspective, the ERS is ideal because it can operate with numerous environmentally friendly working fluids with water being one of them [28, 29]. The ERS has been proven to work well with low-grade thermal energy at temperatures as low as energy 60°C [22]. This opens up the application of the system through the use of solar energy and waste heat [56, 30].

#### 2.4.4.1 The Ejector Device

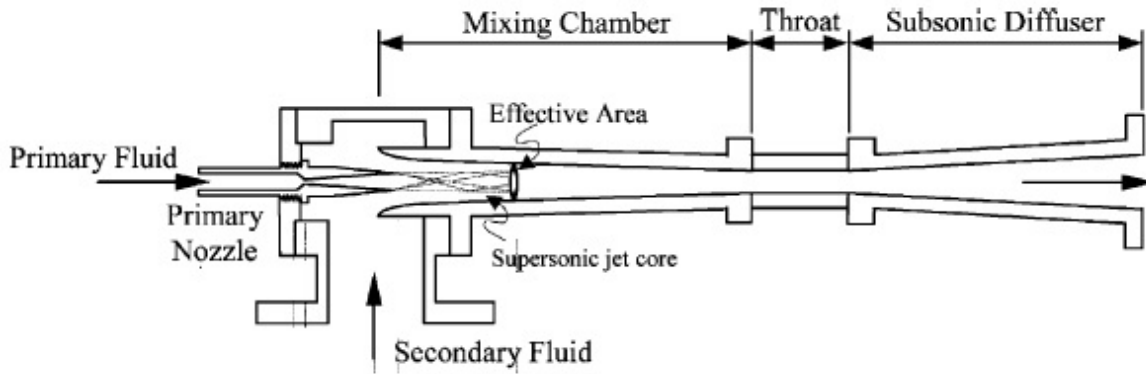


Figure 7: A schematic of the ejector [40]

The ERS makes use of a device called the ejector (shown in [Figure 7](#)) to compress the working fluid from the evaporator pressure to the condenser pressure. To achieve this, it requires a stream of vaporized working fluid (called the primary fluid) which is expanded through the primary nozzle of the ejector. Expansion of the primary fluid through the nozzle increases the exit velocity and a decrease in the exit pressure. This results in the primary fluid exiting the primary nozzle at supersonic-speed which causes a low-pressure region in the mixing chamber region of the secondary nozzle. Due to this low-pressure region, the secondary fluid is entrained into the mixing chamber region of the secondary nozzle.

Depending on the location of the exit plane of the primary nozzle, mixing of the primary and secondary streams can occur at constant pressure or constant area [40, 57]. When positioned within the mixing chamber section of the ejector, mixing of the two streams occurs at constant pressure which is reached after the secondary stream has accelerated to reach a choked mass flowrate [57]. This point of mixing is referred to as the "effective area" as shown in [Figure 7](#). Under constant area mixing, the exit plane of the nozzle is within the throat section of the ejector and the two streams mix within the constant area section of the ejector [40].

Upon exiting the mixing chamber, the flow enters the throat region of the ejector which is shown as a constant cross-sectional area region in [Figure 7](#). Due to the high pressure that exists downstream of the throat region, a normal shock wave occurs at the throat region of the ejector which then results in an abrupt increase in the static pressure and a drop in the velocity of the flow from supersonic to subsonic speeds [40]. After exiting the throat, the flow gets into the diffuser which regains the static pressure of the flow whilst decreasing the velocity.

The parameters used for evaluating the performance of the ejector are the pressure lift ratio ([Equation 3](#)) and the entrainment Ratio ([Equation 4](#)) [[40](#)]. The pressure lift ratio is used to limit the temperature at which heat can be rejected and its magnitude is limited by the critical back pressure of the ejector [[40](#)]. The entrainment ratio is a function of the operating conditions and the geometry of the ejector and it is related to the energy efficiency of the refrigeration cycle.

$$\text{Pressure Lift Ratio} = \frac{\text{Static Pressure at Diffuser Exit}}{\text{Static Pressure of Secondary Flow}} \quad (3)$$

$$\omega = \frac{\text{Mass of secondary flow}}{\text{Mass of primary flow}} \quad (4)$$

Based on the above equations, it can be concluded that the desired ejector is one which has a high entrainment ratio (to have high energy efficiencies) and a high diffuser exit pressure (to increase the temperature in which heat rejection can be done).

#### 2.4.4.2 Performance Studies of the Ejector Refrigerator

Performance analysis of the ERS, through numerical modelling, has been carried out in numerous studies. A summary of a few selected studies is shown in [Table 3](#). Due to the complex nature of the processing taking place within the ejector component, several idealizations have to be made to accurately model the device [[58](#)]. Depending on the nature of the working fluid considered and the operating conditions of the ejector, these idealisations can have a significant impact on the quality of results obtained. These idealisations determine the type of equations used and the mathematical algorithm employed when determining the performance of the ERS [[59](#)].

A one-dimensional (1-D) ideal gas model of the ejector was developed by Huang et al. to approximate the performance of the ejector under critical mode operation [[57](#)]. In this study, the efficiencies of the ejector are determined by making correlations with experimentally determined data. From this study, it was found that the theoretical results closely matched the experimental results when constant primary nozzle and secondary nozzle expansion efficiencies were considered. The mixing efficiency of the ejector was found to be highly dependent on the EAR [[57](#)]. Parametric analysis of the ejector with the objective of finding an optimal EAR (and subsequently COP) was carried out by Saleh [[22](#)]. The optimal EAR was determined from the operating conditions of the ERS whilst considering various working fluids. Since the study was strictly performance-driven, R245ca was found to be the ideal working fluid (as it achieved superior COP values) despite concerns regarding safety and environmental impact of the working fluid [[22](#)].

A real gas model of ejector intended to determine both critical and subcritical performance was developed by Li et al. [60]. The model was used to analyse both wet (R134a) and dry (R245fa and R141b) working fluids whereby the effect of operating parameters and generator superheating was investigated. The model considered the variation of the ejector efficiencies (mixing, primary and secondary expansion efficiencies) with the operating parameters and ejector geometry. Another real gas model was developed by Chen et al. whereby it was found that the real gas model provided more accurate results compared to the ideal gas model when analysing performance in subcritical model [61]. R290 and R134a were selected as ideal working fluids due to performance, economical, environmental, and safety factors. R290 was found to give higher COP values only at lower  $T_c$ . With the objective of determining the performance of the ejector using alternative working fluids, a 1-D ideal gas model was developed by Mwesigye and Dworkin [28]. From the working fluids considered, R1234ze(Z) and R1234zd(d) were found to give superior performance whilst being safe for use. The study considered the effect of variable EAR, ejector efficiencies, and operating parameters.



Table 3: Theoretical studies on the ERS

Study	Model Development	Refrigerant	Performance Analysis
Huang et al. [57]	1- D Ideal Gas	R141b,	Fixed ejector efficiencies EAR dependent mixing efficiency Operation Mode: Critical
Chen et al. [61]	1- D Real Gas	R134a, R141b, R142b R152a, R290, R600 R600a, R717,& R124	Parametric Analysis Constant ejector efficiency coefficients Critical and Sub-critical analysis Ideal refrigerants : R290 & R134a R290 COP: 0.7 ( $T_c = 30$ , $T_g = 90$ , $T_c = 12$ °C) R134a COP: 0.49 ( $T_c = 34$ , $T_g$ , & $T_c = 12$ °C)
Saleh [22]	1- D Ideal Gas	R600a, R236ea, R600 R134a, R227ea, R236fa, R245fa, and R245ca	Optimal COP, EAR based on $T_e$ , $T_g$ , and $T_c$ Fixed ejector efficiency coefficients Ideal refrigerants : R245ca R245ca COP: 0.74 ( $T_g = 90$ , $T_c = 25$ , $T_e = 10$ °C)
Li et al [60]	1- D Real Gas	R134a, R141b, and R245fa	Real gas model validation Wet refrigerant modelling parametric analysis Variable ejector efficiency coefficients
Mwesigye & Dworkin [28]	1- D Ideal Gas	R1233zd(E), RE245fa2, R600, RE245fa, , HFO1336mzz(Z), and R1234ze(Z),	Effect of EAR, $T_e$ , $T_g$ , and $T_c$ Variable ejector efficiency coefficients Ideal refrigerants : R1234ze(Z) & R123ze(d) R1234ze(Z) COP: 0.20 – 0.45 R1233zd(d) COP: 0.14 – 0.30

#### 2.4.4.3 The solar-driven Ejector Refrigerator

As shown in [Figure 6a](#), the solar-powered ejector uses solar collectors to generate thermal energy to vaporize the working fluid within the generator. To ensure that the generator operates at a stable temperature, a storage tank is provided to act as a thermal reservoir and temperature buffer. Key performance indices of a solar-powered ERS are the STR and the Solar Fraction (SF). The STR is a measure of the cooling capacity that the system delivers based on the thermal energy input required by the system [\[27\]](#). This can also be expressed as the product of the collector efficiency and the COP of the system as shown in [Equation 5](#).

$$STR = \frac{\text{Cooling Capacity}}{\text{Thermal Energy Input}} = \eta_{coll} \times COP_{eje} \quad (5)$$

The overall performance of the system ( $COP_{overall}$ ) is evaluated from Equation 6, by taking the product of the solar collector efficiency ( $\eta_{coll}$ ) and the ERS COP.

$$COP_{overall} = \eta_{coll} \times COP_{eje} \quad (6)$$

The SF determines the magnitude of solar energy used within the cooling system over the total energy demand of the system. This is evaluated as shown in .

$$SF = \frac{\text{Solar Energy Used}}{\text{Total System Energy Demand}} \quad (7)$$

#### 2.4.4.4 The solar-powered Ejector Studies

A steady-state study conducted by Dennis et al [35] was focused on finding the optimum primary nozzle diameter for a solar-powered ejector refrigeration cycle. The objective of the analysis was to find the ejector geometry that will maximize performance whilst limiting the demand for thermal energy for powering the system. The analysis was conducted over a discrete range of incident solar radiation ( $I_T$ ) 500 - 1100  $W/m^2$  and over a wide range of ambient temperature ( $T_{am}$ ) values. The results showed that higher  $T_{am}$  required the ejector to operate at higher condenser temperature ( $T_c$ ) values. Higher  $T_c$  values can only be attained at higher generator temperature ( $T_g$ ) values which are dependent on high  $I_T$ . Guo and Shen performed analysis on a solar-powered ejector system by using hourly data of solar radiation and ambient conditions [62]. However, their study did not consider the effects of thermal energy storage and the possibility of performance beyond the availability of solar radiation. Huang et al [63], performed a steady-state analysis of solar-powered ejector by employing a model that was developed from an earlier study [57]. However, the operation of the ejector was only analysed at fixed operating conditions. [46] conducted an hourly performance analysis of an R134a solar-powered ejector over different months in Athens. The analysis considered the hourly variation of  $I_T$  and  $T_{am}$  on the performance of both the solar collectors and the ERS. However, the study did not consider the possibility of performance beyond the availability of solar radiation and does not provide detail on the solar thermal components such as the area of collectors used.

#### 2.4.4.5 Solar Collector Consideration for solar-powered Ejector Refrigerators

A steady-state study by Huang et al. [34] considered the effect of different solar collectors on the overall performance of the system. The considered collectors were Evacuated Tube Collectors (ETC), conventional single glazed flat plate collectors (FPC), and FPC with selective surface. The study found that ETC provided better  $COP_{overall}$  values compared to the FPCs. However, the FPC were eventually considered as they proved to be more affordable.

In a similar study, Tashtoush et al. [26] also found that ETC performed better than doubled glazed and single glazed FPC by considering the annual useful energy gain and system solar fraction. In most of the considered studies (listed in Table 4), ETC are preferred over flat plate collectors because due to higher  $\eta_{coll}$  values which eventually result in higher  $COP_{overall}$  values. From the studies presented in Table 4, it is clear that various collector surface areas ( $A_{Coll}$ ) and various storage volume capacities ( $Vol_{Tank}$ ) were considered when determining the optimal operating parameters of the solar powered ejector.

Table 4: Review of solar-powered ERS studies

Study and Location	Model Development	Refrigerant	Component Parameters	System Performance
Tashtoush et. al.[26] Jordan	Theoretical, EES and TRNSYS	R134a	$A_{Coll}$ : 60 – 70 m <sup>2</sup> $Vol_{Tank}$ : 2 m <sup>3</sup> $Coll_{Fluid}$ : Water	SF: 0,52 – 5,421 ; $\dot{Q}_{Cooling} = 7kW$ $COP_{overall} = 0,32 – 0,47$ ; $COP_{coll} = 0,52 – 0,92$ $COP_{ejector} = 0.39$ ; Collector:ETC and FPC
Vidal et. al.[64] Florianpolis, Brazil	Theoretical, EES and TRNSYS	R141b	$A_{Coll}$ : 20 – 80 m <sup>2</sup> ; $Vol_{Tank}$ : 4 m <sup>3</sup> Auxiliary Heater ; $Coll_{Fluid}$ : Water Collector:ETC and FPC	SF = 0.42 ; $T_c = 32$ °C $COP_{ejector} = 0.39$ , $T_g = 80$ °C $\dot{Q}_{Cooling} = 10.5kW$ , $T_e = 8$ °C
Pridasawas and Lundqvist [37], Bangkok	Theoretical, EES and TRNSYS	R600a	$A_{Coll}$ : 50 – 80 m <sup>2</sup> $Vol_{Tank}$ : 2 m <sup>3</sup> ; $Coll_{Fluid}$ : Water Collector:ETC and FPC	SF = 0.75 ,STR =0.22; $T_g = 70 – 120$ °C $COP_{ejector} = 0.48$ ; $T_c = T_{am}+5$ °C $\dot{Q}_{Cooling} = 3.5kW$ ; $\eta_{coll} = 0.47$ ; $T_e = 15$ °C
Guo and Shen [62], Shanghai, China	Theoretical, NIST REFPROP	R134a	$A_{Coll}$ : 15 m <sup>2</sup> $Coll_{Fluid}$ : Water Collector:ETC	SF =0 – 1.1 $\dot{Q}_{Cooling} = 6$ kW $COP_{overall} = 0.3 – 0.55$ , $T_g = 65–95$ °C $T_c = T_{am}+5$ °C, $\eta_{coll} = 0.47$ , $T_e = 8$ °C
Dennis et al. [35],	Theoretical, steady-state	R245fa	$A_{Coll}$ : 16 m <sup>2</sup> $Vol_{Tank}$ : N/A ; Collector:ETC	$I_T = 500 – 1100$ W/m <sup>2</sup> $T_g = 70 – 120$ °C, $T_e = 10$ °C; $\dot{Q}_{Cooling} = 3.5$ kW
Huang et al. [63],	Theoretical steady-state	R141b	$A_{Coll}$ : 15 m <sup>2</sup> ; $Coll_{Fluid}$ : Water Collector:FPC Auxiliary Heater	$COP_{ejector} = 0.5$ ; $COP_{overall} = 0.22$ ; $\eta_{coll} = 0.5$ $\dot{Q}_{Cooling} = 10.5$ kW, $I_T = 700$ W/m <sup>2</sup> $T_g = 95$ °C, $T_e = 8$ °C, $T_c = 32$ °C,
Alexis & Karayiannis [46],	Theoretical	R134a	Collector:ETC	$T_g = 82 – 92$ °C $T_c = 32–40$ °C, $COP_{overall} = 0.011 – 0.101$ $\eta_{coll} = 0.319–0.507$ ; $T_e = -10 – 0$ °C
Allouche et al. [65], Tunis, Tunisia	Theoretical TRNSYS and EES	Water	$A_{Coll}$ : 60 – 110 m <sup>2</sup> , $Coll_{Fluid}$ : Water Collector:ETC, Auxiliary Heater Hot tank: 0.7 – 3 m <sup>3</sup>	$COP_{ejector} = 0.5$ ; $COP_{overall} = 0.22$ ; $I_T = 700$ W/m <sup>2</sup> $\dot{Q}_{Cooling} = 3.5$ kW ; $T_g = 95$ °C, $I_T = 700$ W/m <sup>2</sup> SF = 0.24 –0.95 ; $T_c = 32$ °C, $T_e = 8$ °C, $\eta_{coll} = 0.5$

#### 2.4.4.6 Working Fluid Selection on Ejector Refrigeration Systems

From the review of the studies carried out on the analysis of the conventional ERS and the solar-powered ERS, it is clear that the type of working fluid considered determines the suitable range of operating parameters that would deliver high-performance. Unfortunately, the selection of working fluids requires considerations beyond the thermodynamic performance of the working fluid. These considerations include the environmental impact of the fluid, which considers the GWP, atmospheric lifetime (ALT) and ODP, and safety aspects such as flammability, toxicity and auto-ignition [22]. The GWP of a working fluid is a measure of how effective the fluid is in trapping heat when released into the atmosphere (compared to the same amount of  $CO_2$ ) over a typical duration of 100 years [22]. The properties of the working fluids considered in the studies listed in Table 3 and Table 4 are shown in Table 5.

Table 5: ERS working fluid selection (Adopted From [22, 66])

Working Fluid	M (kg/kmol)	Boiling Point °C	Critical Temperature °C	Critical Pressure (Mpa)	Fluid Type (wet / dry)	GWP	ODP	Safety Group
R290	44.1	-42,1	96,68	4,25	wet	3	0	A3
R141b	116.95	32,1	204	4,21	dry	725	0,11	A2
R134a	102.03	-26	101	4,1	wet	1370	0	A1
R227ea	170.03	-16,3	101,8	2,93		3580	0	A1
R236fa	152.04	-1,4	124.9	3.20		9820	0	A1
R600a	58.12	-11,7	134.7	3.63	isentropic	20	0	A3
R236ea	152.04	6,2	139.3	3.50		1410	0	-
R600	58.12	-0,55	152.0	3.80	isentropic	20	0	A3
R245fa	134.05	15,1	154.1	3.65	dry	1050	0	B1
R245ca	134.05	25,1	174.4	3.93		726	0	-
R1234ze(Z)	114	9,28	150,1	3,53	wet	6	0	A1 < A2L
R1233zd(E)	131	19	166	3,6	dry	4,5	0	A1 < A2L

Other considerations in the selection of refrigerants have to do with the molecular weight mass (M) of the fluid. A refrigerant with a higher molecular mass results in higher entrainment ratios whilst refrigerants with smaller molecular mass requires lower entrainment ratios [40]. This results in the use of larger ejector geometries for small molecular mass refrigerants for the same system capacity [40]. The slope of the saturated vapour line of the refrigerant determines if the working fluid is considered to be dry, wet or isentropic. Dry and isentropic working fluids are ideal because the negative slope of the saturated vapour line ensures that the refrigerant will remain in the superheated phase whilst undergoing expansion, mixing,

and compression within the ejector [22, 40]. Wet working fluids require a significant amount of superheating to ensure that there is no formation of droplets within the ejector as the working fluid has a negative saturated vapour line [22, 40].

Considerations on the environmental impact of the working fluids have to be in line with both the Montreal Protocol and the Kyoto Protocol with regard to limiting the use of refrigerants with high GWP and ODP. The usage of chlorofluorocarbons (CFCs) (R11, R12) and hydrochlorofluorocarbons (HCFCs) (R22) working fluids was phased out by the Montreal Protocol due to their high ODP [67]. hydrofluorocarbons (HFCs) working fluids (R134a, R410a, R407c) were considered to be environmentally friendly (because of 0 ODP) but their high GWP served as motivation to limit their use by the Kyoto Protocol [59]. Hydrocarbon (R290, R600, and R600a) refrigerants have proven to provide excellent performance of the ERS and also have a benign environmental impact (low GWP and low ODP) [22]. However, these working fluids have high flammability and hence requires extreme safety measures to be in place when using them. Hydrofluoroolefins (HFOs) working fluids (R1233zd(E) and R1234ze(Z)) provide good performance, are environmentally friendly, and safe to use on ERS [28].

Numerous numerical models and experiments have been set to investigate the performance of the ejector refrigeration system. In the work done by Saleh [22], the ideal type of refrigerant for the ejector cycle was investigated. His considerations were based on GWP, ALT, ODP of the working fluids together with the COP of the system under any of the considered working fluids. From his analysis, Saleh [8] found that R600 and R600a had minimum environmental impact due to low ALT, ODP, and GWP values. The major with this working fluid was its high flammability which would mean that a lot of attention would have to be made towards safety when operating a system that functions on this refrigerant. Due to this issue, Saleh [22] then recommended R245ca as the best candidate, despite having some concerns with the environmental and safety issues it has since it had achieved high COPs and entrainment ratios. From his analysis, it can then be seen that more work is needed in finding a refrigerant that will give optimum system performance whilst ensuring that safety and environmental impact are not disregarded.

#### **2.4.4.7 Alternative Applications of the Ejector**

Due to the poor operating efficiency associated with the basic ejector refrigeration cycle, a lot of modified cycles have been developed as an attempt of achieving higher C.O.P values [40] [68]. Some of these modifications employ a compressor which is fitted along the secondary

flow stream of the ejector to increase the pressure and temperature at which the working fluid is entrained into the ejector and hence result in higher ejector efficiencies [68]. In their work, Xu et al. [68] propose a novel ejector refrigeration cycle which employs a separator, a second throttle valve and a compressor as shown in Figure 8.

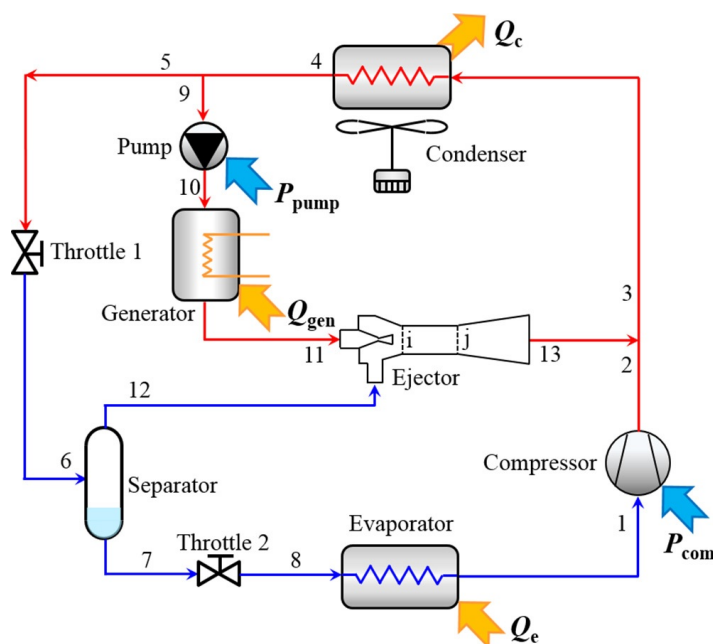


Figure 8: A schematic of a modified ejector compression cycle [68].

The secret behind the success of their proposed system is its ability to increase the cooling capacity of the evaporator from being low-grade to a higher grade cooling effect by making use of the separator [68]. The purpose of the separator is to ensure that only vaporized refrigerant is entrained into the secondary stream of the ejector and that only the liquid part of the refrigerant goes through the evaporator through the second throttling process. SF, FPC

#### 2.4.5 Modified Ejector Coupled Studies

The ejector device has also been incorporated in vapour compression systems to minimize the operating pressure range of the compressor [69, 70]. The ejector has also been incorporated in power cycles whereby it was placed at the exit of the turbine stage which allowed for further expansion of the working fluid in the primary nozzle of the ejector [71].

## 2.5 Solar Energy Within South Africa

The abundance of solar energy within South Africa is signified by daily average Global Horizontal Irradiance (GHI) values within the range of  $4.5 - 7kWh/m^2$  [72, 73, 74]. These values are considered to be far superior to the daily values recorded in most parts of the world [72, 74]. From a PV electricity generation perspective, with a 13% conversion efficiency, approximately  $3000 km^2$  would have been required to meet South Africa's total energy demand in 2000 [73]. When considering only the electric demand (adjusted to the anticipated 2050 demand), only  $1300 km^2$  would be required [73]. From a CSP perspective, the total electricity generation potential of South Africa is over 540 GW[25]. These figures highlight the abundance of solar radiation which explains the heavy subsequent usage of HVAC equipment for space conditioning purposes. The intensity of solar irradiation is usually classified according to the nature of the radiation being considered and the usual groups are DNI, GHI and Diffuse Horizontal Irradiance (DHI) [75]. The variation of these categories is explained as follows:

- DNI [76] is the beam component of the sun (without considering any diffuse irradiance) which is acting at a normal plane to the rays of the sun. Considered when the type of collectors are CSP or Concentrating Photovoltaic (CPV) as it is the only component of the sun's irradiance that can be concentrated or reflected. To maximise the amount of irradiance that is received by a surface, the surface is made to track the sun's path to the normal orientation between the sun and the surface [75].
- DHI is the form of radiation that is received by a surface as a result of scattering of the sun's beam radiation by clouds and other particles within the atmosphere [75].
- GHI is a combination of direct and diffuse irradiance which is measured from a horizontal plane. These values are usually considered when PV panels and solar water heaters are to be used [76]. As a result of the relatively cheap cost of measuring GHI values (against the cost of measuring DNI), there are abundant informative maps showing the magnitude of GHI values.

South Africa happens to be part of the countries that receive quite a significant amount of solar irradiation throughout the globe [42]. The high magnitude of DNI, GHI and DHI values is one of the major factors that have allowed for the exploration of solar energy as a means of generating electricity in some parts of the country. Through these projects, the South African government is not just aiming at using the abundance of solar energy to meet the demands of the country but to also change the energy mix of from being a fossil fuel dominated one to a renewable and sustainable energy dominated mix [77].



# 3 Numerical Modelling and Validation of Ejector Refrigeration System

## 3.1 Introduction

From the previous chapter, the performance of the conventional and solar-powered ERS together with the different type of solar collectors was described. The dynamic performance of the solar-powered ejector can be found through experimentation whereby the effect of both solar radiance and ambient conditions are analysed. However, due to the costly nature of experimentations, numerical studies are an attractive alternative. Numerical analysis enables rapid generation of performance data over a wide range of operating parameters which helps to determine the optimized performance of the system. Nevertheless, numerical analysis of the ejector requires that certain idealisations be made to make it possible to model the behaviour of the system. Some of the idealisations account for energy losses in the working fluid as it goes through various stages of the cycle, while others simplify the calculation procedures to quickly generate the results.

Dynamic modelling of complex energy systems such as the ejector refrigeration cycle has been made easier through the availability of numerical analysis software packages like EES [78]. EES has a built-in library of various working fluids which can be employed in thermodynamic analysis of energy-related problems. The dynamic, solar-related, performance of the ejector was conducted by coupling of both TRNSYS and EES. TRNSYS is a simulation tool for considering the transient performance of systems made of various components (referred to as types) which are built-in the elaborate library of the software [79]. Weather (solar and ambient temperature) related performance of the system is determined by coupling the Typical Meteorological Year 2 (TMY2) weather data, accessed through a TRNSYS Type 15 component, with components requiring weather data for evaluating performance.

Analysis of flow properties in the ERS is done by making use of the mass continuity, momentum conservation, and energy balance equations. Performance analysis of TRNSYS components such as the water storage tank and flow circulatory pumps is also evaluated by employing both the mass and energy balance equations. Performance evaluation of solar collectors is achieved by employing the conservation of energy equation whereby the amount of useful thermal and electric energy generated from solar radiation is determined.

In this section, the development and validation of the ejector refrigeration model will be presented. The performance of the model is adopted and validated with the data from the study conducted by Li *et al.* [60]. It then further used to determine the performance of the environmentally friendly working fluid, R1234ze(Z) which is validated from the data published by Mwesigye and Dworkin [28].

### 3.2 The Ejector Model

In the development of the model, the following assumptions were made:

- The inner wall of the ejector is adiabatic and the flow is one dimensional and steady inside the ejector.
- The kinetic energy of the following flow streams is negligible: primary flow at the nozzle inlet, secondary flow at the suction inlet, and mixed flow stream at diffuser outlet.
- Constant-pressure mixing exists at the critical point. After fanning out of the nozzle, the primary flow entrains but does not mix with the secondary flow before section y-y. The secondary flow is choked at section y-y and starts to mix with the primary flow with a uniform pressure  $P_m = P_{py} = P_{sy}$  before the shock.

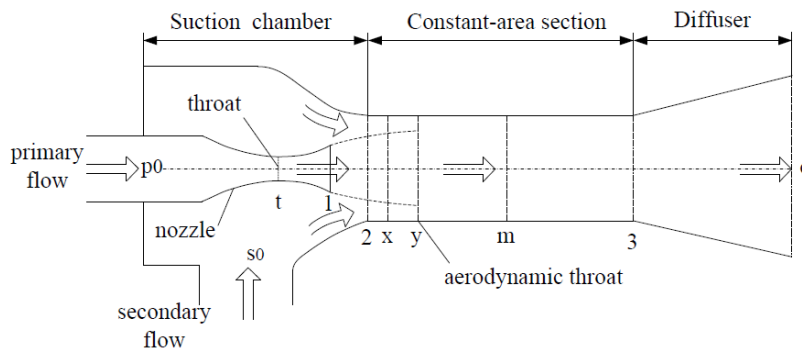


Figure 9: A schematic of flow through an ejector[60]

Modelling the ejector begins with the expansion of the primary fluid through the nozzle after exiting the generator at stagnation pressure ( $P_{po}$ ) and temperature ( $T_{po}$ ). These properties are used to evaluate the enthalpy  $h_{po}$  and entropy  $s_{po}$  at the inlet of the nozzle as indicated in Equation 8 [60].

$$h_{po}, s_{po} = f(T_{po}, P_{po}) \quad (8)$$

These properties are then used to determine the choked velocity at the throat of the nozzle ( $v_t$ ) after undergoing an expansion process through the converging section of the nozzle. This

is done through an iterative process involving the continuous reduction of  $(P_t)$  (the pressure at the throat of the nozzle) which is initially assumed to be equal to  $(P_{po})$  as indicated by the loop enclosing [Equation 9](#) to [Equation 13](#) in [Figure 10](#) [60].

The iterative process starts with using  $(P_t)$  to determine the isentropic enthalpy at the throat of the nozzle  $(h_{ts})$  which is further used to determine the actual enthalpy  $(h_t)$  by considering the expansion efficiency of the nozzle  $(\eta_t)$  as indicated in [Equation 9](#) and [Equation 10](#) respectively [60].

$$h_{ts} = f(s_{po}, P_t) \quad (9)$$

$$h_t = h_{po} - \eta_t(h_{po} - h_{ts}) \quad (10)$$

The density  $(\rho_t)$  and entropy  $(s_t)$  at the throat of the nozzle are evaluated so that they can be used together with  $(P_t)$  to find the choked throat velocity  $(v_t)$  as shown in [Equation 11](#) and [Equation 12](#), respectively [60].

$$\rho_t, s_t = f(P_t, h_t) \quad (11)$$

$$v_t = f(P_t, \rho_t) \quad (12)$$

To evaluate the accuracy of  $(v_t)$ , the enthalpy of the expanded fluid  $(h'_t)$  is evaluated again by making use of the nozzle throat velocity as shown in [Equation 13](#) [60].

$$h'_t = h_{po} - (v_t^2/2) \quad (13)$$

This result is compared against previously determined  $(h_t)$  and the iterative process is repeated until the two values,  $(h_t)$  and  $(h'_t)$ , are equal. With the final choked throat velocity known, [Equation 14](#) is used to determine the mass flow-rate of the primary fluid  $(m_p)$  [60].

$$m_p = \rho_t A_t v_t \quad (14)$$

The exit conditions at the outlet of the nozzle are determined through another iterative process which involves a continuous reduction of the nozzle exit pressure  $(P_{p1})$  which is initially assumed to be equal to  $(P_t)$ . This process (indicated by the loop enclosing [Equation 15](#) to [Equation 17](#) in [Figure 10](#)) begins with the evaluation of the nozzle exit density  $(\rho_{p1})$  and nozzle exit enthalpy  $(h_{p1})$ , as shown in [Equation 15](#), which are used to evaluate the exit velocity  $(v_{p1})$  and the assumed exit plane enthalpy  $(h'_{p1})$  through [Equation 16](#) and [Equation 17](#) [60].

$$h_{p1}, \rho_{p1} = f(P_{p1}, s_{p1}) \quad (15)$$

$$v_{p1} = m_t / (A_{p1} \rho_{p1}) \quad (16)$$

$$h'_{p1} = h_t + (v_t^2/2) - (v_{p1}^2/2) \quad (17)$$

The iterative process is terminated once  $h'_{p1}$  and  $h_{p1}$  are equal.

Evaluation of flow properties of the expanded entrained stream in the suction chamber is done an iterative process which involves a continuous reduction of  $P_{sy}$  (which is initially equated to  $P_{so}$ ).

$$h_{sys} = f(P_{sy}, s_{so}) \quad (18)$$

$$h_{sy} = h_{so} - \eta_s(h_{so} - h_{sys}) \quad (19)$$

The inlet stagnation properties ( $s_{so}$  and  $h_{so}$ ) together with the assumed value of  $P_{sy}$  and nozzle expansion efficiency ( $\eta_s$ ) are used to evaluate the isentropic ( $h_{sys}$ ) and actual enthalpy ( $h_{sy}$ ) of the entrained stream as shown in [Equation 18](#) and [Equation 19](#), respectively [60].  $h_{sy}$  and  $P_{sy}$  are then used to evaluate the density ( $\rho_{py}$ ), entropy ( $s_{so}$ ) and velocity ( $v_{sy}$ ) of the choked secondary stream.

To verify the accuracy of  $v_{sy}$ , the choked enthalpy of the secondary stream is re-evaluated as shown in [Equation 19](#) [60].

$$h'_{sy} = h_{so} - (v_{sy}^2/2) \quad (20)$$

The iterative process is terminated once the difference between  $h'_{sy}$  and  $h_{sy}$  is minimal. Based on the constant pressure mixing assumption, the pressure of the mixed flow stream  $P_m$  is set to be equal to the final expanded pressure of the entrained stream ( $P_{sy}$ ) which is also equal to the expanded primary flow pressure at section y, ( $P_{py}$ ). These properties are then used for evaluating the expanded primary flow properties which include the density ( $\rho_{py}$ ), isentropic enthalpy ( $h_{pys}$ ), actual enthalpy ( $h_{py}$ ), and expanded primary velocity ( $v_{py}$ ) as shown in [Equation 21](#), [Equation 22](#), and [Equation 23](#) [60].

$$h_{pys}, \rho_{py} = f(P_{py}, S_{py}) \quad (21)$$

$$h_{py} = h_{p1} - m(h_{p1} - h_{pys}) \quad (22)$$

$$v_{py} = \sqrt{(2(h_{p1} + (v_{p1})^2/2) - h_{py})} \quad (23)$$

To evaluate the entrained mass flow-rate ( $m_s$ ), [Equation 24](#) is used whereby the cross-sectional area of the secondary fluid at section y ( $A_{sy}$ ) and the cross-sectional area of the primary fluid at section y ( $A_{py}$ ) are evaluated from [Equation 25](#) and, [Equation 26](#), respectively [60]. The constant area mixing section,  $A_3$ , is used as the reference area for evaluating the expanded flow cross-sectional area.

$$m_s = \rho_{sy} A_{sy} v_{sy} \quad (24)$$

$$A_{sy} = A_3 - A_{py} \quad (25)$$

$$A_{py} = m_p / (\phi_m v_{py}) \quad (26)$$

The energy and momentum balance of the two streams (primary and secondary) and the resultant mixed stream is shown in [Equation 27](#) and [Equation 28](#) with ( $h_m$ ), ( $v_m$ ), and ( $\phi_m$ ) being the mixed stream enthalpy, mixed flow velocity, and mixing efficiency, respectively [60].

$$m_p(h_{py} + ((v_{py})^2/2)) + m_s(h_{sy} + ((v_{sy})^2/2)) = (m_p + m_s)(h_m + ((v_m^2)/2)) \quad (27)$$

$$\phi_m(m_p v_{py} + m_s v_{sy}) = (m_p + m_s)v_m \quad (28)$$

The compression shock process is also modelled through another iterative procedure which involves making continuous increments on the aftershock density ( $\rho_3$ ) of flow from the initially assumed value of ( $\rho_m$ ). The assumed aftershock density is used to evaluate the aftershock pressure ( $P_3$ ) as indicated in [Equation 29](#) [60].

$$P_3 = P_m + (\rho_3 - \rho_m)(\rho_3/\rho_m)v_m^2 \quad (29)$$

The accuracy of ( $P_3$ ) is ensured by minimizing the difference between ( $h_3$ ) and ( $h'_3$ ) which are evaluated in [Equation 29](#) and [Equation 31](#), respectively [60].

$$s_3, h_3 = f(P_3, \rho_3) \quad (30)$$

$$h'_3 = h_m + ((P_3 - P_m)/2)((\rho_3/\rho_m) + \rho_m)/\rho_m \rho_3 \quad (31)$$

With the aftershock conditions known, fluid pressure recovery across the diffuser is modelled as shown in [Equation 32](#) to [Equation 35](#) [60].

$$h_{cc} = h_3 + (v_3^2/2) \quad (32)$$

$$v_3 = \sqrt{(2(h_m + (v_m)^2/2) - h_3)} \quad (33)$$

$$h_{cs} = h_3 + d(h_{cc} - h_3) \quad (34)$$

$$P_{cc} = P_{cs} = f(h_{cs}, s_3) \quad (35)$$

In sub-critical mode, expansion of primary flow does not generate sufficient suction pressure to result in full expansion of the secondary stream. Due to the poor expansion of the primary flow, which only reaches section x compared to the much further section y (graphically presented in [Figure 9](#)), its expanded pressure ( $P_{px}$ ) is assumed to be equal to ( $P_{so}$ ) whilst the entropy at this section ( $s_{px}$ ) is equal to that at the exit plane of the nozzle ( $s_{p1}$ ).

Using the nozzle exit conditions and enthalpy at section x ([Equation 36](#)), Equation 29, the velocity of the primary flow at section x ( $v_{px}$ ) is calculated as shown in [Equation 37](#) [60].

$$h_{px} = f(P_{px}, s_{px}) \quad (36)$$

$$v_{px} = \sqrt{(2(h_{p1} + (v_{p1})^2/2) - h_{px})} \quad (37)$$

The evaluation of sub-critical performance of the ejector is done by establishing the condenser break down pressure ( $P_{cb}$ ) which is used together with the actual condenser pressure ( $P_c$ ) and critical condenser pressure ( $P_{cc}$ ) to ascertain the fractional adjustment of the critical entrainment ratio ( $u_c$ ) as shown in [Equation 38](#) [60].

$$u = u_c(P_{cb} - P_c)/(P_{cb} - P_{cc}) \quad (38)$$

The operating conditions of the ejector at the break down point indicate that there is minimal entrainment of the secondary stream as illustrated in Figure 3. To consider the effect of the secondary stream on  $P_{cb}$ , the entrained secondary flow-rate ( $m_{sx}$ ) is set to a small value of  $1e-6$  kg/s and  $v_{sx}$  is evaluated based on the flow density. Equation 20, Equation 27, and Equation 28 are used to evaluate  $h_{sx}$ ,  $h_m$ , and  $v_m$  with  $h_{py}$ ,  $v_{py}$ ,  $h_{sy}$ ,  $\phi_m$ , and  $t$ ,  $v_{sy}$  being replaced by  $h_{px}$ ,  $v_{px}$ ,  $h_{sx}$ ,  $\phi_{mb}$ , and  $v_{sx}$  respectively. The mixed flow properties are further used to assess aftershock properties of the flow through the use of Equation 29- Equation 31. The ejector break down pressure  $P_{cb}$  is evaluated from Equation 32 - Equation 35 through the substitution of  $h_{cc}$  and  $P_{cc}$  with  $h_{cb}$  and  $P_{cb}$ , respectively. A graphical representation of the numerical model is shown in Figure 10.

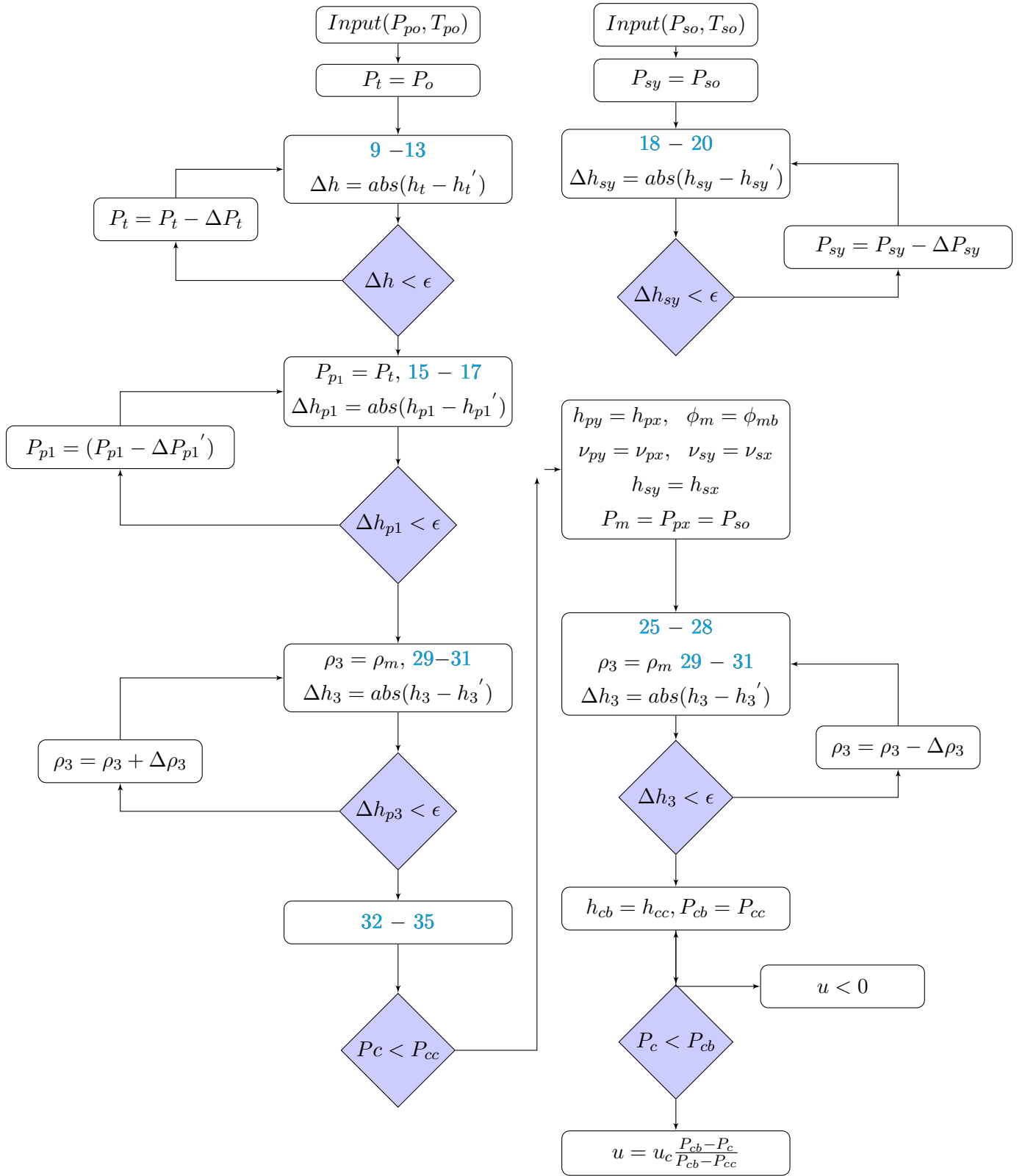


Figure 10: Solar cooling technologies [19]

### 3.3 Model Validation

The validity of the model is verified by comparing the results obtained in the present study against what is in published literature. This is carried out for different working fluids at variable ejector geometries and operating parameters. The working fluids considered are R1234ze(Z), R134a, R245fa, and R290.

#### 3.3.1 Validation of the R1234ze(Z) Ejector Performance

Validation of the model when operating under the refrigerant R1234ze(Z) is done by comparing the obtained results against data from Mwesigye and Dworkin [28]. The considered ejector has an EAR of 7.248 and the operating parameters taken into account are shown in Table 6. The analysis is considered over variable  $T_g$  and  $T_c$  with  $T_e$  fixed at 8 °C. From these results, it can be seen that a majority of deviations in COP are limited within 5% with only two instances having a deviation of 10%. Deviations in  $T_c^*$  are limited to a maximum of 4%. Considering that the results being compared are generated from two different modeling approaches, real gas model and ideal gas model, deviations may be expected in the results obtained in each model. Deviations in results obtained from ideal gas models and real gas models, especially in evaluating performance in subcritical mode, has been highlighted in most real gas model studies [60, 80, 81, 61].

Table 6: Validation of the R1234ze(Z) ejector performance

$T_g$ °C	$T_c$ °C	$T_e$ °C	COP [-] [28]	COP [-] Present Model	$\Delta$ COP , %	$T_c^*$ °C [28]	$T_c^*$ Present Model °C	$\Delta T_c^*$ , %
70, 0	25, 0	8, 0	0, 544	0, 544	0, 055	20, 00	20, 64	3, 200
72, 5	25, 0	8, 0	0, 588	0, 598	1, 616	25, 00	25, 08	0, 320
70, 0	30, 0	8, 0	0, 208	0, 202	3, 029	-	21, 66	-
72, 5	30, 0	8, 0	0, 260	0, 262	0, 731	25, 00	24, 66	1, 360
75, 0	30, 0	8, 0	0, 305	0, 302	0, 852	-	28, 36	-
83, 0	30, 0	8, 0	0, 425	0, 465	9, 318	30, 00	30, 01	0, 033
80, 0	35, 0	8, 0	0, 130	0, 132	1, 769	-	27, 48	
83, 0	35, 0	8, 0	0, 190	0, 199	4, 684	30, 00	28, 90	3, 667
85, 0	35, 0	8, 0	0, 227	0, 226	0, 162	-	31, 67	-
90, 0	35, 0	8, 0	0, 305	0, 305	0, 098	-	33, 63	-
92, 5	35, 0	8, 0	0, 327	0, 312	4, 613	35, 00	35, 43	1, 229
90, 0	40, 0	8, 0	0, 110	0, 111	0, 545	-	33, 39	-
92, 5	40, 0	8, 0	0, 153	0, 149	2, 563	35, 00	35, 30	0, 857
100, 0	40, 0	8, 0	0, 270	0, 244	9, 815	40, 00	40, 22	0, 550



### 3.3.2 Validation of EES Ejector Model for R134a

The behaviour of an ejector refrigeration cycle operating with R134a was studied using the real gas model proposed in the work done by Li et al. [60]. Validation is performed under various  $T_g$ ,  $T_c^*$ , EAR, and  $T_{am}$ . The results of the analysis are shown in Table 7 whereby the maximum absolute error for the  $P_{cc}$ ,  $\mu$ , and  $a_t$  are 0.2 %, 0.5%, and 0.08 % respectively.

Table 7: Validation of R134a ejector model

EAR	$T_g$	$T_e$	Theory	Present	$P_{cc}$	Theory	Present	$\mu$	$a_t$	Present	$a_t$
-	-	-	Model	Model	$\Delta$	$\mu$ [-]	Model	$\Delta$	[m/s]	Model	$\Delta$ [m/s]
	[°C]	[°C]	[60]	$P_{cc}$ [kPa]	[%]	[60]	$\mu$ [-]	[%]	[60]	$a_t$ [m/s]	%
2,77	75	10	0,8969	0,8978	0,1003	0,0844	0,0841	0,367	137,2	137,3	0,0729
2,77	75	12,5	0,9203	0,9216	0,1413	0,1149	0,1145	0,348	137,0	137,0	0,0000
2,77	75	15	0,9426	0,9436	0,1061	0,1472	0,1470	0,136	136,7	136,8	0,0732
3,32	75	10	0,8461	0,8473	0,1418	0,1929	0,1926	0,156	136,9	136,9	0,0000
3,32	75	12,5	0,8685	0,8698	0,1497	0,2325	0,2322	0,129	136,7	136,7	0,0000
3,32	75	15	0,8906	0,8918	0,1347	0,2749	0,2746	0,109	136,5	136,5	0,0000
3,32	80	10	0,9071	0,9084	0,1433	0,1402	0,1396	0,428	134,8	134,8	0,0000
3,32	80	12,5	0,9324	0,9335	0,1180	0,1749	0,1744	0,286	134,5	134,6	0,0743
3,32	80	15	0,9568	0,9581	0,1359	0,2118	0,2117	0,047	134,2	134,3	0,0745
3,32	85	12,5	0,9964	0,9979	0,1505	0,1235	0,1232	0,243	131,9	132,0	0,0758
3,32	85	15	1,0240	1,0260	0,1953	0,1562	0,1558	0,256	131,6	131,7	0,0760
3,96	75	10	0,7984	0,7977	0,0877	0,3195	0,3189	0,188	136,6	136,7	0,0732
3,96	75	12,5	0,8204	0,8199	0,0609	0,3694	0,3691	0,081	136,4	136,5	0,0733
3,96	75	15	0,8431	0,8425	0,0712	0,4237	0,4228	0,212	136,3	136,3	0,0000
3,96	80	10	0,8555	0,8552	0,0351	0,2522	0,2518	0,159	134,4	134,5	0,0744
3,96	80	12,5	0,8797	0,8791	0,0682	0,2966	0,2961	0,169	134,2	134,2	0,0000
3,96	80	15	0,9039	0,9034	0,0553	0,3442	0,3436	0,174	134,0	134,0	0,0000
3,96	85	10	0,9134	0,9128	0,0657	0,1930	0,1924	0,311	131,8	131,9	0,0759
3,96	85	12,5	0,9401	0,9395	0,0638	0,2317	0,2312	0,216	131,5	131,6	0,0760
3,96	85	15	0,9667	0,9661	0,0621	0,2739	0,2730	0,327	131,3	131,3	0,0000

### 3.3.3 Validation of R245fa Ejector Model

The accuracy of the results obtained for an R245fa Ejector Model is validated by making a comparison of the results generated by the model developed by Li et al. [60]. The comparison is conducted at various  $T_g$ ,  $T_e$ , and  $T_c^*$ . Table 8 shows that under all the considered operating conditions, the critical condenser temperature deviates from the literature values

by a maximum absolute relative error of 0.2575 % whilst the  $\mu$  deviates from literature values by a maximum of 4.2281 %.

Table 8: Performance data for an R245fa ejector model

$T_g$	$T_e$	$T_c^*$ [60]	Model $T_c^*$	$ \Delta $ $T_c^*$ %	Critical $\mu$ [60]	Model $\mu$	$ \Delta $ $\mu$ %	Ejector Type [60]
88	16	31, 90	31, 97	0, 2194	0, 6833	0, 6709	1, 8239	2-B
88	12	30, 60	30, 66	0, 1961	0, 5425	0, 5424	0, 0105	2-B
88	8	29, 45	29, 46	0, 0340	0, 4179	0, 4282	2, 4635	2-B
95	16	35, 30	35, 34	0, 1133	0, 5313	0, 5353	0, 7709	2-B
95	12	34, 10	34, 12	0, 0587	0, 4179	0, 4251	1, 7279	2-B
95	8	33, 00	32, 94	0, 1818	0, 3188	0, 3275	2, 7593	2-B
102	16	38, 80	38, 75	0, 1289	0, 4179	0, 4220	1, 0028	2-B
102	12	37, 67	37, 57	0, 2575	0, 3188	0, 3276	2, 7747	2-B
102	8	36, 60	36, 43	0, 4645	0, 2357	0, 2457	4, 2281	2-B

### 3.3.4 Validation of EES Ejector performance: R290

Validation of the model using R290 as a working fluid is considered by evaluating the performance at various  $T_g$ ,  $T_c$ , and  $T_e$ .

**Table 9** shows how accurately the model predicts the effect of  $T_g$  on  $T_c^*$  as the maximum absolute error between the results attained by Chen et. al. [61] and those from the present study is less than 3 °C whilst the COP varies by a maximum relative error of 6.9%. The degree of accuracy of the model when evaluating the effect of  $T_e$  on the COP is shown in **Table 10**

Table 9: Effect of  $T_g$  on the critical  $T_c$  at fixed  $T_e$  (8 °C)

$T_g$ [°C]	Published $T_c^*$ [°C] [61]	Model $T_c^*$ [°C]	Absolute error [°C]	Model COP [-]	Published COP [-] [61]	Relative Error % [-]
65	17, 33	20, 28	2, 95	1, 114	1, 175	5, 1915
70	19, 25	21, 27	2, 02	0, 9732	1, 035	5, 9710
75	21, 22	22, 17	0, 95	0, 8491	0, 9	5, 6556
80	23, 33	22, 96	-0, 37	0, 7395	0, 79	6, 3924
85	25, 35	23, 6	-1, 75	0, 6427	0, 69	6, 8551
90	27, 6	25, 58	-2, 02	0, 5697	0, 59	3, 4407
95	30	27, 93	-2, 07	0, 5226	0, 5166	-1, 1614

Table 10: Validation of the effect of  $T_e$  on the COP at the  $T_g$  of 90 °C

$T_e$	Model COP [-]	Published COP [-] [61]	Relative Error %
5	0, 4974	0, 5350	7, 0280
6	0, 5160	0, 5500	6, 1818
7	0, 5448	0, 5750	5, 2522
8	0, 5697	0, 6000	5, 0500
9	0, 5952	0, 6250	4, 7680
10	0, 6211	0, 6500	4, 4462
11	0, 6480	0, 6750	4, 0000
12	0, 6792	0, 7000	2, 9714
13	0, 7114	0, 7270	2, 1458
14	0, 7443	0, 7550	1, 4172
15	0, 7779	0, 7833	0, 6894

The deviations in the presented results are attributed to the nature in which the efficiency terms are evaluated in the two models. Both models consider the refrigerant as a real gas when evaluating the state properties within the ejector. However, the theoretical study by Chen et. al. [61], uses fixed efficiency values for each ejector geometry whilst the present study varies the efficiency terms according to the geometry and operating conditions ( $T_g$  and  $T_e$ ). The importance of efficiency values in obtaining accurate results has been highlighted in previous studies whereby correlations are formulated to determine efficiencies according to the ejector geometry and operating conditions [60, 82, 83].

# 4 Development and Validation of TRNSYS Model

## 4.1 Introduction

The review of performance analysis studies (in [subsection 2.4.4.2](#)) of the ejector has shown how the system is greatly affected by the evaporator temperature ( $T_e$ ), the condenser temperature ( $T_c$ ), and the generator temperature ( $T_g$ ). With  $T_c$  and  $T_g$  being dependent on ambient conditions and solar radiation, [subsection 2.4.4.4](#) has shown how solar-powered systems can be optimized to operate at adequate  $T_g$  and  $T_c$  values to deliver quality COP values. Since  $T_c$  and  $T_g$  are highly variable throughout the day, it is imperative that the solar-powered ERS be studied under the dynamic variability of  $T_c$  and  $T_g$ .

Unlike steady-state analysis, dynamic analysis of the ejector factors in realistic behaviour such as thermal energy inertia across the solar collectors and water storage tank. The dynamic analysis also enables performance observation under actual ambient temperatures. Optimization of the system under dynamic conditions gives superior COP values throughout the operating period.

## 4.2 The solar-powered Ejector Refrigeration System Model

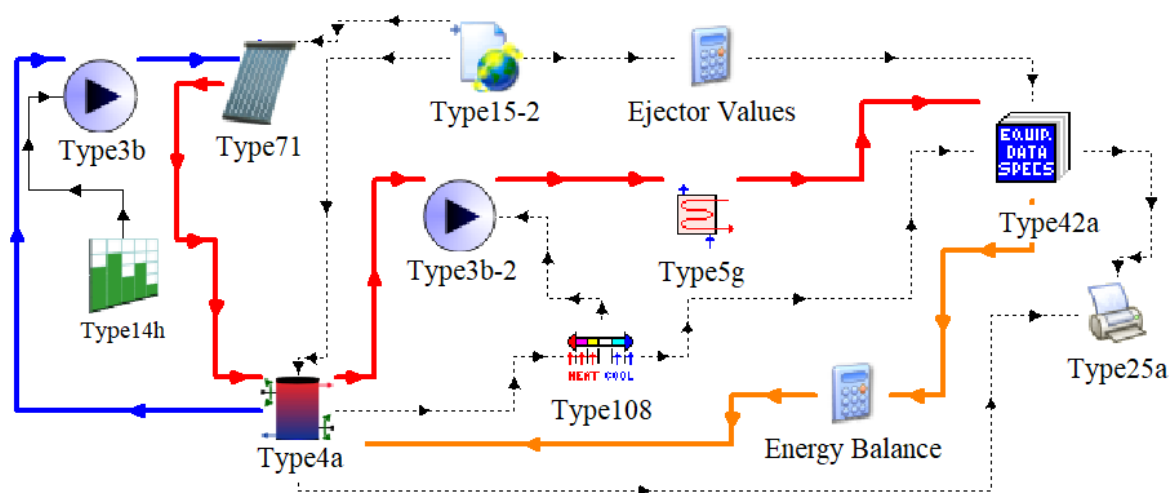


Figure 11: TRNSYS layout of a solar thermal ERS

The dynamic model of the solar-powered ERS is developed in TRNSYS by coupling the performance data of the ERS with the solar thermal components such as the solar collectors, flow circulatory pumps, and storage tank. The components are configured to produce the layout shown in [Figure 11](#) whereby the ETC (Type71) are connected to a flow circulatory pump (Type3b) which transfers water from the bottom node of the storage tank (Type4a). The operation of the pump is controlled by a general forcing function (Type14h). Weather and solar data is accessed through the Type15-2 component and it is connected to the solar collectors, the storage tank, and the ERS (Type42a). The storage tank is further connected to another pump (Type3b), a 5 stage thermostat (Type 108), and a calculator. The pump transfers water from the hottest node of the tank to a heat exchanger (Type5g) which serves as the generator of the ERS. Operation of the pump is regulated by the 5 stage thermostat which monitors the hottest node of the tank and sends an activation signal to the pump and ERS once the desired tank temperature has been reached.  $T_c$  and  $T_e$  are specified through the calculator, labelled "Ejector Values", whereby  $T_c$  is set to be 5 °C above ambient temperatures. To ensure that sufficient energy is supplied to the ERS through the heat exchanger, an additional calculator labelled "Energy Balance", is used to calculate the final water temperature returning to the storage tank.

Specifications of the critical component parameters are listed in [Table 11](#). Performance-related constants are taken from data found in published studies and the rest of the parameters are varied during parametric analysis.

Table 11: System components and their specified values

Component	TRNSYS Label	Function	Specified Quantity
Evacuated Tube Collector	Type71	Collects Solar Thermal Energy and collects thermal energy	Collector Area = 20 m <sup>2</sup> Collector Slope= 42°
Weather File		Stores weather and solar data for a specific location	Location: Johannesburg
Ejector	Type 42 a	contains the performance data of the ejector	
EjectorSelector	Type108	5 stage thermostat calibrated to activate the ejector once appropriate generator temperatures are achieved.	Monitoring Temperature = 65 °C
Collector Pump	Type 114	Circulates flow through the collector	$\dot{m} = 3800$ kg/hr
Type14h	Type14h	Activates (and De-activates ) Flow Through the collectors	Pump Time: 8 AM - 4 PM
Tank Pump	Type 114	Circulates flow through the tanks	$\dot{m} = 10000$ kg/hr
Pump	Type 114	Circulates flow through the generator	$\dot{m} = 750$ kg/hr
Type14h-3	Type14h	Activates (and De-activates ) Flow Through the tanks	
Type14h-6	Type14h	Activates (and De-activates ) Flow Through the generator	
Type5g	Type5g	Shell and Tube Heat Exchanger, used as a generator	Load Side $C_p = 1.4$ kJ/kg.K $U_{Gen} = 5400$ kJ/kg.K [84]
Buffer2	Type4c	Stores thermal energy from Solar Tank	Tank Volume = 5 m <sup>3</sup> Nodes = 3 Start Temp. = 60 °C (All Nodes) Tank Loss Coeff. = 1.8kJ/hr.m <sup>2</sup> [84]
Solar Tank	Type4c	Stores thermal energy from solar collectors	Tank Volume = 2.5 m <sup>3</sup> Number of nodes = 5 Start Temp. = 60 °C (All Nodes) Tank Loss Coeff. = 1.8kJ/hr.m <sup>2</sup>
Ejector Values	Calculator	Specifies the evapoarator and condenser temperature to the ejector	$T_c =$ Ambient + 5 °C Fixed $T_e = 12, 5$ °C

## 4.3 TRNSYS Components Modelling

Performance analysis of the solar-powered ejector is carried out by linking the required components (pumps, collectors, heat exchangers, and the ERS). Most of the components, except for the ERS, are readily available to use within TRNSYS. Mathematical modelling of TRNSYS built-in components is briefly outlined in the following sections.

### 4.3.1 Hot Water Storage Tank Model

The tank considered in the present study is thermally stratified with variable inlet positions (TRNSYS Type 4c, mode 2 operation). This mode of operation enables a high degree of thermal stratification as the inlet flow streams (from the collectors and the generator) enter the tank at the node with the closest stream temperature. The tank model considers uniform thermal losses to surroundings which is coupled to ambient temperature read from the weather file. Other features of the model include two auxiliary heaters which can be configured to operate at different times, activating temperature, and heating capacities. Each heater is positioned in a different tank segment which is referred to as a node.

Evaluation of the thermal performance of the tank considers the flow of thermal energy across each node of the tank by taking an energy balance across the tank nodes as shown in [Equation 39](#).

$$M_{node}C_{pf}\frac{dT_{node}}{dt} = \dot{m}_{net}C_{pf}(\Delta T_{nodal}) \quad (39)$$

From [Equation 39](#),  $M_{node}$  represents the mass of fluid in the tank node,  $\dot{m}_{net}$  is the net mass flow-rate into the tank node, and  $\Delta T_{nodal}$  is the temperature difference across the node. Mathematical modelling of the thermal effects of heat gain from the collectors, heat loss to the load and environment, heat gain from surrounding nodes, and heat gain from the auxiliary heaters is shown in [Equation 40](#), respectively.

$$M_{node}C_{pf}\frac{dT_{node}}{dt} = \dot{m}_{coll}C_{pf}(T_o - T_{node}) + \dot{m}_{load}C_{pf}(T_L - T_{node}) + U_t A_i (T_{am} - T_{node}) + \dot{m}_{net}C_{pf}(\Delta T_{nodal}) + Q_i \quad (40)$$

The additional terms in [Equation 40](#) represent the mass flow rate through the collector ( $\dot{m}_{coll}$ ), the collector outlet temperature  $T_o$ , the temperature of the node being considered ( $T_{node}$ ), the mass flow-rate from the tank to the load ( $\dot{m}_{load}$ ), tank inlet temperature from the load ( $T_L$ ), the loss coefficient between the tank and ambient conditions ( $U_t$ ), the surface area of the tank ( $A_i$ ), and heat gain from the electric heating elements ( $Q_i$ ).

### 4.3.2 Evacuated Tube Collectors Model

Performance evaluation of ETC collectors considers the effect of thermal and optical properties of the collector on the overall heat harvesting capability of the components. The efficiency of ETC ( $\eta_{coll}$ ) is determined by comparing  $\dot{Q}_u$  to the available irradiation. The energy balance of the collector is shown in [Equation 41](#) whereby  $\dot{Q}_u$  is evaluated by determining the temperature difference of the water flowing through the collector while the available solar irradiation is calculated by taking the product of  $A$  (the collector area) and  $I_T$  (the global radiation incident on the solar collector). [\[85\]](#)

$$\eta_{coll} = \frac{Q_u}{AI_T} = \frac{\dot{m}C_{pf}(T_o - T_i)}{AI_T} \quad (41)$$

The efficiency of the collector can also be evaluated by considering the performance parameters of the collector as shown in [Equation 42](#). The considered collector dependent parameters are  $F_R$ ,  $\tau\alpha_n$ ,  $U_L$ ,  $T_o$ ,  $T_i$ .

$$\eta_{coll} = F_R(\tau\alpha)_n - F_R U_L \frac{(T_o - T_i)}{I_T} \quad (42)$$

The accuracy of the model is improved by considering the non-linear variation of the loss coefficient,  $U_L$ , with the temperature difference ( $T_o - T_i$ ). This results in a quadratic equation (shown in [Equation 43](#)) expressing the variation of the collector efficiency with the additional term being the collector thermal loss temperature dependency coefficient,  $U_{L/T}$ .

$$\eta_{coll} = \frac{Q_u}{AI_T} = F_R(\tau\alpha)_n - F_R U_L \frac{(T_o - T_i)}{I_T} - F_R U_{L/T} \frac{(T_o - T_i)^2}{I_T} \quad (43)$$

[Equation 43](#) can further be simplified to suite literature supplied constants (obtained through collector testing procedures) which specify the performance of collectors. The simplified equation is shown in [Equation 44](#).

$$\eta_{coll} = \frac{Q_u}{AI_T} = a_0 - a_1 \frac{(\Delta T)}{I_T} - a_2 \frac{(\Delta T)^2}{I_T} \quad (44)$$

The constants shown in [Equation 44](#) represent, Intercept (maximum) of the collector efficiency ( $a_0$ ), negative of the first-order coefficient in collector efficiency equation ( $a_1$ ), negative of the second-order coefficient in collector efficiency equation ( $a_2$ ). During simulation, the collector constants ( $a_0$ ,  $a_1$ ,  $a_2$ ) are kept at their default values which are 0.7, 2.778  $W/m^2.K$ , and 0.00833  $W/m^2.K$ , respectively [\[79, 26\]](#). TRNSYS also considers the effect of variable operating conditions such as variable working fluid flow-rates, collectors configuration (series/parallel connections), and variable solar radiation incidence angles [\[79\]](#).

For ETC, an Incident Angle Modifier (IAM) is employed to consider the variation of solar (both beam and diffuse) radiation as the sun moves across the horizon. This modification is adopted in the mathematical models by adjusting the constants found in [Equation 44](#).



### 4.3.3 Weather Data Model

TRNSYS Type 15 (weather data processor) is used to access solar and weather data which is stored in TMY2. During operation, Type15 reads the specified TMY2 file and calculates solar radiation (beam, diffuser, ground reflected, and total), the slope and azimuth angle of the collector, and the angle of incidence of beam solar radiation [79].

### 4.3.4 Flow Circulation Pump Model

Flow circulation through the collectors and generator is modelled with a variable speed Type 3b pump. Flow-rate variation is achieved by adjusting the user-specified maximum flow-rate ( $\dot{m}_{max}$ ) with a variable control function ( $\gamma$ ) which can be set between 0 (no flow) and 1 (maximum mass flow). A mathematical equation of the mass flow-rate through the pump is shown in Equation 45, whereby the pump outlet flow rate ( $\dot{m}_o$ ) is obtained by taking the product of the control function and the maximum specified flow-rate.

$$\dot{m}_o = \gamma \dot{m}_{max} \quad (45)$$

The fluid outlet temperature from the pump ( $T_{out,pump}$ ) is calculated by considering a thermal energy balance across the pump as shown in Equation 46.

$$T_{out,pump} = T_{in,pump} + \frac{P_{pump} F_{par}}{\dot{m}_o C_p} \quad (46)$$

The rise in fluid temperature across the pump is due to the conversion of some of the pump's electric power  $P_{pump}$  to thermal energy which is subsequently transferred to the working fluid. The electric to thermal energy conversion factor is represented by  $F_{par}$ .

### 4.3.5 TRNSYS Ejector Modelling

Since TRNSYS does not have a readily available model of the ejector, performance analysis of the ejector was achieved by import the performance data through Type 42a. The performance data was generated from EES and exported as a text file with values obtained at different operating parameters.

In modelling the ejector component, there are three independent variables that are specified namely the condenser temperature (as the first independent variable, with 10 temperature values specified in the third line of the data file), evaporator temperature (the second independent with 5 temperature values listed in the second line of the data file), and the generator temperature which is the primary independent variable and only has 4 specified temperature values. The dependent values are evaluated based on the combination of independent variables that have been selected in a specific case [79].

70.00000	80.00000	90.00000	100.00000						
10.00000	11.25000	12.50000	13.75000	15.00000					
30.00000	32.22000	34.44000	36.67000	38.89000	41.11000	43.33000	45.56000	47.78000	50.00000
<b>1.06200</b>	<b>0.32880</b>	<b>30.00000</b>	!Cooling capacity and COP at Condenser evaporator and generator temperature				<b>30</b>	<b>10</b>	<b>70</b>
0.76080	0.23560	32.22000	!Cooling capacity and COP at Condenser evaporator and generator temperature				32.22	10	70
0.29430	0.09113	34.44000	!Cooling capacity and COP at Condenser evaporator and generator temperature				34.44	10	70
0.00000	0.00000	36.67000	!Cooling capacity and COP at Condenser evaporator and generator temperature				36.67	10	70
0.00000	0.00000	38.89000	!Cooling capacity and COP at Condenser evaporator and generator temperature				38.89	10	70
0.00000	0.00000	41.11000	!Cooling capacity and COP at Condenser evaporator and generator temperature				41.11	10	70
0.00000	0.00000	43.33000	!Cooling capacity and COP at Condenser evaporator and generator temperature				43.33	10	70
0.00000	0.00000	45.56000	!Cooling capacity and COP at Condenser evaporator and generator temperature				45.56	10	70
0.00000	0.00000	47.78000	!Cooling capacity and COP at Condenser evaporator and generator temperature				47.78	10	70
0.00000	0.00000	50.00000	!Cooling capacity and COP at Condenser evaporator and generator temperature				50	10	70

Figure 12: Details of the ejector performance data when stored in the Type 42a data file

An example of how the data is configured within the file is shown in [Figure 12](#) whereby the generator, evaporator, and condenser temperatures are the third, second, and first independent variables, respectively. The data in the enclosed line signifies the cooling capacity (1.06200 kW), COP (0.32880), at the corresponding condenser temperature (30 °C) when the specified operating conditions are 70 °C(generator temperature), 10 °C(evaporator temperature), and 30 °C (condenser temperature).

The details on how the performance data of this component is structured are outline below:

- The first independent variable is the generator temperature and the considered generator values are 70 °C, 80 °C, 90 °C, and 100 °C.
- The second independent variable is the evaporator temperature and the values considered for this variable are 10 °C, 11.25 °C, 12.5 °C, 13.75 °C, and 15 °C.
- The third independent variable is the condenser temperature with the values specified as 30 °C, 35 °C, 40 °C, 45 °C, and 50 °C.

### 4.3.6 Energy Balance Calculator

To ensure that the heat exchanger model supplies the minimal amount of heat required to turn the refrigerant from saturated liquid (at the inlet of the generator) to saturated vapour (at the exit of the generator), the magnitude of the required energy is evaluated throughout the performance of the cycle. [Equation 47](#) shows that the  $\dot{m}_p$  is used together with the enthalpy at the exit of the generator (  $h_{gen,exit}$ , quality being 1 ) and at the inlet of the generator (  $h_{gen,inlet}$ , with is equal to the enthalpy at the exit of the condenser).

$$Q_{ref,min} = \dot{m}_{ref}(h_{gen,exit} - h_{gen,inlet}) \quad (47)$$

To ensure that the solar thermal system is supplying sufficient heat to the ejector's generator, latent heat transfer to the refrigerant (from the hot water,  $Q_{ref,latent}$ ) was also modelled for the hot water stream. Considering this results in a further temperature drop of the water stream whilst the refrigerant temperature ( $T_g$ ) remains constant as it transitions from saturated liquid to saturated vapour which is signified by refrigerant's enthalpy of vaporization  $\Delta h_{fg}$ . The final temperature of the hot water stream ( $T_{water,final}$ ) is evaluated by considering latent heat transfer from the water exiting the heat exchanger as shown in [Equation 48](#) .

$$Q_{ref,latent} = \dot{m}_{ref} \Delta h_{fg} = \dot{m}_{water} C_{p,water} (T_g - T_{water,final}) \quad (48)$$

The total amount of heat input for the working fluid is the sum of sensible and latent heat gain whereby sensible heat gain is evaluated according to [Equation 49](#)

$$Q_{ref,sensible} = \dot{m}_{ref} C_{p,ref} (T_g - T_{cc}) \quad (49)$$

To verify if sufficient heat is supplied, the sum of latent and sensible heat is compared against the COP evaluated head demand of the ejector refrigeration system.

$$Q_{sensible} + Q_{latent} \geq \frac{\dot{Q}_e}{COP} \quad (50)$$

## 4.4 TRNSYS Model Validation

Validation of the solar thermal system is done by comparing the results against what is in published in the study by Tashtoush et al. [26]. The considered parameters are the annual useful heat gain of the collectors and the dynamic performance of the system such as the change in collector exit temperature, storage tank exit temperature, and the effect of the storage tank volume on the performance of the entire system.

### 4.4.1 Validation of Solar Collector and Weather File Coupling

The accuracy of the model was analyzed by comparing the calculated annual useful heat gain at variable collector slope angles against the results published by Tashtoush et al. [26]. The key configuration in question is the coupling of the weather file (TYPE 15 -6) and the solar collectors (FPC, TYPE 1B). Since the weather data of the location considered in the previously mentioned study is not available on TRNSYS, the weather data of a nearby location (Jerusalem) is used. The operating parameters are set as follows

Table 12: Collector operating parameters

Collector Parameters	$a_0$	$a_1$ ( $W/m^2k^2$ )	$a_2$ ( $W/m^2k^2$ )
Collector Type:			
Double Glassed Flat Plate Collector	0, 8	3, 5	0, 0138
Evacuated Tube Collector	0, 8	2, 77	0, 00833
Inlet Flow Rate	100		
Inlet Temperature	20		
Aperture Area	10		

Table 13: Annual useful energy gain at various collector slope angles

Slope [°]	Annual Useful Energy Gain [kW.h] [26]	Current Study [kW.h]	Absolute Error [%]
0, 00	11774.47	11750.00	0.2078
2, 00	12019.71	12000.00	0.1640
4, 00	12246.03	12250.00	0.0324
8, 00	12643.65	12583.33	0.4771
10, 00	12811.95	12750.00	0.4835
14, 00	13095.55	13000.00	0.7296
24, 00	13464.98	13388.90	0.5650
30, 00	13446.51	13388.90	0.4284
36, 00	13272.67	13166.67	0.7986
40, 00	13056.12	13000.00	0.4298
44, 00	12775.71	12700.00	0.5926
50, 00	12238.05	12166.70	0.5830

As seen in [Table 13](#), the annual useful energy gain of the current model is slightly higher than that presented in the validation study. A possible explanation for this could be that the solar radiation experienced in the considered location may be above the values used in the validation study.

#### 4.4.2 Validation of the Solar Thermal System

The model of the solar thermal system developed in the current study is similar to the one found in the work done by Tashtoush et al. [26]. To verify if the solar thermal system has been accurately modelled, the same optimization process (as in Tashtoush et al. [26]) is employed and the output parameters of the two studies are compared. Since the actual ejector component is not needed to perform this analysis, the list of components used includes the

weather data file (Type 15 -2), evacuated tube collectors (Type 71), an un-stratified thermal storage tank (Type 4a), a pump (Type 3b ), equations, and plotters with output file generation capacities.

The accuracy of the model is initially validated by considering the behaviour of the system at variable collector area ( $40m^2$  and  $80m^2$ ) whilst flow through the storage tank (to load) is fixed at 1200 kg/ hr, mass flow-rate through the collector is at  $50\text{kg/hr } m^2$ , and the storage volume is fixed at  $2 m^3$  as presented in [Figure 13](#). With the parameter of interest being the collector exit temperature, in both present model and theory results, it can be noted that the  $80 m^2$  system achieves higher temperature values when compared to the  $40 m^2$  system. Analysis of the degree of variation of the present model results from those in published literature shows that there is an average deviation of 20% in magnitude.

The second validation procedure is undertaken at variable storage volume capacity whereby the collector area is fixed at  $60 m^2$ , with the collector flow rate fixed at  $50 \text{ kg/hrm}^2$ , and the storage tank capacity varied between  $2 m^3$  and  $5 m^3$ . Validation results are presented in [Figure 14](#) and from these, it can be noted that the  $2 m^3$  system operates at higher tank exit temperatures than the  $5 m^3$  in both literature and present study results. The maximum deviation between the present study results and those in literature is 25% due to higher model results figures. A general analysis of the presented results shows that the  $2m^3$  system operates at much higher temperatures than the  $5m^3$ . This is an anticipated outcome as a larger thermal storage tank would require more thermal energy to raise the collector exit temperature compared to a smaller storage tank system ( $2 m^3$ )

The behaviour of the current model is similar to that used for validation. The same trends in the variation of the collector and tank outlet temperatures with changes in the flow rate through the collector are the same. The difference is in the magnitude of the temperature values whereby the current model values are slightly higher than those in [\[26\]](#). The difference between the two sets of results is attributed to the use of different weather input files. The published data uses weather data from a specific location within Jordan (Jordan University of Science and Technology), approximately 150 km from Jerusalem, which may cause different magnitudes of solar radiation and ambient temperatures.

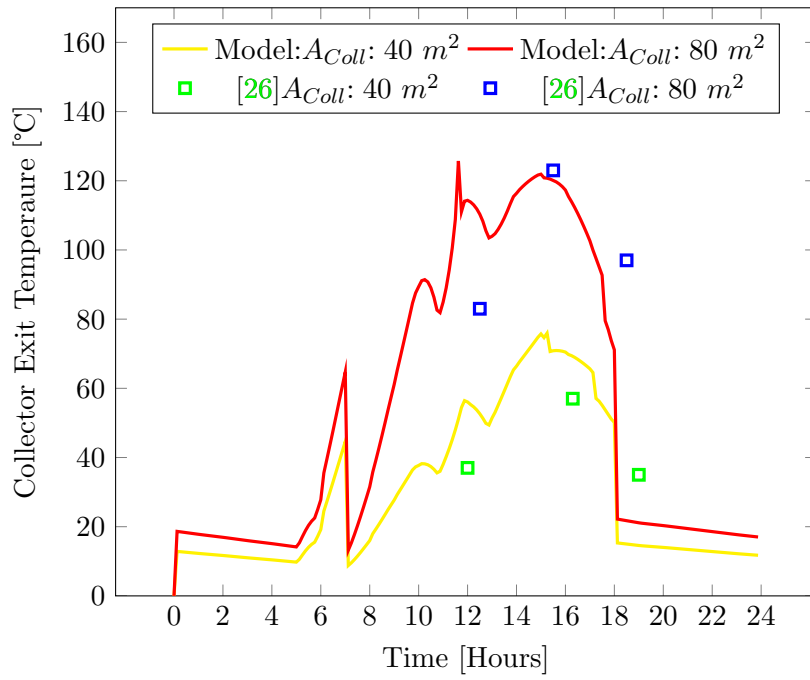


Figure 13: Collector Exit Temperature variation at different collector areas

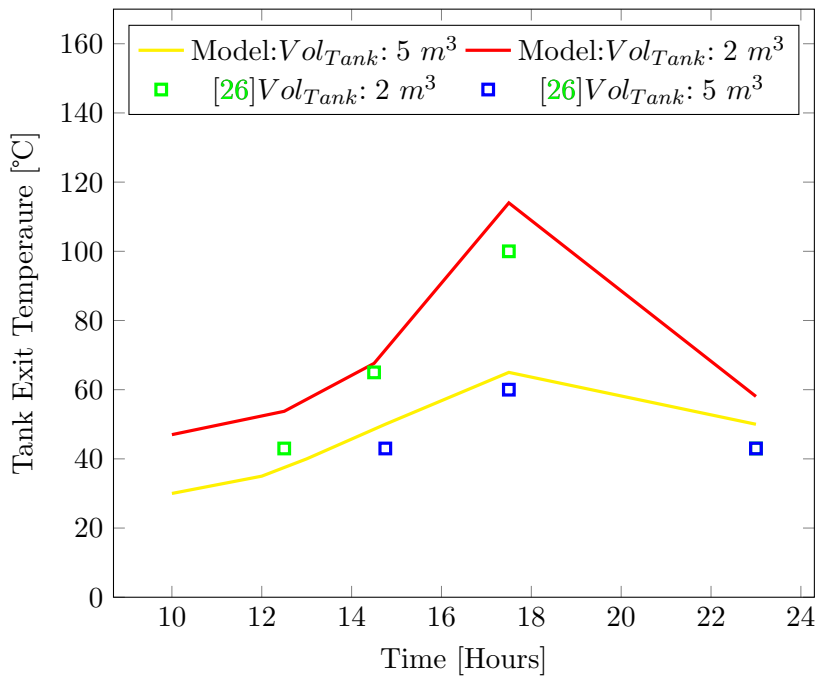


Figure 14: Tank Exit Temperatures at different Tank Storage Volumes

# 5 Results and Discussion

The present chapter focuses on the results generated from both steady-state and dynamic models of the ejector which were presented in the previous chapter.

## 5.1 Steady-State Analysis of the Ejector Refrigeration System

The steady-state analysis of the ejector is carried out on R1234ze(Z) and R134a. These working fluids are considered because they are environmentally friendly (low ODP) and less hazardous. Between the two refrigerants, R1234ze(Z) is ultimately considered because of its low GWP and superior performance (high COP values) compared to R134a.

### 5.1.1 Analysis of R134a ERS in Critical Mode

The steady-state analysis of the ERS is carried out to investigate the effect of the ejector area ratio (EAR), generator temperature ( $T_g$ ), evaporator temperature ( $T_e$ ), and condenser temperature ( $T_c$ ) on the entrainment ratio ( $\mu$ ), cooling capacity ( $\dot{Q}_{cool}$ ), and COP.

#### 5.1.1.1 Effect of EAR, Generator Temperature and Evaporator Temperature on ERS Performance

The effect of the EAR on the performance of the system is determined by evaluating  $\mu$  at different  $T_e$  and  $T_g$  in critical mode of operation. The geometry considered is taken from a published study and is listed in [Table 14](#).

Table 14: Ejector geometry specification [\[60\]](#)

Ejector Tag	Nozzle Tag	Nozzle		Mixing Chamber	EAR
		Throat Diameter (mm)	Exit Diameter (mm)	Diameter (mm)	
AA	A	2, 5	3, 3	4, 16	2.77
BB	B	2, 09	2, 7	3, 81	3.32
BA	A	2, 09	2, 7	4.16	3.96

The EAR values (listed in [Table 14](#)) are used to refer to the considered ejector geometry in the plots. The effect of varying the evaporator temperature ( $T_e$ ) at fixed EAR and generator

temperature is in [Figure 15](#), [Figure 16](#), and [Figure 17](#) whereby it is noted that increasing  $T_e$  results in an increase in the entrainment ratio ( $\mu$ ). This perfectly aligns with the performance characteristics of the ejector as increasing  $T_e$  encourages the ease of evaporation of the secondary fluid and thus enables higher entrainment ratios[28, 22].

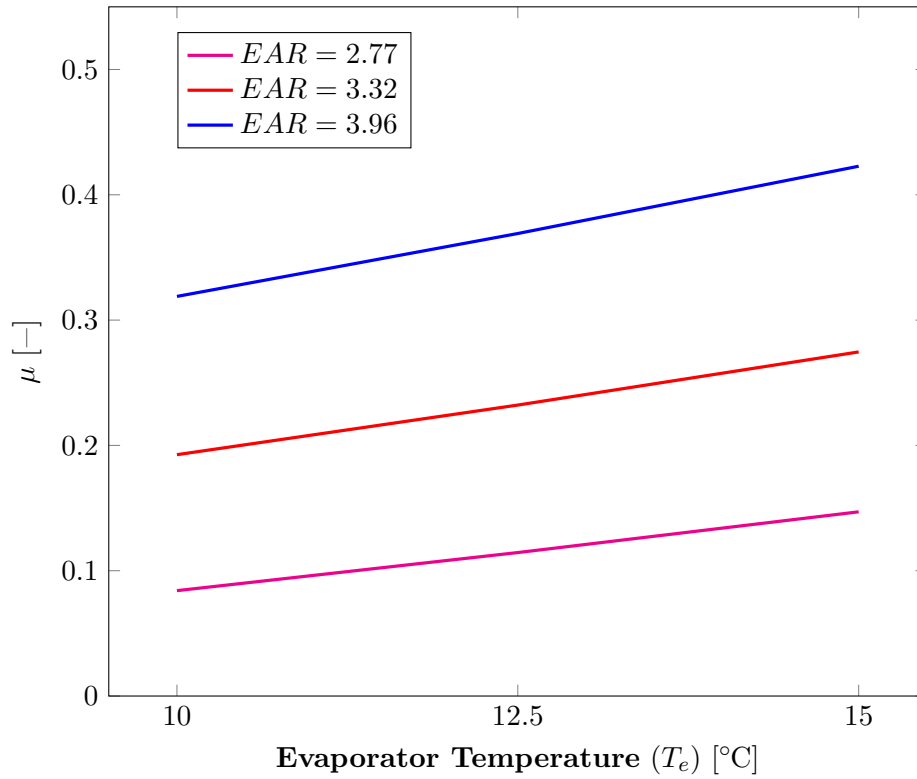


Figure 15: Effect of EAR on performance at  $T_g = 75$  °C



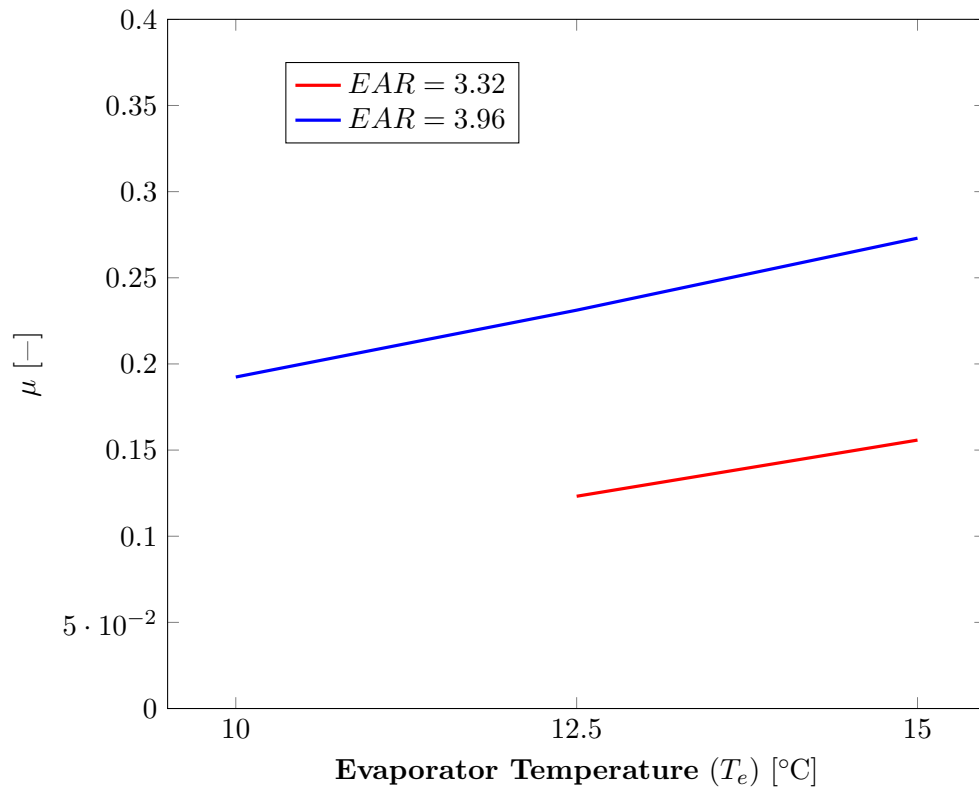


Figure 16: Effect of EAR on performance at  $T_g = 85^\circ\text{C}$

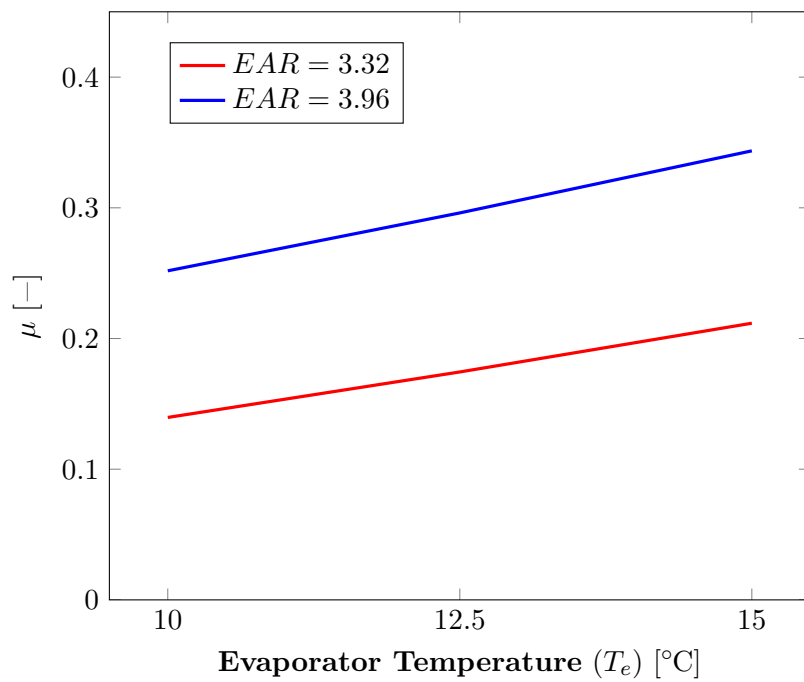


Figure 17: Variation of  $\mu$  at  $T_g = 80^\circ\text{C}$  and variable EAR and  $T_e$

Figure 15, Figure 16, and Figure 17 show that at fixed  $T_e$  and  $T_g$ , increasing the EAR increases the  $\mu$  of the ejector. This is because higher EAR's provide the secondary stream with sufficient space to expand within the ejector.

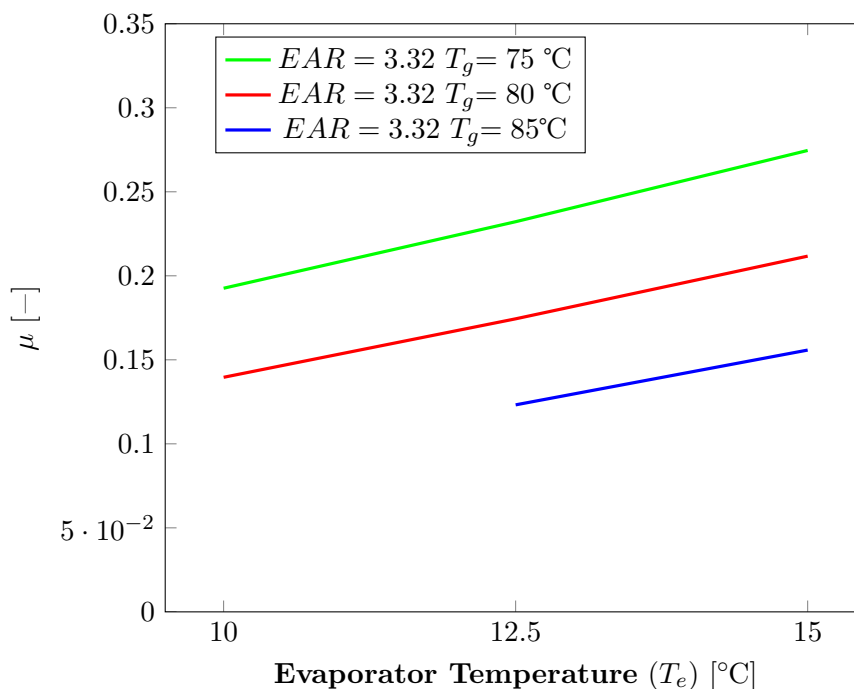


Figure 18: Variation of  $\mu$  at EAR of 3.32, variable  $T_g$  and  $T_e$

Figure 18 shows that an ERS at variable  $T_g$  and fixed EAR and  $T_e$  experiences a decrease in performance due to increments of  $T_g$ . In each of the three considered  $T_g$  values (75, 80, and 85 °C) and three considered evaporator temperatures (10, 12.5, and 15 °C), increasing  $T_g$  results in a decrease of  $\mu$ . High  $\mu$  values at low  $T_g$  values come as a result of the relatively low primary nozzle exit pressure of the motive fluid. This low pressure results in non-excessive expansion of the primary fluid which provides room for the entrainment of the secondary stream within the confined dimensions of the ejector. This also explains why ejectors with larger EAR experience higher  $\mu$  as this results in extra space for entrainment of the secondary stream.

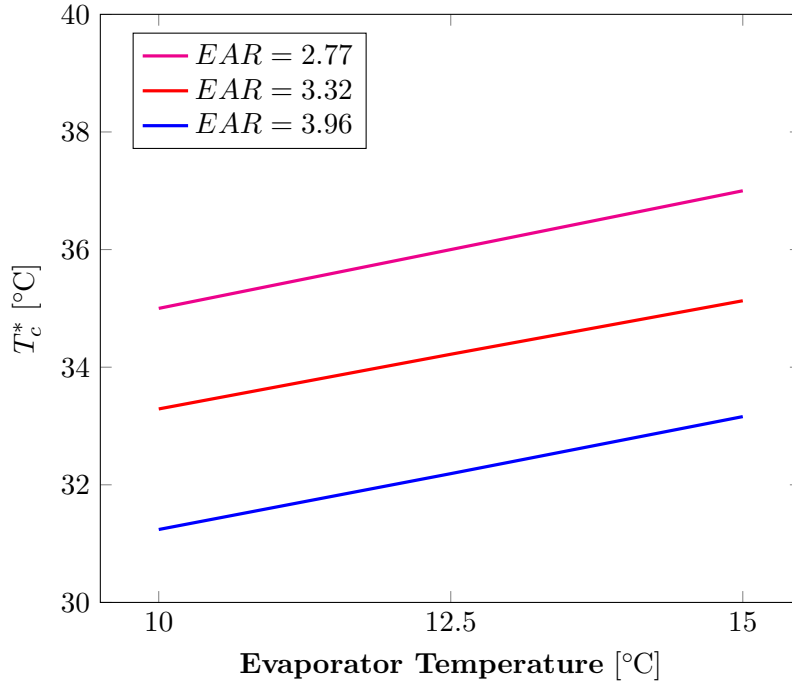


Figure 19: Effect of EAR on performance at  $T_g = 75$

Figure 19 and Figure 20 shows how the EAR,  $T_g$ , and  $T_e$  affect the  $T_c^*$  of the ejector. From Figure 19, it is evident that at low  $T_e$  and small EAR values result in low  $T_c^*$  values. As highlighted in the literature review section, high  $T_c^*$  values ensure that the ejector functions in critical mode when required to operate at high ambient temperatures. By comparing the information in Figure 19 and Figure 20, it can be seen that at  $T_g$  of 75 °C and  $T_e$  of 10 °C (Figure 19), EAR 2.77 can operate at the minimum  $T_c^*$  of 35 °C whilst EAR 3.96 only reaches  $T_c^*$  of 31 °C. This means that at  $T_c$  temperatures above 31 °C and  $T_g$  of 75 °C, EAR 3.96 would perform in subcritical mode whilst EAR 2.77 would perform in critical mode. However, at higher  $T_g$  values (85 °C) and  $T_e$  of 10 °C, EAR3.96 can perform in critical mode at  $T_c$  values above 31 °C since it has a  $T_c^*$  value of 36 °C.

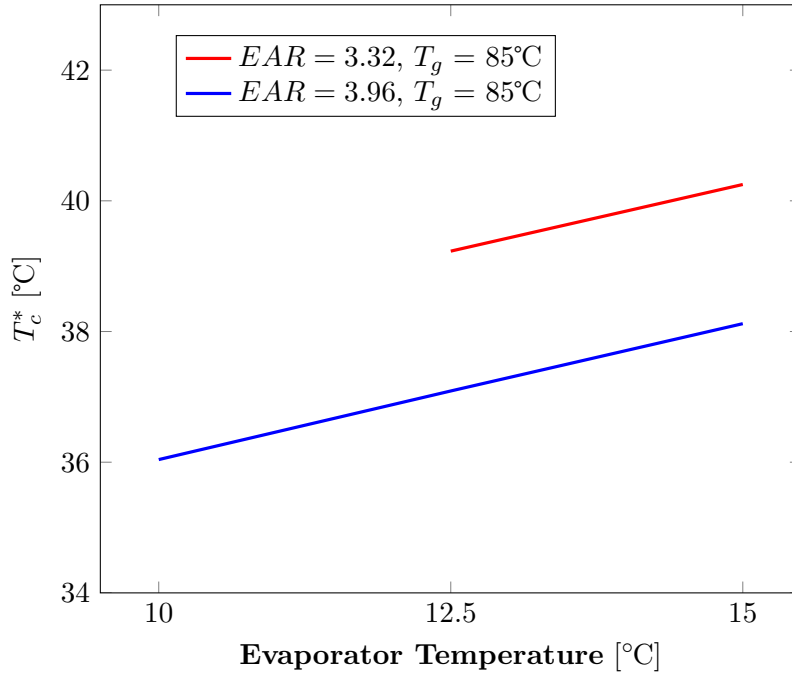


Figure 20: Effect of EAR on performance at  $T_g = 85$

#### 5.1.1.2 Analysis of R134a ERS in Sub-critical Mode

Steady-state analysis of the ejector in subcritical mode is carried out at fixed  $T_g$  values of  $65^\circ\text{C}$  and  $80^\circ\text{C}$ , with variable (ambient and time coupled)  $T_c$ . The variation of  $T_c$  is dependent on  $T_{am}$  which increases from low values in the morning (due to an increase in solar irradiation) to peak values in the afternoon and later on decreases in the evening. The objective of the analysis is to outline the effect of  $T_g$  and  $T_c$  on the  $\dot{Q}_{cool}$  and COP of the ERS.

From [Figure 21](#), the effect of  $T_c$  on the cooling capacity of the ejector is presented. The plot also shows the  $T_c^*$  of the ERS evaluated at  $T_g$  of  $65^\circ\text{C}$  and  $T_e$  of  $12.5^\circ\text{C}$ . From the plot, it can be seen that when  $T_c$  is less than  $T_c^*$  ( $26^\circ\text{C}$ ) the condenser maintains a constant  $\dot{Q}_{cool}$  above 3 kW. Increasing  $T_c$  above  $T_c^*$  results in a sharp decrease in  $\dot{Q}_{cool}$ . The breakdown point in the operation of the ejector is reached at  $T_c$  of  $36^\circ\text{C}$  whereby the system delivers 0 kW  $\dot{Q}_{cool}$ . Decreasing  $T_c$  below  $35^\circ\text{C}$  results in the system regaining  $\dot{Q}_{cool}$ . Under the same operating conditions ( $T_g$  of  $65^\circ\text{C}$ ,  $T_e$  of  $12.5^\circ\text{C}$ , and ambient variable  $T_c$ ) a similar trend is observed on the variation of the COP as highlighted in [Figure 22](#).

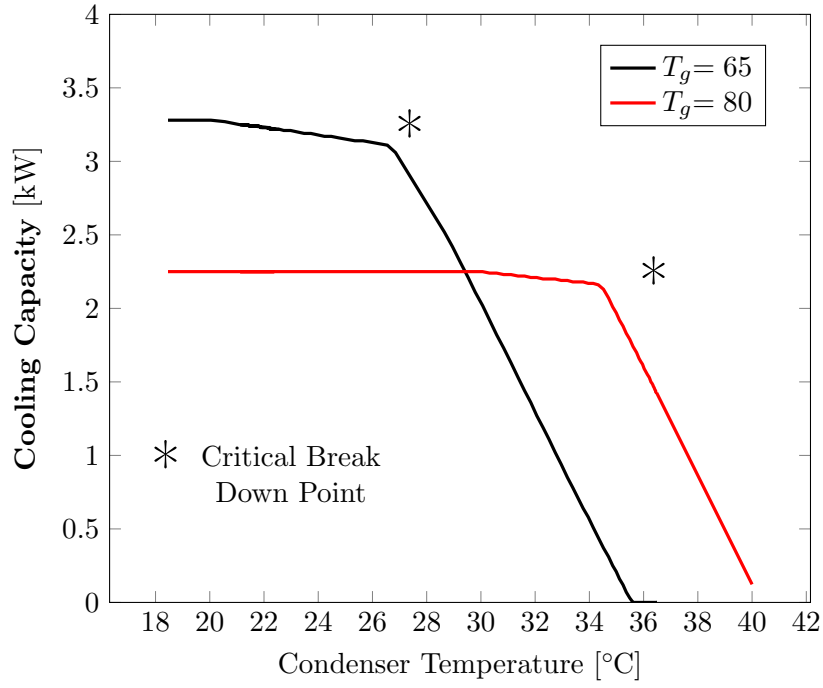


Figure 21: Variation of  $\dot{Q}_{cool}$  and  $T_c$

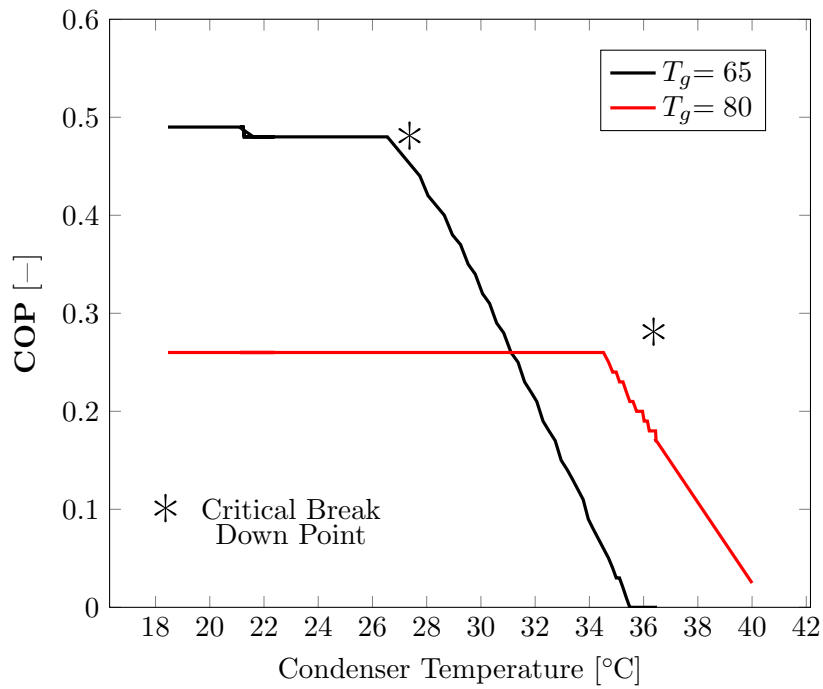


Figure 22: Variation of COP and  $T_c$

Steady-state analysis is also conducted at the constant  $T_g$  and  $T_e$  of 100 °C and 12.5 °C (Figure 23). The inverse relationship between  $\dot{Q}_{cool}$  and  $T_c$  after exceeding  $T_c^*$  is also appreciated. However, due to the higher  $T_g$ , the system has a higher  $T_c^*$  value of 35 °C. As a

result of the high  $T_c^*$  value, the system can operate at higher  $T_c$  temperatures without reaching the critical breakdown point. However, operating at high  $T_g$  results in low  $\dot{Q}_{cool}$  values even in critical operation mode. From [Figure 23](#), it is seen that  $\dot{Q}_{cool}$  reaches the lowest value of 1.5 kW at the peak  $T_c$  of 36 °C. The drop in  $\dot{Q}_{cool}$  from the constant value of 2.3 kW starts when  $T_c$  exceeds  $T_c^*$ .

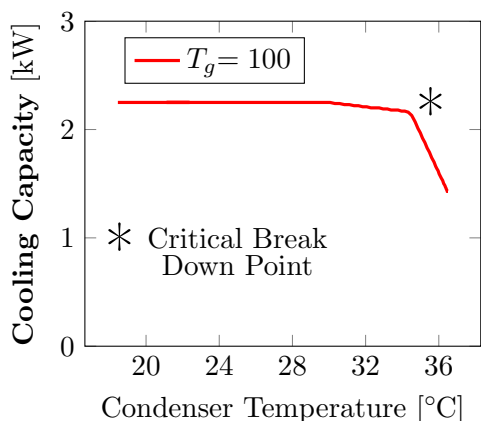


Figure 23: Variation of  $\dot{Q}_{cool}$  and  $T_c$

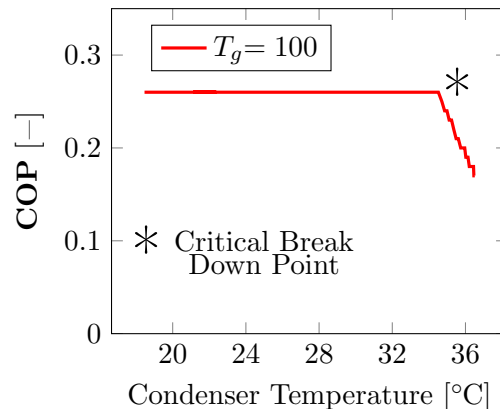


Figure 24: Variation of COP and  $T_c$

### 5.1.2 Performance Analysis of the R1234ze(Z) Ejector

Analysis of the R1234ze(Z) ERS is done under variable  $T_g$  and  $T_c$  with  $T_e$  fixed at 8 °C. The considered EAR is 7.25, and the geometry specifications are shown in [Table 15](#). Analysis is performed for both critical and subcritical mode.

Table 15: Ejector geometry [\[28\]](#)

Nozzle		Mixing Chamber	EAR
Throat Diameter	Exit Diameter	Diameter	
(mm)	(mm)	(mm)	
4, 515	7, 8	12.155	7.25

From [Figure 25](#), it can be seen that the ejector delivers high COP values at low  $T_g$  and  $T_c$ . When configured to operate at  $T_c$  of 25 °C, the COP increases (from 0.544 to 0.588) with  $T_g$  until the  $T_c^*$  (25.08 °C) is reached. Beyond this point, further increments in  $T_g$  result in decreasing COP values.

A similar trend is visible on the other  $T_c$  values (30, 35, and 40 °C) whereby the COP increases until reaching the  $T_c^*$  dependent peak COP value. These results show that in order

to obtain COP values that are above 0.4, the operating parameters should be a maximum  $T_g$  of 80 °C and a maximum  $T_c$  of 30 °C.

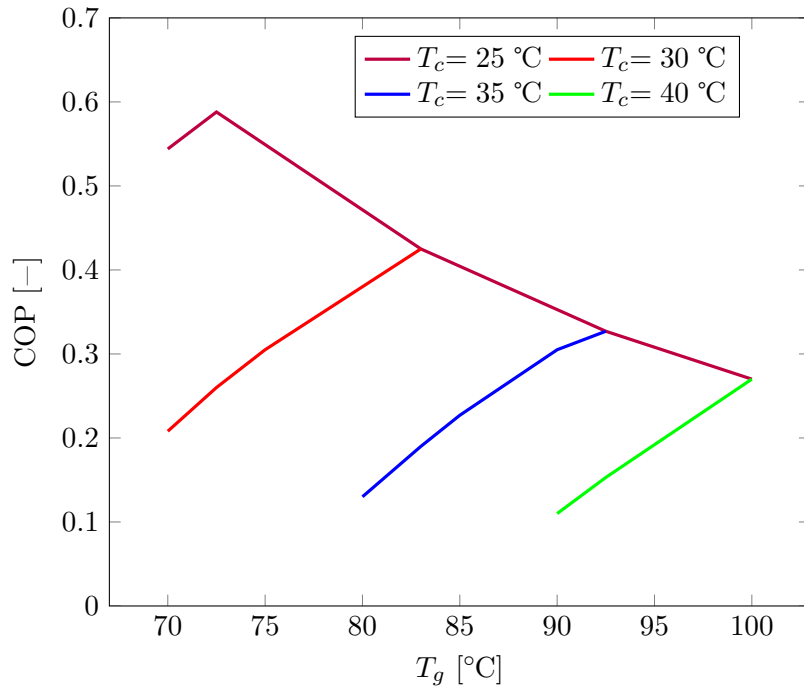


Figure 25: Effect of EAR on performance at  $T_g = 85$  °C

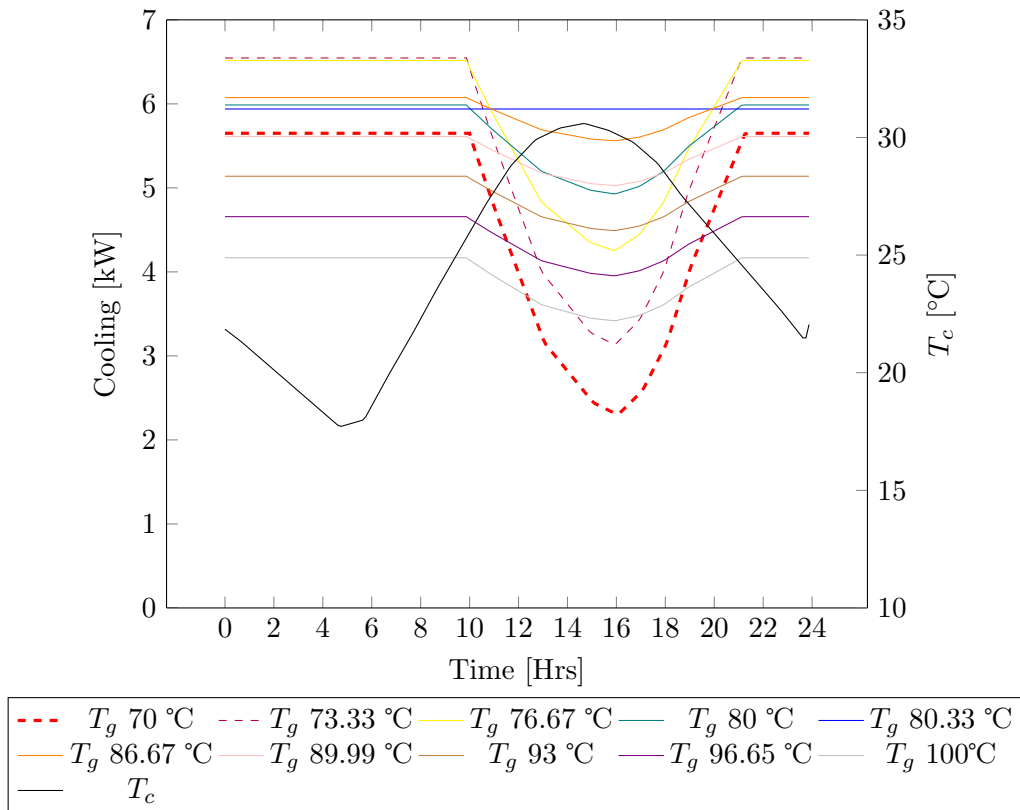


Figure 26: Performance of an R1234ze(Z) ejector at various  $T_g$  and ambient adjusted  $T_c$

**Figure 26**, shows the variation of the cooling capacity at various  $T_g$  temperatures under the same ambient coupled  $T_c$ . The considered nozzle geometry shows that uninterrupted critical mode operation can only be achieved at  $T_g$  80.33 °C.  $T_g$  below 80.33 °C achieve reduced cooling capacity at peak  $T_c$  because of insufficient vacuum pressure from the expanded primary flow to entrain maximum secondary flow whilst  $T_g$  above 80.33 achieve reduced cooling capacity at peak  $T_c$  because of excess primary flow in the ejector which inhibits favourable expansion of the secondary flow into the ejector. To achieve high cooling capacity whilst using less thermal energy,  $T_g$  can be set to 73.33 °C and continuously raised to 80.33 °C when approaching peak  $T_c$ .

Since R1234ze(Z) is a more environmentally friendly working fluid, compared to R134a, it is considered as the main working fluid for this study. Moreover, as proven in the results above, the R1234ze(Z) ejector achieves higher performance figures when compared to the R134a ejector.

## 5.2 Parametric Analysis of the R1234ze(Z) Solar Thermal Ejector

The performance analysis of the solar-powered ejector is considered through parametric analysis of  $A_{Coll}$  and  $Vol_{Tank}$  to determine their effect on the  $T_g$ ,  $T_e$ ,  $T_c^*$ , and COP of the ejector. The objective of the analysis is to optimize the performance of the ejector by ensuring that it functions at optimal COP throughout the day and achieves high daily SF values. The procedure followed in the analysis begins with the determination of the optimal collector area which is then followed by determining the appropriate storage tank volume. The parametric study is considered under Johannesburg, Bloemfontein, Durban, Cape Town, and Upington solar and weather conditions.

## 5.3 Ejector performance results in Johannesburg

The effect of  $A_{Coll}$  on the COP of the ejector is shown in **Figure 27**. The collector area is varied from 20  $m^2$  to 56  $m^2$  with the intermediate areas being 36  $m^2$  and 44  $m^2$ . The storage volume is kept constant at 3.33  $m^3$ . From **Figure 27**, it is evident that increasing the collector area results in an increase in the ejectors active cooling period since the systems with the largest  $A_{Coll}$  (44  $m^2$  and 56  $m^2$ ) start operating at 08:20 and finish at 21:30 whilst the small  $A_{Coll}$  systems (20  $m^2$  and 36  $m^2$ ) start 09:00 with the 20  $m^2$  system stopping at 18:00 and the 36  $m^2$  system stopping at 21:00.



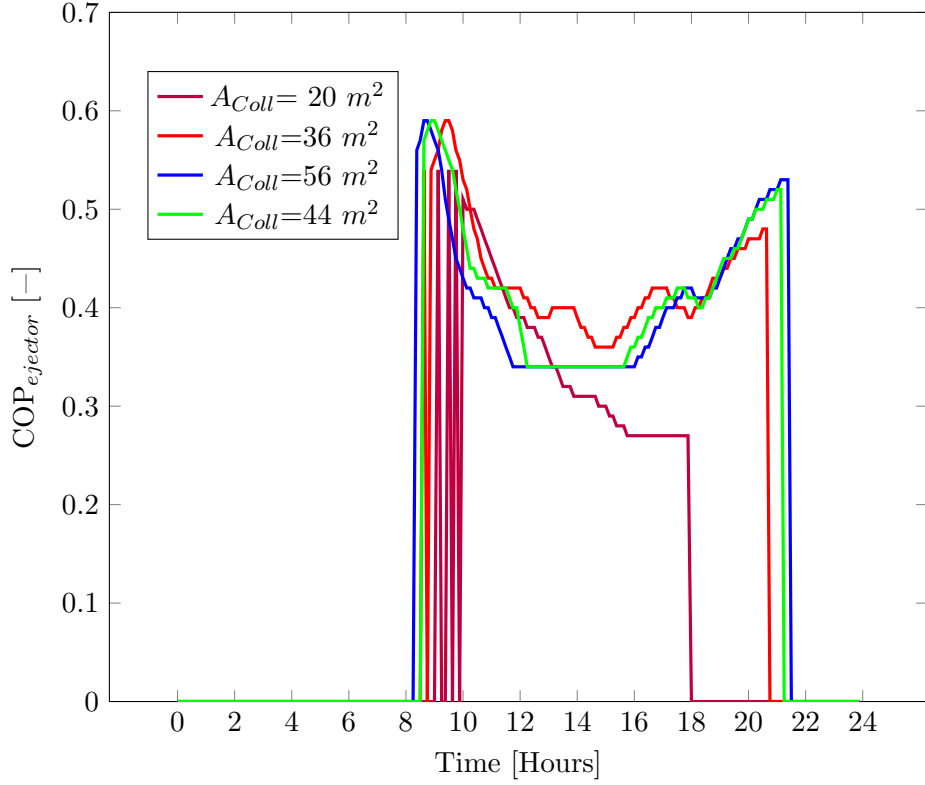


Figure 27: Variation of the ejector's COP at different  $A_{Coll}$

The collector area also plays another major role in the magnitude of the COP that the system experiences during operation. The common trend in performance of the considered configurations is that the COP value starts at a high value of 0.6 and diminishes as the day progresses with low values being experienced between 12:00 and 17:00. Except for the  $20 \text{ m}^2$  system, the evening performance is characterised by increments in COP. High morning and evening COP values come as a result of low  $T_g$  temperatures (shown in Figure 28) that enable the ejector to operate in critical mode. Operation of the system in critical mode is also proven by the  $T_c^*$  values (shown in Figure 29) which are greater than the pre-set ambient coupled  $T_c$ . From Figure 27, it is evident that the  $36 \text{ m}^2$  system provides optimal performance as it gives high COP values during the morning and evening whilst achieving considerably superior COP values between 12:00 and 17:00.

The variation of  $T_g$  at different  $A_{Coll}$  is presented in Figure 28. From the plot, it can be seen that the systems with a large collector area experience a rapid increase in  $T_g$  during startup. The effect of  $T_g$  values on the COP (Figure 27) shows that the system with a  $36 \text{ m}^2$  surface area achieves better performance because of the slightly lower  $T_g$  value. From analysing Figure 29, it is evident that the ideal operational  $T_c^*$  has to be slightly higher than  $T_c$  for the system to operate in critical mode and hence resulting in higher COP values.

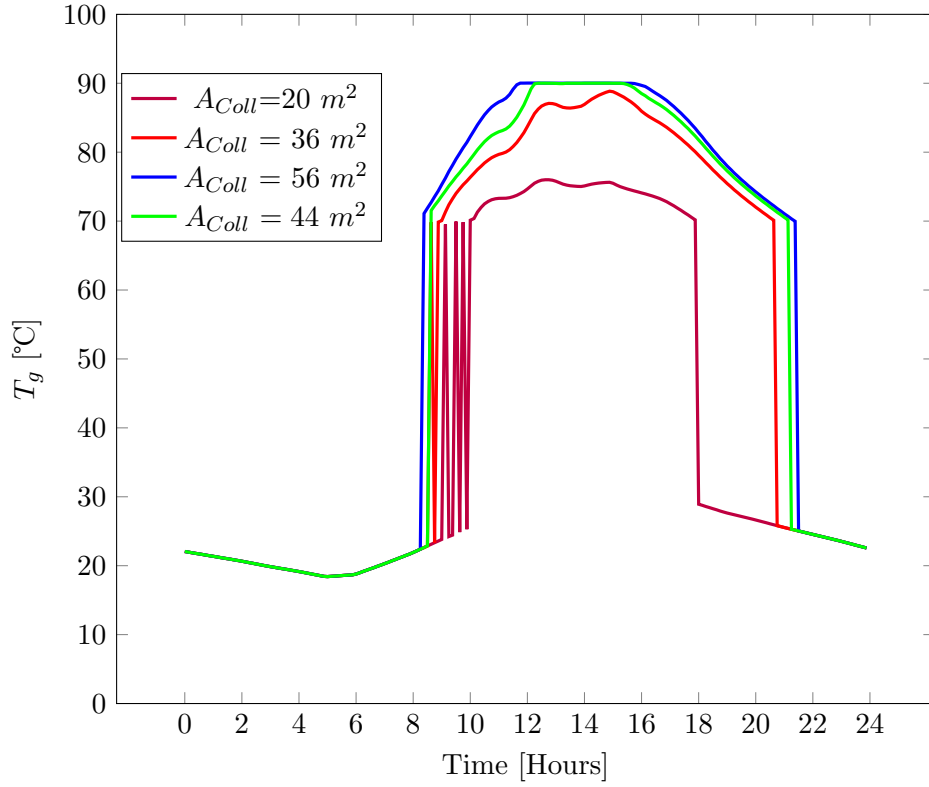


Figure 28: Variation of  $T_g$  with  $A_{Coll}$

Figure 28 shows that the  $36 \text{ m}^2$  system provides  $T_g$  values that result in adequate  $T_c^*$  and COP of the system. Figure 28 also shows that the  $20 \text{ m}^2$  system stops operating early because of low  $T_g$  values which come as a result of insufficient thermal energy harvesting from the small collector area. The system also struggles to maintain the activation temperature of  $70 \text{ }^\circ\text{C}$  which causes fluctuations in the morning  $T_g$  values. The large area systems ( $44 \text{ m}^2$  and  $56 \text{ m}^2$ ) can reach the tank boiling temperature which is set to  $90 \text{ }^\circ\text{C}$ .

Evening variation of  $T_g$  is characterized by a decrease in values. The large collector systems stop operating a few minutes after the  $36 \text{ m}^2$  system. Due to low evening ambient temperatures, three of the considered systems (excluding the  $36 \text{ m}^2$  system) can operate above critical mode as shown by the  $T_c^*$  values which are above  $T_c$ . The critical effect of  $T_g$  in ensuring that the system operates in critical mode is evident in both Figure 27 and Figure 29 whereby it can be seen that higher  $T_g$  values enable the large area systems to have higher  $T_c^*$  values in the evening which results in COP values exceeding those of the  $36 \text{ m}^2$  system.

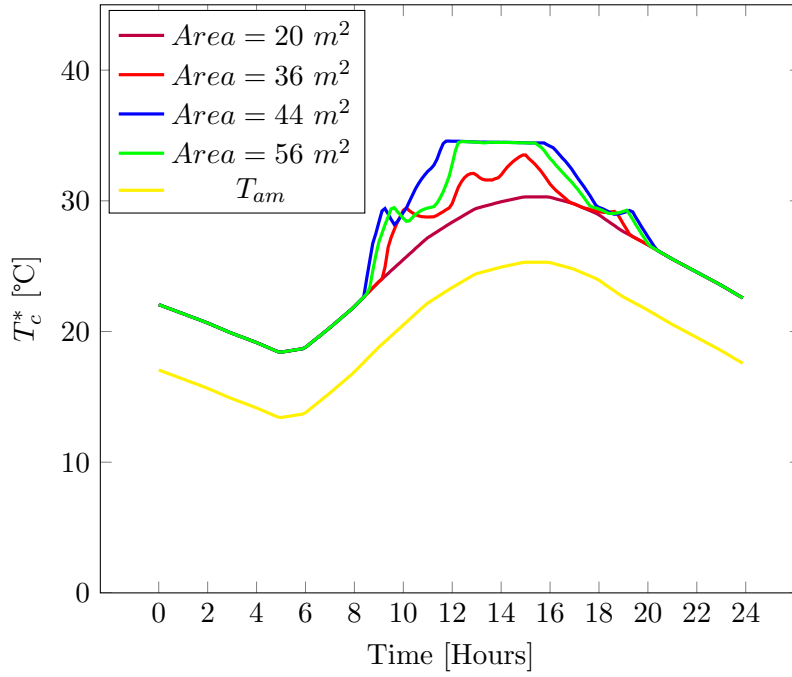


Figure 29: Variation of  $T_c^*$  with  $A_{Coll}$

From the information presented above, it is noted that the  $36 \text{ m}^2$  collector area provides the ideal system operating characteristics (high COP values at low  $T_c^*$  values) when compared to the other collector area values. With the ideal  $36 \text{ m}^2$  identified as  $36 \text{ m}^2$ , an investigation on the effect of the storage tank capacity is carried out at this area. The volume of the storage tank is varied between  $3.33$  and  $6 \text{ m}^3$  with the immediate capacities being  $4.2$  and  $5.11 \text{ m}^3$  as shown in [Figure 30](#). The significance in the performance of the considered volumes is most apparent between 12:00 and 18:00 whereby the  $3.33 \text{ m}^3$  achieves the lowest COP values whilst the larger capacity systems achieve higher COP values. The cause for this variation is clearly shown in [Figure 31](#) whereby the operating  $T_g$  of the ejector is dependent on the storage tank capacity. The results show that the small tank attains the highest  $T_g$  whilst the largest tank operates at a lower  $T_g$  value. The high  $T_g$  values in the smaller tank result in lower COP values as shown in [Figure 30](#).

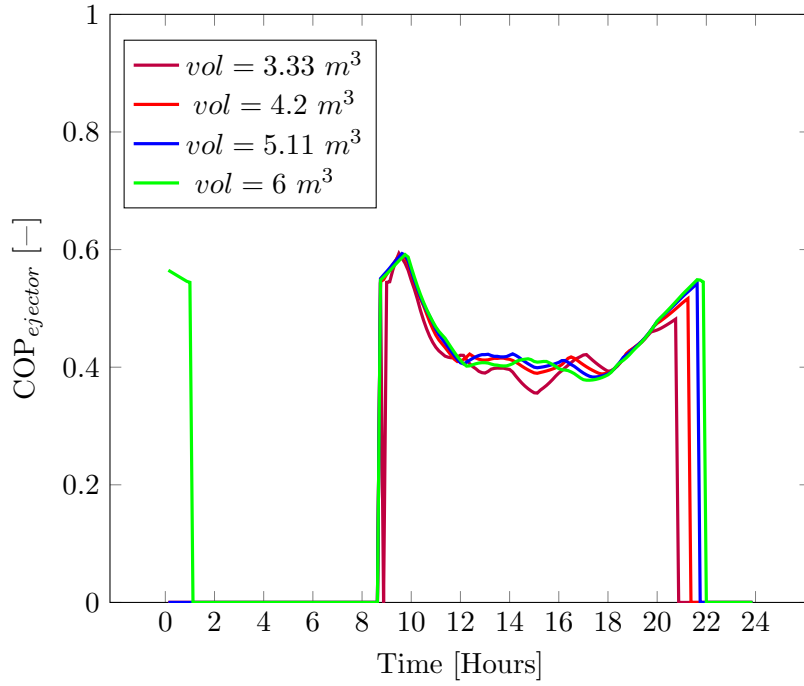


Figure 30: COP variation at different  $Vol_{Tank}$  with  $A_{Coll} = 36$

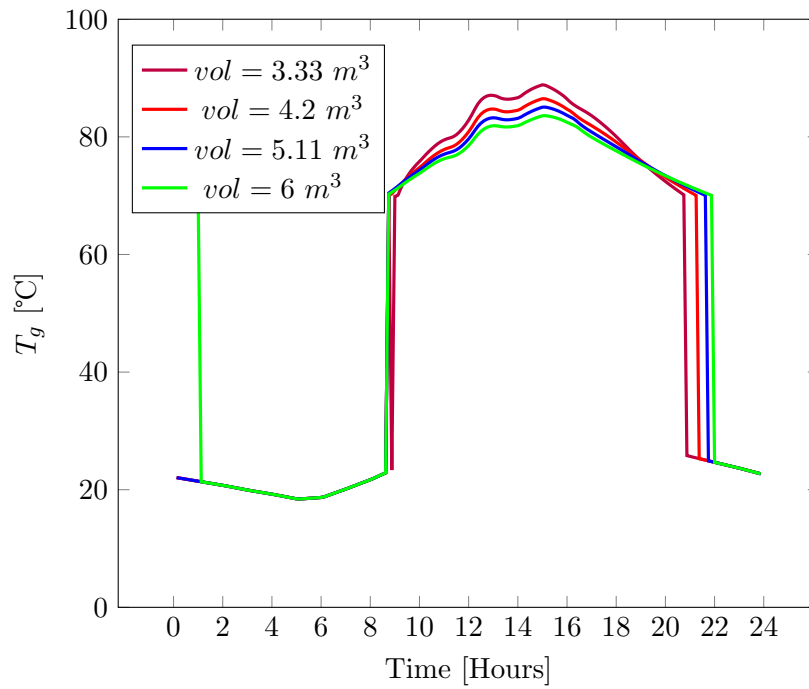


Figure 31:  $T_g$  at various  $Vol_{Tank}$  capacities,  $A_{Coll} = 36 m^2$

Figure 32 shows the variation of the system's cooling capacity at the collector area of  $36 m^2$  with two different storage tanks of  $3$  and  $6 m^3$ . In both of the considered cases, the cooling capacity has a similar characteristic variation with the COP of the system. The  $3 m^3$  system

delivers superior cooling capacity values between 1100 - 1400 and 1600 - 1900 when compared to the 6 m<sup>3</sup> system. During this period, the 3 m<sup>3</sup> system experiences lower  $T_c^*$  (shown in [Figure 33](#)) values whilst it maintains relatively high  $T_g$  (shown in [Figure 31](#)) which enables the ejector to operate in critical mode. Between 1400 and 1600, the 6 m<sup>3</sup> system experiences higher  $\dot{Q}_{cool}$  as a result of operating at low  $T_c^*$  values (which are also above ambient temperature) due to the relatively low  $T_g$  (visible in [Figure 31](#)). As a result of the larger thermal energy storage tank, the 6 m<sup>3</sup> system is able to function for extended period depending on the availability of solar radiation. This is evident in  $T_g$  ([Figure 31](#)),  $T_c^*$  ([Figure 33](#)), and  $\dot{Q}_{cool}$  ([Figure 32](#)) plots whereby the 6 m<sup>3</sup> system is seen to be operational between midnight and 0100 due to the availability of thermal energy harvested from the previous day. Beyond this period, the system stops operating due to  $T_g$  values being lower than the minimum requirement of 70 °C.

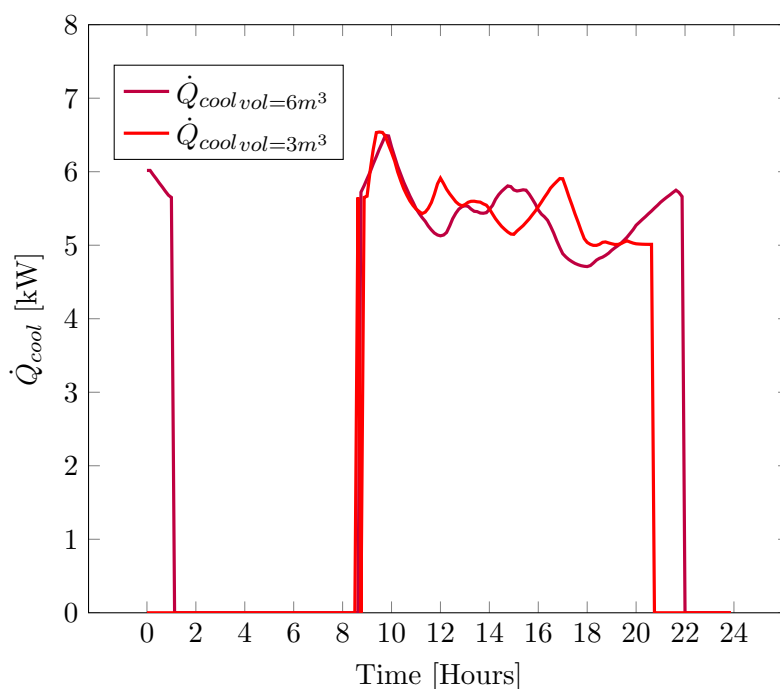


Figure 32:  $\dot{Q}_{cool}$  at various  $Vol_{Tank}$  capacities with  $A_{Coll} = 36$

Variation of the system's COP and  $\eta_{coll}$  is presented in [Figure 34](#) whereby it can be noted that the 6 m<sup>3</sup> system outperforms the 3 m<sup>3</sup> on COP values during the day (from 10:00 to 17:00). Between 17:00 and 18:00, the 3 m<sup>3</sup> achieves higher COP values which eventually become equal to the other system until reaching the stop time at 20:45. From the  $COP_{overall}$  plot, [Figure 35](#), it can be noted that the 6 m<sup>3</sup> system slightly outperforms the 3 m<sup>3</sup> with the only exception being between 17:00 and 18:00.

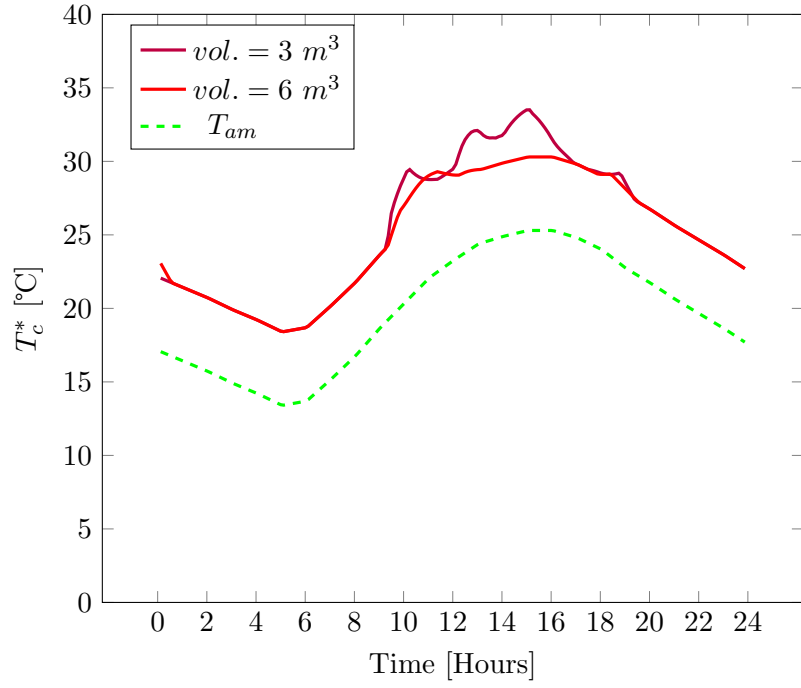


Figure 33:  $T_c^*$  at different  $Vol_{Tank}$ ,  $A_{Coll} = 36$

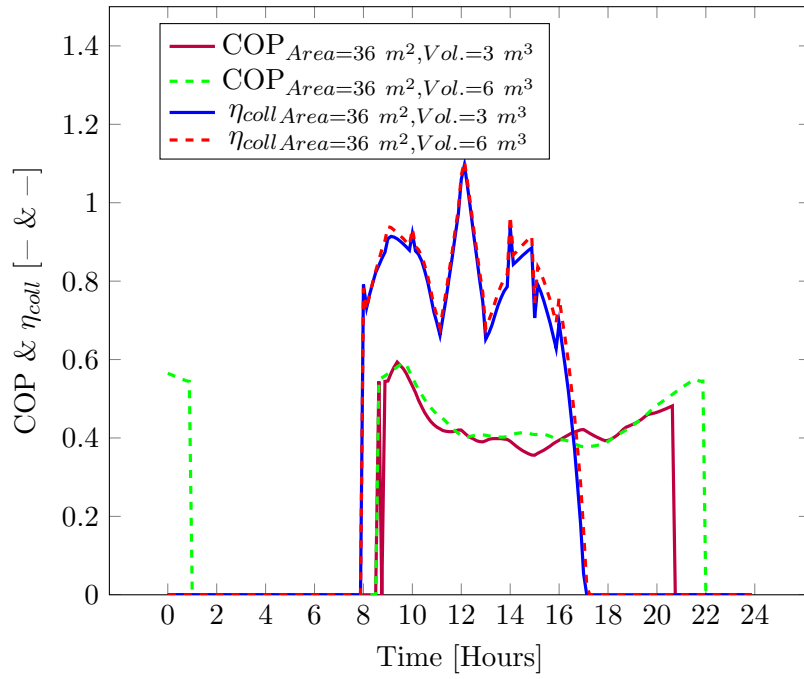


Figure 34: COP &  $\eta_{coll}$  at different  $Vol_{Tank}$  Capacities

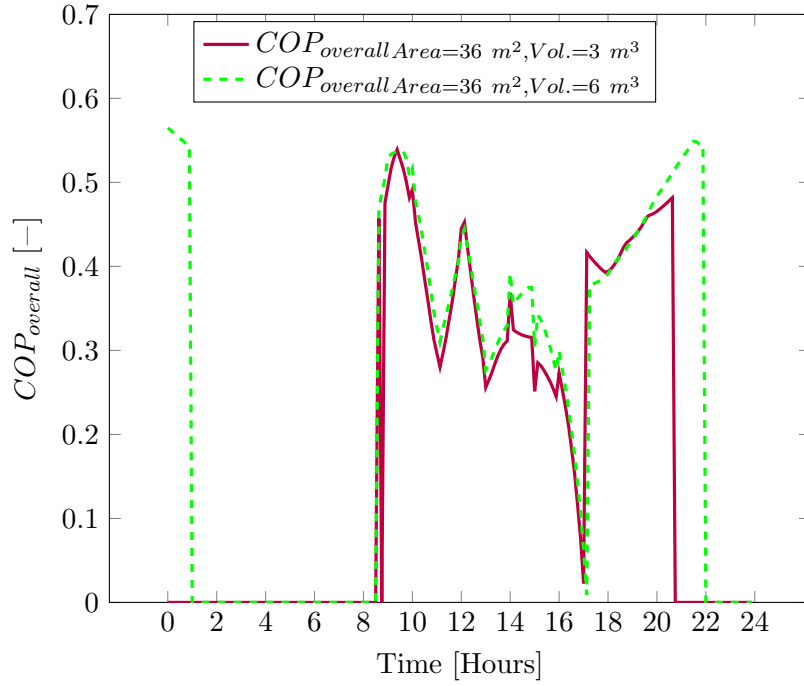


Figure 35:  $COP_{overall}$  at different  $Vol_{Tank}$  Capacities

Considering that the operation of the system is only extended by one hour and fifteen minutes when the storage capacity is doubled from  $3 m^3$  to  $6 m^3$ , for practicality purposes, the smaller tank is considered to be adequate for Johannesburg weather and solar conditions. Further optimization of the system is carried out through an investigation on the optimal slope of the solar collectors.

Analysis begins with finding the optimal collector slope through the parametric examination of the collector's performance at various slopes ( shown in Appendix A5 - [Figure 115](#)). The investigation shows that optimal collector performance is achieved at the collector slope angle of  $33^\circ$ . The behaviour of the solar coupled ERS is again evaluated and compared to the previously obtained results. [Figure 36](#) shows the variation of critical condenser temperature ( $T_c^*$ ) values for the optimized collector slope angle against the previously considered system configuration under the same ambient temperature. From the plot, it is evident that the optimized collector slope system performs at low  $T_c^*$  values in early morning hours (8:00 to 11:00) which results from low generator temperature values (shown in [Figure 37](#)). The combination of these parameters (low  $T_g$  and low  $T_c^*$  values) results in a higher COP (shown in [Figure 38](#)) values when compared to the unoptimized collector slope system. However, as the day progresses (beyond 11:00), the optimized collector slope system achieves slightly higher generator temperature values due to higher operating efficiency figures of the solar collectors. Consequently, the system operates at higher critical condenser temperatures as-well which results in low COP values (mid-day to 15:00) compared to the unoptimized system. From

15:00 to sunset, both systems operate at the same parameters (critical condenser and generator temperatures) which produce the same COP values. The startup operation of both systems is characterized by fluctuations in generator temperature due to insufficient solar irradiation which causes a slow increase in temperature. From the performance plots (especially the COP and  $T_g$  plot), it can be noted that the optimal collector slope system indicates slightly poor energy storage capabilities which results in causing the system to stop operating a few minutes (15 minutes) before the other system.

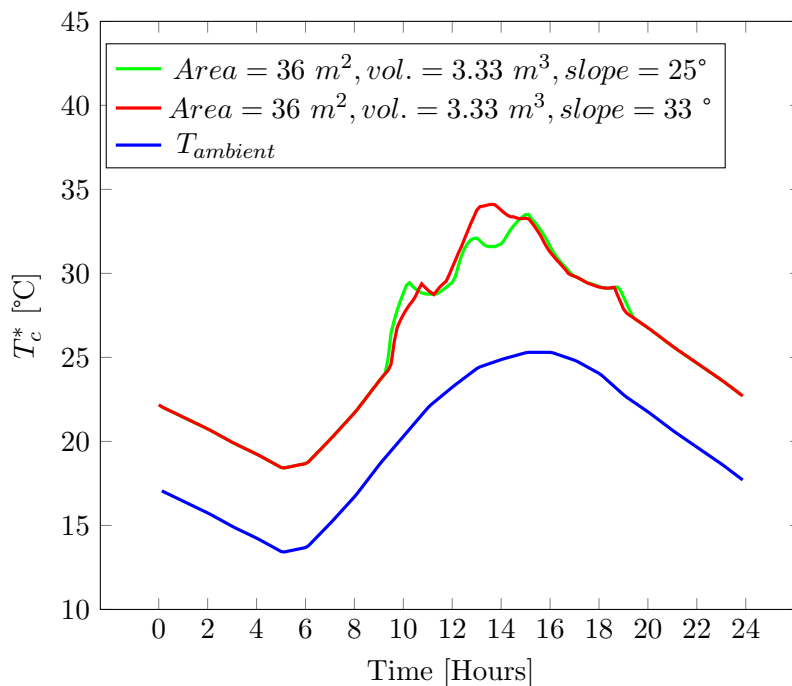


Figure 36:  $T_c^*$  at different  $A_{Coll}$  slope angles

**Figure 39** shows the collector efficiency plot ( $\eta_{coll}$ ) together with the COP of the two considered systems. From the collector efficiency plot, it can be seen that the optimized collector slope attains low morning (8:00 -10:30) values compared to the optimized case. This eventually results in low, but ideal, generator temperatures which are essential in attaining high COP readings. At around 11:00, the optimized collector system attains much higher  $\eta_{coll}$  readings which also causes the system to experience declining and lower COP values as a result of the system operating at much higher generator temperatures. Afternoon performance is characterized by a sharp decline in  $\eta_{coll}$  values as a result of diminishing solar radiation. **Figure 40** shows the overall performance of the system after taking the product of the COP and  $\eta_{coll}$ . The outcome shows significant improvement in midday performance as the unoptimized system (with a collector slope angle of 25 °) functions at significantly lower  $COP_{overall}$  (0.27) values at 11:00 whilst the optimized collector slope attains a  $COP_{overall}$  value of 0.45.



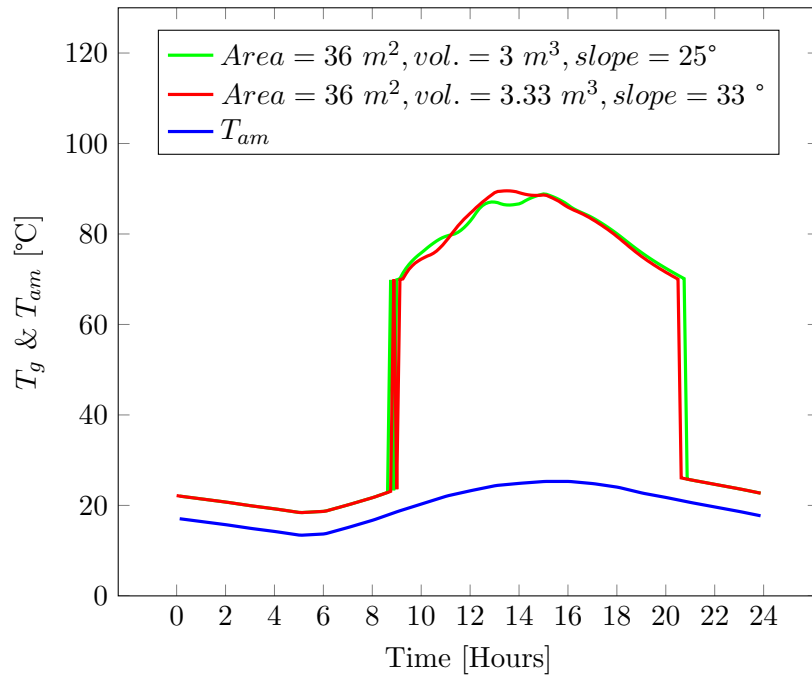


Figure 37:  $T_g$  variation at different  $A_{Coll}$  slope angles

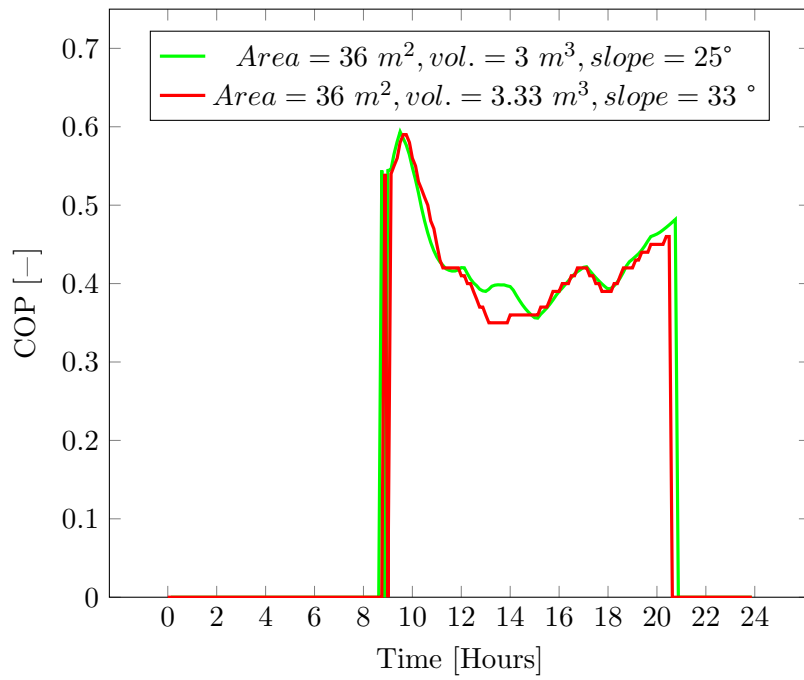


Figure 38: COP variation at different  $A_{Coll}$  angles

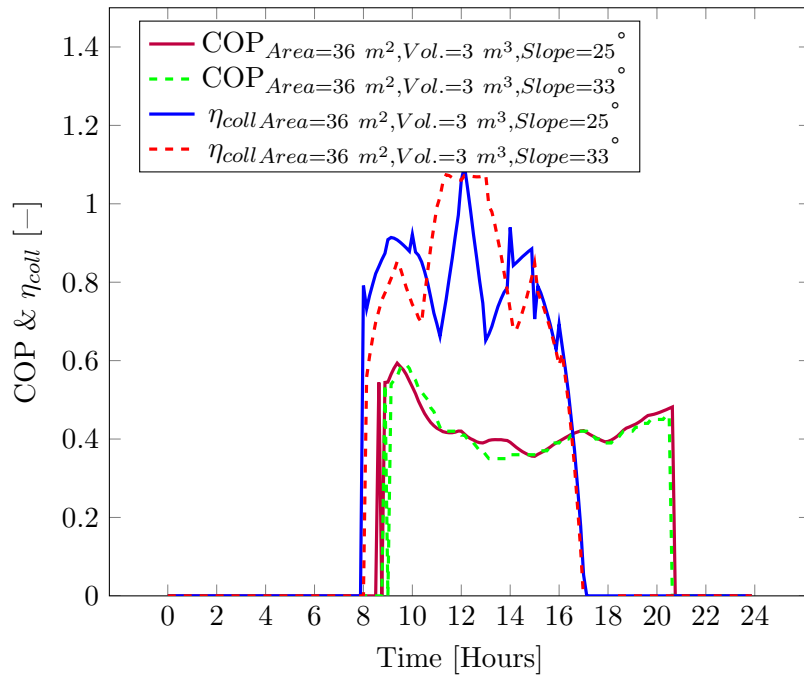


Figure 39: COP and  $\eta_{coll}$  variation at  $A_{Coll}$  slope angles

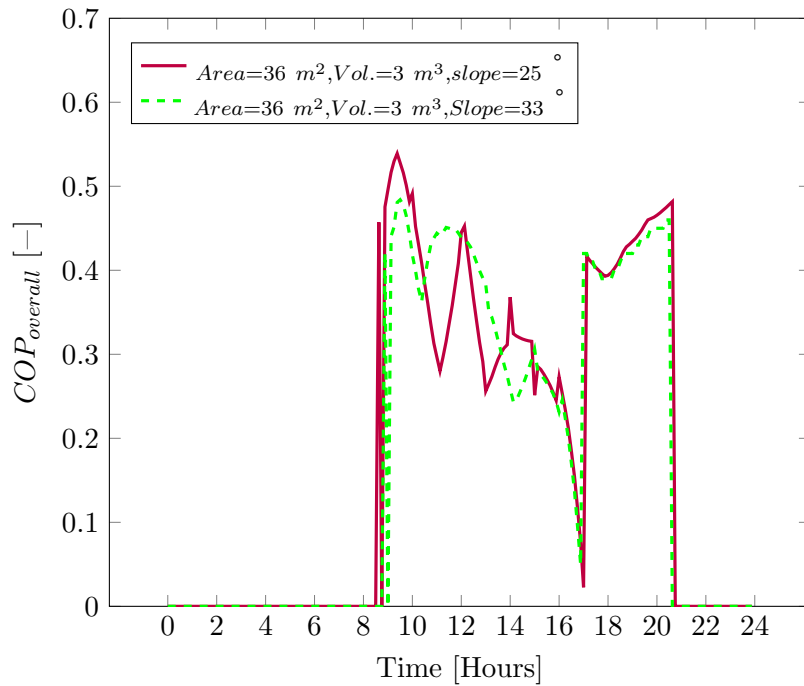


Figure 40:  $COP_{overall}$  variation at different  $A_{Coll}$  Slopes

Figure 40 shows how the optimized system (with a 33 °collector slope angle) attains higher  $COP_{overall}$  values between 10:15 and 13:50 when the 25 °collector slope system experiences sharp declines in  $COP_{overall}$  figures. Coupling this outcome with the results in Figure 39, it can be seen that the efficiency of the solar collectors is key in attaining good quality

$COP_{overall}$  readings. It can also be seen that changing the collector slope angle has a higher effect on the efficiency of the solar collectors than on the COP of the ejector refrigeration system.

## 5.4 Ejector performance results in Uppington

Analysis of the performance of the ejector within Uppington begins with finding the adequate  $T_g$  for the operation of the ejector. This is found by varying the boiling point temperature of the hot water storage tank to limit the maximum operating temperature of the generator. From [Figure 41](#), the variation of the COP at two different tank boiling points (90 and 100 °C) is observed. The plot shows that when the boiling point is at 100 °C, the ejector performs better than when the boiling point is set to 90 °C. At higher temperatures, the ejector achieves higher COP values and prolonged active operation.

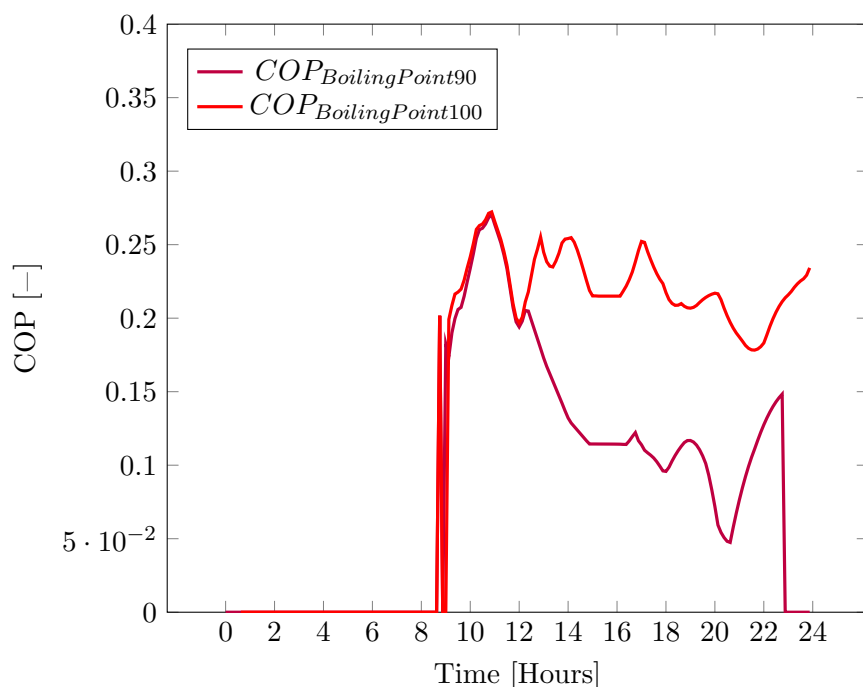


Figure 41: COP at different tank boiling point limits

The explanation of this outcome is shown in [Figure 42](#) whereby it can be seen that the ejector operating at  $T_g$  of 90 °C operates at a  $T_c$  value that is 5 °C above ambient conditions as defined in the programme. This shows that at the given operating conditions, a  $T_g$  value of 100 °C results in sub-critical mode operation of the ejector since it does not have a  $T_c^*$  value that is superior to  $T_c$ . [Figure 42](#) shows that when the tank boiling point is limited to 100 °C, the ejector operates at 5 °C above ambient conditions until the tank exit temperature exceeds 90 °C which subsequently enables the  $T_c^*$  values to be above the ambient coupled

temperature.  $T_c^*$  values above  $T_c$  mean that the ejector is operating at critical mode and this results in higher COP values, as shown in [Figure 41](#). Higher COP values are attained after 12:00 for the tank with a boiling point of 100 °C. Under this boiling point temperature, the ejector continues to operate at COP values above 0.2 even after 16:00 whereby the ejector returns to functioning below critical mode due to low  $T_g$  and high  $T_c$ . This result shows that at sub-critical mode, higher COP values can be achieved by slightly increasing  $T_g$ . This is confirmed by [Figure 43](#) whereby it can be seen that when the tank boiling point is set at 100 °C, the system is able to function at  $T_g$  values that are about 3 °C higher than the system with a tank boiling point of 90 °C. [Figure 41](#) and [Figure 43](#) also shows that the system can operate for an extended period when set to have a 100 °C boiling point tank temperature.

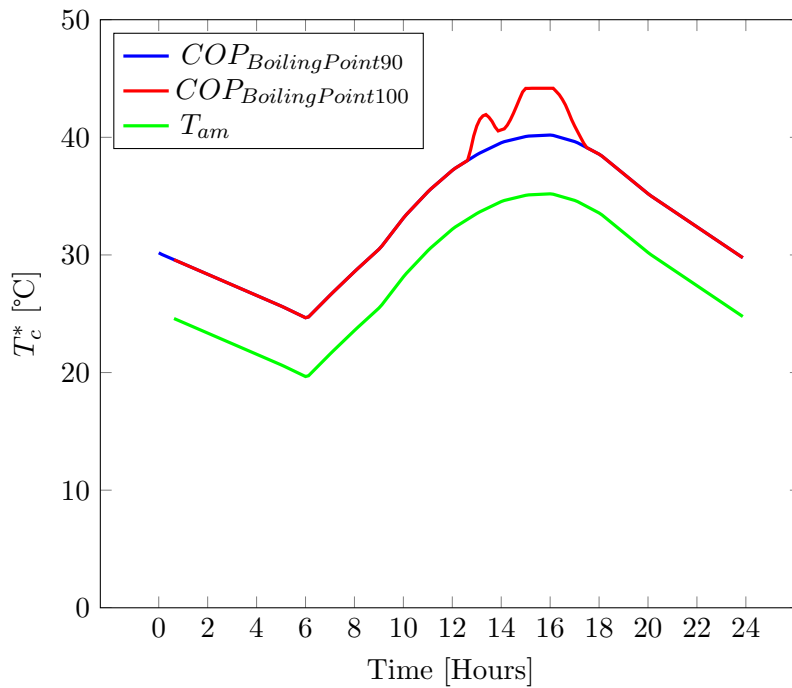


Figure 42:  $T_c^*$  variation at different tank boiling point limits

From [Figure 43](#), it is apparent that the considered collector area required an hour to generate sufficient thermal energy to activate the generator at  $T_g$  of 70 °C. When set to operate at the tank boiling point of 90 °C, the system requires another 3 hours to get to the tank boiling point temperature. This period is extended to 6 hours in the case of the system with a boiling point temperature of 100 °C. This suggests that a larger collector area may be required to quickly attain higher  $T_g$  values.

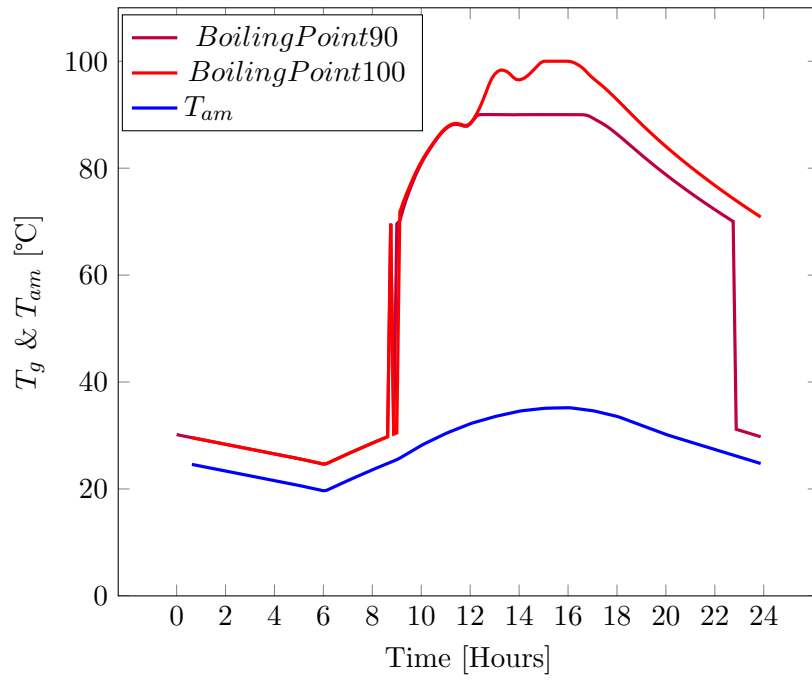


Figure 43:  $T_g$  variation at different tank boiling point limits

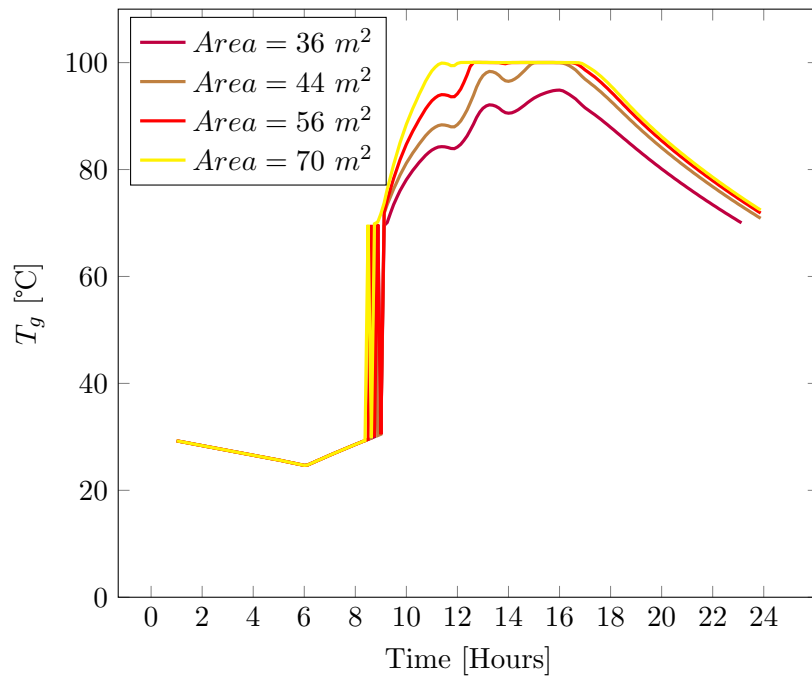


Figure 44:  $T_g$  variation at different  $A_{Coll}$  sizes

Figure 44 shows how the generator temperature varies as  $A_{Coll}$  increases from  $36 \text{ m}^2$  to  $70 \text{ m}^2$ . From the plot, it is clear that larger collector areas result in earlier start time, also reach the tank boiling temperature quicker than smaller  $A_{Coll}$ .

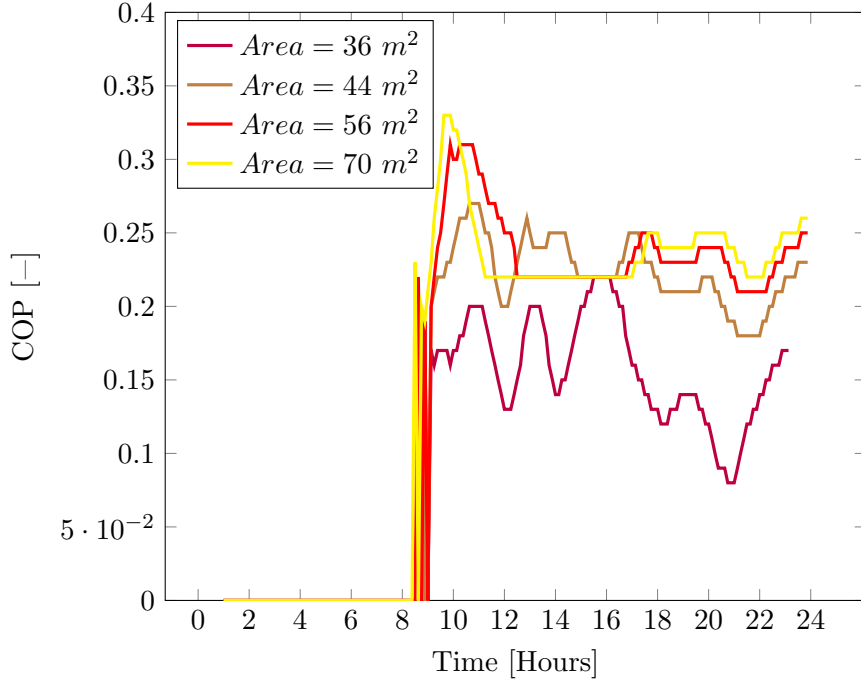


Figure 45: COP variation at different  $A_{Coll}$  sizes

Figure 45 and Figure 46 shows the performance behaviour of the ejector when operating at different collector areas. Analysis of the COP (Figure 45) shows that the  $70 \text{ m}^2$  system is able to achieve higher COP values because of higher  $T_g$  temperatures (shown in Figure 44) which result in higher  $T_c^*$  (Figure 46) values that allow the system to operate in critical mode. After 10:00, the  $56 \text{ m}^2$  system delivers higher COP values because of both higher  $T_g$  and  $T_c^*$  temperatures. The  $56 \text{ m}^2$  system performs better than the  $70 \text{ m}^2$  system because of slightly lower  $T_g$  values which are sufficient to enable the ejector to operate in critical mode as a result of higher  $T_c^*$  values. As the day progresses (after 10:00), the COP values of both  $56$  and  $70 \text{ m}^2$  systems sharply declines due to excessively higher  $T_g$  and  $T_c^*$  values. Between 12:00 and 16:00, the  $44 \text{ m}^2$  system gives superior performance over the other systems as operates at a slightly lower  $T_g$  but higher  $T_c^*$  thus enabling the ejector to operate at critical mode. After 16:00, the  $44 \text{ m}^2$  system's performance drops below that of the  $70$  and  $56 \text{ m}^2$  system. From 16:00 to 18:00, the  $56$  and  $70 \text{ m}^2$  systems perform well due to higher  $T_g$  and  $T_c^*$  which result in critical mode performance of the ejector. After 18:00, all systems operate at the ambient coupled  $T_c$  which indicates sub-critical performance. However, the  $70 \text{ m}^2$  system still maintains higher COP values due to higher  $T_g$  values. Considering that the  $44$  and  $56 \text{ m}^2$  systems perform closely to the  $70 \text{ m}^2$  system, they are chosen for further analysis whereby the effect of the storage tank is closely monitored.

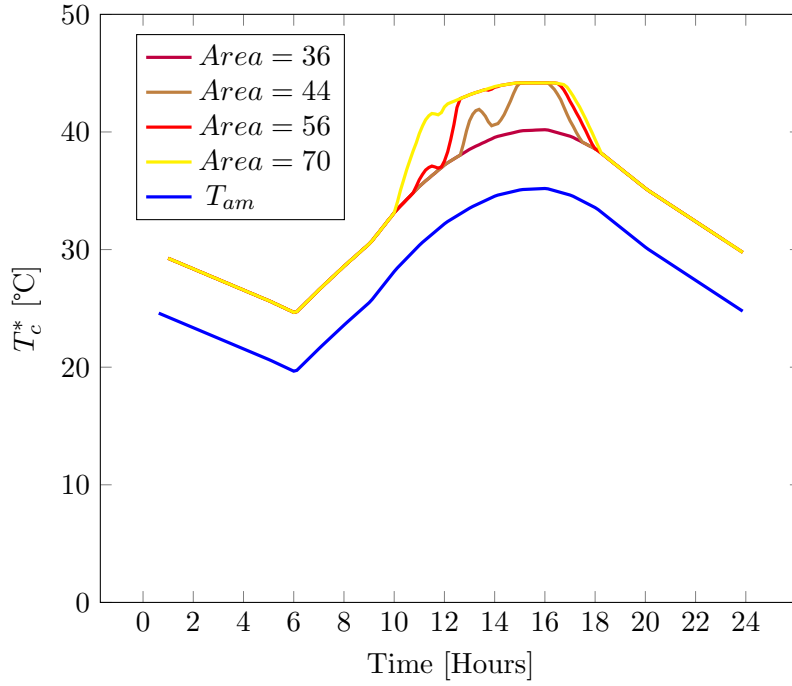


Figure 46:  $T_c^*$  behaviour at different  $A_{Coll}$  sizes

Figure 47, shows 24-hour analysis of  $T_g$  at different collector areas ( $A_{Coll}$ ) and storage tank volume ( $Vol_{Tank}$ ). The considered areas are  $44 \text{ m}^2$  and  $56 \text{ m}^2$  with the storage tank volumes being  $3 \text{ m}^3$  and  $6 \text{ m}^3$ . Analysis begins at 00:00 whereby it is noted that all of the considered configurations are operating as a result of thermal energy storage from the previous day. The  $56 \text{ m}^2$  and  $44 \text{ m}^2$  collector area systems with a  $3 \text{ m}^3$  tank stop operating just before 01:00 as their  $T_g$  value falls below  $70 \text{ }^\circ\text{C}$ . The systems with a  $6 \text{ m}^3$  storage tank continue operating until 04:00 (for the  $44 \text{ m}^2 A_{Coll}$ ) and 06:00 (for the  $56 \text{ m}^2 A_{Coll}$ ) due to their  $T_g$  values being less than  $70 \text{ }^\circ\text{C}$ . Upon start-up, the small storage volume systems ( $3 \text{ m}^3$ ) experience a quicker temperature increase which is attributed to the low thermal inertia of the reservoir. This results in the tanks of the two systems reaching the boiling point temperature of  $100 \text{ }^\circ\text{C}$  before the other two systems. Increments of  $T_g$  on the  $44 \text{ m}^2$  and  $6 \text{ m}^3$  are most slow because of the large thermal inertia of tank and the small collector area which does not provide sufficiently large thermal energy to heat the water. Due to these factors, this system never attains the tank limiting temperature of  $100 \text{ }^\circ\text{C}$ . The system with a  $56 \text{ m}^2 A_{Coll}$  and  $6 \text{ m}^3 Vol_{Tank}$  is able to attain the  $100 \text{ }^\circ\text{C}$  tank boiling point due to the large solar thermal collectors which provide sufficient solar thermal energy. The benefits of a larger storage tank are appreciated after 17:00 when the solar system stops adding energy into the tanks. The smaller tanks  $3 \text{ m}^3$  rapidly lose thermal energy resulting in a drop of  $T_g$  whilst the larger tanks experience a slower decrease in  $T_g$ .

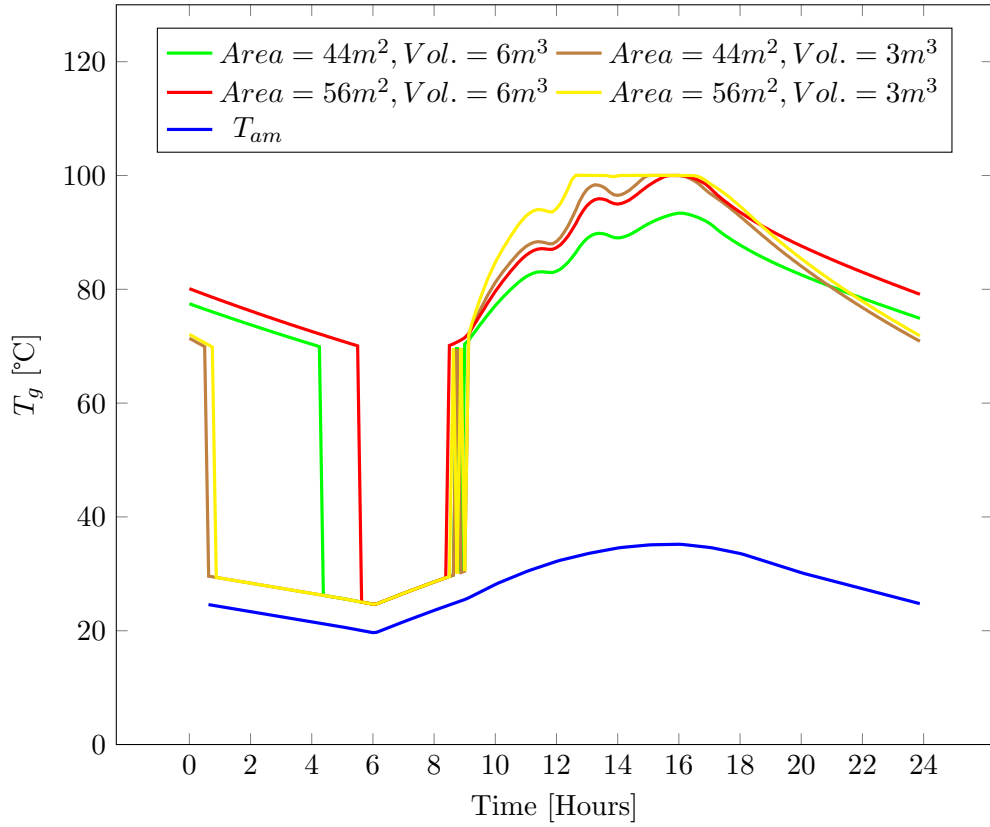


Figure 47:  $T_g$  at different tank sizes,  $A_{Coll}$  and  $Vol_{Tank}$

The effect of the  $A_{Coll}$  and  $Vol_{Tank}$  on the COP of the ERS is presented in [Figure 48](#). Performance analysis begins at 00:00 whereby all systems are operating with thermal energy from the previous day. Systems with the larger tank ( $6 m^3$ ) operate until 04:00 ( $44 m^2$ ) and 05:30 ( $56 m^2$ ) due to good thermal energy storage. Performance characteristics during this period show that the COP increases as the  $T_g$  decreases. Comparing day performance against night performance, for the  $6 m^3$  system, night time (18:00 to 05:30) COP values exceed those experienced during day time (08:00 to 18:00) COP values. The high COP values are due to low  $T_g$  (as a result of no solar irradiation) and  $T_c$  temperatures (as a result of low ambient temperatures). Analysis of daytime performance shows how the small volume tank systems ( $3m^3$ ) can have high start-up COP values due to slightly high  $T_g$  values 09:00 and 12:00. After 12:00, the  $56 m^2$  system with  $3 m^3$  tank reaches the tank boiling temperature of  $100^\circ\text{C}$ , which causes it to operate in critical mode as highlighted by the deviation of  $T_c^*$  from the specified  $T_c$  value. Two other systems ( $A_{Coll} = 44 m^2$ ,  $Vol_{Tank} = 3 m^3$  and  $A_{Coll} = 56 m^2$ ,  $Vol_{Tank} = 6 m^3$ ) also deviate from the ambient coupled  $T_c$  as shown in [Figure 49](#). The effect of this on the COP is evident as these two systems can provide slightly superior COP values between 12:00 and 15:00. After reaching the tank boiling temperature, all three systems have the same COP value. After 18:00, the large tank system with a large collector area functions at the highest  $T_g$  and subsequent COP since the ERS is performing under



sub-critical mode. The drop in COP of the small tank systems (at 19:00) is caused by low  $T_g$  and high  $T_c$  values whilst the large tank system with a small collector area increases its COP values due to slightly higher  $T_g$  values.

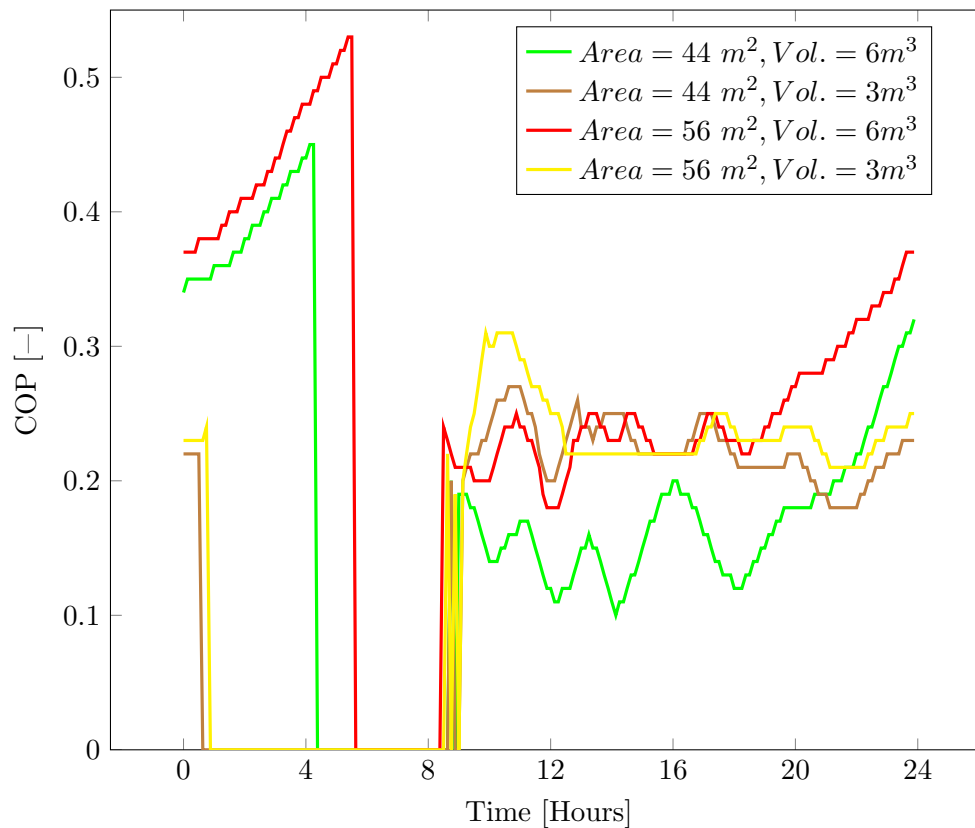


Figure 48: COP at plot different  $Vol_{Tank}$  and  $A_{Coll}$

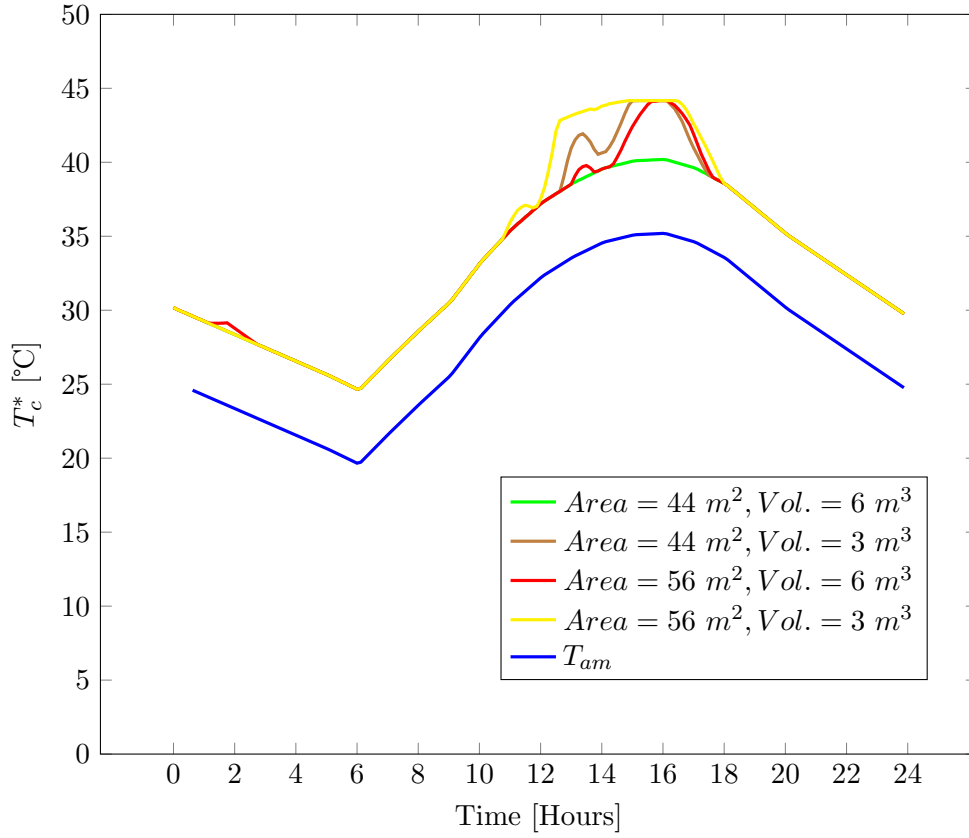


Figure 49:  $T_c^*$  at different tank sizes,  $A_{Coll}$  and  $Vol_{Tank}$

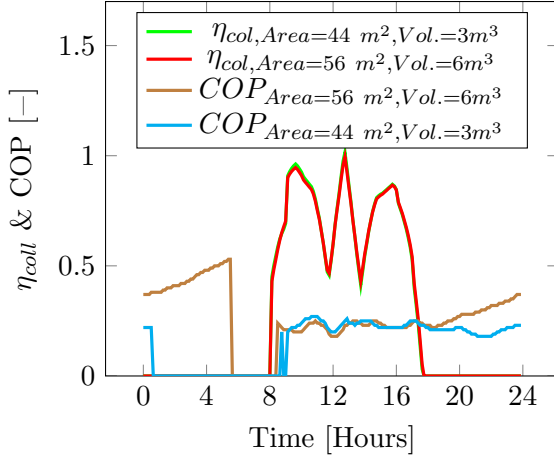


Figure 50:  $\eta_{coll}$  & COP variation at different  $A_{Coll}$  &  $Vol_{Tank}$

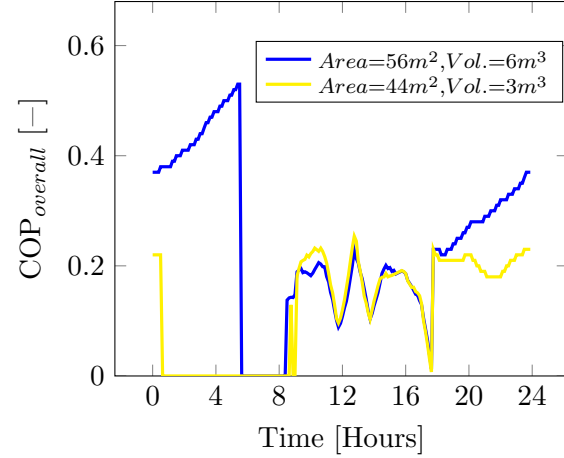


Figure 51:  $COP_{overall}$  variation at different  $A_{Coll}$  &  $Vol_{Tank}$

The performance of the solar collectors  $\eta_{coll}$  and the ERS (COP) over 24 hours is presented in [Figure 50](#). The  $\eta_{coll}$  plots show insignificant deviations in the two considered collector and tank considerations. However, these values indicate the need to optimize the performance of the collectors as both cases show severe performance losses at 12:00 and again at 14:00.

Analysis of COP variation shows that the  $56 \text{ m}^2 A_{Coll}$  system with a  $6 \text{ m}^3 Vol_{Tank}$  operates for a longer duration when compared to the  $44 \text{ m}^2 A_{Coll}$  system with a  $3 \text{ m}^3 Vol_{Tank}$ . This is due to the large collector area and storage tank which enables the system to harvest and store thermal energy which would allow for extended operation of the system. Hourly analysis of COP values shows that the  $56 \text{ m}^2 A_{Coll}$  system starts operating 20 minutes earlier than the  $44 \text{ m}^2 A_{Coll}$  system due to the availability of excess thermal energy from the larger collector surface area. However, the  $44 \text{ m}^2 A_{Coll}$  system achieves higher COP values upon activation (From 9:00 to 13:00). This comes as a result of the higher operating  $T_g$  (shown in [Figure 52](#)) values of the system which are due to the small  $Vol_{Tank}$  of the system. After 13:00, the  $56 \text{ m}^2 A_{Coll}$  system operates in critical mode which enables it to achieve higher COP values whilst having lower  $T_g$  and  $T_c^*$  values. Beyond 17:00, the  $56 \text{ m}^2 A_{Coll}$  continues to give superior COP values thanks to higher  $T_g$  temperatures with the system operating in sub-critical mode.

[Figure 51](#) shows the overall COP of the solar-powered system which has been evaluated from [Equation 6](#). From [Figure 51](#), it can be seen that the  $44 \text{ m}^2 A_{Coll}$  system operates at slightly superior  $COP_{overall}$  values due to high COP figures during solar harvesting hours. An instance whereby the  $56 \text{ m}^2 A_{Coll}$  system operates better is at 15:00 which is due to critical performance at low  $T_g$  values. Beyond 18:00, the  $56 \text{ m}^2 A_{Coll}$  system continues to achieve higher COP values (0.3 - 0.5) as a result of high  $T_g$  temperatures in subcritical operation mode. Such values signify the importance of having a large storage tank to enable sufficient thermal energy storage which allows for system operation at high  $T_g$  values. Another highlight is the effect of the inefficiency of the solar collectors on the overall performance of the system as the two troughs in  $\eta_{coll}$  are evident in the  $COP_{overall}$  plot.

From the analysis carried out in Upington, it can be concluded that a solar-powered ERS with a storage tank volume of  $3 \text{ m}^3$  and collector area of  $44 \text{ m}^2$  is adequate for achieving relatively good day performance of the system (average COP of 0.21). However, the system with a  $56 \text{ m}^2$  area and a storage tank volume of  $6 \text{ m}^3$  is more ideal since it can achieve higher COP values (increasing from 2.25 to 3.85) in the evening (after 18:00 towards 24:00).

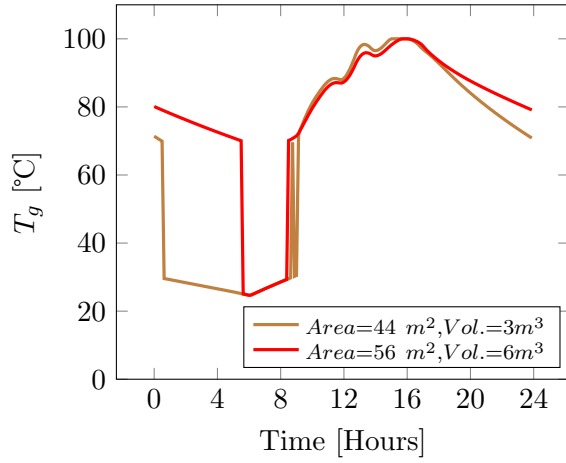


Figure 52:  $T_g$  variation at different  $Vol_{Tank}$ ,  $A_{Coll}$

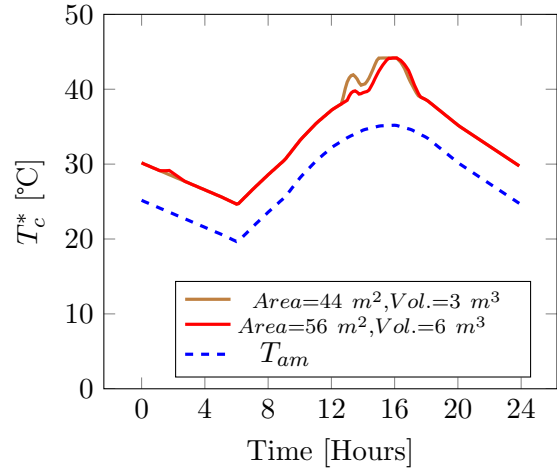


Figure 53:  $T_c^*$  variation at different  $Vol_{Tank}$ ,  $A_{Coll}$

Performance analysis is repeated with the collector slope set to  $32.5^\circ$  after performing a collector optimization study which is presented in [chapter 6.2](#). A comparison of system performance at the two collector slope angles of  $25^\circ$  and  $32.5^\circ$  is presented for  $T_c^*$  ([Figure 54](#)),  $T_g$  ([Figure 55](#)), and COP ([Figure 56](#)). The  $T_c^*$  plot shows that the optimised case operates at higher values when the system is in critical mode. From 9:00 to 12:00, the unoptimised case operates at high  $T_g$  values indicating superior collector heat gain. The optimised collector delivers higher  $T_g$  values between 12:00 and 15:00 with similar values being recorded between 15:00 and 16:00. Beyond 16:00, it can be noted that the unoptimised case operates at slightly higher  $T_g$  values.

COP analysis shows that the unoptimized system operates at higher figures during start-up (9:00 to 11:00). This comes as a result of high  $T_g$  values whilst the ERS is operating in subcritical mode as proven by  $T_c^*$  values equal to  $T_c$ . From 11:00 to 13:00, the optimised system achieves higher COP readings due to high  $T_g$  values which are below the critical  $T_g$  limit which would have resulted in a decline in COP. Between 13:00 and 15:00, the unoptimised case operates superior COP as the system runs at low  $T_g$  values whilst in the critical mode regime. Beyond 17:00, there are insignificant deviations in the performance of the two considered systems.

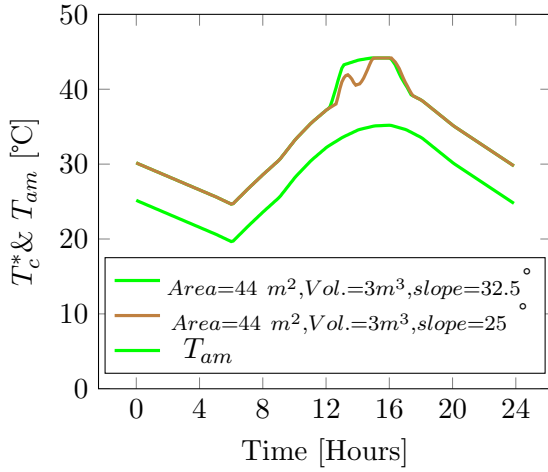


Figure 54:  $T_c^*$  variation at different collector slope angles

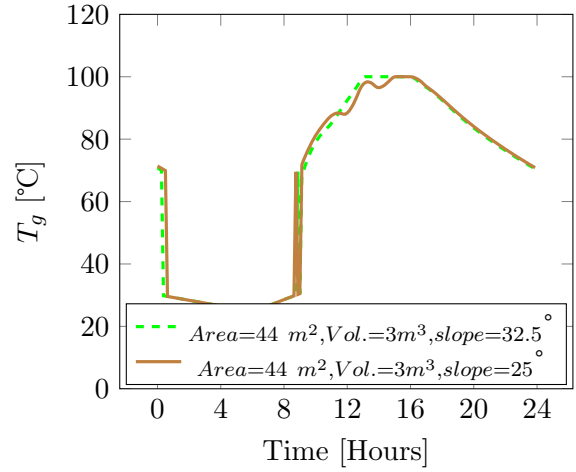


Figure 55:  $T_g$  variation at different collector slope angles

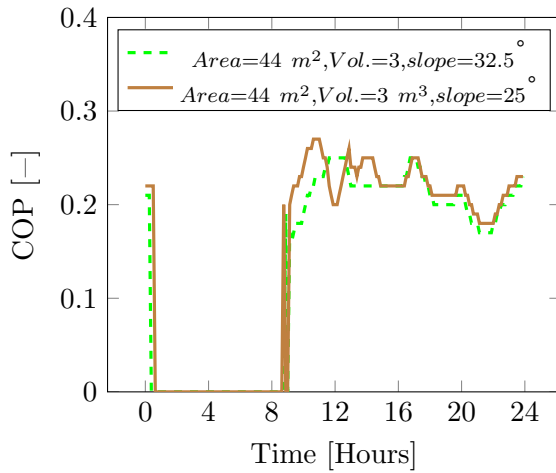


Figure 56: COP variation at different Collector Slope Angles

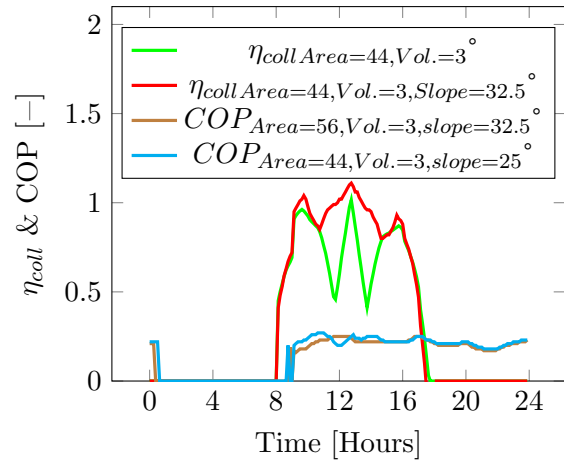


Figure 57:  $\eta_{coll}$  & COP variation at different collector slope angles

An investigation on  $\eta_{coll}$  values (carried out in Appendix A1.1 - [Figure 111](#)) shows that the optimised collector outperforms the 25 °slope configuration by limiting the magnitude of troughs. The effect on the overall performance of the system ( $COP_{overall}$ ) is presented in [Figure 58](#) whereby it can be noticed that the previously dominant troughs in  $COP_{overall}$  at 25 ° are non-existent when the system is operating at 32.5 °.

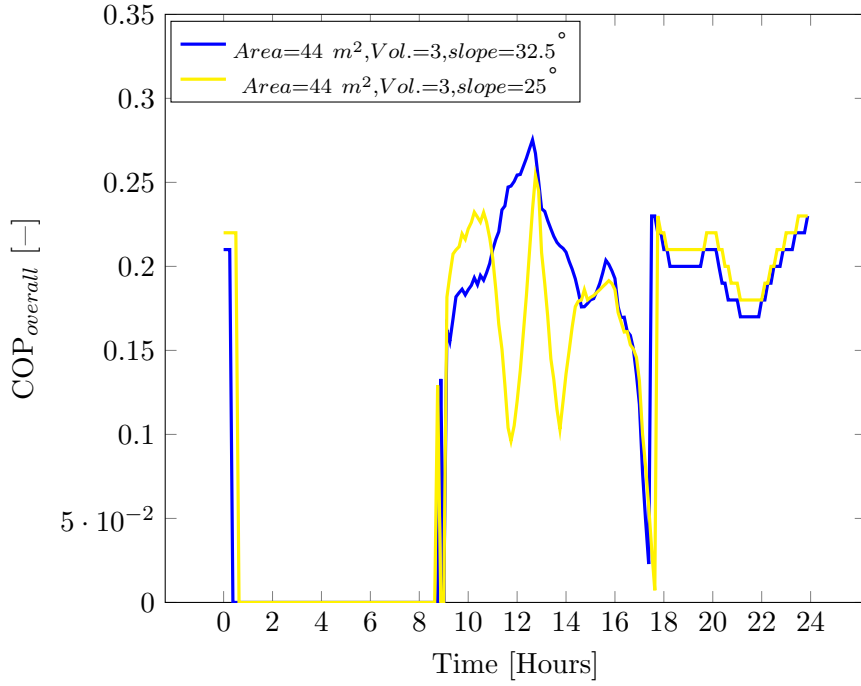


Figure 58:  $COP_{overall}$  variation at different collector slope angles

## 5.5 Ejector performance results in Durban

Performance analysis of the ERS under Durban solar and ambient conditions is presented. Analysis begins with performance evaluation under variable  $A_{Coll}$  and  $Vol_{Tank}$  with the tank boiling point temperature initially set to  $90\text{ }^{\circ}\text{C}$  to observe performance at low  $T_g$  values. From [Figure 59](#), it is clear that system performance does not show any recovery in COP values beyond the availability of solar radiation as witnessed in previous locations. Instead, performance is characterized by the continuous decline in COP values with peak values recorded around 10:00.

Analysis of the results shows that the  $56\text{ m}^2 A_{Coll}$  with  $6\text{ m}^3 Vol_{Tank}$  system achieves highest COP values during early hours (8:00 to 12:00) followed by the  $44\text{ m}^2 A_{Coll}$  with a  $3\text{ m}^3 Vol_{Tank}$  system. The  $44\text{ m}^2 A_{Coll}$  with  $6\text{ m}^3 Vol_{Tank}$  system gives the lowest COP values during the operation. Between 12:00 and 16:00, the  $44\text{ m}^2 A_{Coll}$  with a  $3\text{ m}^3 Vol_{Tank}$  system and the  $56\text{ m}^2 A_{Coll}$  with a  $6\text{ m}^3 Vol_{Tank}$  system give similar COP values with the latter system giving slightly superior values as the day progresses.

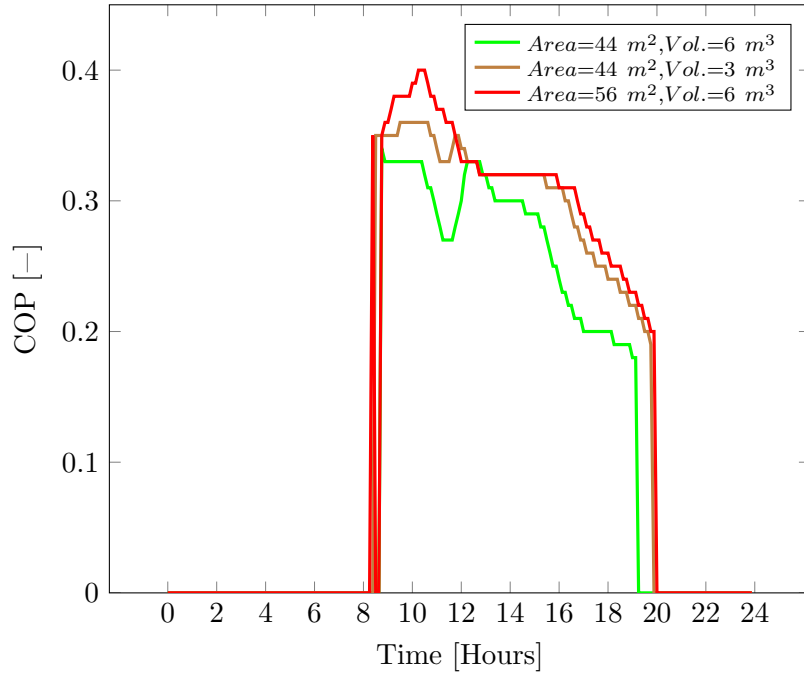


Figure 59: COP variation at different  $A_{Coll}$  and  $Vol_{Tank}$

The reason behind the variation in COP values is found in the  $T_c^*$  plots (Figure 60) and  $T_g$  (Figure 61) which shows how the operating parameters vary through the day. During start-up (08:00 - 12:00), the  $56 \text{ m}^2 A_{Coll}$  with a  $6 \text{ m}^3 Vol_{Tank}$  system achieves the highest  $T_g$  values followed by the  $44 \text{ m}^2 A_{Coll}$  with a  $3 \text{ m}^3 Vol_{Tank}$  system and the  $44 \text{ m}^2 A_{Coll}$  with a  $6 \text{ m}^3 Vol_{Tank}$  system. Figure 60 shows that all three considered systems operate in sub-critical mode during this period as the  $T_c^*$  values are equal to ambient coupled  $T_c$ . Critical operating mode is reached between 12:00 and 15:00 whereby all considered configurations attain  $T_c^*$  temperatures that are above  $T_c$ . During this period,  $T_c^*$  values are limited to a peak value of  $35 \text{ }^\circ\text{C}$  due to the preset tank boiling temperature of  $90 \text{ }^\circ\text{C}$  which prevents any further increase in  $T_g$  as shown in Figure 61.

The effect in COP performance is also evident in Figure 59 whereby the  $56 \text{ m}^2 A_{Coll}$  with a  $6 \text{ m}^3 Vol_{Tank}$  system and  $44 \text{ m}^2 A_{Coll}$  with a  $3 \text{ m}^3 Vol_{Tank}$  system operates at the same COP. The  $44 \text{ m}^2 A_{Coll}$  with a  $6 \text{ m}^3 Vol_{Tank}$  system differs from the other two as it does not attain the tank boiling temperature of  $90 \text{ }^\circ\text{C}$  due to the large thermal inertia of the tank which cannot be heated to such a high temperature by the considered collector area. This explains the low  $T_c^*$  values which show that the ejector is operating in subcritical mode hence it also has low COP values.

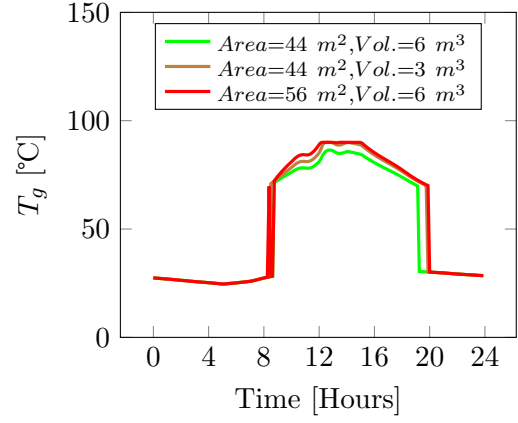
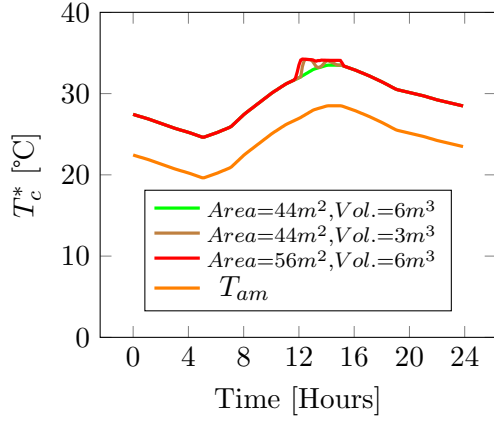


Figure 60:  $T_c^*$  variation at different  $A_{Coll}$  and  $Vol_{Tank}$  and Figure 61:  $T_g$  variation at different  $A_{Coll}$ ,  $Vol_{Tank}$

An investigation of the effect of the boiling point temperature of the tank is undertaken by increasing this value to 100 °C . The variation of the system's COP at various  $A_{Coll}$  and  $Vol_{Tank}$  is presented in Figure 62. Comparing the current results to those in Figure 59, it is evident that increasing the tank boiling point increases the operation period if the system. This can be noted in the 56 m<sup>2</sup>  $A_{Coll}$  with a 6 m<sup>3</sup>  $Vol_{Tank}$  system which increases its operating time by 3 hours from the initial stop time of 20:00. The second-longest active operation time is achieved by the 56 m<sup>2</sup>  $A_{Coll}$  with a 4 m<sup>3</sup>  $Vol_{Tank}$  system which stops at 21:30. The 44 m<sup>2</sup>  $A_{Coll}$  with a 6 m<sup>3</sup>  $Vol_{Tank}$  system operates until 21:00 whilst the 44 m<sup>2</sup>  $A_{Coll}$  with a 4 m<sup>3</sup>  $Vol_{Tank}$  system stops at 20:20. From these results, it can be concluded that a larger collector area and storage volume system experiences longer active cooling hours.

Observation of COP values shows that the 56 m<sup>2</sup>  $A_{Coll}$  with a 4 m<sup>3</sup>  $Vol_{Tank}$  system achieves the highest start-up (8:00 to 12:00) values followed by 56 m<sup>2</sup>  $A_{Coll}$  with a 6 m<sup>3</sup>  $Vol_{Tank}$  system. The 44 m<sup>2</sup>  $A_{Coll}$  with a 6 m<sup>3</sup>  $Vol_{Tank}$  system achieves the lowest start-up COP values. Analysis of  $T_g$  values (Figure 64) also shows the same trend whilst the  $T_c^*$  values are all equal to  $T_c$ , indicating subcritical performance of the ERS. Afternoon operation (12:00 to 16:00) is characterised by equal and constant COP values in the 56 m<sup>2</sup>  $A_{Coll}$  with a 6 m<sup>3</sup>  $Vol_{Tank}$  system and 44 m<sup>2</sup>  $A_{Coll}$  with a 4 m<sup>3</sup>  $Vol_{Tank}$  systems. During this period, the two systems operate at the highest  $T_g$  whilst achieving low but above  $T_c$  values indicating critical mode of performance. The 56 m<sup>2</sup>  $A_{Coll}$  with a 4 m<sup>3</sup>  $Vol_{Tank}$  system achieves the lowest COP values during this period because it operates at very high  $T_g$  values which also results in high  $T_c^*$  values.



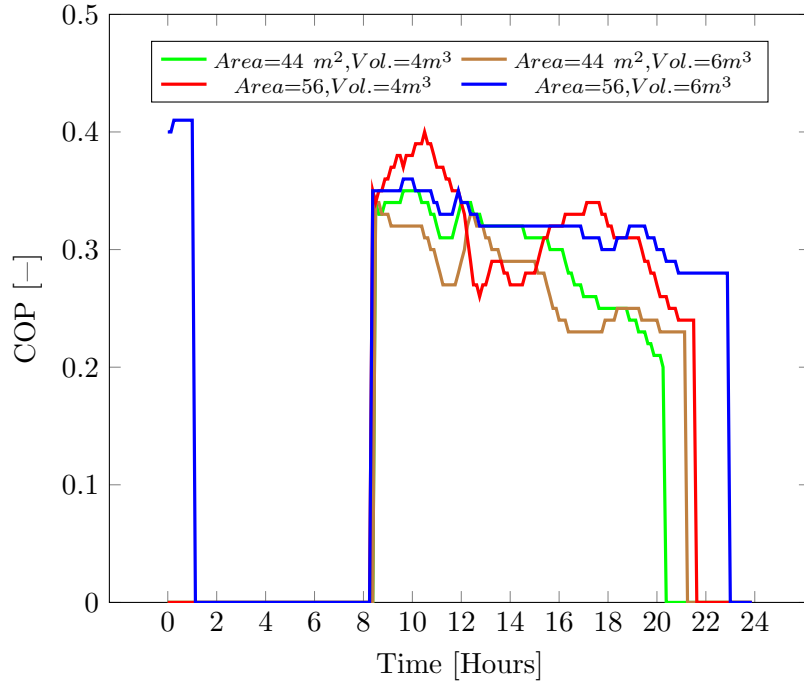


Figure 62: COP variation at different  $A_{Coll}$  and  $Vol_{Tank}$

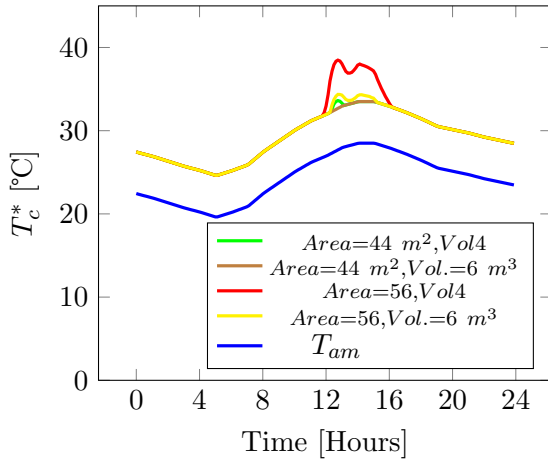


Figure 63:  $T_c^*$  variation at different  $A_{Coll}$  and  $Vol_{Tank}$

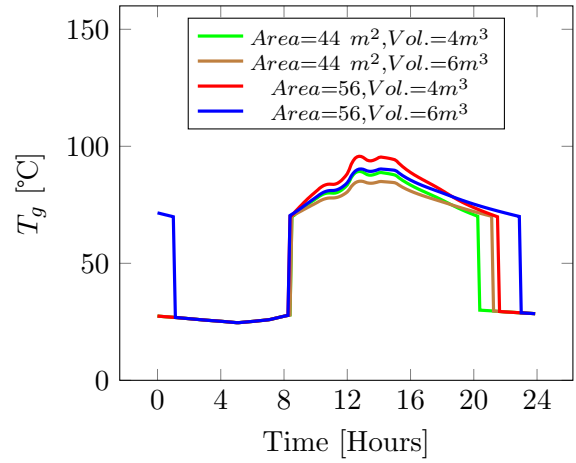


Figure 64:  $T_g$  variation at different  $A_{Coll}$  and  $Vol_{Tank}$

Analysis of the system is carried out at two  $A_{Coll}$  (44 and 56  $m^2$ ) and two  $Vol_{Tank}$  (4 and 6  $m^3$ ). **Figure 62** shows that the system that gives COP values throughout the 24 hour period is the  $A_{Coll}$  system with 56  $m^2$  surface area and both 4 and 6  $m^3$  storage tank volume.

### 5.5.1 Solar Fraction Analysis

Solar coupled performance of the ERS is presented in [Figure 65](#) and [Figure 66](#). The  $\eta_{coll}$  plot (in [Figure 65](#)) shows inefficient performance the collector as it experiences sudden troughs in performance values at 11:00 and 13:00. The COP plot (also in [Figure 65](#)) shows the significant role of the system's storage volume capacity as the 6  $m^3$  system operates for an extended duration even though it has the same  $A_{Coll}$  as the 4  $m^3$  system. COP analysis shows that the 4  $m^3$  system achieves higher startup (8:00 - 12:00) values due to high  $T_g$  values (shown in [Figure 64](#)) whilst the ERS is in sub-critical mode. Thereafter, (12:00 - 16:00) the 6  $m^3$  system operates at slightly higher COP values due to low  $T_g$  values in critical mode operation of the ERS. The low  $T_g$  values come as a result of the large thermal inertia of the storage tank which slows down the increase in temperature of the stored water. From 16:00 to 19:00, the 4  $m^3$  system operates at slightly higher COP as a result of higher  $T_g$  values whilst operating in sub critical mode (as visible in the  $T_c^*$  plot whereby the system is operating at  $T_c$  as shown in [Figure 95](#)).

The  $\eta_{coll}$  plot (in [Figure 65](#)) shows that the 6  $m^3$  system operates at slightly higher values as it has less severe drops inefficiencies and higher evening values.  $COP_{overall}$  shows that the 4  $m^3$  operates at high start-up (8:00 - 12:00) values as a result of high COP values. Between 12:00 and 16:00, the 6  $m^3$  operates at higher  $COP_{overall}$  as a result of higher  $\eta_{coll}$  and COP. From 16:00 to 19:00, the 4  $m^3$  system operates at higher  $COP_{overall}$  due to high COP values. Beyond the availability of solar radiation,  $COP_{overall}$  is equal to COP.

System analysis is further carried out at the optimised collector slope of 36 °as found in [chapter 6.2](#). COP analysis is presented in [Figure 67](#) for the optimised case and the previously preferred collector-system configuration.

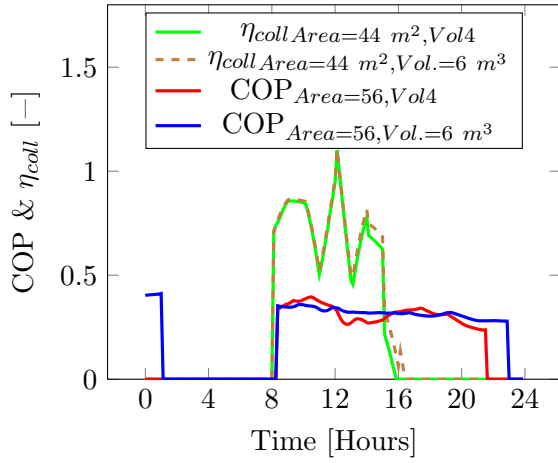


Figure 65: COP &  $\eta_{coll}$  variation at different  $A_{Coll}$  &  $Vol_{Tank}$

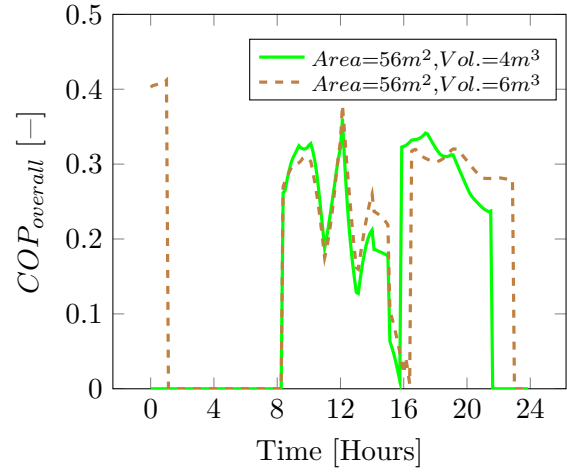


Figure 66:  $COP_{overall}$  variation at different  $Vol_{Tank}$

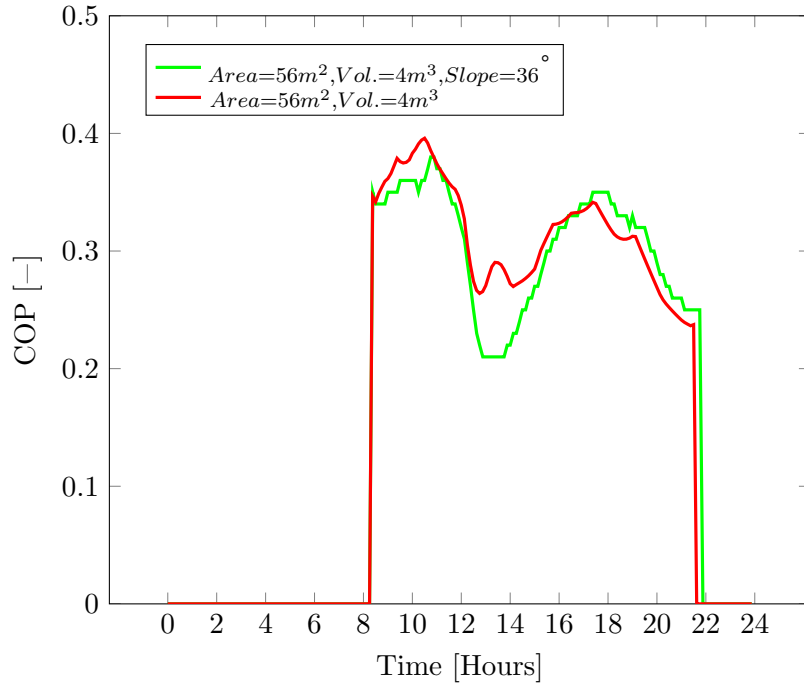


Figure 67: COP variation at different collector slope angles

Figure 67 shows the optimised  $A_{Coll}$  slope system operates at a lower COP compared to the unoptimised slope configuration. However, this is only limited to the period when there is solar radiation. Beyond this period, the optimised system operates at slightly higher COP values. The  $T_g$  plot (Figure 68) and  $T_c^*$  plot (Figure 69) shows that operation beyond the solar radiation dominated region is characterised by sub-critical performance as the system operates at  $T_c^*$  values equal to  $T_c$ . Within this region, high  $T_g$  values result in high COP values.

An investigation of  $T_g$  values shows that the unoptimised case achieves high figures between 8:00 and 12:00. Beyond 12:00, the optimised system achieves greater  $T_g$  values throughout the day.  $T_c^*$  values show that the optimised system achieves higher figures between 11:00 and 17:00 thereafter, both systems operate at the same  $T_c^*$  values. This explains the higher COP values from the unoptimised case between 11:00 and 17:00, since the system operates in critical mode whilst maintaining a lower  $T_g$  and  $T_c^*$  values. Beyond 17:00, both systems operate at sub-critical mode (as evident in [Figure 69](#)) whereby the  $T_c^*$  values are equal to  $T_c$ . This results in higher COP values from the optimal slope as it operated at higher  $T_g$  values.

From the performance plots, it can also be observed that the optimised system operates for a slightly extended duration. This is attributed to the enhanced thermal harvesting capabilities of the optimised slope system which results in the availability of excess solar thermal energy.

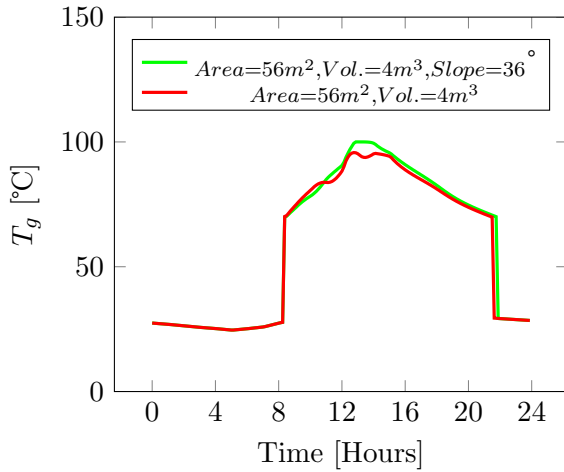


Figure 68:  $T_g$  variation at different collector slope angle

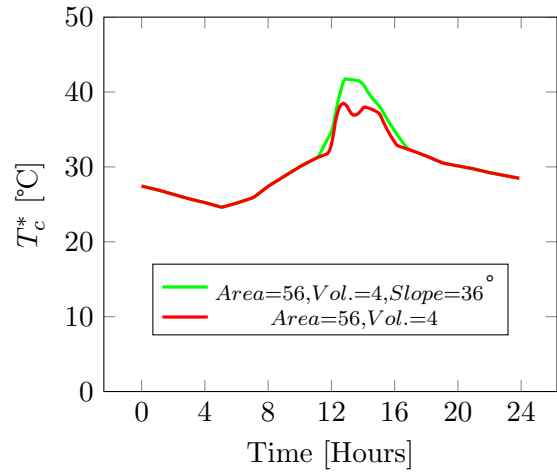


Figure 69:  $T_c^*$  variation at different collector slope angles

A comparison of  $\eta_{coll}$  values ([Figure 70](#)) shows that the optimised slope achieves slightly higher efficiency values but still experiences the sharp declines at 11:00 and 13:00. [Figure 71](#) shows the  $COP_{overall}$  of the two considered systems whereby it can be noted that the optimised system operates at slightly higher figures during the availability of solar radiation. Beyond the availability of solar radiation, the system's  $COP_{overall}$  is equal to COP since the system becomes independent of the solar collectors.

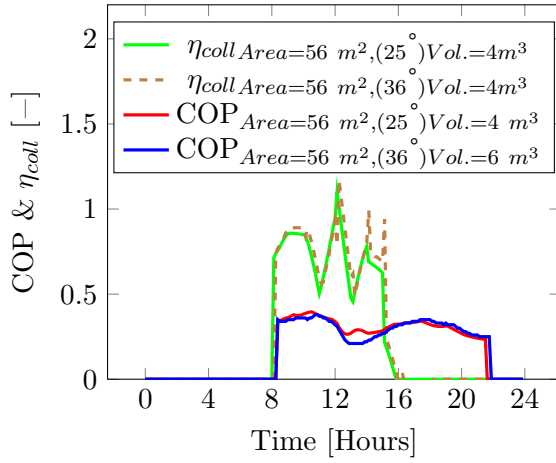


Figure 70: COP variation at different collector slope angles

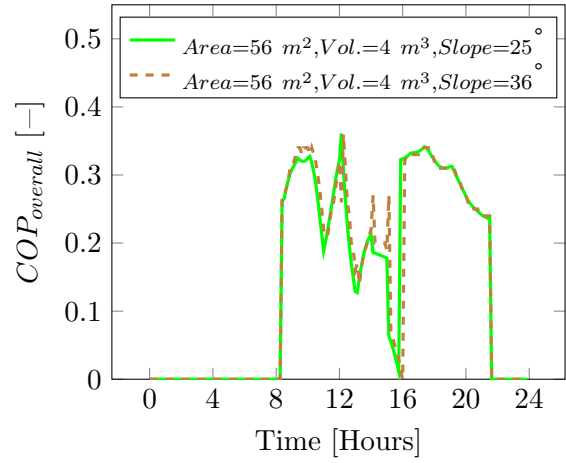


Figure 71:  $COP_{overall}$  variation at different collector slope angles

## 5.6 Ejector performance results in Cape Town

Performance analysis of the solar-powered ERS is carried out under Cape Town solar and ambient conditions. Analysis begins with the consideration of variable solar collector area, from  $36 \text{ m}^2$  to  $56 \text{ m}^2$ , at the fixed storage volume of  $3 \text{ m}^3$ . From the results presented in [Figure 95](#), the operating period of the system extends when  $A_{Coll}$  is increased from  $36 \text{ m}^2$  to  $56 \text{ m}^2$ .

However, large  $A_{Coll}$  results in high  $T_g$  and  $T_c^*$  values as presented in [Figure 73](#) and [Figure 74](#), respectively. Analysis of the time variation of  $T_g$  shows that large  $A_{Coll}$  experience high  $T_g$  values due to the high thermal energy input that the system experiences from the collectors. From the considered  $A_{Coll}$  values, the  $56 \text{ m}^2$  system achieves the highest  $T_g$  values followed by  $44 \text{ m}^2$ , then the  $36 \text{ m}^2$  with the  $28 \text{ m}^2$  system operating at the lowest values. The active cooling period of the system is also proportional to the  $A_{Coll}$  of the system since large  $A_{Coll}$  systems operate for extended hours compared to small area systems.

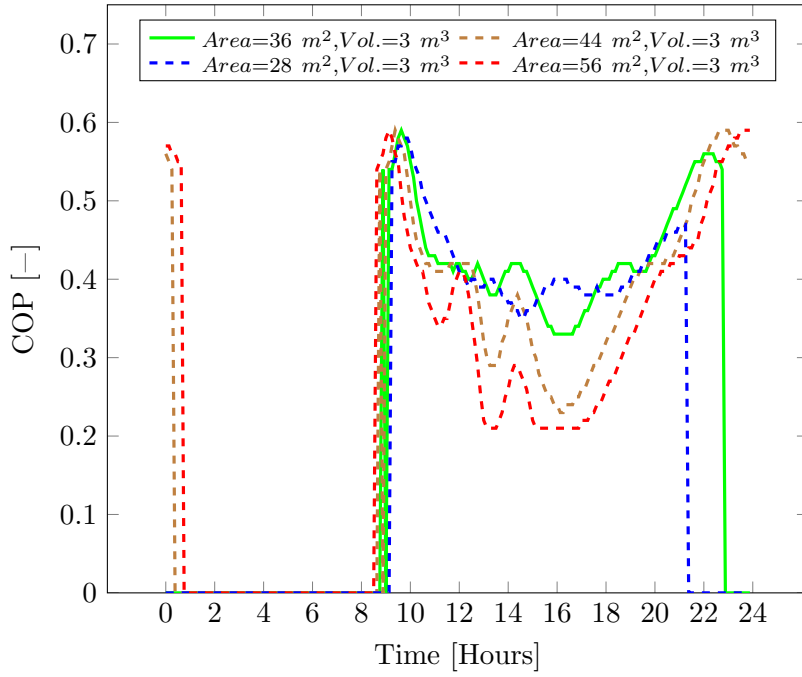


Figure 72: COP variation at different  $A_{Coll}$  and  $Vol_{Tank}$

Analysis of  $T_c^*$  values, shown in [Figure 74](#), gives an idea of the ideal specification of  $A_{Coll}$  and  $Vol_{Tank}$  values based on the degree of deviation of  $T_c^*$  from the ambient coupled  $T_c$  values. From the analysis of [Figure 74](#), it is evident that the  $36 \text{ m}^2$   $A_{Coll}$  with a  $3 \text{ m}^3$   $Vol_{Tank}$  system provides optimal performance since the  $T_c^*$  values experience a minimal deviation from  $T_c$ . This is also evident in [Figure 95](#) whereby the same system achieves the highest COP values on average.

Parametric analysis of variable  $A_{Coll}$  and  $Vol_{Tank}$  show that large  $Vol_{Tank}$  systems operate longer even when  $A_{Coll}$  is fixed. [Figure 73](#) shows that within the systems with  $36 \text{ m}^2$   $A_{Coll}$ , having a  $6 \text{ m}^3$   $Vol_{Tank}$  results in longer active cooling operation whilst having a  $3 \text{ m}^3$   $Vol_{Tank}$  causes shorter cooling duration. A comparison of the effect of  $A_{Coll}$  against the effect of  $Vol_{Tank}$  can be done by considering the  $36 \text{ m}^2$   $A_{Coll}$  system with a  $3 \text{ m}^3$   $Vol_{Tank}$  against the  $28 \text{ m}^2$   $A_{Coll}$  with a  $6 \text{ m}^3$   $Vol_{Tank}$  as presented in [Figure 73](#). From the presented data, it can be seen that the  $36 \text{ m}^2$  system is able to operate for slightly longer hours and achieves better COP values than the  $28 \text{ m}^2$  system.

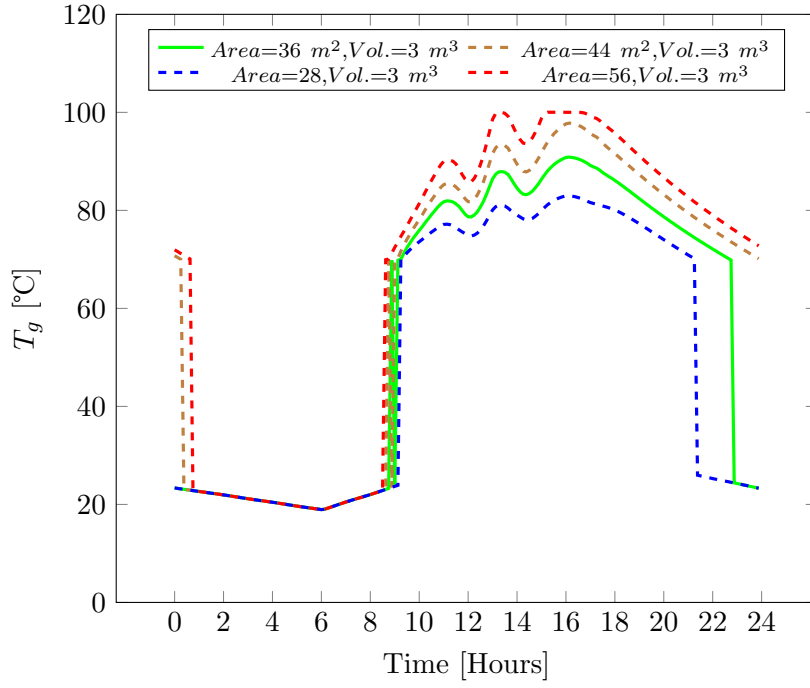


Figure 73:  $T_g$  variation at different  $A_{Coll}$  and  $Vol_{Tank}$

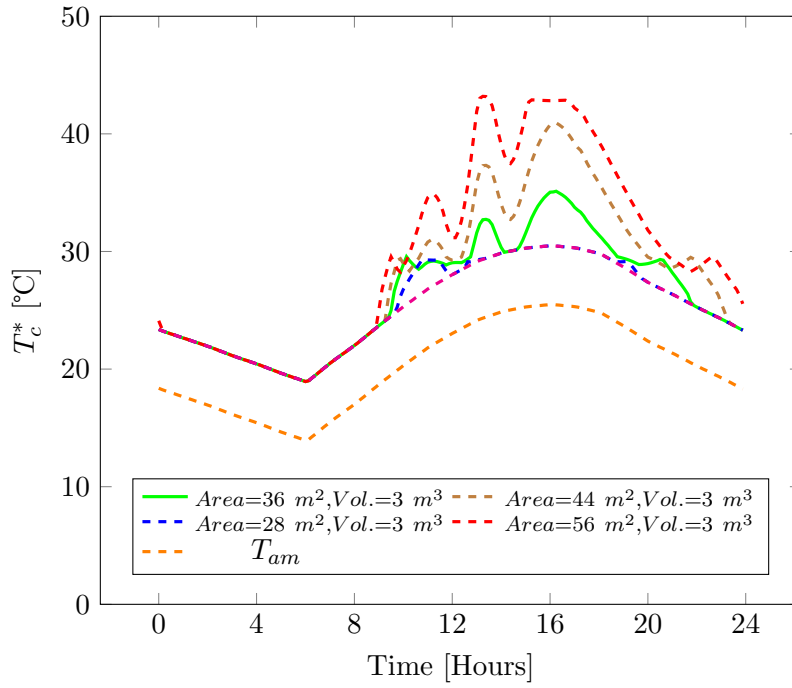


Figure 74:  $T_c^*$  variation at different  $A_{Coll}$  and  $Vol_{Tank}$

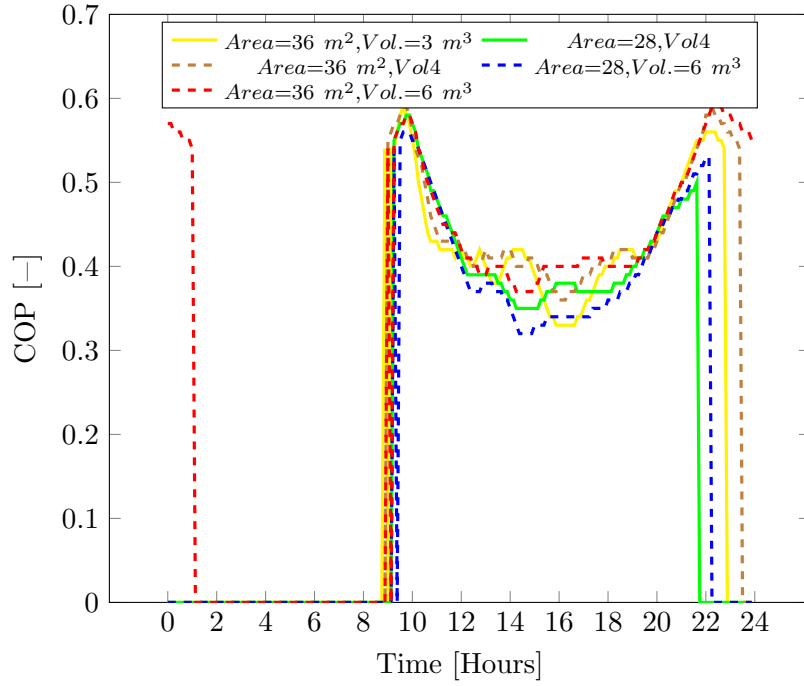


Figure 75: COP variation at different  $A_{Coll}$  and  $Vol_{Tank}$

From a comparison of  $T_g$  values, it can be observed that the  $36\text{ m}^2$   $A_{Coll}$  system with a  $4\text{ m}^3$   $Vol_{Tank}$  achieves the highest values but does not attain the tank boiling point temperature of  $100\text{ }^\circ\text{C}$ . The thermal inertia effect of large storage capacity systems is also appreciated as both systems with a  $6\text{ m}^3$  tank experience a gradual temperature drop during late-night operating hours which result in extended hours of operation over the systems with smaller  $Vol_{Tank}$ .



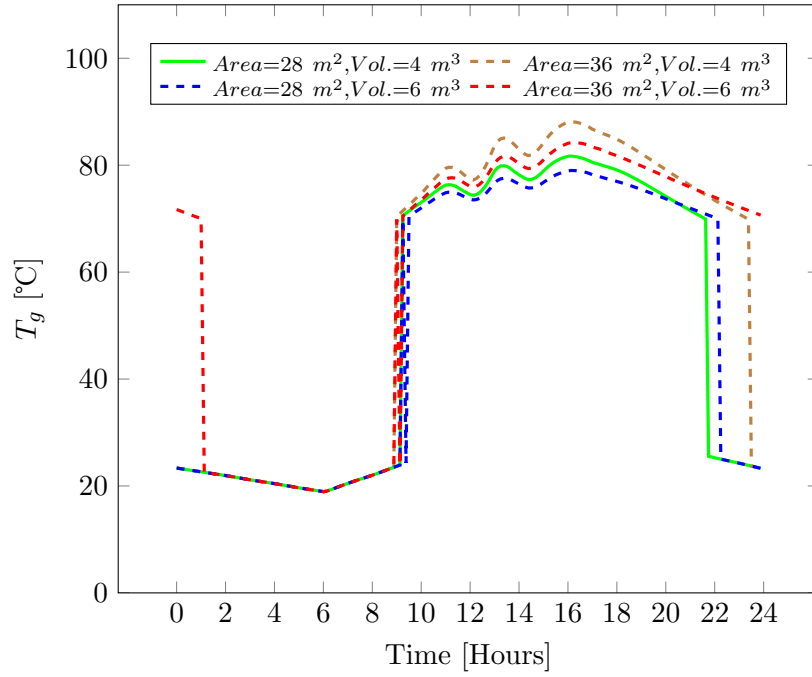


Figure 76:  $T_g$  variation at different  $A_{Coll}$  and  $Vol_{Tank}$

Figure 77 shows that all the considered configurations experience minimal deviations from the ambient coupled  $T_c$ . This suggests subcritical mode performance of the system for a significant part of the operation. The  $36\text{ m}^2$   $A_{Coll}$  system with a  $4\text{ m}^3$   $Vol_{Tank}$  is observed to have the most frequent deviations from the  $T_c$  which signifies critical mode operation which is also proven by the high COP values in Figure 75.

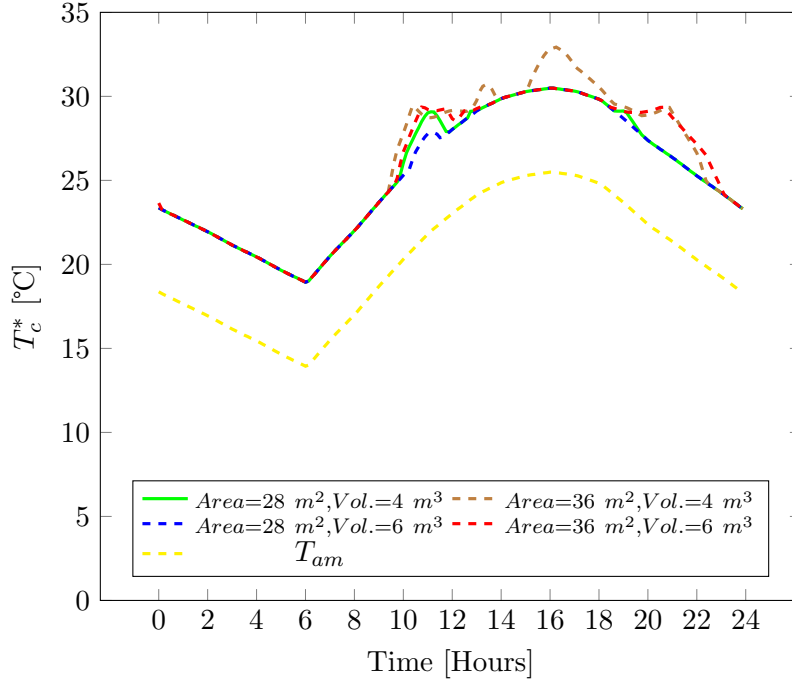


Figure 77:  $T_c^*$  variation at different  $A_{Coll}$  and  $Vol_{Tank}$

The analysis of the performance of the solar collectors based on the collector area and the volume of the storage tank is presented in [Figure 83](#). From the presented data, it is evident that the collectors experience significant inefficiencies during operation which highlights the need to optimise their performance. For comparison purposes, the COP of the ERS is also plotted in [Figure 83](#) to show that the ERS operates at lower efficiency values than the COP. An examination of the performance of the solar collectors shows that the 28 m<sup>2</sup> system achieves slightly improved performance compared to the 36 m<sup>2</sup> system at the same  $A_{Coll}$ . This suggests that the 36 m<sup>2</sup> losses heat to ambient conditions as a result of the limited capacity of the storage tank. However, the enlarged surface area plays a crucial role in extending the operating period of the system as evident in [Figure 83](#).

The overall performance of the system is evaluated from [Equation 6](#) and the results are shown in [Figure 79](#). From these results, it can be seen how  $COP_{overall}$  is significantly affected by  $\eta_{coll}$  since the  $COP_{overall}$  values are lower than COP. It is also worth noting that the lowest values in  $COP_{overall}$  are experienced when  $\eta_{coll}$  is at the lowest. This further motivates the need to optimize the performance of the collectors. Beyond the availability of sunlight,  $COP_{overall}$  is evaluated by equating  $\eta_{coll}$  to one which results in  $COP_{overall}$  being equal to COP.

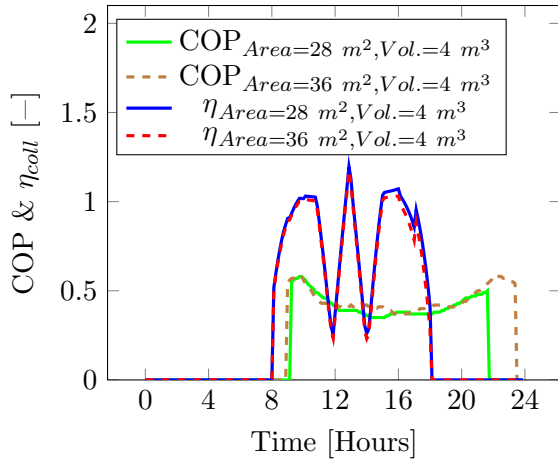


Figure 78: COP &  $\eta_{coll}$  variation at different  $A_{Coll}$  and  $Vol_{Tank}$

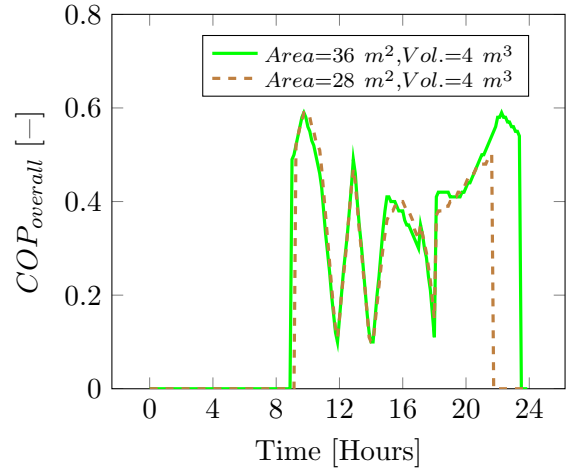


Figure 79:  $COP_{overall}$  variation at different  $A_{Coll}$  &  $Vol_{Tank}$

### 5.6.1 Solar Collector Optimization

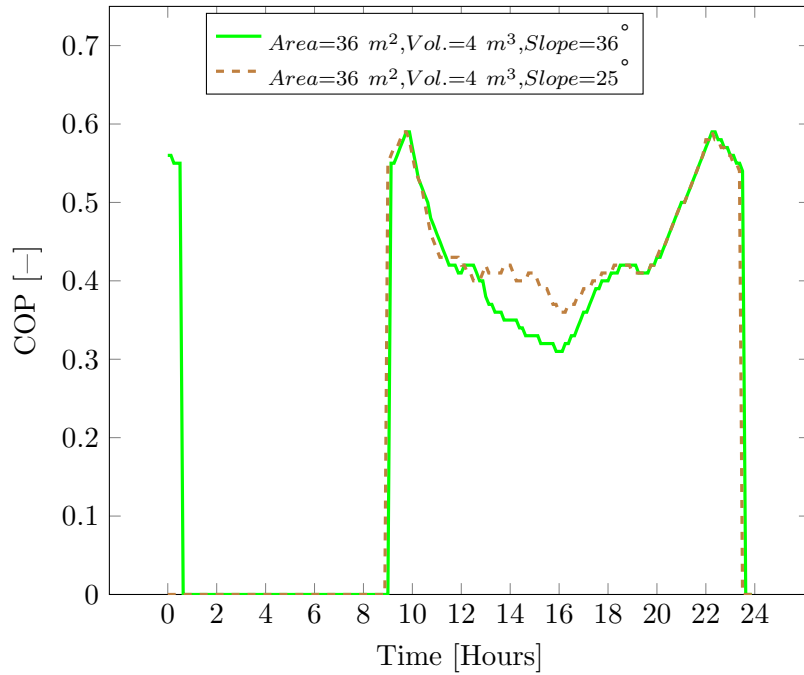


Figure 80: COP variation at different collector slope angles

Figure 80 shows that optimal performance of the collector results in slightly more heat gain which results in longer operating duration over the 24 hour period. However, the optimized collector slope also results in a decrease in COP value between 12:00 and 16:00. From Figure 81 and Figure 82 it can be noted that the system operates at high  $T_c^*$  and  $T_g$  values during the same period which explains the low COP values. Beyond this period, the two

systems operate at the same  $T_c^*$  and  $T_g$  values.

The vitality of an optimised collector slope is appreciated when considering the overall performance of the system,  $COP_{overall}$  as presented in [Figure 98](#). The plotted data is generated by taking the product of the efficiency of the solar collectors ( $\eta_{coll}$ ) and the COP of the ERS. A comparison of  $\eta_{coll}$  in the two considered cases shows how the optimized collector achieves higher values between 11:00 and 14:00. Over this period, the overall performance of the optimized system is higher than the unoptimized slope. Beyond 14:00, the unoptimized slope achieves superior  $\eta_{coll}$  values until the end of solar irradiation.

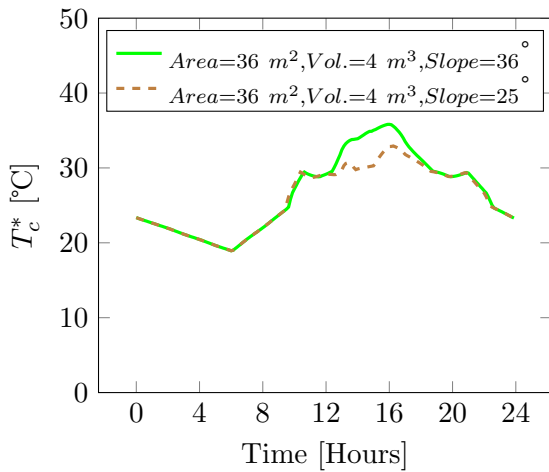


Figure 81:  $T_c^*$  variation at different collector slope angles

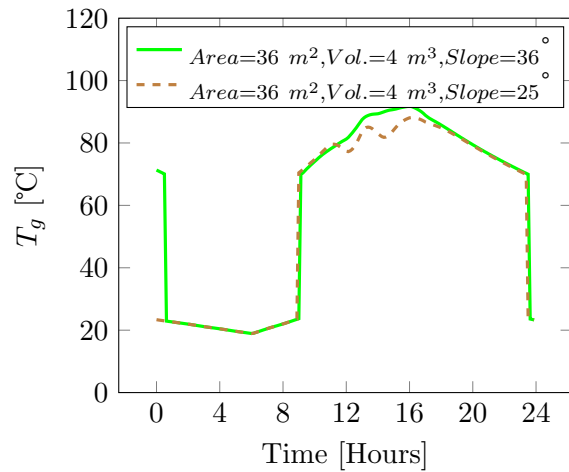


Figure 82:  $T_g$  variation at different collector slope angles

The consequence of the deviation in  $\eta_{coll}$  values is again noted in the  $COP_{overall}$  plot ([Figure 98](#)) whereby higher  $\eta_{coll}$  in unoptimized collector slope results in significantly higher  $COP_{overall}$  during afternoon hours (14:00 and 16:00). However, the performance of the ERS is also responsible for this as the system operates at slightly higher COP due to lower  $T_g$  values which are sufficient for enabling critical mode performance of the system. Critical performance of the ERS can also be noticed in the  $T_c^*$  plot ([Figure 81](#)) whereby the deviation of the system's  $T_c^*$  plot from the ambient coupled  $T_c$  is noticed. This plot also confirms that the unoptimised system operates at lower  $T_g$  values which inherently results in the low  $T_c^*$  values. The high sensitivity of  $COP_{overall}$  on  $\eta_{coll}$  suggests the importance of optimising the performance of the collector which can also be enhanced by introducing a variable tilt angle.

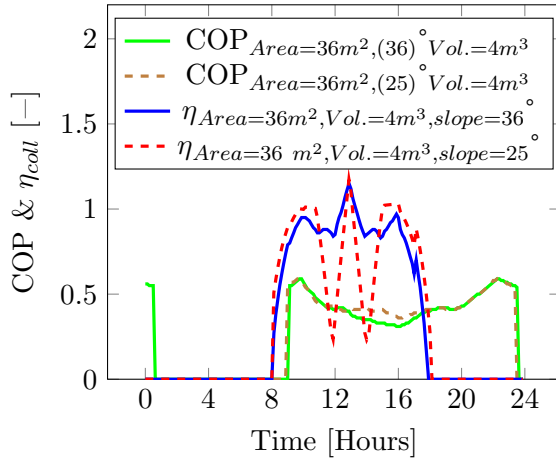


Figure 83: COP &  $\eta_{coll}$  variation at different Collector slope angles

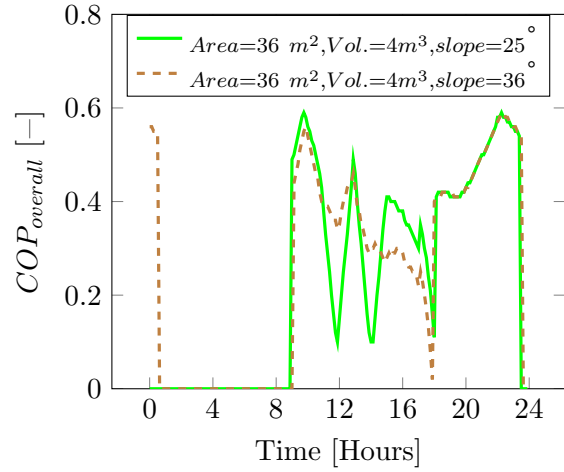


Figure 84:  $COP_{overall}$  variation at different collector slope angles

## 5.7 Ejector performance results in Bloemfontein

Operation of the solar-powered ERS is considered under Bloemfontein solar and ambient data by firstly finding the optimal collector area. This is carried out by varying  $A_{Coll}$  whilst maintaining  $Vol_{Tank}$  at  $3 m^3$ .

From the presented data, it can be seen that the  $36 m^2$  and  $44 m^2$  systems provide extended operation hours whilst the  $28 m^2$  stops around 22:15. Qualitative analysis shows that between 8:00 and 11:00, the  $28 m^2$  and  $36 m^2$  systems achieve higher COP values than  $44 m^2$  systems. However, the  $28 m^2$  system experiences a slight drop in COP between 11:00 and 12:00 due to a sudden drop in  $T_g$  values which is attributed to a drop in solar radiation. During the decline in COP values between 12:00 and 15:00, the  $36 m^2$  operates at the highest COP. Between 15:00 and 17:00, all systems operate at constant COP values with the  $28 m^2$  maintaining the highest value during this period. Afterwards, the  $36 m^2$  system quickly regains COP which results in the system operating at slightly higher values before 19:00 with the  $44 m^2$  system achieving higher values thereafter.

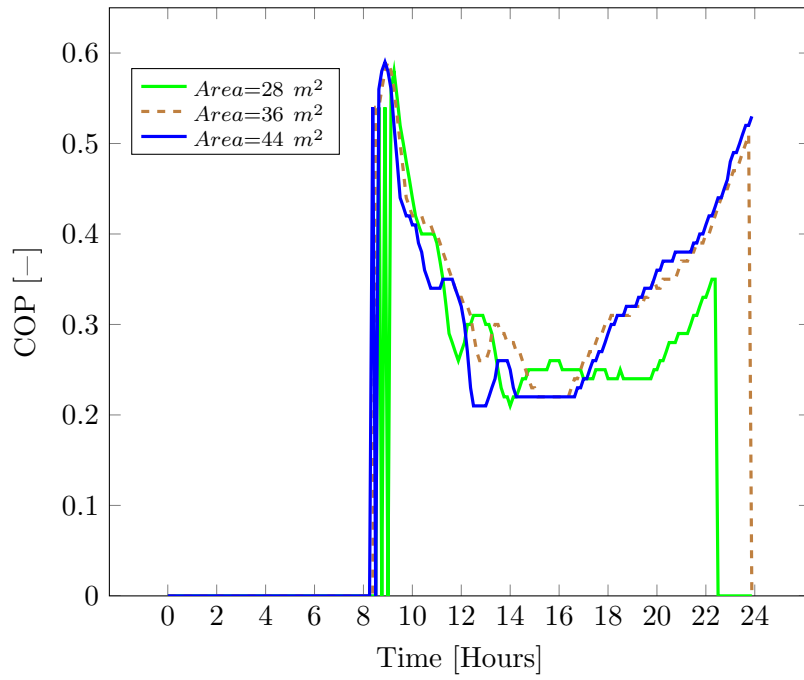


Figure 85: COP variation at different  $A_{Coll}$  with  $Vol_{Tank} = 4 m^3$

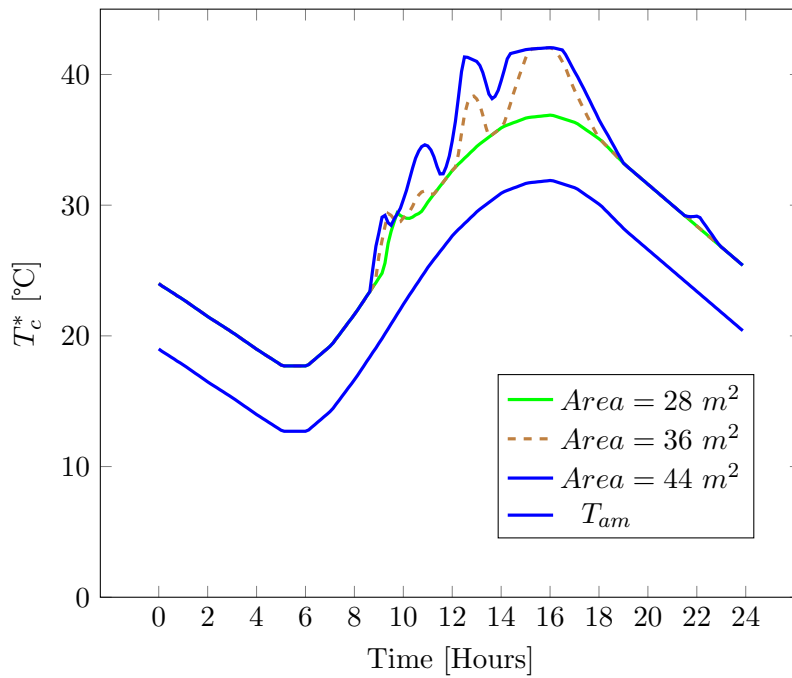


Figure 86:  $T_c^*$  variation at different  $A_{Coll}$  with  $Vol_{Tank} = 4 m^3$

The behaviour of the system's COP values is understood through an investigation of  $T_c^*$  (Figure 86) and  $T_g$  (Figure 87) values. From Figure 86, it can be seen that  $44 m^2$  system experiences the largest deviation from  $T_c$ , followed by the  $36 m^2$ , with the  $28 m^2$  systems being close to  $T_c$  for most of the time. The hierarchy in the variation of  $T_c^*$  matches that of

$T_g$  as plotted in [Figure 87](#).

Relating the variation of  $T_g$  and  $T_c^*$  to the COP of the system, it can be noted that high  $T_c^*$  values are due to high  $T_g$  values which in turn cause low COP values. From [Figure 95](#), it can be seen that the  $28 \text{ m}^2$  and  $36 \text{ m}^2$  systems operate at high COP values (between 08:00 and 16:00). This is due to the system's ability to operate at the minimal required  $T_g$  and  $T_c^*$  values thus allowing critical mode operation of the ejector. During this period, the  $44 \text{ m}^2$  system also operates in critical mode, but due to the availability of excessively high  $T_g$  values, the system ends up functioning at low COP values. After 16:00, high-performance values are obtained from the  $36 \text{ m}^2$  and  $44 \text{ m}^2$  systems which also results from the delivery of adequate  $T_g$  values required to ensure critical performance of the ejector at high  $T_{am}$  conditions. From [Figure 95](#), it can be noted that beyond 19:00, all considered systems operate at ambient coupled  $T_c$  conditions which results from low  $T_g$  values for the considered environment. However, since  $T_{am}$  and  $T_g$  values reduce with time, the COP increases towards the system's stop time. From the presented data, it can be noted that the effect of limiting the tank boiling temperature to  $100 \text{ }^\circ\text{C}$  is also apparent in the  $36 \text{ m}^2$  and  $44 \text{ m}^2$  systems. This is evident in both  $T_g$  and  $T_c^*$  values, whereby these become constant between 12:00 and 16:00. The  $28 \text{ m}^2$  system does not reach this condition due to insufficient solar thermal energy.

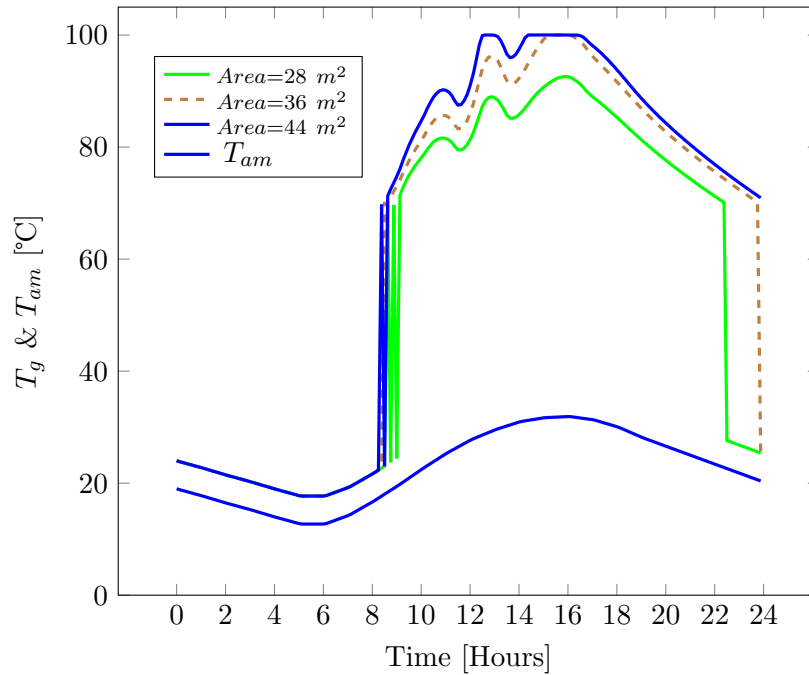


Figure 87:  $T_g$  variation at different  $A_{Coll}$  with  $Vol_{Tank} = 4 \text{ m}^3$

The effect of the storage tank volume on the performance of the system is explored through a parametric analysis of both  $A_{Coll}$  and  $Vol_{Tank}$  as presented in the [Figure 88](#), [Figure 89](#), and [Figure 90](#). The considered configurations are a  $36 \text{ m}^2$   $A_{Coll}$  with a  $4 \text{ m}^3$  and  $6 \text{ m}^3$   $Vol_{Tank}$

system and a  $44 \text{ m}^2$   $A_{Coll}$  with a  $4 \text{ m}^3$  and  $6 \text{ m}^3$   $Vol_{Tank}$  system. From [Figure 88](#), it can be noted that the  $44 \text{ m}^2$   $A_{Coll}$  with a  $4 \text{ m}^3$   $Vol_{Tank}$  is the only system that is able to attain the tank boiling point temperature of  $100 \text{ }^\circ\text{C}$ . The results show an expected performance characteristic of large  $A_{Coll}$  with smaller  $Vol_{Tank}$  systems operating at higher  $T_g$  values than other configurations. The  $36 \text{ m}^2$   $A_{Coll}$  with a  $6 \text{ m}^3$   $Vol_{Tank}$  operates at the lowest  $T_g$  temperatures.

Analysis of COP values (shown in [Figure 88](#)) indicates similar performance values in the early hours (between 8:00 and 10:00) and in the evening hours (17:00 and 22:00) with the exception of low evening COP values from the  $6 \text{ m}^2$   $A_{Coll}$  with a  $6 \text{ m}^3$   $Vol_{Tank}$ . Beyond these time slots, scrutiny of COP values shows that the  $44 \text{ m}^2$   $A_{Coll}$  with a  $6 \text{ m}^3$   $Vol_{Tank}$  retains higher values than the other systems whilst operating for the longest period as-well. The system with a  $36 \text{ m}^2$   $A_{Coll}$  and  $6 \text{ m}^3$   $Vol_{Tank}$  operates at the lowest COP values due to low  $T_g$  values which inherently result in low  $T_c^*$  values proving sub-critical operation of the system. The system with a  $44 \text{ m}^2$   $A_{Coll}$  and  $4 \text{ m}^3$   $Vol_{Tank}$  also operates at low COP values during mid-day (12:00 to 17:00) which comes as a result of high  $T_g$  (shown in [Figure 88](#)) and  $T_c^*$  (shown in [Figure 90](#)).

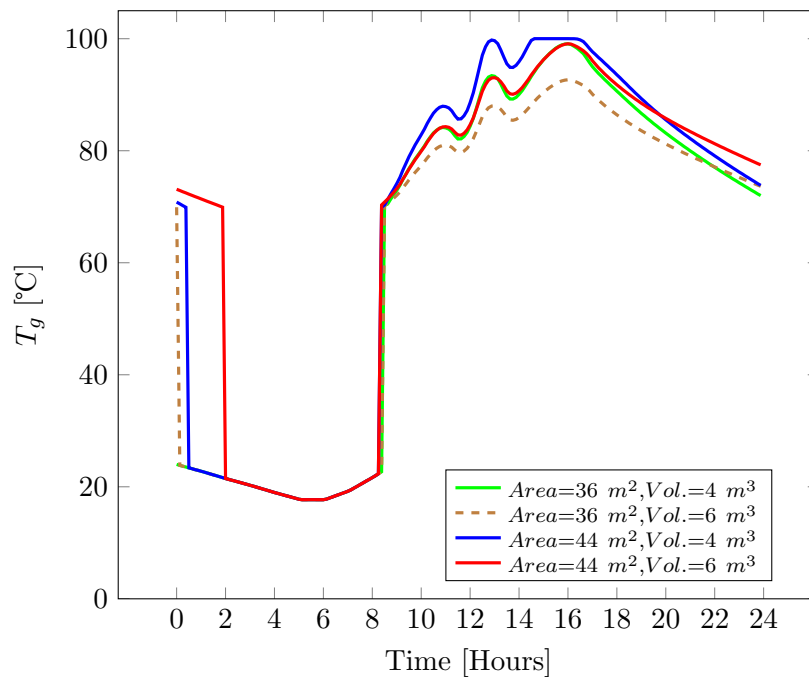


Figure 88:  $T_g$  variation at different  $A_{Coll}$  and  $Vol_{Tank}$



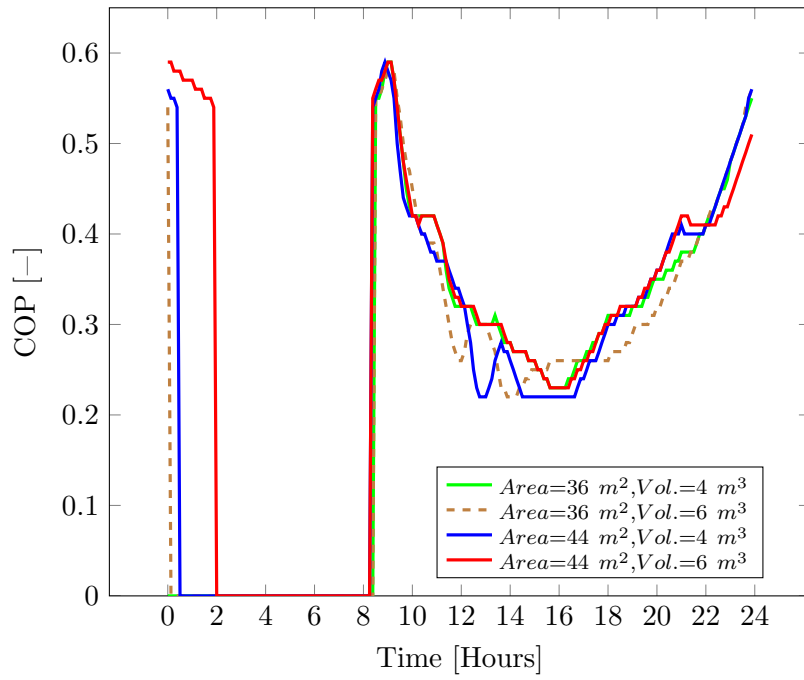


Figure 89: COP variation at different  $A_{Coll}$  and  $Vol_{Tank}$

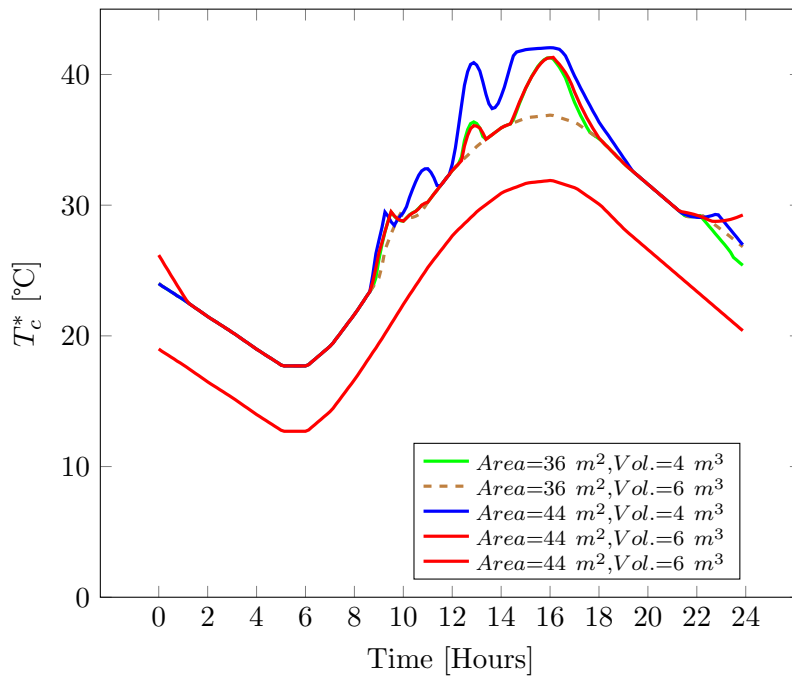


Figure 90:  $T_c^*$  variation at different  $A_{Coll}$  and  $Vol_{Tank}$

Performance comparison between the  $3\text{ m}^3$ ,  $4\text{ m}^3$  and  $6\text{ m}^3$  storage capacity systems shows that the larger storage capacity systems function for an extended period due to an accumulation of thermal energy within the reservoir. Overall, the systems with a  $36\text{ m}^2$  and  $44\text{ m}^2$  collector area and a storage capacity of  $4\text{ m}^3$  archive similar COP values. For comparison

purposes, the overall performance of the  $44 \text{ m}^2$  collector area with a  $6 \text{ m}^3$  will be considered together with the  $36 \text{ m}^2$ ,  $4 \text{ m}^3$  system.

Performance evaluation of the solar-related behaviour of the system is presented in [Figure 97](#) and [Figure 92](#). Similar to the previously considered location, preliminary analysis of solar collectors highlights the need to optimise performance in order to eliminate the losses demonstrated in [Figure 97](#). Despite the large magnitude of losses, the solar collectors operate at much higher efficiency values compared to the COP of the ERS. In the two considered configurations,  $A_{Coll}$  of  $36 \text{ m}^2$  with a  $Vol_{Tank}$  of  $3 \text{ m}^3$  and  $6 \text{ m}^3$ , the solar collector achieves the same performance values. Examination of ERS behaviour shows similar COP values in both configurations with deviations beginning at around 20:00 whereby the  $6 \text{ m}^3$  system achieves higher COP values. At 22:00, the  $4 \text{ m}^3$  system regains its COP values and outperforms the  $6 \text{ m}^3$  system. As highlighted in previous sections, after sunset performance is primarily affected by the stored thermal energy capacity of the system.

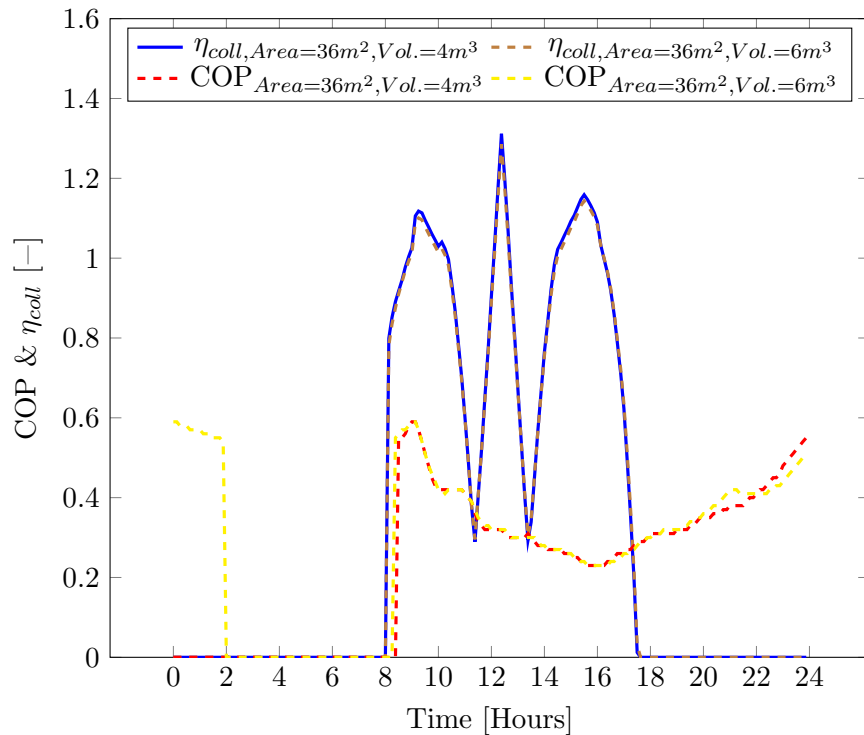


Figure 91: COP &  $\eta_{coll}$  variation at  $A_{Coll} = 36 \text{ m}^2$  with variable  $Vol_{Tank}$

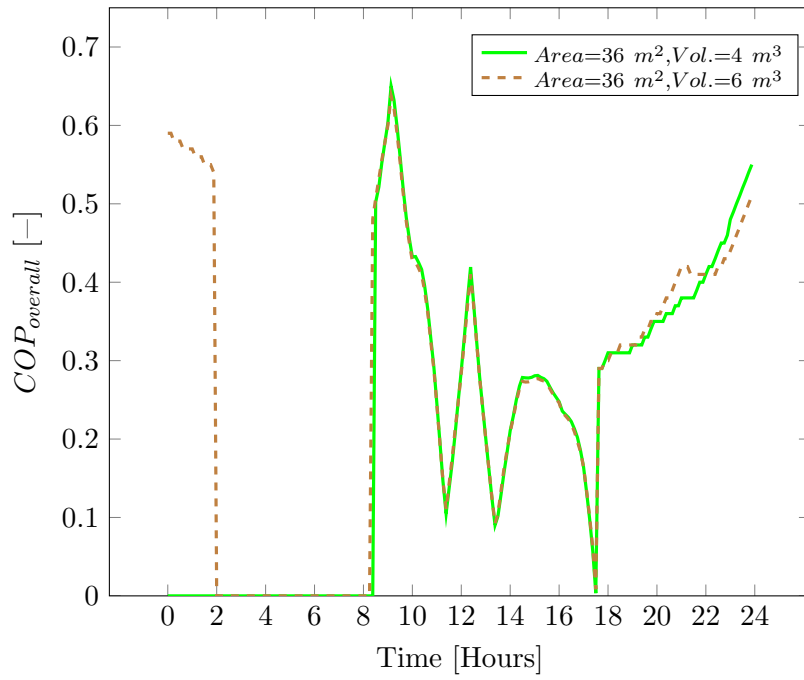


Figure 92:  $COP_{overall}$  variation at  $A_{Coll} = 36 \text{ m}^2$  with variable  $Vol_{Tank}$

Comparing the degree of variation between the COP (Figure 97) and  $COP_{overall}$  (Figure 92) of the ERS, the effect of the efficiency of the solar collectors on the performance of the system is greatly appreciated. From Figure 92, peak operation is observed at around 9:00 when both the ERS and the solar collectors are at their optimal performance. Thereafter, performance is highly affected by the fluctuations in  $\eta_{coll}$  whereby the two troughs on  $\eta_{coll}$  result low  $COP_{overall}$ .

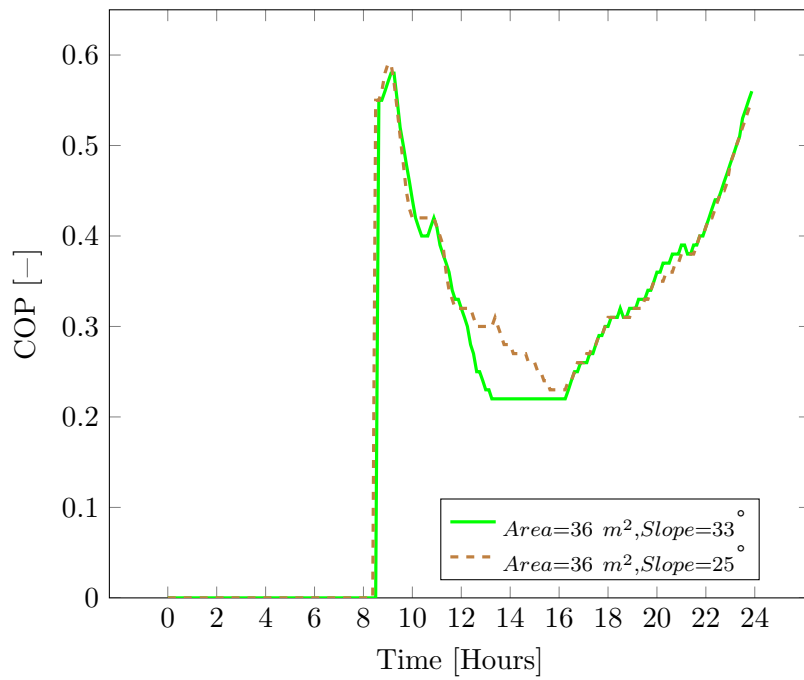


Figure 93: COP variation at different collector slope angles

Following the collector optimization procedure carried out in [chapter 6.2](#), the performance of the solar-powered ERS is analysed and compared against the previously considered configuration. [Figure 93](#) shows that the system with an optimised collector slope operates at slightly higher COP values between 12:00 and 16:00. Beyond this period, there is an insignificant difference in the COP of the two considered systems.

[Figure 94](#), shows that the optimized collector system operates at higher  $T_g$  and  $T_c^*$  values than the previously considered case. This occurs between 12:00 and 16:00 which inherently causes the system to experience lower COP values.

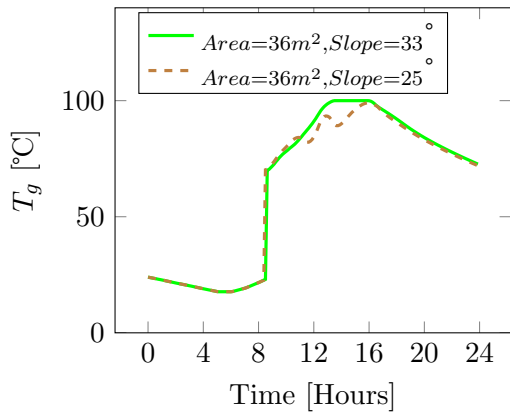


Figure 94:  $T_g$  variation at different collector slope angles

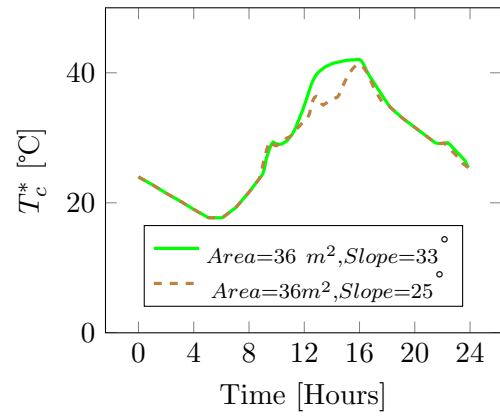


Figure 95:  $T_c^*$  variation at different collector slope angles

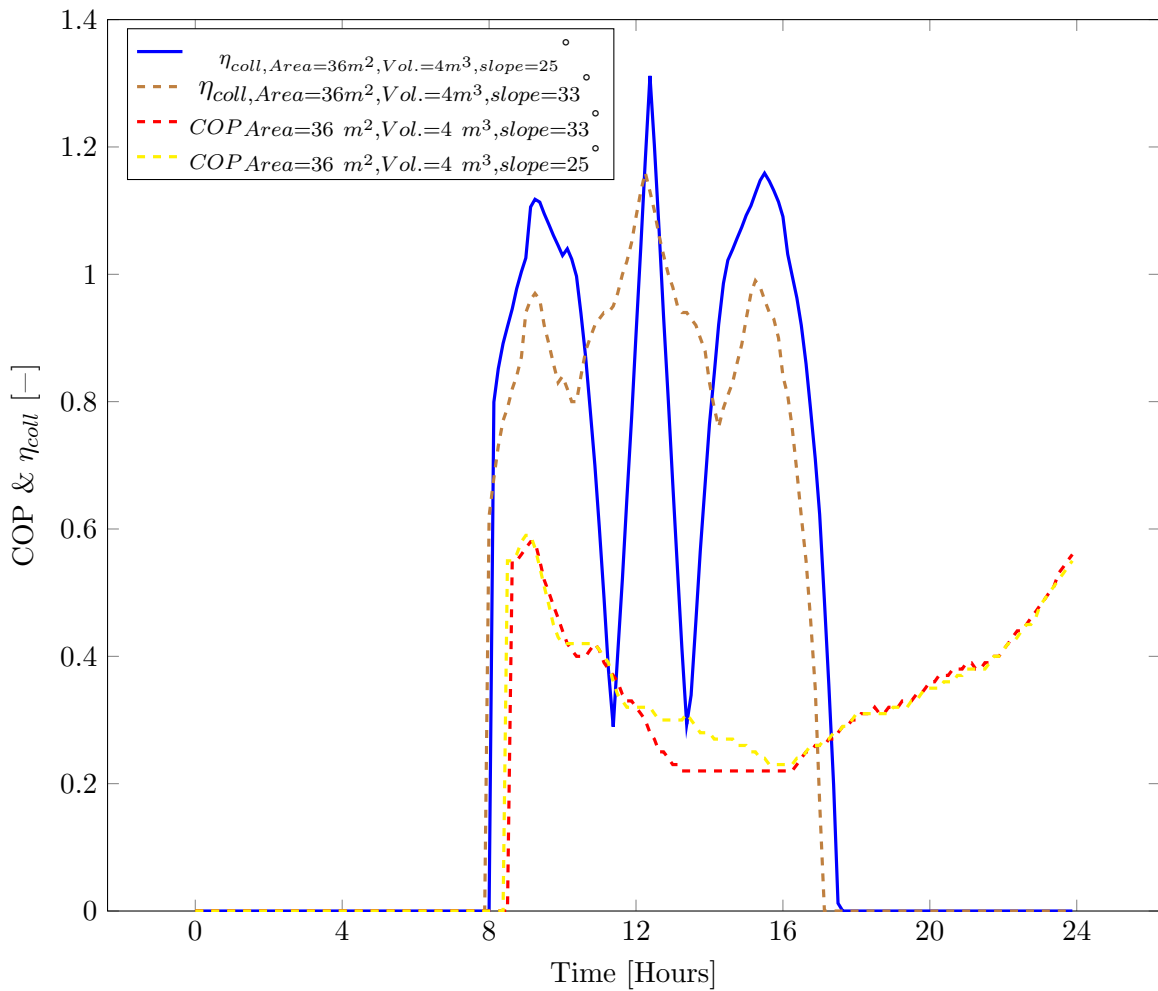


Figure 96: COP &  $\eta_{coll}$  variation at different collector slope angles

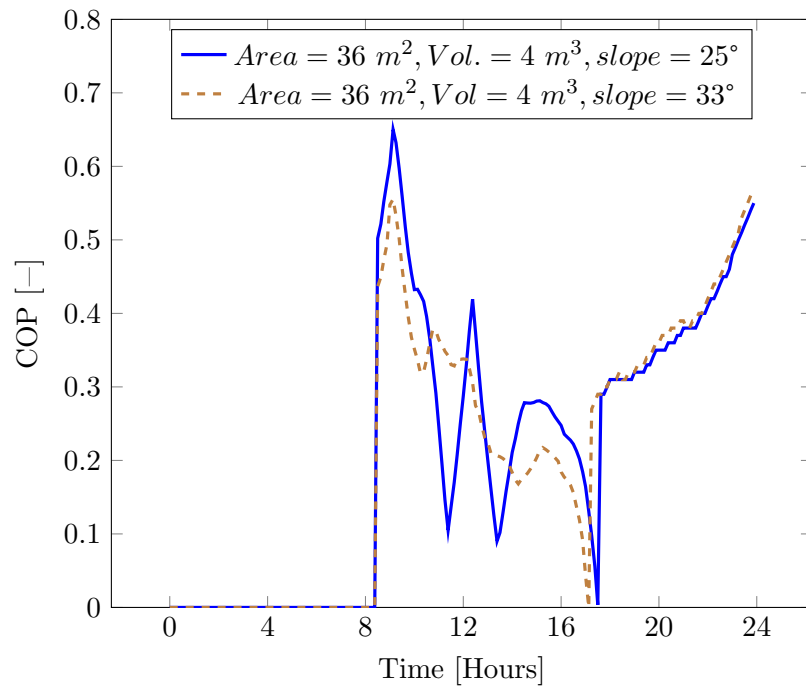


Figure 97:  $COP_{overall}$  variation at different collector slope angles

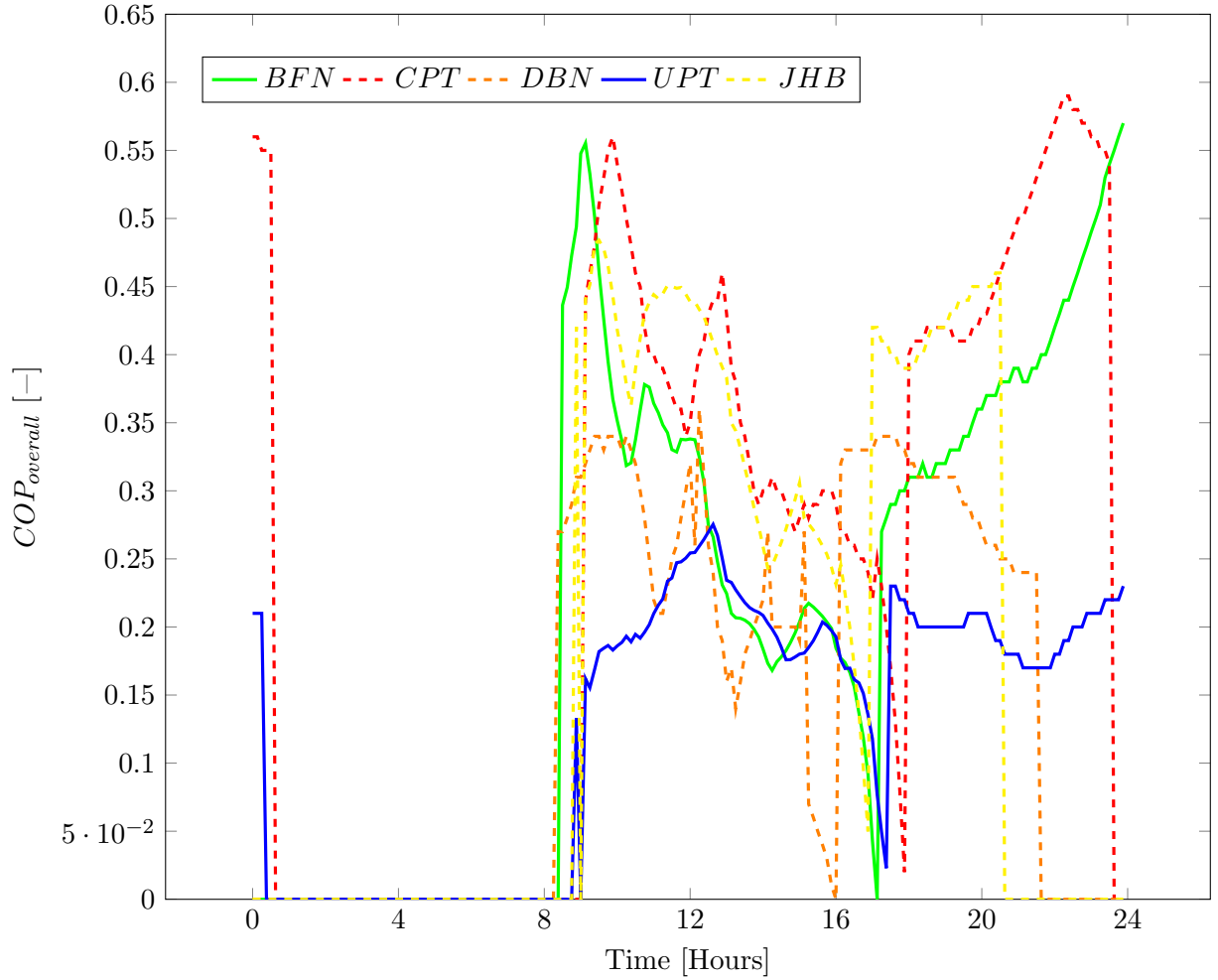


Figure 98: Overall COP variation at different  $A_{Coll}$ ,  $Vol_{Tank} = 3 m^3$

## 5.8 $COP_{overall}$ Analysis for Cape Town and Upington

From the optimization exercise carried out in [section 5.4](#) (Upington) and [section 5.6](#) (Cape Town), the optimum system configuration parameters (presented in [Table 16](#)) were found to give optimal performance in those considered locations. These parameters are used in the present section to compare the performance of the system across the different locations.

Table 16: Optimised system configuration

	Location	
	Cape Town	Upington
Collector Area	36 $m^2$	44 $m^2$
Collector Slope	36 °	32, 5 °
Storage Volume	4 $m^3$	3.33 $m^3$

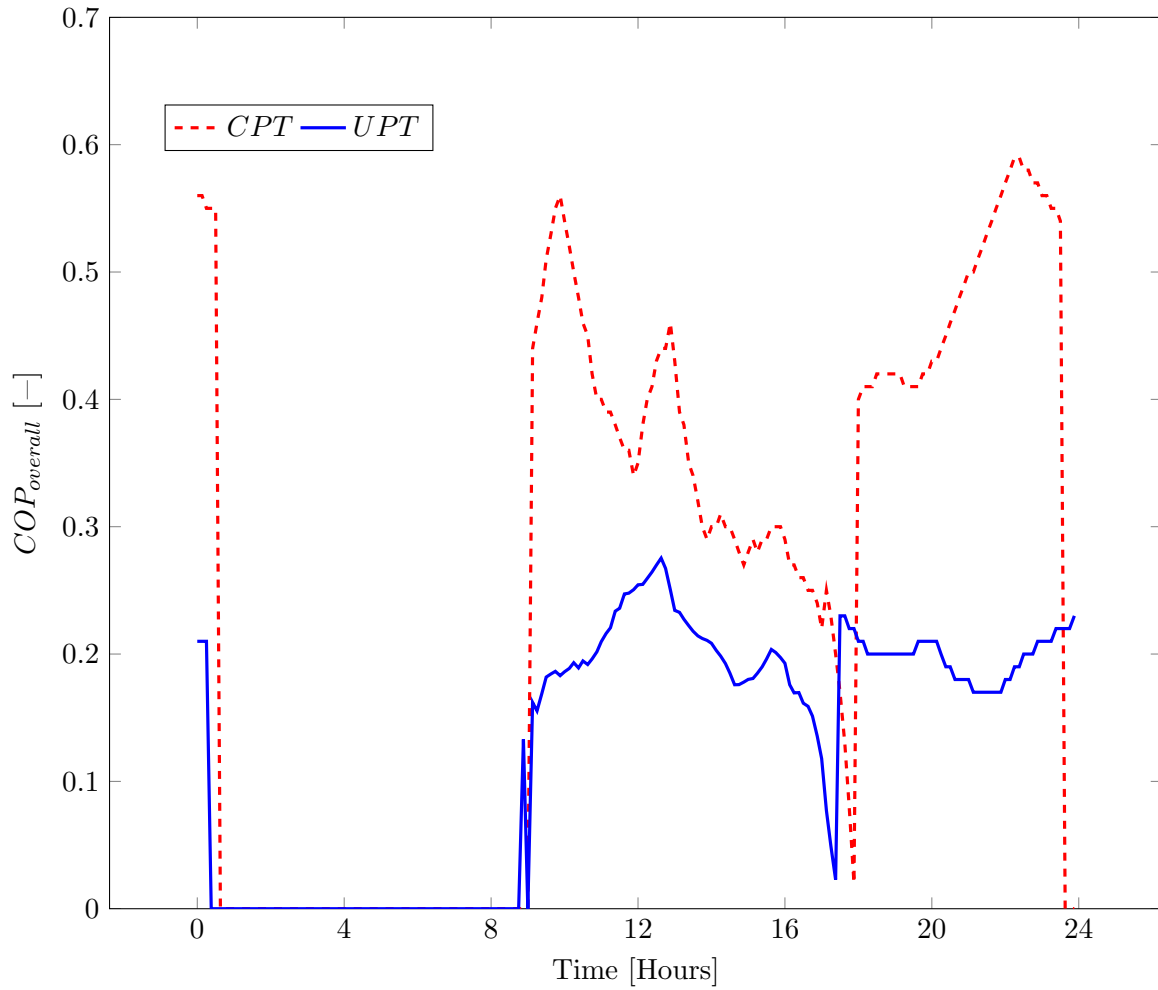


Figure 99: Optimized  $COP_{overall}$  variation at Cape Town and Upington

Figure 99 shows the  $COP_{overall}$  variation of the ERS when analysed over CapeTown and Upington Weather conditions under the optimized configuration parameters as listed in Table 16. The results show that the solar-powered ERS in Cape Town outperforms the one in Upington by a significant magnitude. Under Cape Town weather conditions, the system starts at a high  $COP_{overall}$  of 0.57 which gradually decreases through the day to eventually become 0.23 at 17:50. Beyond sunset, the system operates using the stored solar thermal energy, which eliminates the need to consider losses across the collectors, and hence resulting in high  $COP_{overall}$  values. Inspection of Upington values shows that  $COP_{overall}$  increases from the initial start-up 0.16 to reach a peak value of 0.3 at 13:00. Beyond 13:00,  $COP_{overall}$  values decrease until sunset whereby performance analysis shifts towards non-solar related operation as the system is powered by stored thermal energy. During this period (17:00 to 24:00), the system starts at a high  $COP_{overall}$  value of 0.25 and gradually decreases with time. However, at 21:00,  $COP_{overall}$  values start increasing again until reaching the end of the 24 hour period.



Figure 100 and Figure 101 shows the operating parameters ( $T_g$  and  $T_c^*$ ) of the two considered systems which are responsible for  $COP_{overall}$  values shown in Figure 99. The  $T_g$  plot (Figure 100), shows that the system at Upington operates at higher  $T_g$  values when compared to the system in Cape Town. This is attributed to the large collector surface area and high-intensity irradiation values experienced in Upington. Figure 101 shows that Upington also experiences high  $T_{am}$  as a result of high solar radiation values. To operate in critical mode, under Upington conditions, the ERS is required to have  $T_c$  values which are achieved from high  $T_g$  values. With the low solar radiation and  $T_{am}$  conditions, it can be noted that the Solar ERS operates at significantly lower  $T_c^*$  values compared to the system at Upington. This is achieved at significantly lower  $T_g$  values as well when compared to the Upington system. Considering the variation of  $T_g$  and  $T_c^*$  across the two locations, it can be concluded that the Cape Town system achieves high COP values due to being to operate in critical mode at low  $T_g$  and  $T_c$  values.

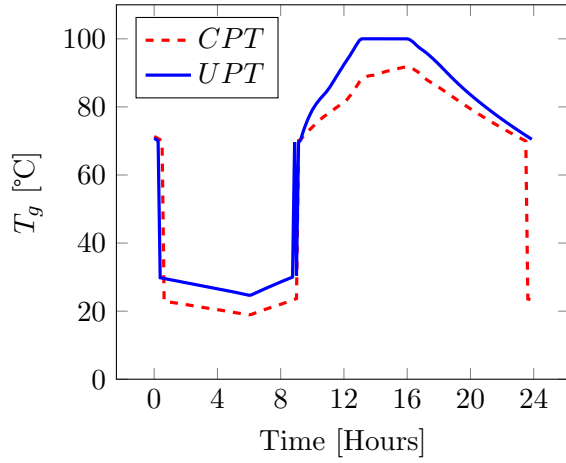


Figure 100:  $T_g$  variation at Cape Town and Upington

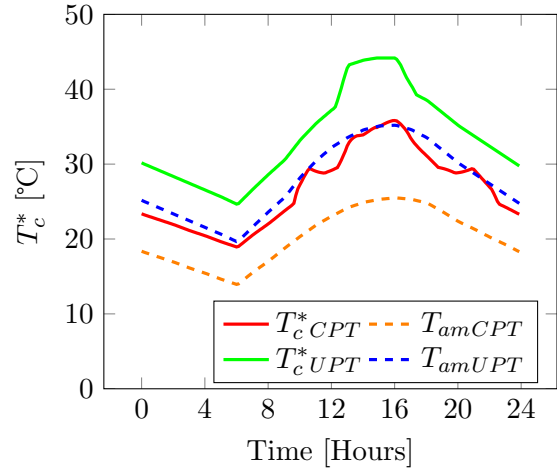


Figure 101:  $T_c^*$  variation at Cape Town and Upington

## 5.9 $COP_{overall}$ Analysis for Johannesburg, Durban, and Bloemfontein

A comparison of the system's performance across Bloemfontein, Durban, and Johannesburg weather conditions is undertaken by using the optimized system configuration parameters (shown in [Table 17](#)) which were obtained in the location based optimization exercise presented in [section 5.3](#), [section 5.5](#), and [section 5.7](#), respectively.

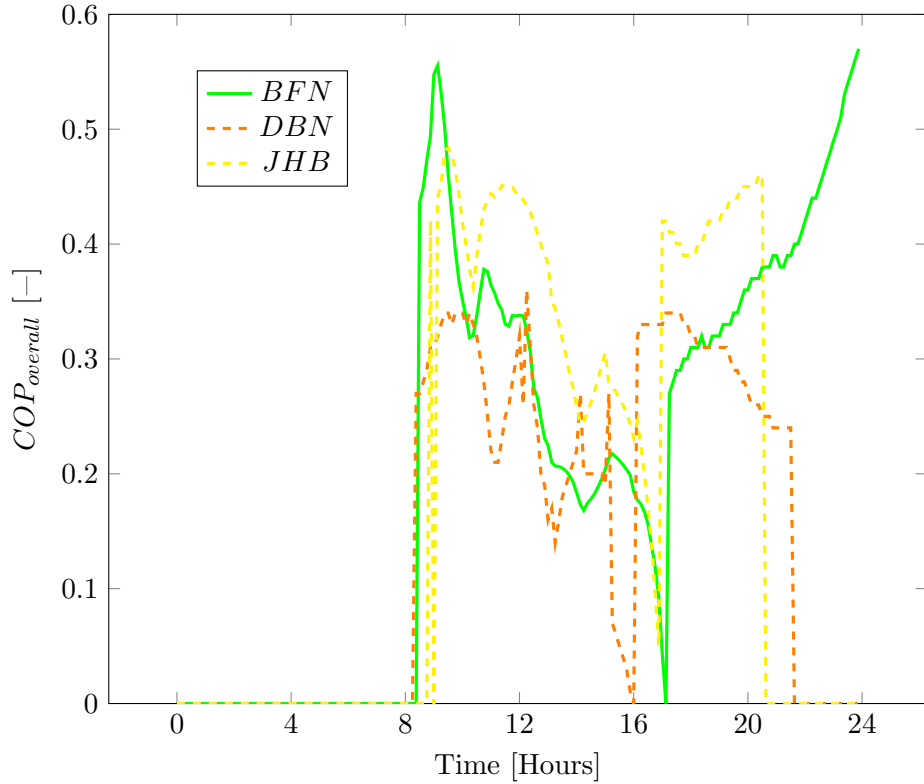


Figure 102: Optimized  $COP_{overall}$  variation in Bloemfontein, Durban, and Johannesburg

Table 17: Optimized system configuration

	Location		
	Durban	Bloemfontein	Johannesburg
Collector Area ( $m^2$ )	56	36	36
Collector Slope ( $^\circ$ )	36	33	36
Storage Volume ( $m^3$ )	4	4	3.33

The  $COP_{overall}$  plot in [Figure 102](#) shows the performance of the solar ERS at three different locations (Bloemfontein, Durban, and Johannesburg) under the parameters specified in [Table 17](#). An overview of the presented data shows that the ERS in Johannesburg achieves superior daytime performance over the two other locations. Hourly analysis shows that between 8:00 and 10:00, the Bloemfontein system attains peak  $COP_{overall}$  values followed by Johannesburg and Durban. From 10:00 to 16:00, the solar ERS at Johannesburg experiences high but gradually reducing COP values starting from 0.45 to 0.2. Similar behaviour is observed in the other two locations whereby the  $COP_{overall}$  values reduce as the day progresses. As highlighted in all previous analysis, night time performance is independent of solar collectors but it is reliant on stored solar thermal energy hence all considered ERS experience high  $COP_{overall}$  values beyond sunset. Since it is the first system to switch to stored thermal

energy, due to quicker diminishing of high-grade solar radiation, the Durban system achieves high COP values between 16:00 and 17:00. Upon switching to stored thermal energy, at 17:00, the Johannesburg system outperforms both Durban and Bloemfontein systems. Due to the small storage tank of the Johannesburg ERS, night time performance is limited between 17:00 and 20:30. The Bloemfontein system operates for beyond the 24 hour period with night time performance characterised by continuously increasing COP values.

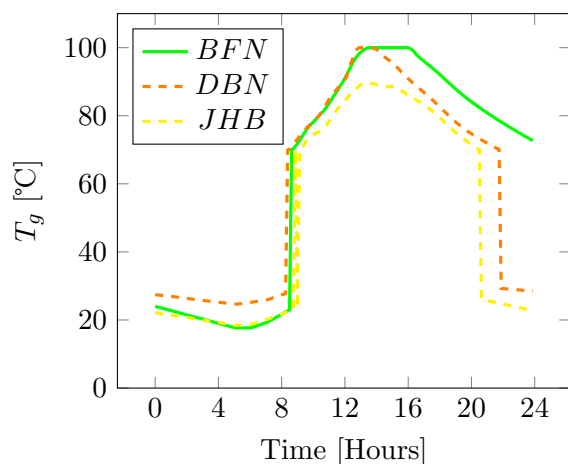


Figure 103:  $T_g$  variation across Bloemfontein, Durban, and Johannesburg

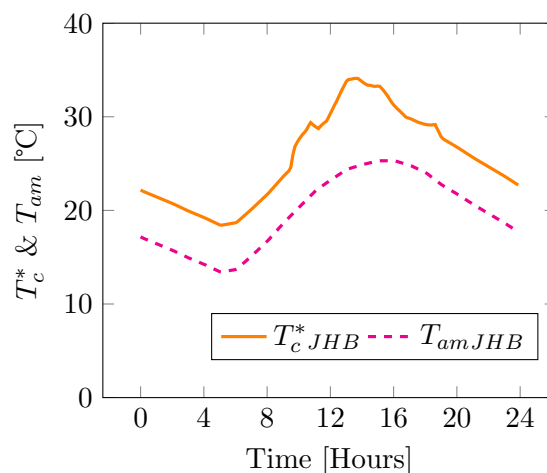


Figure 104:  $T_c^*$  and  $T_c$  variation in Johannesburg

To understand the behaviour of the solar ERS presented in [Figure 102](#), the operating parameters of the system at the three considered locations are presented in [Figure 103](#) to [Figure 106](#). Starting with the  $T_g$  plot, it can be noted that over the 24 hour period, the Bloemfontein system operates at the highest  $T_g$  values followed by Durban with Johannesburg experiencing the lowest  $T_g$  values. Looking at Durban and Bloemfontein data, it can be seen that the two systems experience the same morning to mid-day values even though the Durban system has a larger collector surface area ( $56 \text{ m}^2$ ). This indicates that Bloemfontein has superior solar radiation values which result in high  $T_g$  values at smaller  $A_{Coll}$  ( $36 \text{ m}^2$ ). This is further proven by the drop in Durban  $T_g$  values after 13:00, indicating that there is low grade solar thermal energy. With a smaller  $A_{Coll}$ , the Bloemfontein system reaches the maximum tank temperature of  $100 \text{ }^\circ\text{C}$  and maintains this value until 16:00 whereby the  $T_g$  values start dropping as the sunsets. The Johannesburg system the same  $A_{Coll}$  as Bloemfontein but the system operates at much lower  $T_g$  values and hence indicating that Johannesburg has low grade solar thermal energy compared to Bloemfontein.

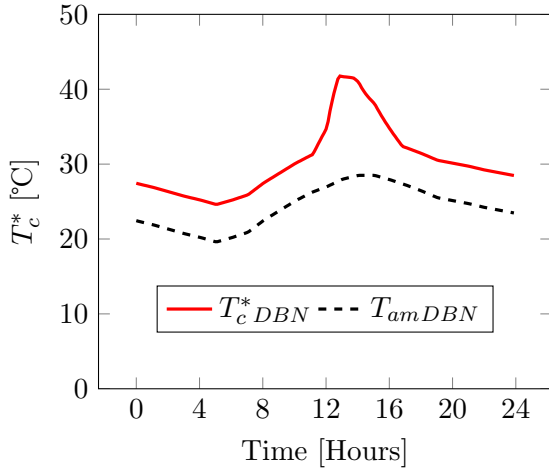


Figure 105:  $T_c^*$  variation in Durban

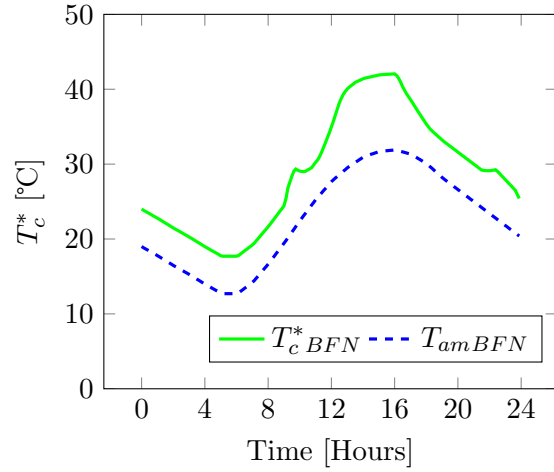


Figure 106:  $T_c^*$  variation in Bloemfontein

A comparison of  $T_{am}$  across all three considered areas (Figure 107) shows that day time temperatures are highest in Bloemfontein followed by Durban with Johannesburg having the lowest. Since  $T_{am}$  values determine the ERS's  $T_c$  ( $5\text{ }^\circ\text{C}$  higher than  $T_{am}$ ), a similar trend is viewed on  $T_c^*$  values. Tanking into account these parameters, it can be noted that the Johannesburg system operates at higher daytime (10:00 to 17:00 ) COP values, due to low  $T_g$  and  $T_c^*$  values. The Bloemfontein and Johannesburg system experiences high start-up COP values as a result of low  $T_{am}$  which enable critical performance at low  $T_g$  and  $T_c$  values. Due to high morning (8:00 to 12:00)  $T_{am}$  values in Durban, the system operates at low  $COP_{overall}$  values as it is forced to operate in sub-critical mode. Between 12:00 and 15:00, the Durban and Bloemfontein systems operate at almost similar low  $COP_{overall}$  values due to both high  $T_c^*$  and  $T_g$  values compared to the system in Johannesburg. Beyond sunset performance of the Durban ERS starts with higher COP values between 16:00 and 18:00 due to low (but above ambient)  $T_c^*$  values compared to the Bloemfontein. However, the slow rate of decrease in evening  $T_{am}$  values at Durban results in sub-critical performance of the ejector as it operates at low  $T_g$  temperatures and  $T_c$  values that are less than  $5\text{ }^\circ\text{C}$  more than  $T_{am}$ . Compared to all the four other locations, it can be observed that this situation is unique to Bloemfontein as all the other systems experience increasing COP values towards stop time.

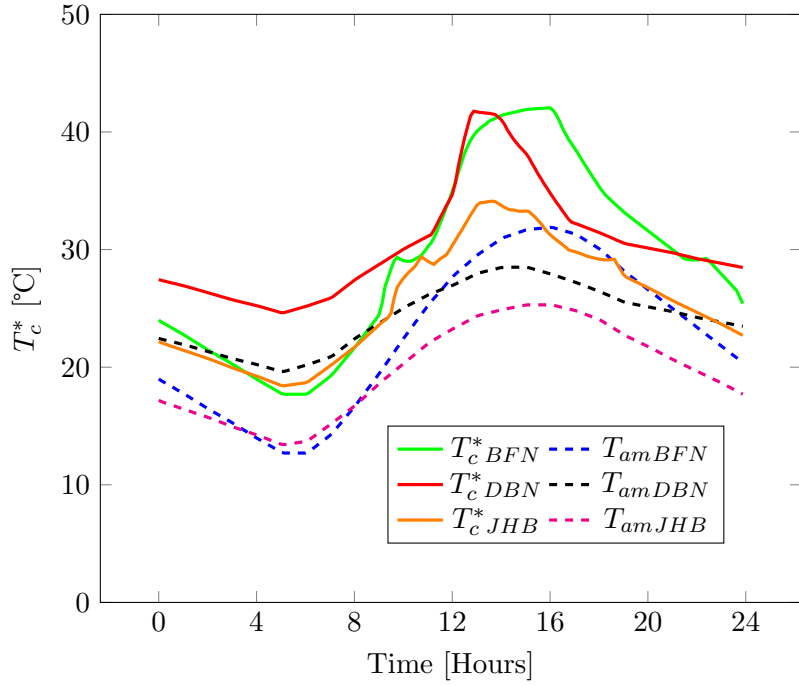


Figure 107:  $T_c^*$  and  $T_{am}$  variation in Bloemfontein, Durban, and Johannesburg

**Figure 108** compares the Cape Town ERS against those operating under Bloemfontein and Johannesburg weather conditions. From the plot, it can be seen that similar daytime performance characteristics exist for both Cape Town and Johannesburg systems. The Bloemfontein system underperforms when compared to the two systems. Considering the hourly performance of the two superior systems, it can be observed that the Cape Town system experiences higher start-up [8:30-10:00] COP values. From **Figure 109** and **Figure 110** it can be seen that during this period, the Cape Town solar ERS operates at lower  $T_c^*$  and  $T_g$  values whilst enabling critical mode performance. This effect also explains the switch in superior  $COP_{overall}$  values between 10:00 and 12:15 for the two locations. Beyond 12:15, it can be observed that the Cape Town system operates at higher  $T_g$  values which cause higher  $T_c^*$  values.

Since the Johannesburg ERS has a smaller  $Vol_{Tank}$ , it quickly consumes stored thermal energy faster than the Cape Town system which is proven by the early decrease in  $T_g$  values. This results in an earlier shift to stored thermal energy use in the Johannesburg system and consequentially an earlier stop time compared to the Cape Town ERS.

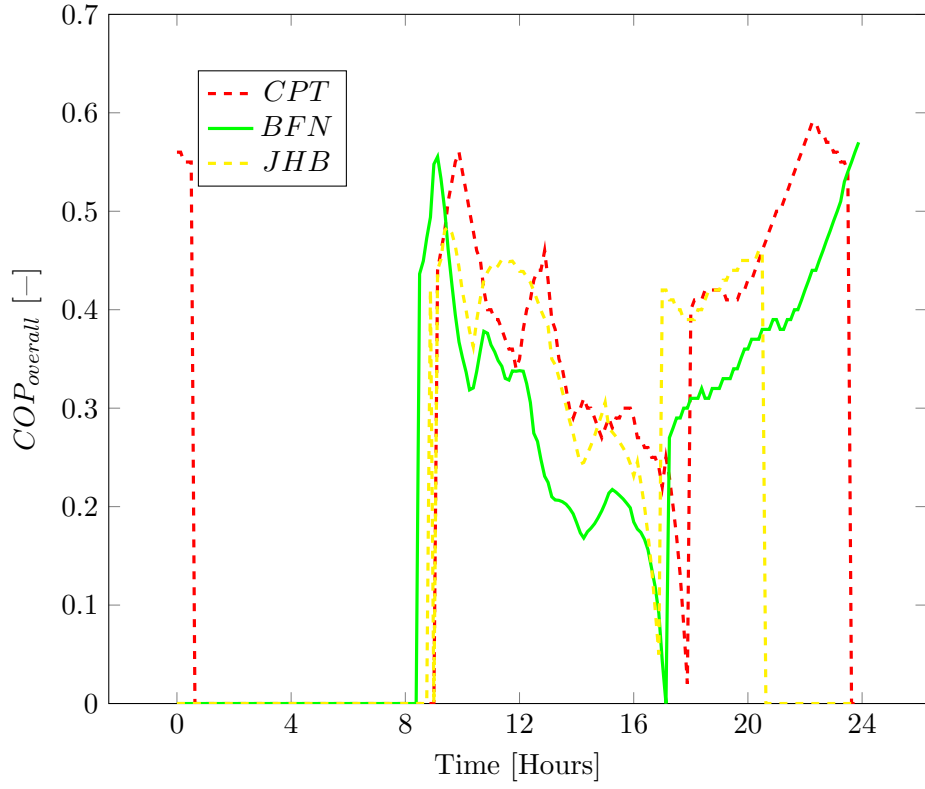


Figure 108: Optimized  $COP_{overall}$  variation across Cape Town, Bloemfontein, and Johannesburg

Table 18: Optimized system configuration

	Location		
	Cape Town	Bloemfontein	Johannesburg
Collector Area [ $m^2$ ]	36	36	36
Collector Slope [ $^\circ$ ]	36	33	36
Storage Volume [ $m^3$ ]	4	4	3, 33

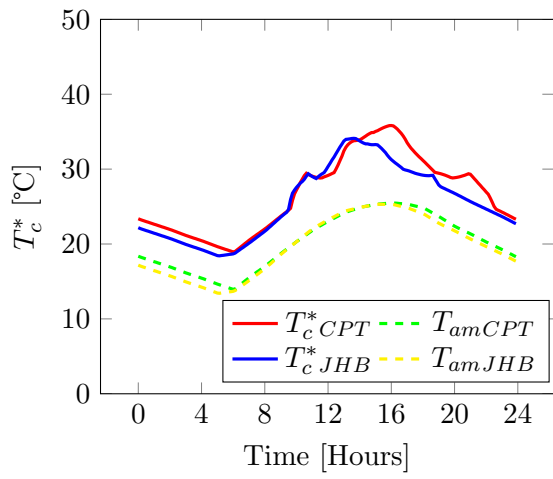


Figure 109:  $T_c^*$  and  $T_{am}$  variation in Johannesburg and Cape Town

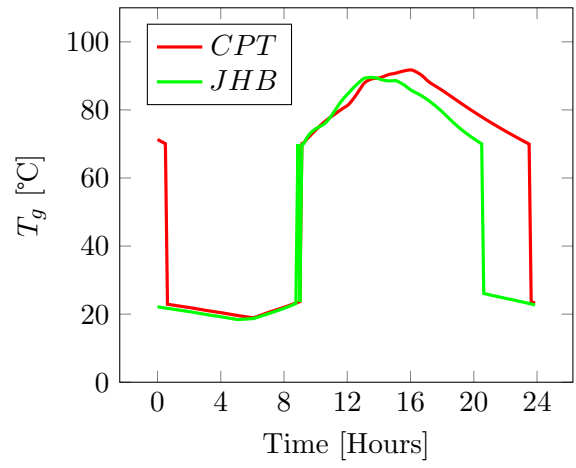


Figure 110:  $T_g$  variation in Johannesburg and Cape Town



## 6 Conclusions and Recommendations

A model of a solar thermal powered ejector refrigeration system was developed and thoroughly validated to study the performance of the system across various cities in South Africa. To optimize performance across different locations, the considered areas were Johannesburg, Durban, Upington, Bloemfontein and Cape Town. To perform this study, a thermodynamic model of an ejector refrigeration cycle was developed and validated for different working fluids (R134a, R245fa, R290, and R1234ze(Z)) using the EES software. Validation was carried out by comparing the obtained results to those published in various studies. R1234ze(Z) was found to be the ideal working fluid as it is an environmentally friendly working fluid and also gives better coefficients of performance.

The R1234ze(Z) ERS model was then coupled with the solar thermal system (solar collectors, water storage tank, and pump) in TRNSYS to study the transient, solar dependent performance of the system across the previously stated locations. The solar system was independently validated from published data. The ERS performance data was imported through the Type 42a component. The complete model was used to determine performance in each location, whereby optimization was conducted by finding the optimal collector slope, storage tank capacity, and solar collector area. The considered optimization criterion was system operation at high COP values whilst extending cooling generation beyond sunset.

### 6.1 Conclusions

From the investigation carried out in the study, the following conclusions have been drawn:

- A preliminary study of working fluid selection for an ejector refrigeration system indicated that R1234ze(Z) was the ideal refrigerant for the system. Performance analysis of the steady state - real gas-model of the ejector refrigeration system was carried out for different working fluids (R134a, R245fa, R290, and R1234ze(Z)) whereby it was found that R1234ze(Z) achieved the highest COP values. Environmental considerations revealed that R1234ze(Z) had low GWP and ODP values hence it was considered as the ideal working fluid.
- The solar-powered ERS gives better COP values at low ambient temperatures ( $T_{am}$ ) and poor COP values at higher ambient temperatures values. The transient behavior

of the solar-powered ERS was monitored from a dynamic model of the system under variable solar radiation and ambient conditions. This was carried out in Johannesburg, Durban, Uppington, Bloemfontein and Cape Town whereby the following findings were made on the transient performance of the ERS:

- i. High ambient temperatures require the ERS to operate at high generator temperature values to achieve critical performance and high COP values. Since high ambient temperatures values are dominant during midday and afternoon hours, the COP curve in all locations is characterized by low values during this period. The Uppington ERS operates at peak noon ambient temperatures values of 32 – 35 °C which requires the system to have condenser temperature ( $T_c$ ) values of 37 – 40 °C in order to achieve the desired heat rejection across the condenser. During this period, the system operates at the generator temperature of 92 – 100 °C with  $COP_{overall}$  of 0.254 – 0.193.
  - ii. Low ambient temperatures values enable ERS operation at low generator temperature values whilst guaranteeing critical performance. With low ambient temperatures values being prevalent during the morning and late evening hours, the COP curve of the ERS is characterized by high values during this period. Since ambient temperatures increase in the morning, the COP values tend to diminish from the high start time value in the morning to low midday values. In the evening, COP values increase due to diminishing generator temperature and ambient temperatures values. The ERS system under Cape Town solar and weather conditions achieves the highest morning  $COP_{overall}$  values of 0.44 – 0.35 at the generator temperature range of 70.1 – 81.3°C . During this period, Cape Town has low ambient temperatures values of 18.9 – 23 °C which enable the system to operate at condenser temperature values of 23.9 – 28 °C . With the evening experiencing similarly low ambient temperatures (25 – 18.72 °C ) values, the system can achieve high  $COP_{overall}$  values of 0.29 – 0.54.
- Optimization of transient performance of the ERS was conducted by varying the slope of the solar collectors, the collector area size ( $A_{Coll}$ ), and the storage tank capacity ( $Vol_{Tank}$ ). From the investigation, the following conclusions were drawn:
    - i. The rate at which generator temperature values increase in the morning is dependent on the size of  $A_{Coll}$ , and the capacity of storage tank capacity whereby a large collector surface area coupled with a small capacity storage tank capacity results in a high rise in generator temperature values during start-up operation. A high rate of increment in morning generator temperature values guarantees critical mode operation of the system as condenser temperature values will be greater than the prescribed value of 5 °C above ambient temperatures. Due to high morning

ambient temperatures values, (25 – 32 °C ) in Upington, the solar-powered ERS is optimized to have a collector surface area of 44  $m^2$  and storage tank capacity of 3.33  $m^3$  in order to achieve high generator temperature values of 70– 92.47 °C which are required to achieve critical performance. The solar-powered ERS in Cape Town has a smaller collector surface area of 36  $m^2$  and a larger storage tank capacity of 4  $m^3$  to allow for a slower increment in morning generator temperature values (70– 81.3 °C ) required for critical performance at the lower morning ambient temperatures values (18.4 – 23 °C ).

- ii. The variation of COP values in the evening is also characterized by the rate of change of generator temperature values whereby this determines critical or sub-critical performance based on the magnitude of ambient temperatures values. The Cape Town ERS achieves higher evening COP values (0.29 – 0.54) as a result of continuously decreasing generator temperature values (91.8 - 70 °C ) which result from diminishing solar radiation and low evening ambient temperatures values (25 – 18.72°C ). The Upington system experiences a similar trend of gradually increasing evening COP values (0.193 – 0.230) which are lower than those in Cape Town due to the system operating at higher generator temperature (100 – 70.5°C) and condenser temperature values (40.17 – 29.79°C). The Upington system achieves higher evening generator temperature values as a result of the larger collector surface area (44  $m^2$ ) which is further coupled to a smaller storage tank capacity (3.33  $m^3$ ) whereas the Cape Town system operates at lower generator temperature values as a result of the smaller collector surface area (36  $m^2$ ) which is coupled to a larger storage tank capacity (4  $m^3$ ).
- iii. Systems sized to have larger than required collector surface area experience high generator temperature values which results in excessively high critical condenser temperature values and hence reduce the COP of the ERS even though the system is in critical mode.
- iv. Systems with a small collector surface area experience low generator temperature values which results in low critical condenser temperature values and sub-critical performance which also contributes to low COP values.
- v. The capacity of storage tank capacity can be used in regulating generator temperature values as larger storage tank capacity values result in low generator temperature values. storage tank capacity also helps in extending the operating duration of the ERS since larger storage tank capacity values provide more thermal energy storage capacity and hence enable operation beyond the availability of solar radiation.

- Location-based analysis of the solar ERS showed that the system is best suited for locations with low ambient temperatures (18 – 25°C). From the cities considered, Johannesburg and Cape Town provided the highest daytime  $COP_{overall}$  values (0.345 and 0.334, respectively) over the 24 hour period. The ERS in Bloemfontein closely follows the performance of systems in Johannesburg and Cape Town (especially between 8:00 and 10:00) due to the low ambient temperatures. Thereafter, the COP values degrade to become similar to those experienced in Durban due to high ambient temperatures values which require system operation at high generator temperature values. The Upington ERS attains the lowest COP values as a result of the extremely high ambient temperatures value which demand system operation at high generator temperature values. The respective daytime  $COP_{overall}$  values of the system under Durban, Bloemfontein, and Upington conditions are 0.278, 0.237, and 0.187.

## 6.2 Recommendations

For further research into the behavior of the ERS, the following recommendations may be explored:

- Further optimization studies are recommended to investigate the improved performance of the ERS, especially in high ambient temperatures areas. To enhance operation in such conditions, alternative heat rejection methods (water to air) are recommended to enable the condenser to operate at lower condenser temperature values. This would then enable operation at lower generator temperature values and hence improve the  $COP_{overall}$  of the system.
- Since the solar-powered ERS achieves superior performance at low ambient temperatures, night time only operation mode is worth exploring. During such operation, the solar system would harvest and store heat during the day and the ERS would generate cooling during low ambient temperatures hours at night.
- Considering that the location based assessment of the solar-powered ERS was purely based on the technical performance of the system, a detailed economic viability study is also recommended.

# Bibliography

- [1] N. P. Nkosi and J. Dikgang, “Pricing electricity blackouts among south african households,” *Journal of Commodity Markets*, vol. 11, pp. 37 – 47, 2018.
- [2] M. M. Bah and M. Azam, “Investigating the relationship between electricity consumption and economic growth: Evidence from south africa,” *Renewable and Sustainable Energy Reviews*, vol. 80, pp. 531 – 537, 2017.
- [3] H. Tom, “Eskom: Experts reveal how much money load shedding is costing South Africa - <https://www.thesouthafrican.com/news/eskom-how-much-money-does-load-shedding-cost-south-africa/>,” 2019,. [Online]. Available: <https://www.thesouthafrican.com/news>
- [4] S. Eskom, “Eskom integrated report 31 march 2019.”
- [5] B. B. Ateba, J. J. Prinsloo, and R. Gawlik, “The significance of electricity supply sustainability to industrial growth in south africa,” *Energy Reports*, vol. 5, pp. 1324 – 1338, 2019.
- [6] H. Khobai, “Exploring the nexus of electricity supply and economic growth in south africa,” *International Journal of Energy Economics and Policy*, vol. 7, no. 4, 2017.
- [7] R. de Groot, V. van der Veen, and A. Sebitosi, “Comparing solar pv (photovoltaic) with coal-fired electricity production in the centralized network of south africa,” *Energy*, vol. 55, pp. 823 – 837, 2013.
- [8] A. J. Cohen, M. Brauer, R. Burnett, H. R. Anderson, J. Frostad, K. Estep, K. Balakrishnan, B. Brunekreef, L. Dandona, R. Dandona, V. Feigin, G. Freedman, B. Hubbell, A. Jobling, H. Kan, L. Knibbs, Y. Liu, R. Martin, L. Morawska, C. A. Pope, H. Shin, K. Straif, G. Shaddick, M. Thomas, R. van Dingenen, A. van Donkelaar, T. Vos, C. J. L. Murray, and M. H. Forouzanfar, “Estimates and 25-year trends of the global burden of disease attributable to ambient air pollution: an analysis of data from the global burden of diseases study 2015,” *The Lancet*, vol. 389, no. 10082, pp. 1907 – 1918, 2017.
- [9] A. Sguazzin and L. Ramalepe, “People Are Dying From Eskoms Pollution in South Africa - <https://www.bloomberg.com/news/features/2019-06-27/eskom-is-killing-south-africans-with-its-china-level-pollution/>,” 2019. [Online]. Available: <https://www.bloomberg.com/news/features/2019-06-27/>
- [10] EDF, *SOUTH AFRICA: AN EMISSIONS TRADING CASE STUDY*, Environmental Defense Fund. [Online]. Available: <https://www.edf.org/sites/default/files/south-africa-case-study-may2015.pdf>

- [11] H. L. Wlokas, “The impacts of climate change on food security and health in Southern Africa,” *Journal of Energy in Southern Africa*, vol. 19, pp. 12 – 20, 00 2008.
- [12] M. Noro and R. M. Lazzarin, “Solar cooling between thermal and photovoltaic: An energy and economic comparative study in the Mediterranean conditions,” *Energy*, vol. 73, pp. 453–464, 2014.
- [13] Eskom-Integrated-Demand-Management. (2016, June) Heating, ventilation and air conditioning (hvac) systems: energy-efficient usage and technologies. [Online]. Available: <http://www.eskom.co.za/sites/idm/Documents/AdvisoryServicesHVACSystemBrochure.pdf>
- [14] L. Prez-Lombard, J. Ortiz, and C. Pout, “A review on buildings energy consumption information,” *Energy and Buildings*, vol. 40, no. 3, pp. 394 – 398, 2008.
- [15] D.-B. Kim, D. D. Kim, and T. Kim, “Energy performance assessment of hvac commissioning using long-term monitoring data: A case study of the newly built office building in south korea,” *Energy and Buildings*, vol. 204, p. 109465, 2019.
- [16] M. Santamouris, A. Sfakianaki, and K. Pavlou, “On the efficiency of night ventilation techniques applied to residential buildings,” *Energy and Buildings*, vol. 42, no. 8, pp. 1309 – 1313, 2010.
- [17] M. Santamouris, “Cooling the buildings past, present and future,” *Energy and Buildings*, vol. 128, pp. 617–638, 2016. [Online]. Available: <http://dx.doi.org/10.1016/j.enbuild.2016.07.034>
- [18] D. K. Bhamare, M. K. Rathod, and J. Banerjee, “Passive cooling techniques for building and their applicability in different climatic zones the state of art,” *Energy and Buildings*, vol. 198, pp. 467 – 490, 2019.
- [19] M. Zeyghami, D. Y. Goswami, and E. Stefanakos, “A review of solar thermo-mechanical refrigeration and cooling methods,” *Renewable and Sustainable Energy Reviews*, vol. 51, pp. 1428 – 1445, 2015.
- [20] P. Kohlenbach and U. Jakob, *Solar Cooling: The Earthscan Expert Guide to Solar Cooling Systems*, ser. Earthscan Expert. Taylor & Francis, 2014. [Online]. Available: <https://books.google.co.za/books?id=lb3cAwAAQBAJ>
- [21] T. Ge, R. Wang, Z. Xu, Q. Pan, S. Du, X. Chen, T. Ma, X. Wu, X. Sun, and J. Chen, “Solar heating and cooling: Present and future development,” *Renewable Energy*, pp. –, 2017.
- [22] B. Saleh, “Performance analysis and working fluid selection for ejector refrigeration cycle,” *Applied Thermal Engineering*, vol. 107, 2016.

- [23] P. Gauché, T. W. von Backström, and A. C. Brent, “A concentrating solar power value proposition for South Africa,” *Journal of Energy in Southern Africa*, vol. 24, pp. 00 – 00, 01 2013.
- [24] E. Joubert, S. Hess, and J. V. Niekerk, “Large-scale solar water heating in south africa: Status, barriers and recommendations,” *Renewable Energy*, vol. 97, pp. 809 – 822, 2016.
- [25] T. P. Fluri, “The potential of concentrating solar power in south africa,” *Energy Policy*, vol. 37, no. 12, pp. 5075 – 5080, 2009.
- [26] B. Tashtoush, A. Alshare, and S. Al-Rifai, “Hourly dynamic simulation of solar ejector cooling system using trnsys for jordanian climate,” *Energy Conversion and Management*, vol. 100, pp. 288 – 299, 2015.
- [27] W. Pridasawas, “Solar-driven refrigeration systems with focus on the ejector cycle,” Ph.D. dissertation, KTH Royal Institute of Technology, 2006.
- [28] A. Mwesigye and S. B. Dworkin, “Performance analysis and optimization of an ejector refrigeration system using alternative working fluids under critical and subcritical operation modes,” *Energy Conversion and Management*, vol. 176, pp. 209 – 226, 2018.
- [29] V. Nguyen, S. Riffat, and P. Doherty, “Development of a solar-powered passive ejector cooling system,” *Applied Thermal Engineering*, vol. 21, no. 2, pp. 157 – 168, 2001.
- [30] A. Meyer, T. Harms, and R. Dobson, “Steam jet ejector cooling powered by waste or solar heat,” *Renewable Energy*, vol. 34, no. 1, pp. 297 – 306, 2009.
- [31] R. M. Lazzarin, “Solar cooling: {PV} or thermal? a thermodynamic and economical analysis,” *International Journal of Refrigeration*, vol. 39, pp. 38 – 47, 2014, solar Cooling.
- [32] J. Abdulateef, K. Sopian, M. Alghoul, and M. Sulaiman, “Review on solar-driven ejector refrigeration technologies,” *Renewable and Sustainable Energy Reviews*, vol. 13, no. 6, pp. 1338 – 1349, 2009.
- [33] R. Yen, B. Huang, C. Chen, T. Shiu, C. Cheng, S. Chen, and K. Shestopalov, “Performance optimization for a variable throat ejector in a solar refrigeration system,” *International Journal of Refrigeration*, vol. 36, no. 5, pp. 1512 – 1520, 2013.
- [34] B. Huang, V. Petrenko, I. Samofatov, and N. Shchetinina, “Collector selection for solar ejector cooling system,” *Solar Energy*, vol. 71, no. 4, pp. 269 – 274, 2001.
- [35] M. Dennis, T. Cochrane, and A. Marina, “A prescription for primary nozzle diameters for solar driven ejectors,” *Solar Energy*, vol. 115, no. Supplement C, pp. 405 – 412, 2015.

- [36] C. Pollerberg, A. Heinzl, and E. Weidner, "Model of a solar driven steam jet ejector chiller and investigation of its dynamic operational behaviour," *Solar Energy*, vol. 83, no. 5, pp. 732–742, 2009. [Online]. Available: <http://dx.doi.org/10.1016/j.solener.2008.11.003>
- [37] W. Pridasawas and P. Lundqvist, "A year-round dynamic simulation of a solar-driven ejector refrigeration system with iso-butane as a refrigerant," *International Journal of Refrigeration*, vol. 30, no. 5, pp. 840 – 850, 2007.
- [38] R. Best and W. Rivera, "A review of thermal cooling systems," *Applied Thermal Engineering*, vol. 75, pp. 1162–1175, 2014.
- [39] A. Al-Alili, Y. Hwang, and R. Radermacher, "Review of solar thermal air conditioning technologies," *International Journal of Refrigeration*, vol. 39, pp. 4–22, 2014.
- [40] K. Chunnanond and S. Aphornratana, "Ejectors: applications in refrigeration technology," *Renewable and Sustainable Energy Reviews*, vol. 8, no. 2, pp. 129 – 155, 2004.
- [41] M. Suri, T. Cebecauer, A. J. Meyer, and J. L. van Niekerk, "Accuracy - enhanced solar resource maps of south africa," *Third Southern African Solar Energy Conference*, no. 11 - 13 May, pp. 450–456, 2015.
- [42] S. Wild. (2015, October) Is south africa really the worlds third-best solar location? - <https://mybroadband.co.za/news/energy/141100issouthafricaareallytheworldsthirdbestsolarlocation.html>. Africa Check. [Online]. Available: <https://mybroadband.co.za/news/energy/>
- [43] G. Grazzini, A. Milazzo, and D. Paganini, "Design of an ejector cycle refrigeration system," *Energy Conversion and Management*, vol. 54, no. 1, pp. 38 – 46, 2012.
- [44] R. Yapc and F. Akkurt, "Experimental investigation on ejector cooling system performance at low generator temperatures and a preliminary study on solar energy," *Journal of Mechanical Science and Technology*, vol. 26, no. 11, pp. 3653–3659, 2012.
- [45] Y. Allouche, C. Bouden, and S. Riffat, "A Solar-Driven Ejector Refrigeration System for Mediterranean Climate: Experience Improvement and New Results Performed," *Energy Procedia*, vol. 18, pp. 1115–1124, 2012.
- [46] G. Alexis and E. Karayiannis, "A solar ejector cooling system using refrigerant {R134a} in the athens area," *Renewable Energy*, vol. 30, no. 9, pp. 1457 – 1469, 2005.
- [47] J. Chen, K. Zhu, Y. Huang, Y. Chen, and X. Luo, "Evaluation of the ejector refrigeration system with environmentally friendly working fluids from energy, conventional exergy and advanced exergy perspectives," *Energy Conversion and Management*, vol. 148, pp. 1208 – 1224, 2017.



- [48] Y. A. engel and M. A. Boles, *Thermodynamics: An Engineering Approach*, 5th ed. McGraw-Hill, 2005.
- [49] R. Hoffman. (2017, June) Reducing hvac energy consumption. Consulting - Specifying Engineer Media : <http://www.csemag.com/single-article/reducing-hvac-energy-consumption/668ecedbad7e5798c5b0ab32761ac740.html>.
- [50] S. Suman, M. K. Khan, and M. Pathak, “Performance enhancement of solar collectors a review,” *Renewable and Sustainable Energy Reviews*, vol. 49, pp. 192 – 210, 2015.
- [51] W. Beckman, S. Klein, and J. Duffie, *Solar heating design, by the f-chart method*, ser. A Wiley-Interscience publication. Wiley, 1977. [Online]. Available: <https://books.google.co.za/books?id=mdZSAAAAMAAJ>
- [52] G. Angrisani, E. Entchev, C. Roselli, M. Sasso, F. Tariello, and W. Yaci, “Dynamic simulation of a solar heating and cooling system for an office building located in southern italy,” *Applied Thermal Engineering*, pp. 377–390, 2016.
- [53] SOLAIR. Desiccant cooling systems. [Online]. Available: <http://www.solairproject.eu/146.0.html>
- [54] P. B. Shah, “Review of adsorption refrigeration technologies,” *Institute of Technology, Nirma University, Ahmedabad*, 2011.
- [55] J. Chen, S. Jarall, H. Havtun, and B. Palm, “A review on versatile ejector applications in refrigeration systems,” *Renewable and Sustainable Energy Reviews*, vol. 49, no. Supplement C, pp. 67 – 90, 2015.
- [56] A. Khalil, M. Fatouh, and E. Elgendy, “Ejector design and theoretical study of r134a ejector refrigeration cycle,” *International Journal of Refrigeration*, vol. 34, no. 7, pp. 1684 – 1698, 2011, ejector Technology.
- [57] B. J. Huang, J. M. Chang, C. P. Wang, and V. A. Petrenko, “1-D analysis of ejector performance,” *International Journal of Refrigeration*, vol. 22, no. 5, pp. 354–364, 1999.
- [58] S. Elbel and N. Lawrence, “Review of recent developments in advanced ejector technology,” *International Journal of Refrigeration*, vol. 62, pp. 1–18, 2016.
- [59] S. He, Y. Li, and R. Z. Wang, “Progress of mathematical modeling on ejectors,” *Renewable and Sustainable Energy Reviews*, vol. 13, no. 8, pp. 1760–1780, 2009.
- [60] F. Li, Z. Chang, Q. Tian, C. Wu, and X. Wang, “Performance predictions of dry and wet vapors ejectors over entire operational range,” *Energies*, vol. 10, no. 7, 2017.
- [61] W. Chen, C. Shi, S. Zhang, H. Chen, D. Chong, and J. Yan, “Theoretical analysis of ejector refrigeration system performance under overall modes,” *Applied Energy*, vol. 185,

- no. Part 2, pp. 2074 – 2084, 2017, clean, Efficient and Affordable Energy for a Sustainable Future.
- [62] J. Guo and H. Shen, “Modeling solar-driven ejector refrigeration system offering air conditioning for office buildings,” *Energy and Buildings*, vol. 41, no. 2, pp. 175 – 181, 2009.
- [63] B. Huang, J. Chang, V. Petrenko, and K. Zhuk, “A solar ejector cooling system using refrigerant r141b,” *Solar Energy*, vol. 64, no. 46, pp. 223 – 226, 1998.
- [64] H. Vidal, S. Colle, and G. dos Santos Pereira, “Modelling and hourly simulation of a solar ejector cooling system,” *Applied Thermal Engineering*, vol. 26, no. 7, pp. 663 – 672, 2006.
- [65] Y. Allouche, S. Varga, C. Bouden, and A. C. Oliveira, “Dynamic simulation of an integrated solar-driven ejector based air conditioning system with PCM cold storage,” *Applied Energy*, vol. 190, no. Supplement C, pp. 600–611, 2017.
- [66] J. Chen, H. Havtun, and B. Palm, “Screening of working fluids for the ejector refrigeration system,” *International Journal of Refrigeration*, vol. 47, pp. 1 – 14, 2014.
- [67] J. I. Kroschwitz and A. Seidel, *Kirk-Othmer encyclopedia of chemical technology.*, 5th ed. Hoboken, N.J. SE - 27 volumes : illustrations ; 26 cm: Wiley-Interscience, 2004.
- [68] Y. Xu, N. Jiang, Q. Wang, X. Han, Z. Gao, and G. Chen, “Proposal and thermodynamic analysis of an ejectioncompression refrigeration cycle driven by low-grade heat,” *Energy Conversion and Management*, vol. 145, pp. 343 – 352, 2017.
- [69] H. Vidal and S. Colle, “Simulation and economic optimization of a solar assisted combined ejectorvapor compression cycle for cooling applications,” *Applied Thermal Engineering*, vol. 30, no. 5, pp. 478 – 486, 2010.
- [70] M. Sokolov and D. Hershgal, “Solar-powered compression-enhanced ejector air conditioner,” *Solar Energy*, vol. 51, no. 3, pp. 183 – 194, 1993.
- [71] Y. Dai, J. Wang, and L. Gao, “Exergy analysis, parametric analysis and optimization for a novel combined power and ejector refrigeration cycle,” *Applied Thermal Engineering*, vol. 29, no. 10, pp. 1983 – 1990, 2009.
- [72] SolarGIS, “Solar resource maps and GIS data for 180+ countries,” 2020. [Online]. Available: <https://solargis.com/maps-and-gis-data/download/world>
- [73] D. Banks and J. Schäffler, “The potential contribution of renewable energy in South Africa prepared for,” RAPS Consulting Pty Ltd, Tech. Rep., 2006. [Online]. Available: <http://www.earthlife.org.za/wp-content/uploads/2009/04/potential-of-re-in-sa-feb06.pdf>

- [74] L. Scholtz, K. Muluadzi, K. Kritzinger, and M. Mabaso, “Renewable Energy: Facts and Futures The energy future we want - [https://www.wwf.org.za/our\\_research/publications//?21841/renewable-energy-facts-and-futures](https://www.wwf.org.za/our_research/publications//?21841/renewable-energy-facts-and-futures),” Tech. Rep., 2017.
- [75] First-Green-Consulting. (2017, June) Differentiate between the dni, dhi and ghi? First-Green-Consulting. [Online]. Available: <https://firstgreenconsulting.wordpress.com/2012/04/26/differentiatebetweenthednidhiandghi/>
- [76] R. Meyer, Ed., *CSP and Solar Resource Assessment*. Centre for Renewable and Sustainable Energy Studies University of Stellenbosch, February 2013.
- [77] National Planning Commission, *National Development Plan Our future - make it work*. The Presidency Republic of South Africa, 2011.
- [78] S. Klein and S. Alvarda, “Engineering equation solver (ees),” *F-chart software*, WI, 2007.
- [79] S. Klein, W. Beckman, J. Mitchell, J. Duffie, N. Duffie, T. Freeman, J. Mitchell, J. Braun, B. Evans, J. Kummer *et al.*, “A transient system simulation program,” *Solar Energy Laboratory, University of Wisconsin-Madison, Madison, WI, USA*, 2000.
- [80] W. Chen, M. Liu, D. Chong, J. Yan, A. B. Little, and Y. Bartosiewicz, “A 1D model to predict ejector performance at critical and sub-critical operational regimes,” *International Journal of Refrigeration*, vol. 36, no. 6, pp. 1750–1761, 2013.
- [81] C. Shi, H. Chen, W. Chen, S. Zhang, D. Chong, and J. Yan, “1D Model to Predict Ejector Performance at Critical and Sub-critical Operation in the Refrigeration System,” *Energy Procedia*, vol. 75, pp. 1477–1483, 2015. [Online]. Available: <http://dx.doi.org/10.1016/j.egypro.2015.07.271>
- [82] J. Chen, H. Havtun, and B. Palm, “Parametric analysis of ejector working characteristics in the refrigeration system,” *Applied Thermal Engineering*, vol. 69, no. 1, pp. 130 – 142, 2014.
- [83] F. Li, Q. Tian, C. Wu, X. Wang, and J.-M. Lee, “Ejector performance prediction at critical and subcritical operational modes,” *Applied Thermal Engineering*, vol. 115, no. Supplement C, pp. 444 – 454, 2017.
- [84] E. Bellos and C. Tzivanidis, “Optimum design of a solar ejector refrigeration system for various operating scenarios,” *Energy Conversion and Management*, vol. 154, no. Supplement C, pp. 11 – 24, 2017.
- [85] J. Duffie and W. Beckman, *Solar Engineering of Thermal Processes*. Wiley, 2013. [Online]. Available: <https://books.google.co.za/books?id=5uDdUfMgXYQC>

# APPENDICES

## Appendix A - Collector Slope Optimization

### Appendix A1 - Uppington Collector Performance Study

To maximize the amount of heat collected from solar radiation across the collectors, an optimal collector slope has to be determined. This slope is determined by observing the variation of useful heat gain  $\dot{Q}_u$  across the collector at various solar collector slope angles.

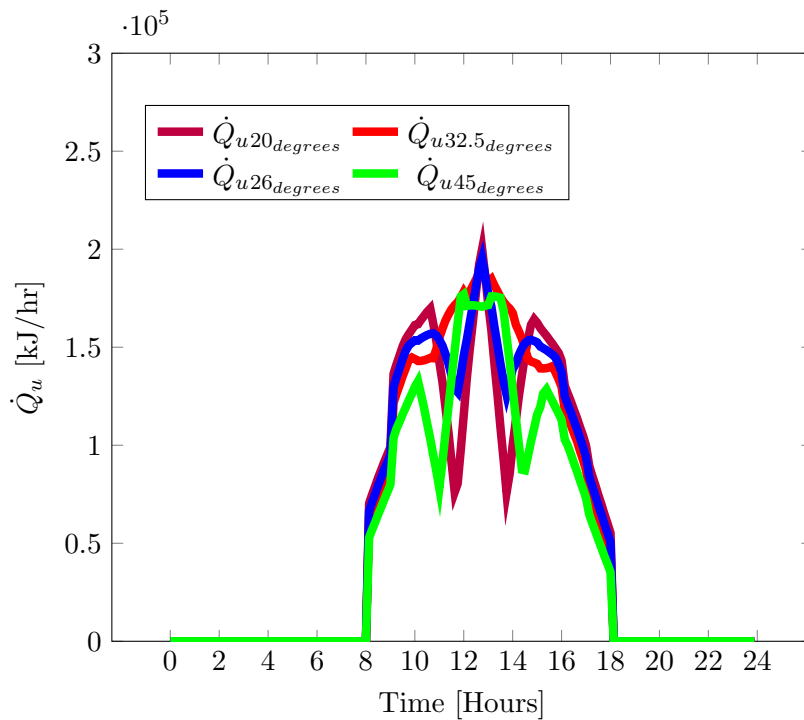


Figure 111: Uppington optimal collector slope angle

From [Figure 111](#), it can be noted that four slope angles are considered. The general behavior of the collectors indicate that most configurations experience a sudden drop in of  $\dot{Q}_u$  during late morning and mid afternoon hours. Optimization is undertaken to find an angle that will minimize the magnitude of the sudden drop in  $\dot{Q}_u$  and hence maximize the amount of heat collected. From the information presented in [Figure 111](#), it is noted that the 32.5 °angle minimizes the drop in  $\dot{Q}_u$  whilst achieving reasonably high values throughout operation.

## Appendix A2 - Durban Optimal Solar Collector Slope Optimization

An optimal collector slope investigation is carried out to maximize the magnitude of useful collector heat gain, under Durban solar conditions, as presented in [Figure 112](#). The four considered collector angles are between 18 °and 45 °. The results show a common trend of rapid decrease in useful heat gain in late morning and early afternoon values especially for the 18 °and 45 °. However, this does not occur for at the 30 °and 36 °angles. Between these two angles, the 36 °slope is considered to be more superior since it maintains high  $\dot{Q}_u$  values between 12:00 and 13:00, which is critical for maintaining high  $T_g$  values required at high  $T_{am}$  values.

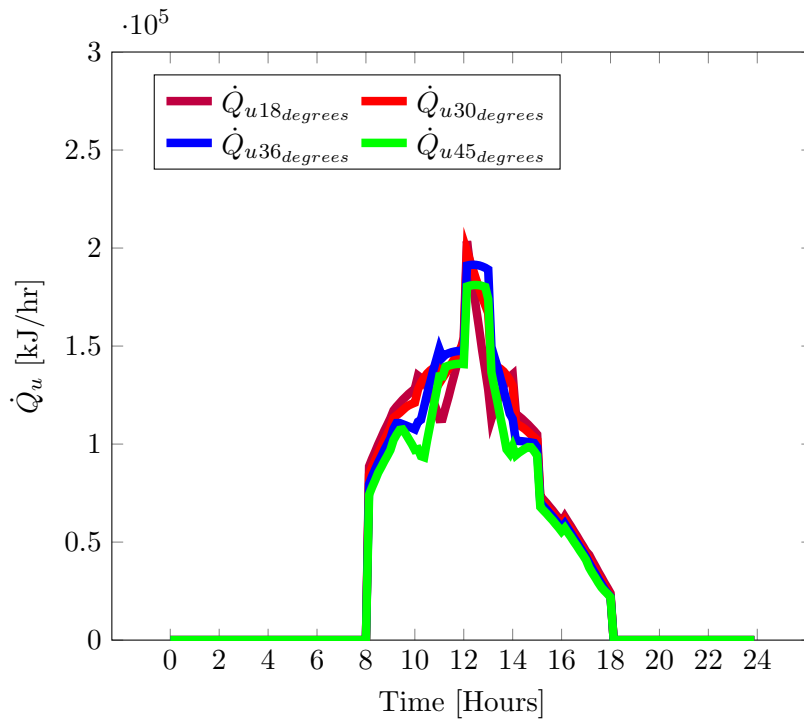


Figure 112: Durban optimal collector slope angle

## Appendix A3 - Cape Town Optimal Solar Collector Slope Optimization

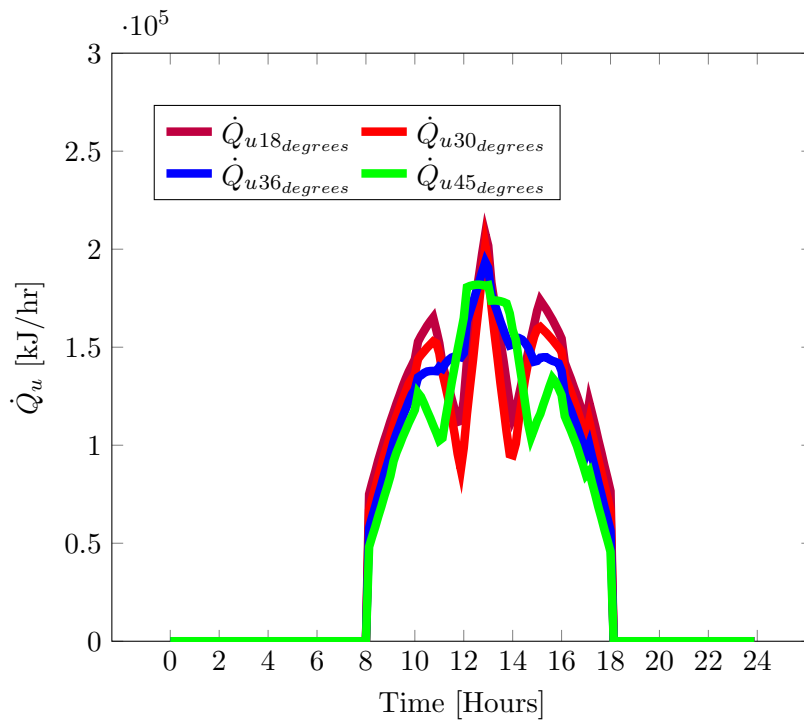


Figure 113: Cape Town optimal collector slope angle

A collector slope optimization investigation (presented in [Figure 113](#)) is carried out under Cape Town solar and weather data to determine the optimal slope for achieving high  $\dot{Q}_u$  values. The results indicate a common trend of sudden decline in  $\dot{Q}_u$  values during late morning and early afternoon hours which motivates the need to find the collector slope angle which will minimize the occurrence of these surges. From the presented results it is evident that the 36 °slope achieves optimal performance.

## Appendix A4 - Bloemfontein Solar Collector Slope Optimization

The optimum angle of inclination of the solar collectors is obtained from a parametric analysis study of different collector slope angles as shown in [Figure 114](#). The results show that the peak  $\dot{Q}_u$  values decrease as the collector slope increases. However, high peak values of the system also occur with significantly high thermal energy losses as the day progresses. The 10 °slope system achieves the highest useful heat gain with values of  $2.95 \times 10^5$  kJ/hr. This system also experiences a sharp decline in useful heat gain values with the lowest values being  $1.5 \times 10^5$  kJ/hr occurring at 11:00 and 13:00. Similar performance also occurs at the 20 °slope whereby a peak value of  $2.6 \times 10^5$  kJ/hr occurs at 13:00 with the lowest values ( $0.5 \times 10^5$  kJ/hr) being experienced at 11:00 and 13:00. Optimal performance is experienced at the collector slope of 33 °with the peak ( $2.5 \times 10^5$  kJ/hr) occurring at 13:00. Under this slope, there is minimal decline in useful heat gain unlike all the other systems being considered. At 45 °, the system experiences the lowest peak of  $2.25 \times 10^5$  kJ/hr between 12:00 and 14:00. The troughs are shifted to 10:30 and 14:00 with the common value being  $0.58 \times 10^5$  kJ/hr.

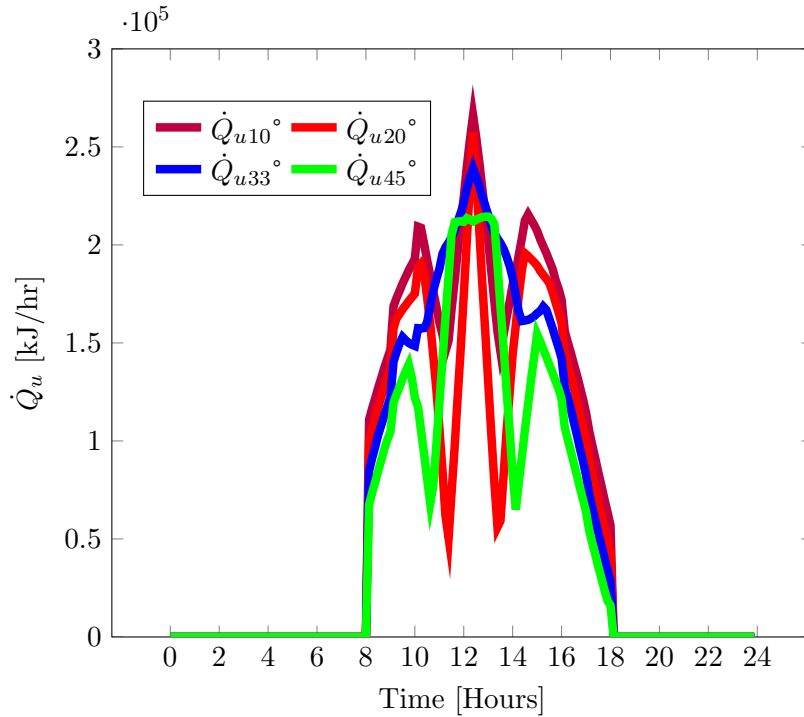


Figure 114: Bloemfontein optimal collector slope angle

From [Figure 114](#), it is clear that the optimal collector slope is 33 °.

## Appendix A5 -Johannesburg Solar Collector Slope Optimization

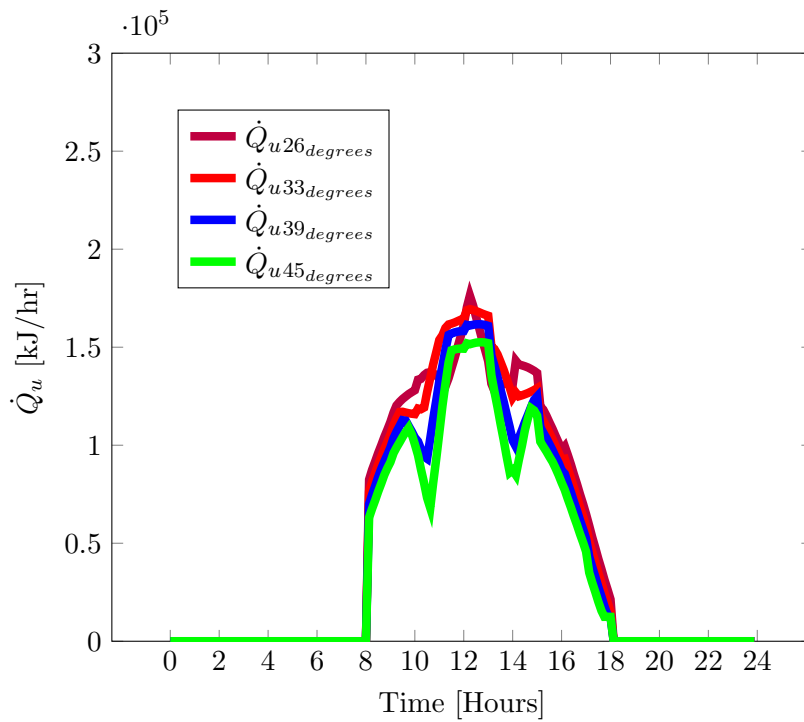


Figure 115: Johannesburg optimal collector slope angle

To ensure high  $\eta_{coll}$  values which will result in high  $COP_{overall}$  values, a collector slope optimization exercise is carried out as shown in [Figure 115](#). From the considered collector slope angles, the 33 °slope is found to be optimal as it does not experience any severe surges in  $\dot{Q}_u$  which occurs in the other slope angles.



## Appendix B - The EES MODEL

```

1: $UnitSystem SI K kPa mass
2: "!"
3: Updates from the previous model::: Include Pump Work in COP evaluation
4: "
5: " This works for the data in the parametric tables
6: Runs : 70-90(10)
7: 100(11.25) - 100(15)
8: "
9:
10:
11: "=====
12: START OF PROCEDURES
13: ====="
14: Procedure subcritical(v_sx,P_c,P_cc,m_p,m_s,P_so,s_p1,v_p1,h_p1,h_so,eta_d,phi_mb:u,P_cb, P_msub,rho_msub
,P_3sub,rho_3sub)
15: "For Exergy calculation: I require the condenser exit T,P,S,h;
16: "
17: If (P_c <= P_cc) Then "If the operating condenser pressure (Pc) is less than the Pcc (critical condenser pressure) ,then we
are in the critical regime of the ejector"
18: u = m_s/m_p " meaning that we are in the critical region"
19: P_cb = 1
20: P_msub = 1
21: rho_msub = 1
22: P_3sub = 1
23: rho_3sub = 1
24: Else
25: P_px = P_so "we are in the subcritical regime, the back pressure is too high and the ejector has to adjust the flow to match
the back pressure"
26: s_px = s_p1
27: h_px = enthalpy(R1234ze(Z),P = P_px, s = s_px)
28: v_px = sqrt(2 * ((h_p1*convert(kJ/kg,m^2/s^2) + ((v_p1)^2)/2)) -h_px*convert(kJ/kg,m^2/s^2) ))
29: m_sx = (10^(-6)) [kg/s] "The mass flow rate of the entrained flow at the break down point"
30: "v_sx = (10^(-6)) [m/s]"
31: h_sx = h_so - (((v_sx)^2)/2)*convert(m^2/s^2,kJ/kg)
32: v_msub = (phi_mb*(m_p * v_px + m_s * v_sx))/(m_p + m_s)
33: h_m = (m_p*(h_px + ((v_px ^2)/2)*convert(m^2/s^2,kJ/kg) )+ m_s * ( h_sx + ((( v_sx )^2)/2)*convert(m^2/s^2 , kJ/kg) ) )
/(m_s + m_p ) - (((v_msub)^2)/2)*convert(m^2/s^2, kJ/kg)
34: P_msub = P_px
35: rho_msub = density(R1234ze(Z), P = P_msub , h = h_m)
36: Call shockvalue(P_msub,rho_msub,v_msub,h_m:P_3sub,h_3sub,v_3sub,s_3sub,rho_3sub)
37: h_cb = h_3sub + (((v_3sub)^2)/2)*convert(m^2/s^2,kJ/kg) "break down enthalpy"
38: h_cs = h_3sub + eta_d*(h_cb - h_3sub)
39: P_cb = pressure(R1234ze(Z), h = h_cb, s = s_3sub) "break down pressure"
40:
41: If (P_c <= P_cb) Then
42:
43: u = (m_s / m_p)*((P_cb - P_c)/(P_cb - P_cc)) "this means that the EJECTOR exit temperature and pressure are equal to
what is set on the condenser"
44: "P_c does not change, the properties remain constant. "
45:
46: Else
47: u = 0
48: Endif
49:
50: Endif
51:
52:
53: End
54:
55: "(P_co;P_cc;T_cc;T_co:s_5;h_5;sdsdsdsdsdsddd sdsdsdsds;h_5.sdsdsds;P_5:ssdsdsds;T_5) "
56: Procedure ejectorexitergy(P_co,P_cc,T_cc,T_co:s_ejector_exit,h_ejector_exit,P_ejector_exit,T_ejector_exit)

```

```

57: T_ck = converttemp(C,K,T_cc)
58: T_cok = converttemp(C,K,T_co)
59: If (P_co <= P_cc) Then
60: "This is when the specified condenser pressure is
61: less than the critical condenser pressure"
62: "This means that the ejector is in critical mode
63: and hence use Tcc values for evaluating exergy
64: "
65: P_ejector_exit = P_cc
66: T_ejector_exit = Tck
67: s_ejector_exit = entropy(R1234ze(Z),T = T_ck, x = 1) "This is applicable in the critical regime"
68: h_ejector_exit = enthalpy(R1234ze(Z),T = T_ck, x = 1) "This is applicable in the critical regime"
69: Else "this is the case when the condenser pressure is greater than the tcc pressure"
70: P_ejector_exit = P_co
71: s_ejector_exit = entropy(R1234ze(Z),T = T_cok, x = 1) "This is applicable in the subcritical section"
72: h_ejector_exit = enthalpy(R1234ze(Z),T = T_cok, x = 1) "This is applicable in the subcritical section"
73: T_ejector_exit = T_cok
74: Endif
75: End
76:
77: Procedure chokedvelocity(P_t,rho_t:a)
78: rho_v=density(R1234ze(Z),P=P_t,x=1) "Density at the saturated vapour point"
79: rho_l=density(R1234ze(Z),P=P_t,x=0) "Density at the saturated liquid point"
80: If (rho_t >= rho_v) Then
81: a_v=soundspeed(R1234ze(Z),x=1,P=P_t)
82: a_l = soundspeed(R1234ze(Z),x=0,P=P_t)
83: alpha = (rho_t - rho_l)/(rho_v - rho_l)
84: a = sqrt((1/rho_t)*((alpha/(rho_v * (a_v)^2))+((1-alpha)/(rho_l *(a_l)^2))))
85: Else
86: a = soundspeed(R1234ze(Z),v=1/rho_t,P=P_t)
87: Endif
88: End
89:
90: Procedure nozzleexit(s_t,h_t,m_t,A_p1,P_t,v_t:h_p1,v_p1,S_p1,P_p1)
91: S_p1 = s_t
92: P_p1 = 0.5*P_t "initial assumption of the exit pressure"
93: "At T-g 92,5 C, P_p1 = 97,38 kPa whilst p_t = 677,8 kPa"
94: Repeat
95: P_p1 = P_p1 - 0.0001*P_p1
96: rho_p1 = density(R1234ze(Z),P = P_p1, s = S_p1)
97: h_p1 = enthalpy(R1234ze(Z),P = P_p1, s = S_p1)
98: v_p1 = m_t / (rho_p1 * A_p1)
99: h_p1_prime = h_t + (((v_t)^2)/2)*convert(m^2/s^2,kJ/kg) - (((v_p1)^2)/2)*convert(m^2/s^2,kJ/kg)
100: Until abs(h_p1 - h_p1_prime)<=0.01
101: End
102:
103: Procedure pressurethroat(T_p,P_p,eta_t,A_t:m_p,h_t,P_t,s_t,v_t)
104: S_po = entropy(R1234ze(Z),T= T_p,x=1) "I have to take it at the saturated vapour point"
105: h_po = enthalpy(R1234ze(Z),T = T_p,x=1)
106: P_t=0.7*P_p "Initial guess value of P_t is P_p"
107: "At T-g 92,5 C, P_p = 1145 kPa whilst p_t = 677,8 kPa"
108: Repeat
109: P_t = P_t - 0.0001*P_t
110: h_ts = enthalpy(R1234ze(Z),s = S_po,p = P_t)
111: h_t = h_po - eta_t * (h_po - h_ts)
112: rho_t = density(R1234ze(Z),p =P_t,h= h_t)
113: s_t = entropy(R1234ze(Z),p = P_t,h = h_t)
114: Call chokedvelocity(P_t,rho_t:V_t)
115: h_t_prime = h_po - (((V_t)^2)/2)*convert(m^2/s^2,kJ/kg)
116:

```

```

117: Until abs(h_t - h_t_prime)<=0.01
118: rho_t = density(R1234ze(Z),p =P_t,h= h_t)
119: m_p = rho_t*A_t*V_t
120: End
121:
122: Procedure entrainedstream(T_so,P_so,eta_s: P_sy,v_sy,rho_sy,h_sy,h_so)
123: s_so = entropy(R1234ze(Z),T = T_so,x = 1) "At the saturated vapour point"
124: h_so = enthalpy(R1234ze(Z),T = T_so,x = 1) "At the saturated vapour point"
125: P_sy = P_so "This value has to be assumed, and the highest value that it will ever be is the evaporator pressure"
126: Repeat
127: P_sy = P_sy - P_sy*(0.00001)
128: h_sys = enthalpy(R1234ze(Z), P = P_sy,s = s_so)
129: h_sy = h_so - eta_s*(h_so - h_sys)
130: rho_sy = density(R1234ze(Z), P = P_sy,h = h_sy)
131: s_sy = entropy(R1234ze(Z), P = P_sy,h = h_sy)
132: Call chokedvelocity(P_sy,rho_sy:v_sy)
133: h_sy_prime = h_so - (((v_sy)^2)/2)*convert(m^2/s^2,kJ/kg)
134: Until (abs(h_sy - h_sy_prime )<=5.5)
135: End
136:
137: Procedure shockvalue(P_m,rho_m,v_m,h_m:P_3,h_3,v_3,s_3,rho_3)
138: "assume rho_3 The density after the shock"
139: rho_3 = rho_m*1.1 "Initiating the pressure increase" ! The multiplier has to be reduced for subcritical conditions: Use *1,001"
140: Repeat
141: P_3 = P_m + ((rho_3 - rho_m)*(rho_m/rho_3)*(v_m)^2*(convert(kg/(m s^2),kPa))) ! There has been an error with this equation as it was written in Figure 6"
142: h_3 = enthalpy(R1234ze(Z), P= P_3, v =1/ rho_3) !The inverse of density is the specific volume"
143: s_3 = entropy(R1234ze(Z), P = P_3,v =1/ rho_3)
144: h_3_prime = h_m + ((P_3 - P_m)/2)* (((rho_m + rho_3))/(rho_m*rho_3))*convert(kPa/(kg/m^3) , kJ/kg)
145: rho_3 = rho_3 + 0.0001*rho_3
146: Until abs(h_3- h_3_prime)<0.01
147: v_3 = sqrt(2*(h_m*convert(kJ/kg,m^2/s^2)+ (((v_m)^2)/2) - h_3*convert(kJ/kg,m^2/s^2)))
148: End
149:
150:
151: !=====
152: =====Begin HERE=====
153: =====
154: ! 
155: Exergy reference state
156: "
157: T_oc = 25 [C]
158: P_o = 101.32 [kPa]
159: T_o = converttemp(C,K,T_oc)
160: h_o = enthalpy(R1234ze(Z),T = T_o,P =P_o)
161: "h_o = 236,09 [kJ/kg] ! Setting this as the reference"
162: s_o = entropy(R1234ze(Z),T = T_o,P =P_o)
163: h_ow = enthalpy(Water,T = T_o,P =P_o)
164: s_ow = entropy(Water,T = T_o,P =P_o)
165: "=====
Ejector Geometry =====
166: =====
167: "Geometry: 1-A "
168: "$ifnot parametric table"
169: D_t = 4.515[mm]
170: "$endif"
171: "$ifnot parametric table"
172: D_1 = 7.8 [mm]
173: "$endif"

```

```

174: "$ifnot parametric table"
175: D_3 = 12.155 [mm]
176: "$endif"
177: A_p1 = ((D_1*convert(mm,m)/ 2)^2)*pi
178: A_3 = ((D_3*convert(mm,m)/ 2)^2)*pi
179: A_t = ((D_t*convert(mm,m)/ 2)^2)*pi
180: EAR = ((D_3*convert(mm,m)/ 2)^2)/((D_t*convert(mm,m)/ 2)^2)
181: A_rt = A_p1/A_t
182: "=====
183: ===== Operating Conditions =====
184: ====="
185: "!"
186: Secondary Stream Properties
187: "
188: "Generator"
189: $ifnot parametric table
190: T_10 = 105 [C]
191: $endif
192:
193: $ifnot parametric table
194: m_dot_10 = 1000 [kg/s] "This is tank to load flow rate"
195: $endif
196:
197: T_10_k = converttemp(C,K,T_10)
198: s_10 = entropy(R1234ze(Z), T = T_10_k, P = P_o) "Entropy at generator exit"
199: h_10 = enthalpy(R1234ze(Z), T = T_10_k, P = P_o) "Enthalpy at generator exit"
200: h_P_10_T_o = enthalpy(R1234ze(Z), P = P_po, T = T_10_k)
201: s_P_10_T_o = entropy(R1234ze(Z), P = P_po, T = T_10_k)
202: e_10T = (h_10 - h_P_10_T_o) - T_o*(s_11 - S_P_10_T_o)
203: e_10M = (h_P_10_T_o - h_ow) - T_o*(S_P_10_T_o - s_ow)
204: e_10 = e_10T + e_10M
205: $ifnot parametric table
206: T_11 = 100 [C]
207: $endif
208: T_11_k = converttemp(C,K,T_11)
209: s_11 = entropy(R1234ze(Z), T = T_11_k, P = P_o) "Entropy at generator exit"
210: h_11 = enthalpy(R1234ze(Z), T = T_11_k, P = P_o) "Enthalpy at generator exit"
211: h_P_11_T_o = enthalpy(R1234ze(Z), P = P_po, T = T_11_k)
212: s_P_11_T_o = entropy(R1234ze(Z), P = P_po, T = T_11_k)
213: e_11T = (h_11 - h_P_11_T_o) - T_o*(s_11 - S_P_11_T_o)
214: e_11M = (h_P_11_T_o - h_ow) - T_o*(S_P_11_T_o - s_ow)
215: e_11 = e_11T + e_11M
216: "Condenser"
217: $ifnot parametric table
218: T_13 = 20 [C] "This can be set to the ambient temperature"
219: $endif
220: T_13_k = converttemp(C,K,T_13)
221: s_13 = entropy(R1234ze(Z), T = T_13_k, P = P_o) "Entropy at generator exit"
222: h_13 = enthalpy(R1234ze(Z), T = T_13_k, P = P_o) "Enthalpy at generator exit"
223: h_P_13_T_o = enthalpy(R1234ze(Z), P = P_po, T = T_13_k)
224: s_P_13_T_o = entropy(R1234ze(Z), P = P_po, T = T_13_k)
225: e_13T = (h_13 - h_P_13_T_o) - T_o*(s_13 - S_P_13_T_o)
226: e_13M = (h_P_13_T_o - h_ow) - T_o*(S_P_13_T_o - s_ow)
227: e_13 = e_13T + e_13M
228: $ifnot parametric table
229: T_12 = 27 [C]
230: $endif
231: T_12_k = converttemp(C,K,T_12)
232: s_12 = entropy(R1234ze(Z), T = T_12_k, P = P_o) "Entropy at generator exit"
233: h_12 = enthalpy(R1234ze(Z), T = T_12_k, P = P_o) "Enthalpy at generator exit"

```

```

234: h_P_12_T_o = enthalpy(R1234ze(Z), P = P_po, T = T_12_k)
235: s_P_12_T_o = entropy(R1234ze(Z), P = P_po, T = T_12_k)
236: e_12T = (h_12 - h_P_12_T_o) - T_o*(s_12 - S_P_12_T_o)
237: e_12M = (h_P_12_T_o - h_ow) - T_o*(S_P_12_T_o - s_ow)
238: e_12 = e_12T + e_12M
239: "Evaporator"
240: $ifnot parametric table
241: T_14 = 15 [C]
242: $endif
243: T_14_k = converttemp(C,K,T_14)
244: s_14 = entropy(R1234ze(Z), T = T_14_k, P = P_o) "Entropy at generator exit"
245: h_14 = enthalpy(R1234ze(Z), T = T_14_k, P = P_o) "Enthalpy at generator exit"
246: h_P_14_T_o = enthalpy(R1234ze(Z), P = P_po, T = T_14_k)
247: s_P_14_T_o = entropy(R1234ze(Z), P = P_po, T = T_14_k)
248: e_14T = (h_14 - h_P_14_T_o) - T_o*(s_14 - S_P_14_T_o)
249: e_14M = (h_P_14_T_o - h_ow) - T_o*(S_P_14_T_o - s_ow)
250: e_14 = e_14T + e_14M
251:
252: $ifnot parametric table
253: T_15 = 10 [C]
254: $endif
255: T_15_k = converttemp(C,K,T_15)
256: s_15 = entropy(R1234ze(Z), T = T_15_k, P = P_o) "Entropy at generator exit"
257: h_15 = enthalpy(R1234ze(Z), T = T_15_k, P = P_o) "Enthalpy at generator exit"
258: h_P_15_T_o = enthalpy(R1234ze(Z), P = P_po, T = T_15_k)
259: s_P_15_T_o = entropy(R1234ze(Z), P = P_po, T = T_15_k)
260: e_15T = (h_15 - h_P_15_T_o) - T_o*(s_15 - S_P_15_T_o)
261: e_15M = (h_P_15_T_o - h_ow) - T_o*(S_P_15_T_o - s_ow)
262: e_15 = e_15T + e_15M
263:
264: "Generator"
265: $ifnot parametric table
266: T_poc = 83 [C]
267: $endif
268: T_po = converttemp(C,K,T_poc)
269: P_po = pressure(R1234ze(Z), T = T_po, x = 1)
270: s_4 = entropy(R1234ze(Z), T = T_po, x = 1) "Entropy at generator exit"
271: h_4 = enthalpy(R1234ze(Z), T = T_po, x = 1) "Enthalpy at generator exit"
272: h_P_4_T_o = enthalpy(R1234ze(Z), P = P_po, T = T_o)
273: S_P_4_T_o = entropy(R1234ze(Z), P = P_po, T = T_o)
274: e_4T = (h_4 - h_P_4_T_o) - T_o*(s_4 - S_P_4_T_o)
275: e_4M = (h_P_4_T_o - h_o) - T_o*(S_P_4_T_o - s_o)
276: e_4 = e_4T + e_4M
277: "Evaporator"
278: $ifnot parametric table
279: T_soc = 8[C]
280: $endif
281: T_so = converttemp(C,K,T_soc)
282: P_so = pressure(R1234ze(Z), T = T_so, x = 1)
283: s_9 = entropy(R1234ze(Z), T = T_so, x = 1) "Entropy at evaporator Inlet"
284: h_9 = enthalpy(R1234ze(Z), T = T_so, x = 1) "Enthalpy at evaporator Inlet"
285: h_P_9_T_o = enthalpy(R1234ze(Z), P = P_so, T = T_o)
286: S_P_9_T_o = entropy(R1234ze(Z), P = P_so, T = T_o)
287: e_9T = (h_9 - h_P_9_T_o) - T_o*(s_9 - S_P_9_T_o)
288: e_9M = (h_P_9_T_o - h_o) - T_o*(S_P_9_T_o - s_o)
289: e_9 = e_9T + e_9M
290:
291: "Condenser"
292: $ifnot parametric table
293: T_co = 35 [C]

```

```

294: $endif
295: T_c = converttemp(C,K,T_co)
296: P_c = pressure(R1234ze(Z),T = T_c, x = 1)
297: "The exit conditions of the condenser do not change and the flow properties are evaluated based on the specified value."
298: "Exit conditions of the condenser"
299:
300:
301: "$ifnot parametric table"
302: v_sx = (10^(-2)) [m/s]
303: "$endif"
304:
305:
306: "=====
307: ===== Efficiency Values =====
308: ====="
309: "
310: Efficiency values are to be based on Aggrey's Work
311: "
312: "!"
313: A parametric analysis of R will be done on the parametric table.
314: "
315:
316: "!"
317: Evaluation of R value and k:
318: "
319: cp=cp(R1234ze(Z),T=T_po,P=P_po-0.0009[kPa]) "! -0,0009[kPa] has been included to ensure that I am not evaluating any of the properties at the saturation point. This condition ensures that I am in the superheated region"
320: cv =cv(R1234ze(Z),T=T_po,P=P_po-0.0009[kPa])
321:
322: k = cp/cv "This is how I evaluate the specific heat constant"
323:
324: R_ref = Cp - Cv "This is how I calculate the refrigerant's gas constant"
325:
326: cp_air = cp(Air,T=T_po)
327: cv_air = cv(Air,T=T_po)
328: R_air = cp_air-cv_air "This is how I calculate air's gas constant"
329: "$ifnot parametric table"
330: R = (R_ref/R_air) "This is the dimensionless R value"
331: "$endif"
332: "!"
333: The importance of R is that it determines the magnitude of eta_m which eventually controls the entrained mass flowrate!!!!
334: A high R reduces the entrained mass flowrate.
335: "
336:
337: "eta_m = 1,139 + 0,01768*(EAR) - 0,02*(Pr) - 1,08*R"
338: $ifnot parametric table
339: eta_m = 0.2233 "1,139 + 0,01768*(EAR) - 0,009797*(Pr) - 1,08*R" "Primary fluid expansion from motive nozzle::::: phi p"
340: $endif
341:
342:
343: "$ifnot parametric table"
344: eta_s = 0.85 [-] "Secondary flow expansion"
345: "$endif"
346:
347: "$ifnot parametric table"
348: eta_t = 0.95 "Primary flow expansion"
349: "$endif"
350:

```

```

351: eta_d = 1 [-] "I am changing this to 0,95 so that I can reduce Tcc values" "! Reducing the diffuser efficiency is very helpful with reducing Tcc and the COP"
352: Pr = (P_po / P_so)
353:
354: "! Mixing Efficiency"
355: "
356: phi_m = 0,8264 - 0,01254*(EAR) + 0,015*(Pr) + 0,4589*0,1*R
357:
358: "
359: $ifnot parametric table
360: phi_m = 0.889 "0,8264 - 0,01254*(EAR) + 0,005804*(Pr) + 0,4589*R" "Mixing Efficiency"
361: $endif
362:
363: $ifnot parametric table
364: phi_mb = 0.889 "0,8802 - 0,09203*(EAR/A_rt)+0,00158*(Pr)^k" "Break Down Mixing Efficiency"
365: $endif
366: "!=====
367: ===== Primary Nozzle =====
368: ====="
369: Call pressurethroat(T_po,P_po,eta_t,A_t:m_p,h_t,P_t,s_t,v_t)
370: Call nozzleexit(s_t,h_t,m_p,A_p1,P_t,v_t:h_p1,v_p1,S_p1,P_p1)
371:
372: "!=====
373: ===== Secondary Stream =====
374: ====="
375:
376: Call entrainedstream(T_so,P_so,eta_s: P_sy,v_sy,rho_sy,h_sy,h_so)
377:
378: "!=====
379: =====MOTIVE Flow Conditions at section Y=====
380: ====="
381:
382: S_py = S_p1 "at section Y, the entropy of the motive flow is equal to the nozzle exit entropy"
383: P_py = P_sy "at section Y, the pressure of the primary flow is equal to that of the etraind flow"
384: P_m = P_sy
385: rho_py = density(R1234ze(Z), P = P_py, s = S_py)
386: h_pys = enthalpy(R1234ze(Z), P = P_py, s = S_py)
387: h_py = h_p1 - eta_m * (h_p1 - h_pys)
388: v_py = sqrt(2 * ((h_p1*convert(kJ/kg,m^2/s^2) + (((v_p1)^2)/2)) - h_py*convert(kJ/kg,m^2/s^2) ))
389:
390: A_py = (m_p)/(rho_py * v_py)
391: A_sy = A_3 - A_py
392: m_s = rho_sy*A_sy*v_sy
393:
394: m_p * (h_py + (((v_py)^2)/2)*convert(m^2/s^2,kJ/kg) ) + m_s*(h_sy + (((v_sy)^2)/2)*convert(m^2/s^2,kJ/kg) ) = (m_p + m_s)
*(h_m + ((v_m ^2)/2)*convert(m^2/s^2,kJ/kg) )
395:
396: phi_m * (m_p* v_py + m_s*v_sy) = (m_p + m_s) * v_m
397:
398: rho_m = density(R1234ze(Z), p = P_m, h = h_m)
399:
400: Call shockvalue (P_m,rho_m,v_m,h_m:P_3,h_3,v_3,s_3,rho_3)
401:
402: "!=====
403: ===== DIFFUSER CONDITIONS =====
404: =====
405: "
406: h_cc = h_3 + (((v_3)^2)/2)*convert(m^2/s^2,kJ/kg)
407: h_cs = h_3 + eta_d * (h_cc - h_3)
408: P_cc = pressure(R1234ze(Z), h = h_cs, s = s_3)

```



```

409: T_cc = converttemp(K,C,temperature(R1234ze(Z),P = P_cc, x =1))
410: "Escaping from the fixed Tcc Point, the above Tcc is actually lower than it should"
411: "T_cc_unfixed = converttemp(K;C;temperature(R1234ze(Z);P = P_cc; s =s_3))"
412:
413: "Actual Ejector Exit Performance Values"
414:
415:
416: "!"
417: Entrainment Ratio
418: "
419: Call subcritical(v_sx,P_c,P_cc,m_p,m_s,P_so,s_p1,v_p1,h_p1,h_so,eta_d,phi_mb:u,P_cb, P_msub,rho_msub,P_3sub
,rho_3sub)
420: "!" =====
421: =====Performance Ratios =====
422: ====="
423:
424:
425: "Throat Pressure Ratio"
426: TPR = P_t/P_po
427: "Nozzle Exit Pressure Ratio"
428: NEPR = P_p1/P_t
429: "Entrained Flow Pressure Ratio"
430: EFPR = P_sy/P_so
431: "Shock Density Ratios"
432: SDR = rho_3/ rho_m
433:
434: "Pressure Lift"
435:
436: PLR = P_po/ P_so
437:
438: "!" =====
439: =====Conditions at condenser Inlet / Ejector Exit =====
440: ====="
441: " Ejector Exit Exergy / Condenser Inlet"
442: " This decides whether the ejector exit conditions are at critical condition (Tcc, Pcc) or sub critical (T_co or P_co) "
443: Call ejectorexiteergy(P_c,P_cc,T_cc,T_co:s_5,h_5,P_5,T_5)
444:
445: "!" =====
446: " Ejector Exit Exergy / Condenser Inlet Calculations"
447: "!" =====
448: h_P_5_To = enthalpy(R1234ze(Z),P = P_5,T =T_o) "!constant pressure"
449: s_P_5_To = entropy(R1234ze(Z),P = P_5,T =T_o) "!constant pressure"
450: e_5T = (h_5 - h_P_5_To) - T_o*(s_5 - s_P_5_To)
451: e_5M = (h_P_5_To - h_o) - T_o*(s_P_5_To - s_o)
452: e_5 = e_5T + e_5M
453: "!" =====
454:
455: "!" =====
456: "Condenser Exit / Pump Inlet / Evaporator /Throttle Valve Inlet / Calculations"
457: "!" =====
458: h_6 = enthalpy(R1234ze(Z),P = P_5, x = 0)
459: s_6 = entropy(R1234ze(Z),P = P_5, x = 0)
460: h_P_6_To = enthalpy(R1234ze(Z),P = P_5,T =T_o) "!constant pressure"
461: s_P_6_To = entropy(R1234ze(Z),P = P_5,T =T_o) "!constant pressure"
462: e_6T = (h_6 - h_P_6_To) - T_o*(s_6 - s_P_6_To)
463: e_6M = (h_P_6_To - h_o) - T_o*(s_P_6_To - s_o)
464: e_6 = e_6T + e_6M
465: "!" =====
466: "Evaporator Inlet Calculations"
467: "!" =====

```

```

468: h_8 = h_6
469: s_8 = entropy(R1234ze(Z),P = P_so, h = h_8)
470: h_P_8_To = enthalpy(R1234ze(Z),P = P_so,T=T_o) "!constant pressure"
471: s_P_8_To = entropy(R1234ze(Z),P = P_so,T=T_o) "!constant pressure"
472: e_8T = (h_8 - h_P_8_To) - T_o*(s_8 - s_P_8_To)
473: e_8M = (h_P_8_To - h_o) - T_o*(s_P_8_To - s_o)
474: e_8 = e_8T + e_8M
475: "! ====="
476: "Pump Exit / Generator Inlet" "Taken from An exergy analysis of a solar-driven ejector refrigeration system"
477: "! ====="
478: W_pump_in = 0.16 [kW]
479: W_pump_in = m_p * (h_7 - h_6) "Pump exit enthalpy"
480: s_7 = entropy(R1234ze(Z),h = h_7, P =P_po)
481: T_7 = temperature(R1234ze(Z),h = h_7, P =P_po)
482:
483: h_P_7_To = enthalpy(R1234ze(Z),P = P_po,T=T_o) "!constant pressure"
484: s_P_7_To = entropy(R1234ze(Z),P = P_po,T=T_o) "!constant pressure"
485: e_7T = (h_7 - h_P_7_To) - T_o*(s_6 - s_P_6_To)
486: e_7M = (h_P_7_To - h_o) - T_o*(s_P_7_To - s_o)
487: e_7 = e_7T + e_7M
488: "= enthalpy(R1234ze(Z);T=converttemp(C;K;T_cc);x = 0)" "Condenser exit is at saturated liquid which is also the enthalpy at evaporator inlet"
489:
490: "! ====="
491: =====Cooling Capacity =====
492: =====
493: Delta_h_evap = ((enthalpy(R1234ze(Z),T= T_so,x = 1))- h_5)
494: Q_e = m_p*u *(Delta_h_evap)
495: "! ====="
496: =====COP =====
497: =====
498:
499: "!"
500: This might be the only spot where superheating is applied
501: "
502: Delta_h_gen = ((enthalpy(R1234ze(Z),T= T_po,x = 1))- h_5)" (enthalpy(R1234ze(Z);T= T_po;x = 0))"
503:
504: COP = u*(Delta_h_evap / Delta_h_gen)
505:
506: "! ====="
507: =====Exergy Calculation =====
508: =====
509: =====Solar Collector=====
510: E_dot_F_SC = m_dot_15*( e_15 - e_13)
511: $ifnot parametric table
512: G = 1373 [W/m^2]
513: $end
514:
515: $ifnot parametric table
516: m_dot_15 = 1000*(1/3600) [kg/s]
517: $end
518: I_sc = 1373 [W/m^2]
519:
520: E_dot_P_SC = m_dot_14*( (h_15 - h_14) ) - T_o*(s_15 - s_14))
521: "h_14 = enthalpy(Water; T = T_14; P = P_o)"
522: "s_14 = entropy(Water; T = T_14; P = P_o)"
523: "h_15 = enthalpy(Water; T = T_15; P = P_o)"
524: "s_15=entropy(Water; T = T_15; P = P_o)"
525:
526: E_dot_D_SC = E_dot_F_SC - E_dot_P_SC

```

```

527: "=====Storage Tank====="
528: E_dot_F_ST = m_dot_15*( e_15 - e_13)
529: E_dot_P_ST = m_dot_10*( e_10 - e_11)
530: E_dot_D_ST = E_dot_F_ST - E_dot_P_ST
531: "=====Generator====="
532: m_dot_4 = m_p
533: E_dot_F_GE = m_dot_10*( e_10 - e_11)
534: E_dot_P_GE = m_dot_4*( e_4 - e_7)
535: E_dot_D_GE = E_dot_F_GE - E_dot_P_GE
536: "=====Condenser====="
537: m_dot_5 = m_p*u + m_p
538: m_dot_12 = 1.904 [kg/s]
539: E_dot_F_CO = m_dot_5*( e_5 - e_6)
540: E_dot_P_CO = m_dot_12*( e_12 - e_13)
541: E_dot_D_CO = E_dot_F_CO - E_dot_P_CO
542: "=====Evaporator====="
543: m_dot_8 = m_p*u
544: m_dot_14 = 0.477 [kg/s]
545: E_dot_F_EV = m_dot_8*( e_9 - e_8)
546: E_dot_P_EV = m_dot_14*( e_14 - e_15)
547: E_dot_D_EV = E_dot_F_EV - E_dot_P_EV
548: "=====Ejector====="
549: E_dot_F_EJ = m_dot_4*( e_4 - e_5) "Fuel: motive mass*( Gen Exit - Ejector Exit )"
550: E_dot_P_EJ = m_dot_8*( e_5 - e_9) "Product: evaporator mass*( Ejector Exit - Evapoator Exit )"
551: E_dot_D_EJ = E_dot_F_EJ - E_dot_P_EJ
552: "=====Pump====="
553: E_dot_F_PM = W_pump_in
554: E_dot_P_PM = m_p*( e_7 - e_6)
555: E_dot_D_PM = E_dot_F_PM - E_dot_P_PM
556: "=====Throttling Valve====="
557: E_dot_F_TV = m_dot_8*( e_6M - e_8M + e_6T)
558: E_dot_P_TV = m_dot_8*( e_8T)
559: E_dot_D_TV = E_dot_F_TV - E_dot_P_TV
560:
561:
562:
563:
564:
565:
566:
567:

```

